January 2015

Ceres – VIS-IR Surface Composition Analysis: A Review In Advance Of The DAWN Mission

Daniela Henckel

Recommended Citation

Henckel, Daniela, "Ceres – VIS-IR Surface Composition Analysis: A Review In Advance Of The DAWN Mission" (2015). *Theses and Dissertations*. 1783.
https://commons.und.edu/theses/1783

CERES – VIS-IR SURFACE COMPOSITION ANALYSIS: A REVIEW IN ADVANCE OF THE DAWN MISSION

by

Daniela Henckel
Bachelor of Science, University of Potsdam, 2010

A Thesis

Submitted to the Graduate Faculty

of the

University of North Dakota

in partial fulfillment of the requirements

for the degree of

Master of Science

Grand Forks, North Dakota

May 2015

This thesis, submitted by Daniela Henckel in partial fulfillment of the requirements for the Degree of Master of Science from the University of North Dakota, has been read by the Faculty Advisory Committee under whom the work has been done and is hereby approved.

Dr. Michael J. Gaffey

Ronald A. Fevig

Dr. Ron Fevig

Seelan

Dr. Santosh Seelan

Dr. Gabriele Arnold

This thesis is being submitted by the appointed advisory committee as having met all of the requirements of the School of Graduate Studies at the University of North Dakota and is hereby approved.

____

Wayne Swisher

Dean of the School of Graduate Studies

____

Date

PERMISSION

Title	Ceres – A VIS-IR surface composition analysis: A review in advance of the DAWN mission
Department	Space Studies Department
Degree	Master in Science

In presenting this thesis in partial fulfillment of the requirements for a graduate degree from the University of North Dakota, I agree that the library of this University shall make it freely available for inspection. I further agree that permission for extensive copying for scholarly purposes may be granted by the professor who supervised my thesis work or, in his absence, by the Chairperson of the department or the dean of the School of Graduate Studies. It is understood that any copying or publication or other use of this thesis or part thereof for financial gain shall not be allowed without my written permission. It is also understood that due recognition shall be given to me and to the University of North Dakota in any scholarly use which may be made of any material in my thesis.

Daniela Henckel

Daniela Henckel

30. April 2015

TABLE OF CONTENT

LIST OF FIGURES

Figure Page

LIST OF TABLES

ACKNOWLEDGEMENT

Foremost, I would like to express my sincere gratitude to my primary advisors Dr. Michael J. Gaffey from the UND and Dr. Gabriele Arnold from the DLR for the continuous support of my Master thesis study and research, for their patience, motivation, enthusiasm, and immense knowledge. Their guidance helped me in all the time of research and writing of this thesis. I could not have imagined having better advisors and mentors for my Master thesis study. Besides my advisors, I would like to thank the rest of my thesis committee: Dr. Santosh Seelan and Dr. Ron Fevig from the UND for their encouragement, insightful comments, and hard questions.

I thank my fellow lab mate at the DLR Berlin, Kathrin Markus, for the stimulating discussions, for all the help and assistance she gave me during my thesis work and for all the fun we have had during our time at the DLR laboratory. Also I thank all the people that offered me the chance to conduct my research: Dr. Addi Bishop of the University of Münster, who provided me with the meteoritic samples for my research; Ines Büttner, who was helping and advising me during my laboratory work at the DLR and Dr. Ralf-Thomas Schmitt, the curator of the Naturkundemuseum in Berlin providing me with important minerals for my measurements.

Last but not the least, I would like to thank my family and friends: my parents Eva-Maria Henckel and Peter Henckel, for giving birth to me in the first place and supporting me spiritually and financially throughout my life; my aunt Marion Graupner, for being my travel companion and being a great support during this time and my best friend Anke Graap, who always listens to my ideas and thoughts and has been a real friend during this hard working time of my life.

ABSTRACT

Ceres has been heavily investigated during the last years prior to the DAWN mission. Although it is the largest object in the Main Asteroid Belt, its properties, especially the surface composition, are not well understood. Studies of Ceres surface composition and texture are of particular importance to generally analyze the interior and evolution of Solar System objects as well as the surface processes that are/were active on those bodies. VIS-IR spectroscopy is an effective method to detect characteristic absorption bands in the spectra of surface materials which can be related to the surface composition of planets and asteroids.

The primary aim of this work is to review the previous visible and infrared earth-based observations and the supporting laboratory work that have been done so far to get an overview on the possible surface composition of Ceres prior to DAWN's arrival. These data will be compared with complementary spectral measurements in the wavelength range of the VIR instrument onboard the DAWN spacecraft between 0.5 to 5 µm. Measured analogue materials include meteorites (CM, CO, and CV chondrites) and minerals (brucite, cronstedtite, tochilinite, buddingtonite). Additional spectra were collected from databases like Relab to increase the range of data. These data include spectra of meteorites, especially CM, CO, CV and CI chondrites, and of terrestrial analogue materials, e.g. montmorillonite, carbonates, water ice and frost, pyrite,

magnesite. Diagnostic spectral characteristics, like the wavelength of slope change, the spectral slopes in the VIS and NIR, and absorption bands, have been defined and analyzed in the available spectra. They are a useful tool to identify Ceres' surface materials and to draw implications for the DAWN composition analysis.

CHAPTER 1

INTRODUCTION

1.1. Motivation

Although Ceres is the largest object in the Main Asteroid Belt (MAB), its physical properties are still not well understood. While it is expected to have retained a large amount of primordial water ice in its interior or surface, many questions about the composition of Ceres' surface and sub-surface layers, the properties of its regolith and its degree of differentiation, are unanswered and have only been investigated based on models or telescope observations. It is expected that Ceres could have experienced many processes related to planetary evolution and survived the Late Heavy Bombardment nearly intact and without major resurfacing processes (McCord and Sotin, 2005). Thus, Ceres provides an excellent laboratory to gain knowledge on the accretion of the planetoids during the history of the Solar System and on the role of the volatile elements during those early stages of the Solar System history. It is fundamental to get a basic understanding of the development during the early stages of the Solar System and of the basic planetary processes (McCord and Sotin, 2005; Li et al., 2006). Furthermore, Ceres is of extremely high importance to understand the processes of planetary accretion and formation of the low-albedo primitive asteroids in the outer part of the Main Belt (Carry et al., 2008).

1 Ceres and 4 Vesta were chosen for the DAWN mission as both bodies are very different, but share the fact, that both objects are intact survivors from the early Solar System time (Russell et al., 2011). They span the region of the rocky inner solar system bodies and the wetter outer Solar System bodies. Both objects had undergone thermal evolution but with different maximum internal temperatures (Russell et al., 2006). 4 Vesta is assumed to be a dry body following the evolutionary processes of the magma ocean model and it is assumed that the HED meteorites (Howardites-Eucrites-Diogenites) are fragments of an impact event on Vesta (Russell et al., 2006). The situation is different for 1 Ceres as there are no known cerean meteorites which give hints about the evolution of the dwarf planet (Russell et al., 2004). It is assumed that Ceres could contain a large amount of water with a high probability of liquid water resulting in the lower density of the object (Russell et al., 2006). There are some similarities to the icy moons like Ganymede which has a similar density, surface and craters (Russell et al., 2006). The evolution of 1 Ceres is explained by the wet body model and the dwarf-planet could be completely frozen with a frozen solid crust overlying a convecting ice mantle. There are no current estimates for the age of Ceres' crust (Russell et al., 2006).

Studies of Ceres surface composition and texture are of particular importance to get information on the interior and evolution of solar objects as well as the surface processes of those bodies. VIS-IR spectroscopy (visual and infrared) is an effective method to detect absorption features to get information on the composition of planetary and asteroidal surfaces. Thus, this work will mainly focus on the spectral investigation of possible surface materials of Ceres in order to get information on the composition and the processes shaping Ceres' surface. The measurements are carried out at the spectral laboratory at the German Aerospace Institute (DLR) in Berlin Adlershof, Germany.

This work will elaborate in Chapter 1 the data gained in the pre-DAWN time including the physical properties, the evolution, the surface properties and the relevant data necessary for the DAWN mission. Chapter 2 will be on the methodology of this work. Chapter 3 will focus on the spectral data and analysis, Chapter 4 will discuss these results and Chapter 5 will be the conclusion.

1.2. State of Research

1.2.1. Facts and figures

Ceres is the largest body of the MAB and is situated in the middle of the asteroid belt (McCord and Sotin, 2005, Coradini et al., 2011). It contains nearly 1/3 (30-40%) of the total mass of the MAB (Rogozin, 2014) and observations indicate that Ceres is a G-type asteroid with low porosity (Tholen, 1984; Bus et al., 2002, Carry et al., 2008). G-type asteroids are a subgroup of carbonaceous asteroids (C-type; Barucci et al., 1987; Bus et al., 2002). They are low temperature condensates and have undergone little or no heating (Gaffey et al., 1993). It was the first object in the asteroid belt that was discovered. Giuseppe Piazzi, an Italian astronomer, spotted Ceres in 1801 while he was searching for a suspected planet, using the Titius-Bode law, in the gap between the orbits of Jupiter and Mars. Ceres was first classified as a planet, later reclassified as an asteroid and since 2006 Ceres belongs to the dwarf planets along with Pluto and Eris. Ceres was named after the Roman goddess of corn and harvest (NASA, a). It is assumed that Ceres could have experienced many processes that are related to planetary evolution (McCord and Sotin, 2005). During the last two decades there has been significant progress in the understanding of Ceres' surface and its interior due to increasing interest in the object, especially since the Dawn mission was launched, and due to the availability of new technology like sophisticated telescopes (Carry et al., 2008).

1.2.1.1. Orbit

Ceres has a mean heliocentric distance of a=2.767 AU (Solar System Dynamics; figure 1-1). The rotational period (see table 1-1) was determined to be between 9.07417 hours (NASA, b; Chamberlain et al., 2007) and 9.076 hours (Lagerkvist and Magnusson, 1990). The most recent determinations of the poles are:

- a = 973 ± 7km, c = 908 ± 9 km (Drummond and Christou, 2008) and
- Carry et al. (2008) derived a pole at 288+66km, with a =b = 959.4±4.6 and c = 888.8±4.2 km.

The eccentricity determined by Hilton (1998) is e=0.097 (osculating element). The NASA webpage states a value of e=0.079138251 (proper element, NASA, b) and the Solar Systems Dynamic Site states the eccentricity to be 0.07582. The proper element describes the time averaged value of the eccentricity, whereas the osculating element describes the eccentricity that was observed at a particular time or epoch. The values established for Ceres' inclination are 9.73 degrees (McCord and Sotin, 2005) and 10.59 degrees stated on the NASA webpage (NASA, b). Ceres obliquity is roughly 4 degrees (Carry et al., 2008; Chamberlain et al., 2009; figure 1-2). Ceres aphelion distance is 2.984 AU and its perihelion distance is 2.547 AU (NASA, b).

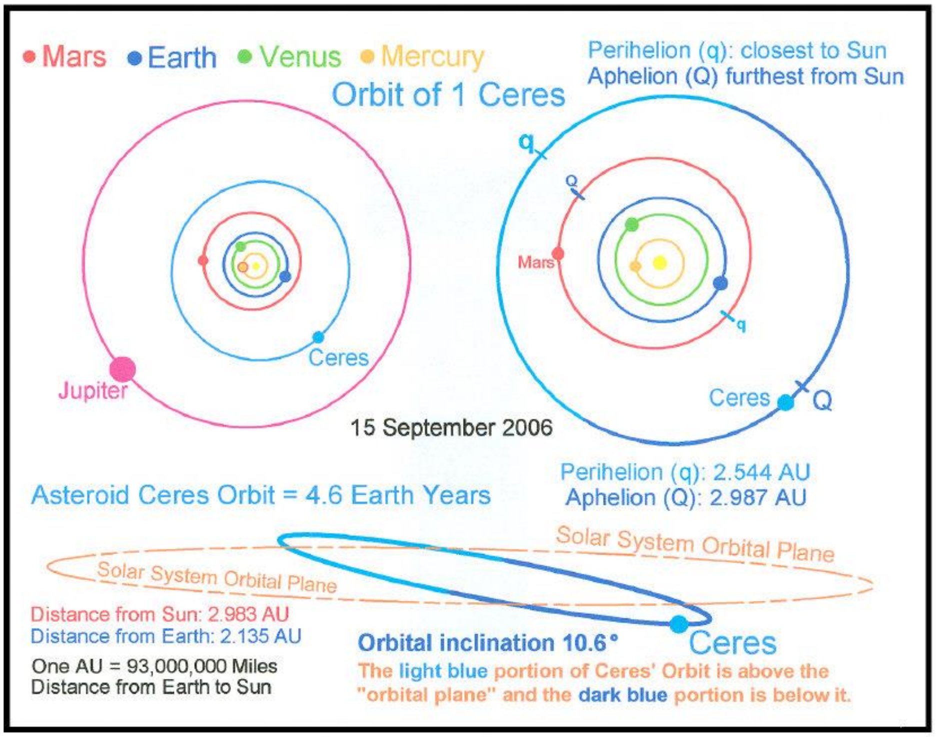

Figure 1-1. *The diagram illustrates the orbit of Ceres (light blue) and several planets. The segments of orbits below the ecliptic are plotted in darker color. The top left diagram is a polar view that shows the location of Ceres in the gap between Mars and Jupiter. The top right is a close-up demonstrating the locations of the perihelia (q) and aphelia (Q) of Ceres and Mars. Interestingly, the perihelia of Ceres (as well as those of several other of the largest MBAs) and Mars are on the opposite sides of the Sun. The bottom diagram is a perspective view showing the inclination of the orbit of Ceres compared to the orbits of Mars and Jupiter. From Solar System Dynamics.*

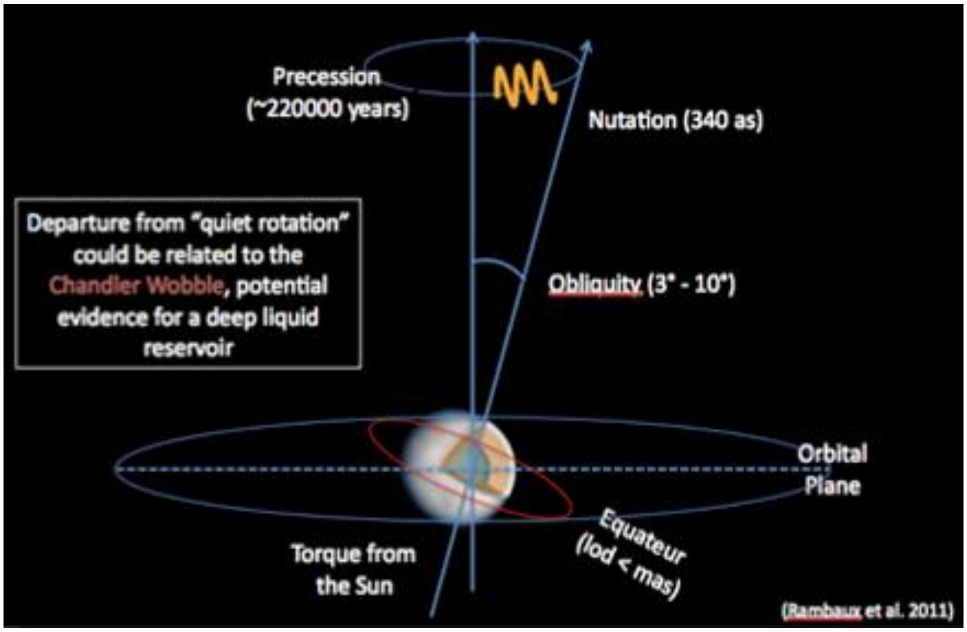

Figure 1-2. *Ceres' unique rotation shows potential evidence for a deep liquid reservoir within its interior. From: NASA (a).*

Table 1- 1. *Overview of the most recent published physical properties of Ceres and its orbit. Sources of the individual values are stated within the table.*

ORBIT *Semi-major axis*	2.7 AU	NASA (b)
Orbital period	4.6 yrs	AstDys
Rotational period	9.074170 hrs	Warner et al. (2009)
Pole orientation	291° RA and 59° Dec	Parker et al. (2006)
Eccentricity	0.079138251	NASA (b)
Inclination	10.59	NASA (b)
Average orbital velocity	17.88 km/second	NASA (b)
Perihelion	2.547 AU	NASA (b)
Aphelion	2.984 AU	NASA (b)
Obliquity	12.31°	Bills and Nimmo (2011)
Mean radius	476.2 km	NASA (b)
Diameter	952.4 km	JPL Small-Body Database
Mass	$4.679 \pm 0.033 \times 10^{-10}$ M_{Sun}	Konopliv et al. (2011)
Density	2.09 g/cm^3	NASA (b)
SURFACE PROPERTIES		
Albedo	~0.08 0.09 (visible)	Zolotov (2009) Li et al. (2006, 2009)
Temperature	167 K (surface) 235 K (equator)	Rousselot et al. (2011) Li et al. (2006)
Surface gravity	0.28 m/s^2	NASA (b)
Thermal inertia of the regolith	$3.8 \pm 1.4 \times 10^4$ erg cm^{-2} $sec^{-1/2}$ K^{-1}	Saint-Pe et al. (1993)

1.2.1.2. Shape and Size

Although there have been investigations of Ceres for many years its true mass and dimensions are still uncertain (Zolotov, 2009). Pre-DAWN, three methods have been used to determine the size and shape of Ceres: 1) the occultation of a star by Ceres, 2) the Earth-orbital Hubble Space Telescope (HST) camera direct imaging, and 3) adaptive optics (McCord and Sotin, 2005). Table 1-1 shows the most recently published values on the shape and size of Ceres. Ceres is assumed to be a relaxed object which means that its shape is determined by hydrostatic equilibrium (Thomas et al, 2005; Carry et al., 2008).

Early estimates showed that Ceres has an equatorial radius of 479.6±2.4 km and a polar radius of 453.4±4.5 km (occultation; Millis et al, 1987). Ceres axes determined by HST observations are 487.5 km for its equatorial radius and 454.5 km for its polar radius (Parker et al, 2006). Carry et al. (2008) determined the semi-axes with a=b=479.7±2.3 km and c=444.4±2.1 km. Ceres mean radius varies between 467.6±2.2 km (Carry et al., 2008) and 484±20 km (Saint Pe et al., 1993), or 476.2±1.7 km published by Thomas et al. (2005).

According to Parker et al. (2002) it is more likely to assume the higher density for Ceres of 2.206±0.043 g/cm^3 (Carry et al., 2008) as this is consistent with an object that is homogenous and in hydrostatic equilibrium. Objects with a lower density and with the size and rotation period of Ceres would have differences in the equatorial and polar radius of roughly 40 km due to rotational flattening. However, the difference between the polar and the equatorial radius occurs to be only 18.4±7.8 km. This implies that there is no significant rotational flattening and thus, an internally homogenous body is unlikely (Parker et al., 2002).

As illustrated in figure 1-3 and measured with Limb profiles, it is believed that Ceres is a rotationally symmetric, oblate spheroid (Millis et al., 1987; Parker et al., 2002; Drummond and Christou, 1998; Thomas et al, 2005; Carry et al., 2008). Chamberlain et al. (2009) assumed that it is a smooth, oblate spheroid-shaped and gravitationally relaxed object differentiated into a rocky core and ice-rich mantle. This is supported by Thomas et al. (2005) who showed that Ceres is a polar flattened object which is consistent with a relaxed differentiated body with a rocky core and an icy mantle.

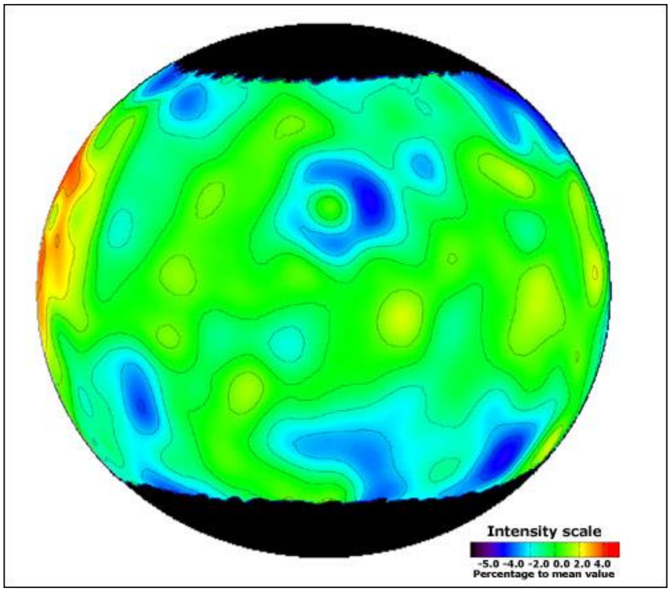

Figure 1-3. *Ceres has the shape of an oblate spheroid. Green areas are close to zero elevation, blue areas are related to -3.0 to -4.0 (low) and red areas are equal to +4.0 (high). From W.M. Keck Observatory.*

1.2.1.3. Mass

The mass of Ceres is determined by measuring the perturbations of Ceres' mass on the orbits of other bodies like Mars or other asteroids (McCord and Sotin, 2005) or by measuring the gravitational perturbations experienced during the approach at close encounters of Ceres with other large asteroids (e.g. 5303 Parijskij; Kovacevic and

Kuzmanoski, 2007). The most recent determination of Ceres' mass is 9.47 x 10^{20} kg stated by NASA fact sheet on Ceres (NASA, b).

1.2.1.4. Density

The values of Ceres' density found vary between 2.03±0.05 g/cm^3 (Michalak, 2000) and 2.206±0.043 g/cm^3 (Carry et al., 2008).

Ceres' density is similar to the density of the CM chondrites (average density of CM chondrites is 2.20 g/cm^3; Macke et al., 2011), of Pallas (2.8 g/cm^3) and of icy moons like Ganymede (1.936 g/cm^3; Anderson et al., 1996; McCord and Sotin, 2005; Mousis and Alibert, 2005) or Callisto (1.8344±0.0034 g/cm^3; Anderson et al., 2001).

Ceres density is low compared with other differentiated objects. Possible explanations for this low density of the body are:

1. Studies done by Cyr et al. (1998) and Mousis and Alibert (2005) suggest that Ceres contains a significant amount of volatiles like H_2O, CO_2, CO, CH_4, N_2, NH_3, Ar, Xe and Kr in its interior contributing to the low density of the object.
2. A water ice amount of roughly 20% of the total mass could also contribute to the low density of Ceres (Mousis and Alibert, 2005). McCord and Sotin (2005) suggest a possible water content of 17-27% by mass, the rest might be anhydrous material. This is supported by the detection of a tenuous atmosphere around Ceres indicating water ice on the surface (A'Hearn and Feldman, 1992; Mousis and Alibert, 2005).

3. Zolotov (2009) assumes that the low density implies a significant amount of low-density material made of hydrated and OH-bearing minerals like phyllosilicates, salts or hydroxides, ices, clathrate hydrates and organic compounds.
4. The internal structure is differ substantially from the assumed models including a regolith layer with a significant porosity (Mousis and Alibert, 2005). However, this seems unlikely as objects with a volume of $\geq 10^7$ km^3 become near-spherical in shape as the pore space is eliminated by compression due to gravity (McCord and Sotin, 2005; Thomas et al, 2005).

1.2.1.5. Topography

The extensive observational studies did not identify any specific geologic feature at the surface of Ceres (Castillo-Rogez and McCord, 2010). The true topography will be revealed by the DAWN spacecraft arriving at Ceres in spring 2015.

Despite this situation, some work has been done showing that topography is still possible. Calculations done by Carry et al. (2008) imply that the highest relief on Ceres could be 10 to 20 km. If water ice is incorporated into Ceres' near surface regions, the reliefs in large impact basins on icy satellites like Tethys will be a good equivalent for Ceres possible topography (Thomas et al., 2005). Normally, on icy satellites the largest craters are shallower than the small ones (Thomas et al., 2005). Thus, relief on Ceres might be reduced due to higher surface temperatures than on the icy moons, but a substantial crater record is possible without affecting Ceres' basic relaxed shape (Thomas et al., 2005). The assumed smoothness of Ceres' relief is supported by HST observations.

They show that the body deviates a maximum of 5 km from a relaxed spheroid (Thomas et al., 2005; Castillo-Rogez and McCord, 2010; Bland, 2013).

The crater morphology on Ceres is affected by the composition of the possible ice layer, its particulate fraction and density (Li et al., 2006; Bland et al., 2013; Bland, 2013). Bland (2013) modeled the crater morphology as a function of temperature and material strength. The results indicate that the crater density in the equatorial region could be much lower than it would be expected for a rocky body.

1.2.1.6. Evolution

Ceres is assumed to be a differentiated object based on the density, shape and size data, where the heavy material sank to the core and the lighter phases built the outer parts of Ceres. The size and orbit of Ceres suggest that the body was not fragmented and remains in its size and location from formation (McCord and Sotin, 2005). According to compositional ideas such as CC material plus an unknown amount of water ice, Ceres is expected to have been accreted from a mixture of ice and rock (McCord and Sotin, 2005) or an accretion from anhydrous minerals, organics and water ice (Fanale and Savail, 1989). There is little or no direct evidence concerning Ceres' formation time (Castillo-Rogez and McCord, 2010) but there are models suggesting an early accretion (Castillo-Rogez and McCord, 2010) and a late accretion (Zolotov, 2009). Two possible evolution models are explained as follows: one is assuming a differentiated object with a near surface ice-layer hundreds of km thick whereas the other is assuming a homogenous, ice-poor interior structure. There is currently little evidence on the surface of Ceres for an active geologic past (Bland, 2013). The real composition of Ceres remains unclear until the arrival of the DAWN's spacecraft in spring 2015.

Model after Zolotov (2009). The model after Zolotov (2009) is shown in figure 1-4 and assumes an undifferentiated body that consists of low-density hydrated material, like phyllosilicates, hydrated salts or organics, with a grain density similar to the CI-chondrites (Zolotov, 2009). It implies that Ceres accreted late but rapidly in the Solar System history from pervasively hydrated planetesimals, or by in situ aqueous alteration of contained ice, with no porosity collapse during heating by long-lived radiogenic species (Castillo-Rogez, 2011). The inertial temperature was 200 Kelvin (K). The center of the body reached temperatures greater than those of the melting point of ice in less than 5 million years. In the next 10 million years the temperature profile was controlled by ice melting. After that period, the body began to cool down and reached it recently assumed temperature of 350 K. Using this model it is expected that there is still liquid water in Ceres' interior even today (McCord and Sotin, 2005), most likely in the form of an aquifer, a rocky matrix where the porosity is filled with liquid water (Dr. Gaffey, personal communication).

This model leads to an object with a homogenous mixture of ice and silicate grains divided into a homogenous rock-ice core overlain by a water layer (McCord and Sotin, 2005).

Model from McCord and Sotin (2005) and Parker et al. (2005). This model assumes a differentiated Ceres with a rocky core surrounded by an icy mantle (figure 1-4) or a rocky core surrounded by a deep layer of anhydrous silicates and an icy mantle (Castillo-Rogez and McCord, 2010). A differentiated Ceres would indicate that the dwarf planet accreted early in the Solar System's history and was followed by hydrothermal activity driven by the decay of short-lived radiogenic species like ^{26}Al and ^{60}Fe (Castillo-

Rogez and McCord, 2010). The hydrothermally altered core could later dehydrate with volume changes causing disruption of the surface (McCord and Sotin, 2005). The dehydration would create a layered core structure that could enable partial melting of the silicates (Castillo-Rogez and McCord, 2010). The water segregates from the silicates when the temperature exceeds the ice melting temperature. This would occur quickly on Ceres within geological timescales of roughly 10 million years after accretion. The ice and rock did not melt to the surface and the thickness of the ice layer is controlled by the heat flux. The thermal evolution is controlled by the water layer which led to a cooling from above and results in a 3-layer structure: original ice silicate mixture, a liquid mantle and a silicate core. This evolution model would lead to an inner core density of 3.44 g/cm^3 and an outer liquid water layer in the form of an aquifer with a thickness or roughly 100 km (McCord and Sotin, 2005).

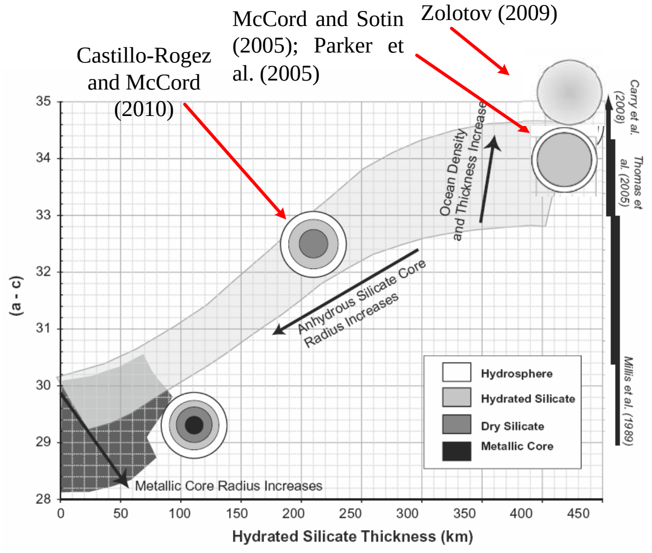

Figure 1-4. *Summary of possible thermal evolution models compared against shape data available for Ceres (modified after Castillo-Rogez and McCord, 2010). A-C is the equatorial minus the polar radius. There are four models for Ceres evolution: a) a porous hydrated mineral assemblage (Zolotov, 2009) b) a structure stratified in an icy shell and a core dominated by hydrated silicates (McCord and Sotin, 2005; Thomas et al., 2005), b) same as b) but with a deep layer of anhydrous silicates (Castillo-Rogez and McCord, 2010) and d) a fully differentiated Ceres.*

It is still under debate whether Ceres accreted in its current position in the asteroid belt (Zolotov, 2014; McCord and Sotin, 2005) or whether it has its origin deeper in the Solar System and moved later to its current position. The latter could be supported by the abundant amount of free water on Ceres (McCord and Sotin, 2005). Mousis and Alibert (2005) support this thesis as icy planetesimals that have been developed in distances greater than 5 AU can drift inwards to the current location of Ceres and may be accreted by the forming asteroid. This theory was also considered by O'Brien and Sykes (2011). They assumed that Ceres has a significant amount of water ice and might has accreted somewhere beyond the ice line. The snowline divides the Solar System objects into dry bodies (ranging to the AMB) and icy bodies in the region beyond the asteroid belt (McKinnon, 2008; McKinnon, 2012; Küppers et al., 2014). O'Brien and Sykes stated that Ceres might have had a greater distance to the Sun than it has today. Its current semi-major axis is 2.76 AU and C-type asteroids (Ceres is assumed to be a rare G-type asteroid, a subclass of the C-type) have a peak abundance at 3 AU. Thus, it could be possible that Ceres was scattered inwards (O'Brien and Sykes, 2011).

1.2.1.7. Internal Structure

Interior models of Ceres are strongly dependent on the assumed compositions of Ceres (Mousis and Alibert, 2005). There are currently four models describing the internal structure of Ceres (see figure 1-5):

a) an undifferentiated, homogenous (water and high density silicates), porous interior and no relaxation (Thomas et al., 2005; McCord and Sotin, 2005)

b) a differentiated Ceres with high-density core equivalent to Vesta with a core radius of 350 km or a low-density serpentine core with a radius of 425 km (McCord and Sotin, 2005)

c) same as b but including anti-freezing materials like ammonia maintaining a liquid layer (McCord and Sotin, 2005). This would require that the crust is composed predominantly of water ice, if not, the crust would sink down as rock does not flow on water (Dr. Gaffey, personal communication) and

d) a fully differentiated model of Ceres with an inner iron core (McCord and Sotin, 2005).

This last model seems highly unlikely as the inclusion of a significant amount of water ice into the body would prevent internal temperatures from approaching the melting point of rocky/metallic phases (Dr. Gaffey, personal communication).

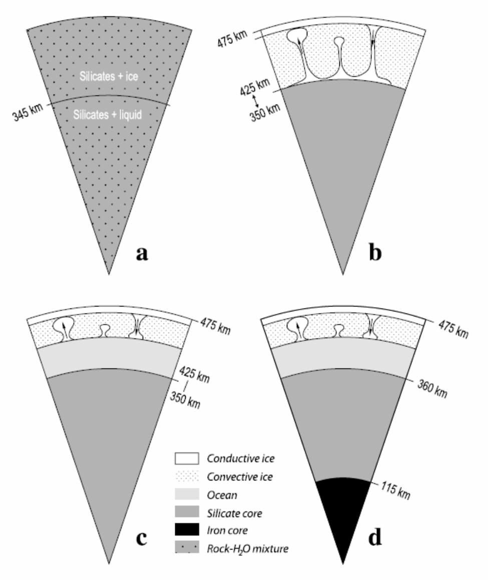

Figure 1-5. *Different internal structures based on different scenarios. A) homogenous asteroid made of a mixture of water and high-density silicates, b) differentiated Ceres with high-density core equivalent to Vesta and a core radius of 350 km or a low-density serpentine core with a radius of 425 km, c) same as b but including anti-freezing materials like ammonia which maintain a liquid layer and d) fully differentiated model of Ceres within an inner iron core. From McCord and Sotin (2005).*

The most reasonable and by HST observations supported model is a differentiated Ceres with a rocky inner core covered by an icy mantle layer and a dusty surface layer (figure 1-5 b and c, 1-6 and 1-7). There is a 30 km difference between the observed polar and equatorial radius indicating an internal mass distribution. This is supporting a differentiated, not homogenous Ceres, with an internal structure somewhere between the 2 end-members (figure 1-5, a,d; McCord and Sotin, 2005). According to Mousis and Alibert (2005), this model is in accordance with the oblateness of Ceres. Investigations done by Thomas et al. (2005) indicate that there is a mass concentration toward the center of the object. According to Ceres low density, it is expected that Ceres is composed of rock and variable amounts of water ice (maximal 25%; McCord and Sotin, 2005). The uniformly spheroidal shape, the deprived strong surface and topographic features and the low density of Ceres indicate that volatile elements in the interior of Ceres are possible (Carry et al., 2008). If Ceres contains volatile elements in its interior, they were most likely to be in the form of clathrate hydrates, hydrates or pure condensates (Mousis and Alibert, 2005).

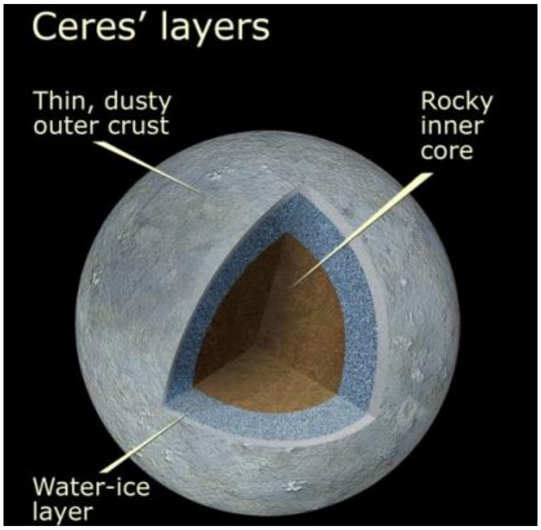

Figure 1-6. *Cutaway view of Ceres showing the differentiated layers of the dwarf planet. From NASA (b).*

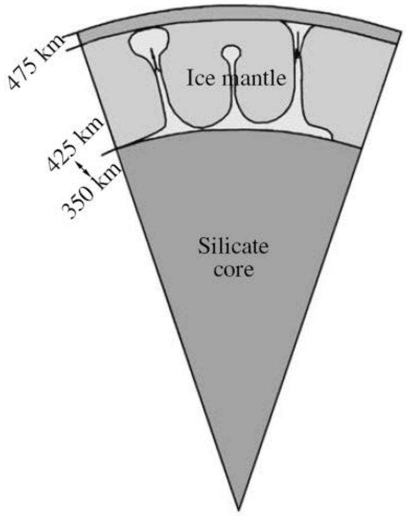

Figure 1-7. *The model of the internal structure of Ceres according to McCord and Sotin (2005).*

Recent investigations of Ceres with the Herschel telescope lead to the detection of water vapor on Ceres. The telescope found plumes shooting-up periodically. This is proof that Ceres has an icy surface and an atmosphere. There is a clear spectral signature in the FIR for water ice but the signal strength varies over time due to its rotation (ESA).

1.2.2. Surface Properties

Early observations of Ceres started with the study done by Herschel in 1802 (Herschel, 1802). The work on the reflectance spectra of asteroids began in the 1920s and 1930s (e.g. Bobrovnikoff, 1929; Johnson, 1939) but the first reliable spectral information on Ceres was found in the 1970s for example by Chapman et al. (1973). It was recognized that the surface is dark and spectrally neutral as there are no diagnostic absorption features in the spectrum of Ceres (Chapman et al. 1973; Cruikshank and Morrison, 1973; Zellner et al. 1974). According to the modelling of the spectral properties of carbonaceous chondrites and the measurement of their properties in the wavelength range of 0.4-2.5 µm done by Chapman and Salisbury (1973), Johnson and Fanale, (1973) and Gaffey (1976), Ceres is associated with the C-class asteroids and the carbonaceous (CC) chondrites (Lebofsky, 1978). More recent investigations infer that Ceres belongs to the G-type asteroids, a sub-group of the C-type asteroids (Rivkin et al., 2010). C-type asteroids, first classified by Chapman et al. (1973), have a low albedo (3.5-5%; Bowell et al., 1978) and have a chondritic composition. The spectra of C-type asteroids are bluish (the reflectance diminishes with increasing wavelengths), flat and weakly featured (see figure 1-8; Gaffey et al., 1993). These asteroids are composed of hydrated silicates, carbon, organics, opaque materials and shock-darkened silicates (Nelson et al., 1993). The meteorite analogues for C- and G-type asteroids are CI (Ivuna-like CCs) and CM (Murchison-like CCs) chondrites (Bell et al., 1989).

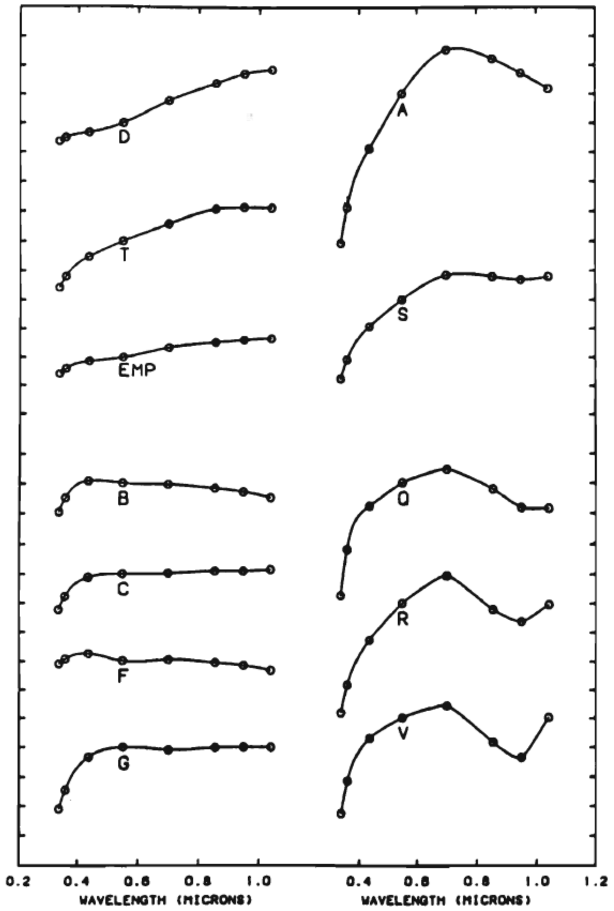

Figure 1-8. *Mean reflectance spectra for Tholen asteroid classes. Tick marks on the ordinate are spaced 0.2 magnitudes apart. From Tholen and Barucci (1989)*

1.2.2.1. Spectral Properties

Ceres has been subjected to intensive studies in the past. In general, there are very little rotational variations in the 0.4-4.0μm region that suggest that the surface features and the background regions have very similar mineralogies differing from one another only slightly (Rivkin et al., 2010). The spectral region with the greatest sensitivity to surface heterogeneity at 3 μm is poorly constrained by Earth observations due to the strong interference from atmospheric water vapor (Dr. Gaffey, personal communication). Ceres' spectrum has a strong blue slope (decreasing reflectance with increasing wavelength) in the far- to mid-UV, a slightly red slope (increasing reflectance with increasing wavelengths) in the VIS and IR (Parker et al., 2002).

Composition of carbonaceous chondrites: CI chondrites. CI chondrites are an important group of the CCs to understand the origin and evolution of the Solar System. This group of CC meteorites is composed of a diversity of subgroups that have exhibited various degrees of thermal and/or aqueous alteration, but they are all characterized by a general dark appearance and similar spectral shapes (Cloutis et al., 2011a). CI chondrites have an astro-biological importance as their carbon-bearing phases are organic and include many biological precursor materials (Nagy, 1975). Furthermore, these meteorites could have been an important source of water for the Proto-Earth (Morbidelli et al., 2000). CI chondrites contain 50-60 vol% phyllosilicates, predominantly serpentines and saponite, intergrown with ferrihydrite, oxides (magnetite and maghemite), accessory sulfides (pyrrhotite, pentlandite, cubanite), carbonates and sulfates (Richardson, 1978; Zolensky and McSween, 1988; Buseck and Hua, 1993; Zolensky et al., 1993; Brearley and Jones, 1998; Gounelle and Zolensky, 2001). CI chondrites have the highest matrix abundance compared to other CCs (Buseck and Hua, 1993). Table 1-2 summarizes the modal mineralogy of an Orgueil CI chondrite.

Table 1-2. *Modal mineralogy of the Orgueil CI chondrite after Bland et al. (2004).*

Phase	Wt%	Vol%
Olivine Fo 100	2.4	2.1
Olivine Fo80	3.3	2.6
Olivine Fo 60	1.5	1.1
Troilite	2.1	1.2
Pyrrhotite	4.5	2.7
Ferrihydrite	5.0	3.7
Magnetite	9.7	5.1
Saponite-serpentine	64.2	73.8
serpentine	7.3	7.7

Composition of carbonaceous chondrites: CM chondrites. CM chondrites are important meteorites in understanding the origin and evolution of the Solar System as they are among the oldest and most primitive rocks (Cloutis et al., 2011b). CM chondrites are aqueously altered rocks and thus, belong to the petrologic group 2 (Cloutis et al., 2011b). They contain roughly 9 wt% (weight percent) water which is bound in the phyllosilicates (Rubin et al., 2007). CM chondrites contain roughly 20 vol.% (volume-%) chondrules, 1-11 vo.% inclusions, 4-21 vol.% mineral fragments, up to 3vol.% opaque phases and 57-85 vol.% phyllosilicates-rich matrix (e.g. Grossman and Olsen, 1974; McSween, 1979). Other minor compounds include carbonates and sulfides (Zolensky and McSween, 1988). The most abundant phases are Mg-serpentine (49-59vol.%) and Fe-cronstedtite (43-50 vol.%; Cloutis et al., 2011b). Cold Bokkeveld contains more Mg-serpentine (up to 59 vol.%) than Fe-cronstedtite (maximal 27 vol.%) (Howard et al. 2009 2011). Table 1-3 shows the composition of the CM chondrite Murchison.

Table 1- 3: *Modal mineralogy of the Murchison CM2 chondrite after Bland et al. (2004).*

Phase	Wt%	Vol%
Olivine Fo 100	7.4	6.8
Olivine Fo80	2.2	1.9
Olivine Fo 50	2.0	1.6
Clinoenstatite En 98	2.2	1.9
Pyrrhotite	2.9	1.8
Pentlandite	0.5	0.3
Magnetite	0.4	0.2
Serpentine	22.8	26.2
Cronstedtite/tochilinite	58.5	58.1
calcite	1.1	1.2

Composition of carbonaceous chondrites: CO chondrites. CO chondrites (Ornans-like CCs) have the petrologic type 3 (McSween, 1977; Barber, 1985, Brearley and Jones, 1998) which have to be affected by metamorphism (Greenwood and Franchi, 2004). They are dominated by olivine of variable composition with only little phyllosilicates (Rubin et al., 1985; Zolensky et al., 1993). The matrix of CO chondrites is composed of fine-grained olivine (dominant phase is $Fa_{30\text{-}60}$) with a lesser amount of pyroxene (McSween, 1979a; Brearly and Jones, 1998; Buseck and Hua, 1993), few kamacite, taenite, chromite, ferrihydrite and minor serpentine (Zolensky et al., 1993). Phyllosilicates are just a minor component in CO chondrites (Keller and Buseck, 1990a, b) and are, if present, alteration products from pre-exiting matrix olivine. Fe-rich serpentine is the dominant phase of phyllosilicates (Keller and Buseck, 1990b). Opaque phases are pre-dominantly carbonaceous phases, NiFe metal and troilite (Cloutis et al., 2012a).

Composition of carbonaceous chondrites: CV chondrites. CV chondrites (Vigarano-like CCs) are of importance as the Allende meteorite gave the best estimates for the age of the Solar System and the timing of formation (Chen and Wasserburg, 1981). Furthermore, they have been linked to a number of possible parent bodies by using spectral criteria (Burbine et al., 2001). CO chondrites are petrologic type 3 (McSween, 1977, 1979a) and are composed of olivine (>75vol%), lesser amounts of enstatite, plagioclase, magnetite, sulfides and metal (Howard et al., 2009a) and 0.01-1.5wt% carbon (Pearson et al., 2006; Alexander et al., 2007), decreasing with increasing metamorphic grade (Guimon et al., 1995). Aqueously alteration ranges from highly alteration to extremely low alteration (Brearley and Jones, 1998; Gyollai et al., 2011). Phyllosilicates in CO chondrites are mainly low-Al, fine-grained saponites and various micas (Keller and Buseck, 1990b; Keller and McKay, 1993), serpentine and chlorite are also present (Keller and McKay, 1993). In table 1-4 is shown the modal mineralogy of the CV chondrite Allende after Bland et al. (2004).

Table 1-4. *Modal mineralogy of the CV chondrite Allende after Bland et al. (2004).*

Phase	Wt%	Vol%
Olivine Fo 100	20.5	23.4
Olivine Fo80	14.6	15.4
Olivine Fo50	21.4	20.6
Olivine Fo60	20.8	20.6
Olivine Fo25	4.3	3.9
Pentlandite	11.1	8.0
Clinoenstatite	5.9	6.6
Magnetite	0.3	0.2
Plagioclase (An100)	0.9	1.2
Fe-metal	0.2	0.1

Ceres in the ultraviolet wavelength range (UV, 0.01-0.4 µm). Generally, there is a lack of laboratory data and diagnostic absorption features at UV wavelength of Ceres. However, as Ceres is related to the G-type asteroids, it has a very strong UV absorption (Lupishko and Mohamed, 2009; Rivkin et al., 2010). Normally, reflectance values for all asteroids decrease at UV wavelength, which could be explained by strong charge-transfer absorption of iron-bearing minerals (Cloutis et al., 2008). The reflectance drop in Ceres spectrum in the UV is relatively sharp and occurs at ~400 nm (0.4 µm, see figure 1-9) which is shorter than that for other asteroids and could be explained by a lack of iron-rich materials on the surface of Ceres (Rivkin et al., 2010). Parker et al. (2002) detected an absorption band centered at ~280 nm (0.28 µm), seen in figure 1-9. A'Hearn and Feldman (1992) detected an OH emission at 0.3085 µm (see figure 1-9). This is not supported by studies done by Rousselot et al. (2011) who did not detect any OH absorption lines in their spectra.

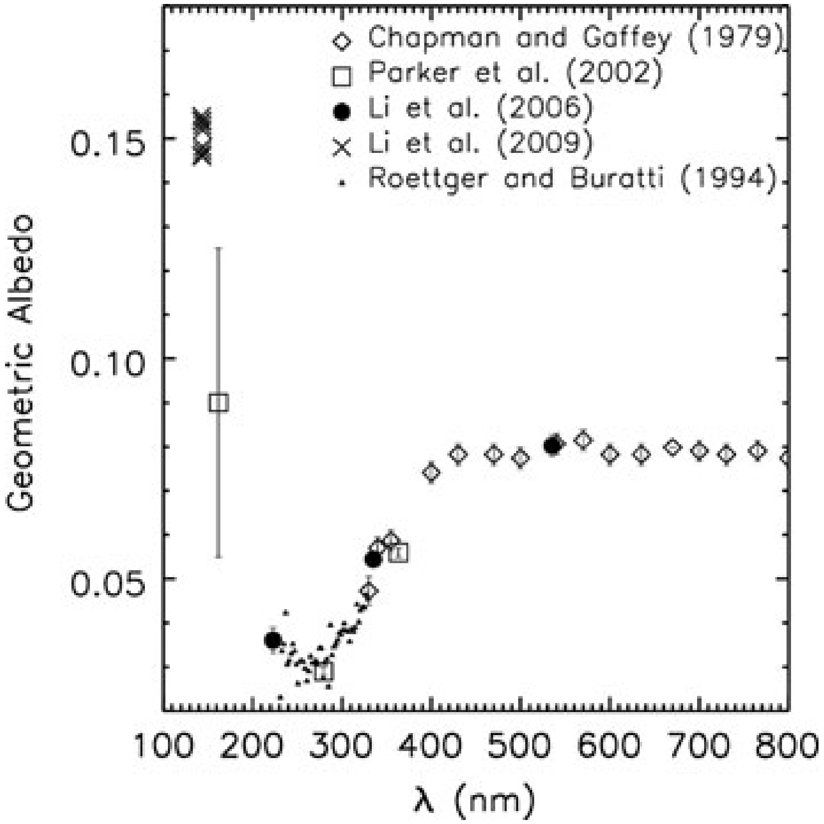

Figure 1-9. *UV spectrum of Ceres. The data was taken from different observations. Diamond symbols are from the 24-color survey (Chapman and Gaffey, 1979). Squares are from HST/FOC (Parker et al., 2002). Filled circles are from HST/ACS/HRC (Advanced Camera for Surveys/High Resolution Channel; Li et al. 2006). Crosses are from HST/ACS/SBC (Solar Blind Channel; Li et al. 2009), but are likely an overestimate of the albedo of Ceres due red leaks in the filter. The small triangles are from International Ultraviolet Explorer (IUE; Roettger and Buratti 1994). The error bars are actually smaller than the size of symbols. The 24-color survey data are normalized to HRC measurement at 550 nm. The IUE data are scaled to match HST measurements from 220 to 330 nm. All other data are independently radiometrically calibrated for the albedo. From Rivkin et al. (2011).*

Ceres in the visible wavelength range (VIS, 0.4-0.8 µm). The VIS and NIR are the most accessible spectral regions to investigate asteroids as there are abundant diagnostic features in these spectral ranges to get information on the possible surface composition of the object (Rivkin et al., 2011). The reflectance spectrum of Ceres is weakly featured in this wavelength range (figure 1-10: Lebofsky, 1978; Rivkin et al., 2011; Hiroi et al., 1996; Cloutis et al., 2011a,b&2012a,b).

The Ceres's spectrum between 0.4-1.0 µm is flat and featureless with a strong decrease in reflectance shortward of about 0.45 µm (figure 1-10; McCord and Sotin, 2005). Absorption features of Ceres' spectrum are shown in figure 1-10. A weak feature is seen near 0.6 µm (figure 1-10) attributable to charge transfer in aqueous alteration products. Similar features are found at longer wavelengths in carbonaceous chondrites (Rivkin et al., 2010, De Sanctis et al., 2012).

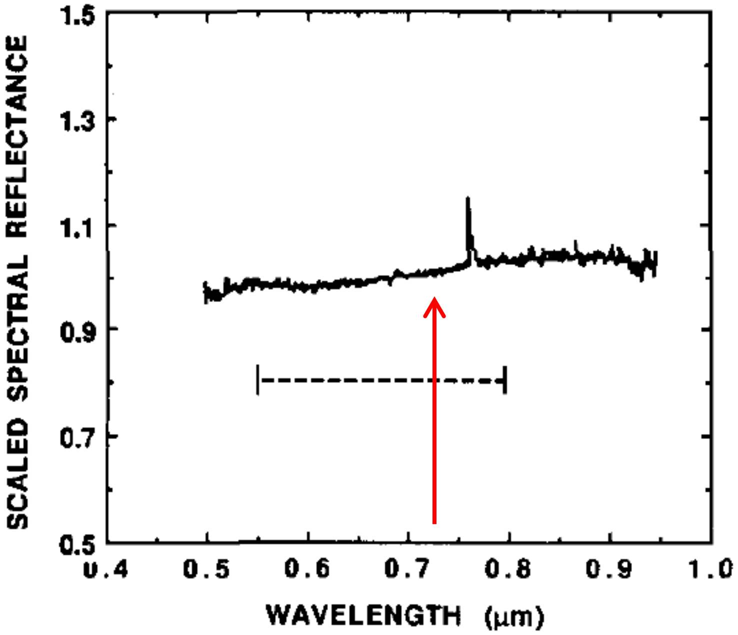

Figure 1-10. *CCD reflectance spectrum of 1 Ceres. The dashed line marks the wavelength range of the weak absorption feature and the red arrow marks it minimum at 0.6 µm. The peak at ~0.765 µm is due to O_2-A. From Vilas et al. (1993)***.**

Ceres in the near-infrared wavelength (NIR, 0.8 – 2.5 µm). In the NIR region the spectrum shows slightly rising reflectance toward the longer wavelengths with no discernable absorption features (McCord and Sotin, 2005; see figure 1-11). There is a broad absorption feature centered near 1.2 µm and it is suggested that this is due to magnetite (Rivkin et al., 2010). There is no feature seen at 1.9 µm (see figure 1-11) indicative for extensive water on the surface (McCord and Sotin, 2005). A possible explanation for the missing features is that the feature is too weak to overcome the effects of the opaque phase or phases (Dr. Gaffey, personal communication). The main feature in the VNIR spectra of Ceres is the decrease in reflectance shortward of 0.4 µm (see figure 1-11). This feature could be attributed to an intervalence charge transfer band of iron oxides (Fe^{2+}/Fe^{3+}) (Rivkin et al., 2011) and is indicative for identifying the different types of C-class asteroids according to the Tholen classification (Tholen and Barucci, 1989; Rivkin et al., 2011).

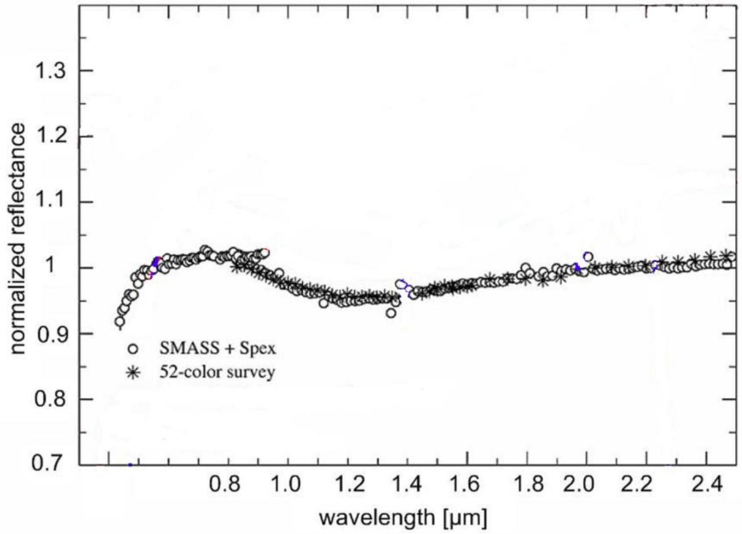

Figure 1-11. *Ceres' spectrum in the 0.4–2.5 µm region is largely free of diagnostic absorptions. It possesses a drop off in reflectance in the UV spectral region, due to oxidized iron and common to many materials. It also has a band centered near 1.2 µm, which is likely due to* Fe^{2+}. *This feature is also seen in some CC's. It is suggested that this feature is due to magnetite or lizardite. SMASS/SPEX data are from Bus and Binzel (2002a, 2002b) and 52-color survey data are from Bell et al. (1988). Modified after Rivkin et al. (2011).*

Ceres in the mid-infrared (MIR, 2.5 – 16 µm). In the spectral region beyond 2.5 µm (see figure 1-12) there are a number of vibrational absorptions like those of water, hydroxyl, organic matter, carbonates, carbon dioxide, ammonia and other volatiles (Rivkin et al., 2011). Especially the 3 µm region allows first suggestions on the surface composition but it is difficult to observe this spectral range from Earth as there is interference from water and methane in Earth's atmosphere (Rivkin et al., 2010). A feature near 3 µm would indicate that there are hydrated minerals present (King et al., 1992; De Sanctis et al, 2012). There is currently no data available for the spectral range around 2.7 to 2.8 µm (see figure 1-13) as the Earth's atmosphere is opaque in this wavelength region due to water vapor (Dr. Gaffey, personal communication).

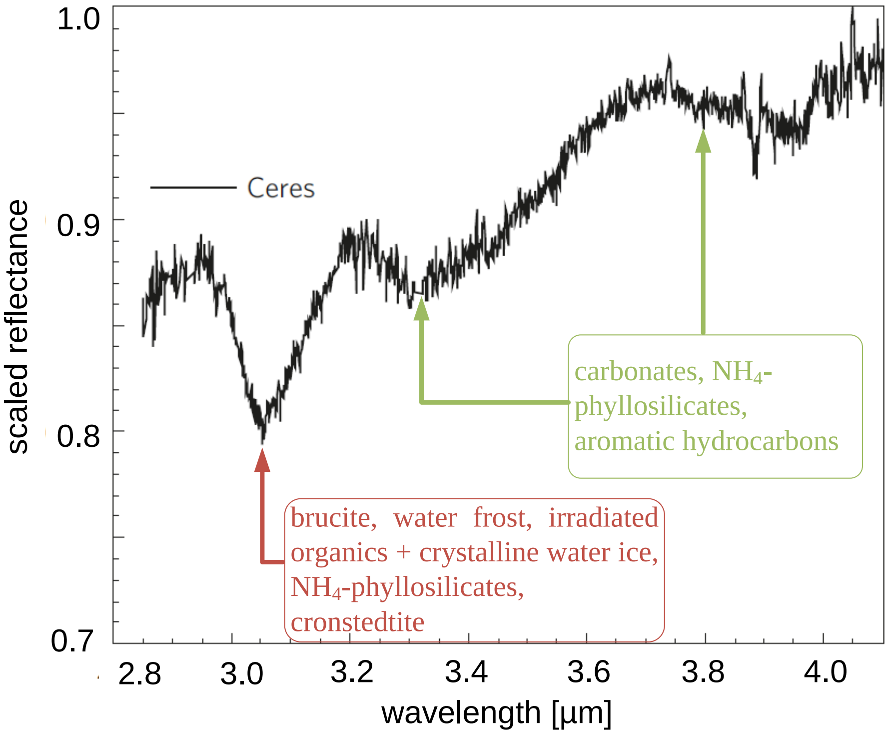

Figure 1-12. *Spectrum of Ceres in the wavelength range between 2.8 and 4.0 µm. The red and green arrows mark the features and the minerals that are associated with this absorption feature. Modified after Milliken and Rivkin (2009).*

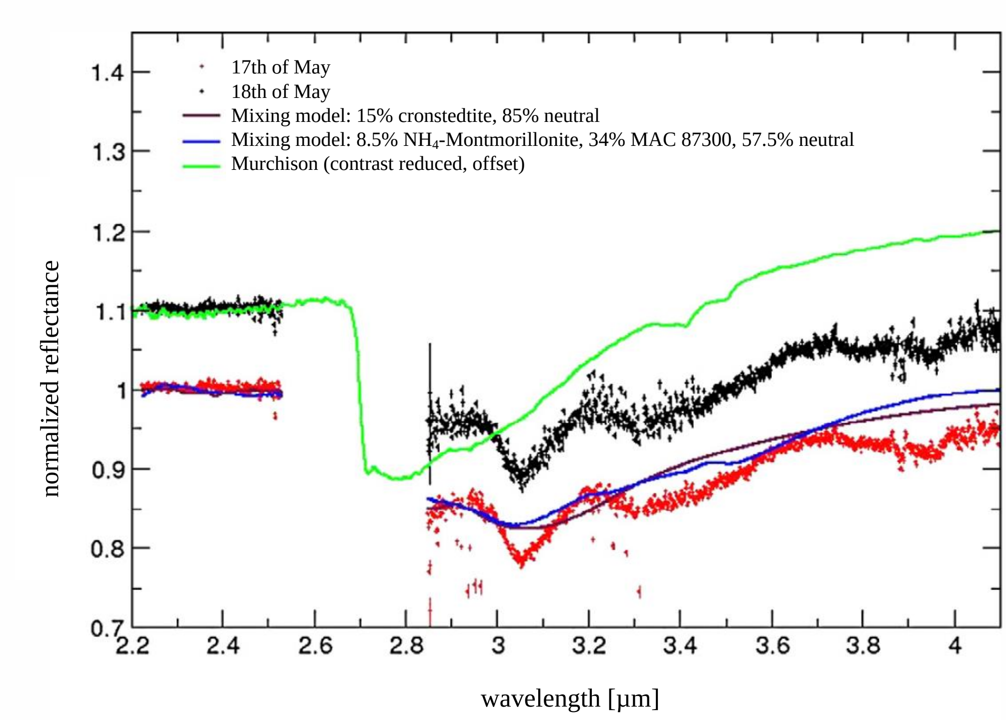

Figure 1- 13: *2.2–4.1 µm spectra of Ceres from 17 May and 18 May 2005, normalized to 1 at 2.2 µm. The 18 May spectrum (black) is offset from the 17 May spectrum for clarity. Also shown as solid lines are model spectra generated using a Hapke theory-based mixing model. These models use a carbonaceous chondrite, a neutral material, carbonates, and either an ammonium-bearing or iron-rich phyllosilicate as end-members. The figure also shows the CM meteorite Murchison, showing the very different band shapes between it and Ceres. The end-member spectra were obtained from the Relab and ASTER database. Data between 2.52 and 2.85 µm were omitted due to excessive spectral contamination from water in the Earth's atmosphere. From Rivkin et al. (2006).*

As the spectrum of Ceres is generally flat shortward of 2.5 µm, it shows a strong feature near 3.06 µm which could be attributed to phyllosilicates, hydrated water (De Sanctis et al., 2012), OH, CO_3, SO_4 or other ions containing oxygen (McCord and Sotin, 2005), crystalline water ice plus irradiated asphaltite (Vernazza et al., 2005) or hydrated salts (McCord and Sotin, 2005). Lebofsky (1978) concluded that the shape and depth of the curves in the 3 to 4 µm region are similar to those of the CM chondrites and that 10-15 % water of hydration could be present in the surface material of Ceres. Lebofsky et al. (1981) interpreted the feature near 3.1 µm as frost whereas King et al. (1992) stated that this feature is too narrow and too long in wavelength to be water ice, but more likely due to NH_4-bearing minerals like buddingtonite or saponite. However, these minerals are inconsistent with the MIR spectra of Ceres (De Sanctis et al., 2012). According to Rivkin et al. (2006) it is more likely that the 3.06 µm feature is caused by iron-rich clay like cronstedtite (serpentine group, see figure 1-14 and 1-15). Milliken and Rivkin (2009) identified the 3.06 µm feature to be brucite ($Mg(OH)_2$) as this mineral is consistent with most of Ceres spectrum in the 3-14 µm range (figure 1-14 and 1-15). The Ceres' spectrum misses some brucite bands between 1 to 3 µm (figure 1-15; Zolotov, 2014). Furthermore, brucite is not a major component in carbonaceous chondrites, but C2 chondrites do contain the mineral tochilinite, a mineral that consists of interlayered sheets of sulphide and brucite sheets (Milliken and Rivkin, 2009).

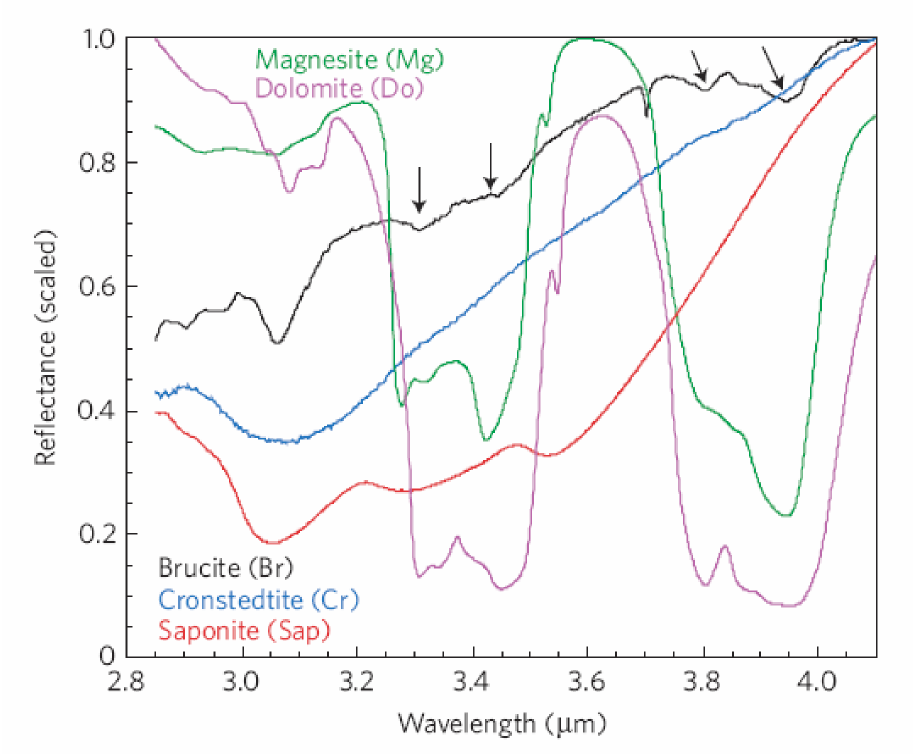

Figure 1-14A. *Linear mixing model results for the near-infrared reflectance spectrum of Ceres. Laboratory reflectance spectra of brucite, magnesite, dolomite, cronstedtite and ammoniated saponite were scaled to one at their maximum reflectance point as inputs to the model. The reagent-grade brucite spectrum shows weak spectral features indicative of minor contamination by carbonate (black arrows). From Milliken and Rivkin (2009).*

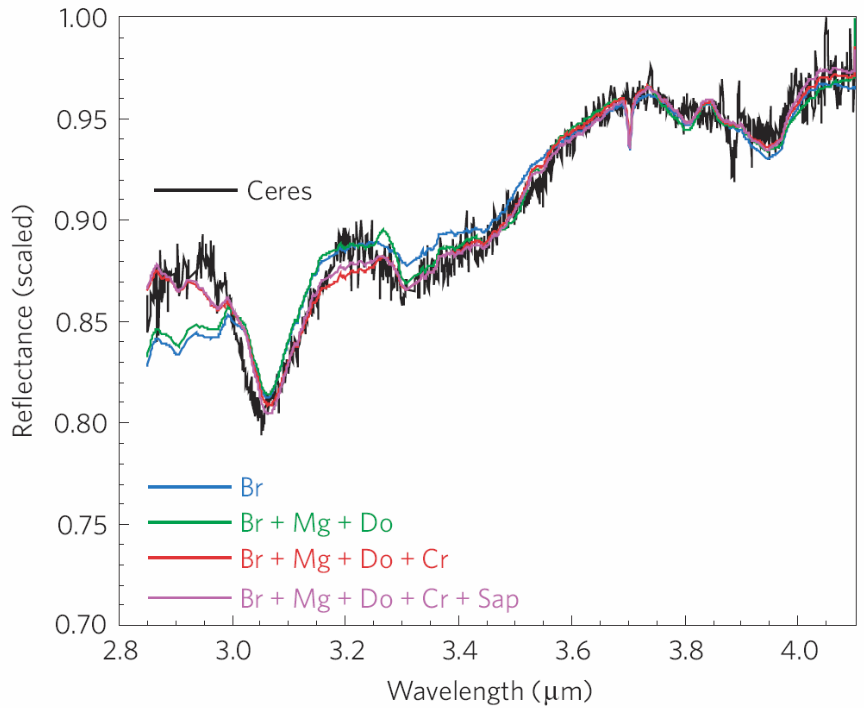

Figure 1-14B. *Mixings of different minerals. Models that used subsets of the endmember spectra produced slightly different results, showing that Ceres' major spectral features can be modelled by the presence of brucite, carbonates and an opaque phase (sloped line). Including cronstedtite in the model improved the fit near 3:4 µm and at wavelengths <3:0 µm, whereas including ammoniated saponite had a negligible effect. From Milliken and Rivkin (2009).*

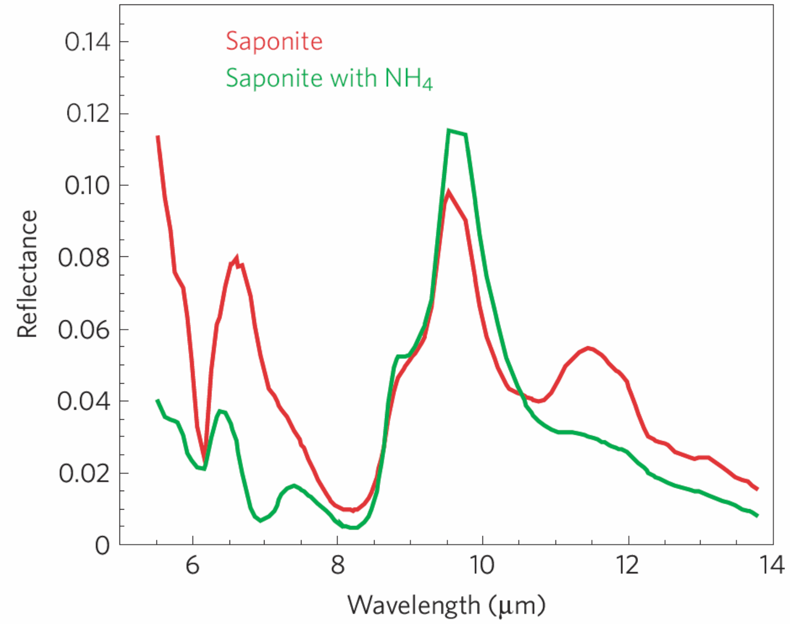

Figure 1-15A. *Linear mixing model results for the mid-infrared reflectance spectrum of Ceres. The figure shows laboratory reflectance spectra of saponite and ammoniated saponite. From Milliken and Rivkin (2009).*

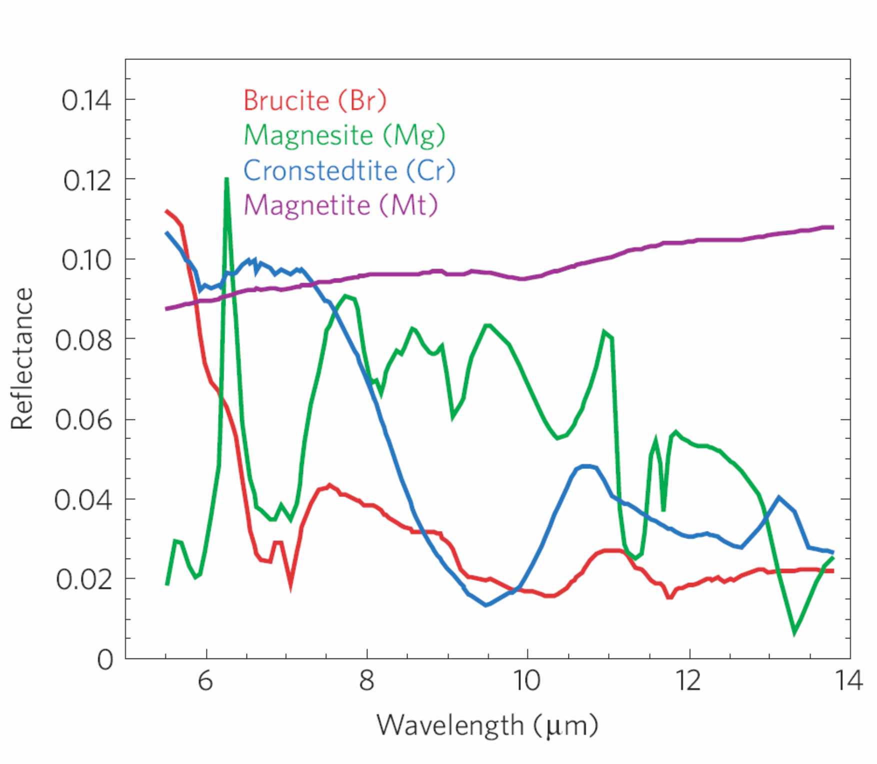

Figure 1-15B. *The figure shows the spectra of brucite, magnesite, cronstedtite and magnetite. Model results show that the broad absorption centered near 10 µm can be fitted by either cronstedtite or brucite, but carbonate is required to fit absorptions near 7 and 11 µm. Differences in the strength of absorption features between the Ceres and model spectra are probably caused by differences in the particle size ranges and scattering properties between Ceres and the laboratory samples. From Milliken and Rivkin (2009).*

There are more absorption features in Ceres spectrum at 3.3 µm, 3.44 µm, 3.8 µm and 3.94 µm indicating that carbonates are present at Ceres surface (see figure 1-12-1-14; Milliken and Rivkin, 2009). The 3.3-3.4µm was originally interpreted as NH_4-bearing phyllosilicates by King et al. (1992), but could also be attributed to aromatic hydrocarbons (Rivkin et al., 2006).

Emission data on Ceres over the spectral range of the MIR (5-14 µm) can also be used to gain information on the possible composition of Ceres (Milliken and Rivkin, 2009). The MIR range of Ceres' spectrum is unique among asteroids as it shows a strong variation of spectral emissivity (Rivkin et al., 2010). In figure 1-16 is shown the MIR spectrum of Ceres. It shows three absorption features: two narrow peaks near 6.6 µm and 11.4 µm due to carbonates (Milliken and Rivkin, 2009) and a broader minimum centered near 10 µm (Cohen et al., 1998). This feature at 10 µm could be explained by the lack of finer materials on the surface as finer materials reduce the contrast in the MIR (Rivkin et al., 2010). There is a broad absorption feature between 8 to 11 µm (Milliken and Rivkin, 2009). This feature might be indicative of brucite and/or cronstedtite. The brucite spectrum shows weak features at 8.3 µm and 9.9 µm (figure 1-15b) and cronstedtite has a strong decrease in reflectance between 7.5 to 9.5 µm (figure 1-15b; Milliken and Rivkin, 2009). Cohen et al. (1998) identified with the Christiansen frequency (CF) the maximum near 9.5 µm. The CF is the wavelength at which the reflectivity and emissivity are independent of the grain size of the sample (Conel, 1969; Salisbury, 1993). Rivkin et al. (2006) included in their linear mixing model magnesite $(Mg)CO_3$ (figures 1-15b and 1-16) as the resulting spectra better matches the significant wavelength in the MIR and improved the quality of the 3 µm spectral region fit.

The feature around 11.4 µm according to Rivkin et al. (2010) was not re-observed in later observations. It is assumed that this feature is related to a geographically localized area on Ceres, possibly showing an increase in the abundance of carbonates or due to a localized change in the surface texture, particle size and/or cementation. A region of high spectral contrast could be an indicator for local geologic activity and the exposure of fresh and recently re-crystallized material (Rivkin et al., 2010).

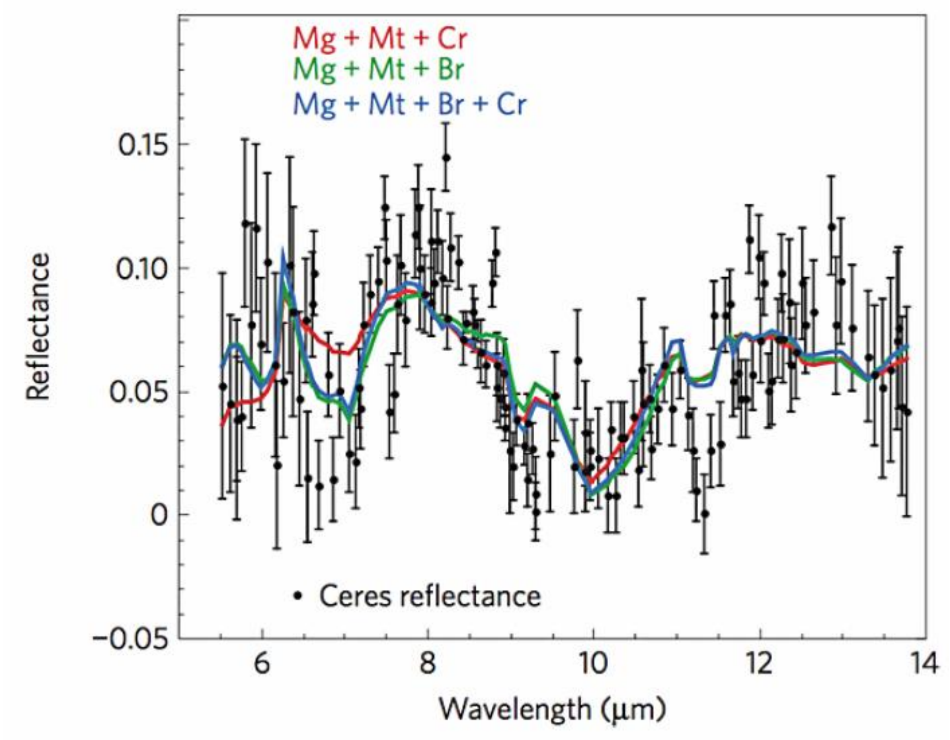

Figure 1- 16: *This figure shows fits to the mid-IR spectrum of Ceres, with fits to the spectrum by mixtures of magnesite (magnesium carbonate: Mg in the figure), magnetite (Mt), brucite (Br), and cronstedtite. From Milliken and Rivkin (2009).*

Ceres in the FIR, millimeter and radio wavelength (>16 μm). Mitchell et al. (1996) did radar observation of three asteroids (Vesta, Pallas and Ceres) to characterize their surface properties. They concluded in their work that Ceres has a smoother surface at decimeter scales than the Moon, but a much rougher surface on larger scales. A possible reason for this is the difference in material strength of both objects. Ceres has a low radar albedo of 0.042±0.006 which is in the range expected for CC mineralogy. Mitchell et al. (1996) determined the regolith density of Ceres based on the calculated reflectivities to be 1.24±0.10 g/cm^3 and concluded that differences in the regolith density (see figure 1-17) of the three investigated objects, especially between Ceres and Pallas, are mainly due to different porosities or due to differences in the mineralogy.

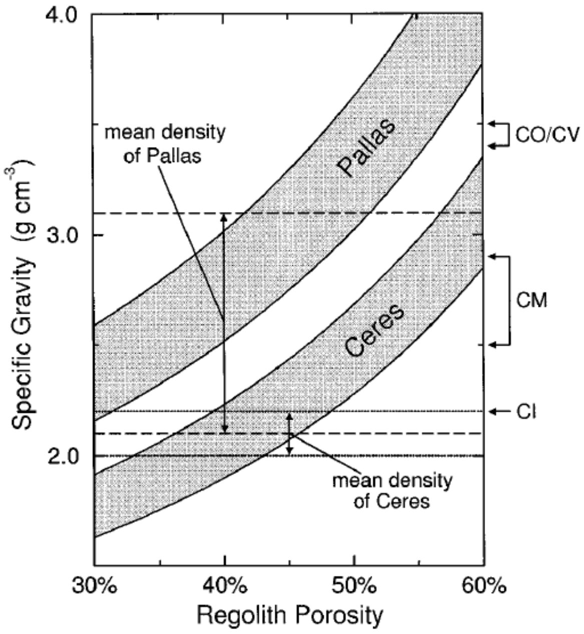

Figure 1-17. *Radar constraints on the surface densities of Ceres and Pallas provide a joint constraint on regolith porosity and specific gravity (zero-porosity density; shaded regions). These are compared with typical densities of solid CC meteorites (types CI, CM, CO, and CV). Constraints on the mean densities of Ceres (dotted lines) and Pallas (dashed lines) are obtained by dividing each object's total mass by the volume of its a priori shape. From Mitchell et al. (1996).*

Summary (table 1-5). To summarize, there is no real match for Ceres' spectrum among the available meteorites and mineral spectra (McCord and Sotin, 2005). In previous works there were CC-like laboratory mixes created (montmorillonite, carbon black, hydrated silicate minerals) to mimic Ceres' spectrum, whereas other authors proposed an opaque-rich assemblages like carbonaceous material to be the best fit (McCord and Sotin, 2005). Interpretation ranges from primitive carbonaceous hydrous silicate mixtures (C1) to metamorphosed mafic silicates and iron oxides (C4) (McCord and Sotin, 2005). All data suggest that Ceres contains H_2O- and/or OH-bearing phases and organic compounds (Zolotov, 2009). Ceres' spectrum has no clear signature of many primary minerals such as olivine, pyroxene, feldspars and Mg-rich phyllosilicates like saponite or serpentine which are common in chondrites (Zolotov, 2014). The absence/deficiency of these primary phases indicates that the object has undergone alteration processes (Milliken and Rivkin, 2009). Ceres' spectrum in the VIS and NIR is associated with CC-type meteorites (McCord and Sotin, 2005). The mixture of Mg-bearing carbonates, brucite, cronstedtite and magnetite provides a good fit for Ceres' spectra at 3-14 µm (Milliken and Rivkin, 2009). This model indicates a similarity to CM chondrite materials that contain these aqueously altered materials (Zolotov, 2014). But some uncertainties remain, e.g. the deeper depth of brucite at 3.06 µm and carbonate at 3.3 to 3.4 µm and 3.8 to 3.9 µm bands in darker regions disagree with the low albedo of these minerals (Rivkin et al., 2010). There is a limited variation in the band depth of the 3.06 and the 3.35 µm bands and a greater band depth correlate with region of lower albedo. This effect is not consistent with space weathering and is inconsistent with changes when mixing brucite and carbonates (Rivkin et al., 2010). Ceres MIR spectral features could be explained by carbonate, magnetite and brucite/cronstedtite, whereas the spectra of saponite and other smectite clays show an opposite trend to the Ceres' spectrum at these wavelengths (Milliken and Rivkin, 2009).

Table 1- 5: *Summary of the diagnostic features in the wavelength range between 0 to 5 µm based on the previous sections.*

Mineral	Wavelengths	Reference
carbonates	~3.3-3.4 µm, ~3.8-3.9 µm, ~11.2 µm	Rivkin et al. (2006), Milliken and Rivkin (2009)
brucite	~3.06 µm	Milliken and Rivkin (2009)
magnetite	~1.1 µm	Larson et al. (1979)
OH?	~0.25 µm	Parker et al. (2002), Li et al. (2006)
silicates	~10 µm	Cohen et al. (1998), Lim et al. (2005)
tochilinite		Milliken and Rivkin (2009)
cronstedtite	0.4 µm cutoff, 0.6 µm; 0.67 µm, 1.0 µm	Milliken and Rivkin (2009); Feierberg et al. (1981), Vilas and Gaffey (1989)
water frost		Lebofski et al. (1981); Feierberg et al. (1981)

Tabke 1-5. *Cont.*

Mineral	Wavelengths	Reference
saponite	3.06 µm	King et al., (1992)
crystalline water ice + asphaltite	3.06 µm	Vernazza et al. (2005)
tholin	11.4 µm	Rivkin et al. (2011)
magnetite	1.1-1.2 µm	Larson et al. (1979)

1.2.2.2. Surface Composition

The current knowledge of the surface composition of Ceres is based on telescopic observations in the UV, VIS, NIR and MIR spectral ranges (Zolotov, 2014) but the exact surface composition will remain unclear until the arrival of the DAWN spacecraft in spring 2015. Ceres' surface appears to be dark (Thomas et al., 2005) and rather uniform (Carry et al., 2008). The uniform surface suggests that the surface did not experience any giant impacts such as in Vesta's South Pole (Rivkin et al., 2010). It is also possible that resurfacing events have erased any significant variations that might have resulted from impacts (Rivkin et al., 2010). It is expected that Ceres surface will be found to be covered with a regolith layer tens of meters thick (Lupishko and Mohamed, 2009). Lebofsky et al. (1981) assumed that the phyllosilicates on Ceres are covered by a fine layer (≈0.01 µm thick) of water ice.

Ceres position in the Solar System could be far enough away so that primordial elements could have been preserved from strong heating during the T-Tauri phase of the Sun (Carry et al., 2008). The dwarf planet has been identified as a carbonaceous asteroid with surface material similar to type I and type II carbonaceous chondrites (Lebofsky et al., 1978; Castillo-Rogez and McCord, 2010). This is supported by the density of Ceres being between the densities of CC material type I (2.6-2.9 g/cm^3) and type II (2.2-2.3

g/cm^3) (Lebofsky et al., 1978). These CC meteorite materials were aqueously altered from its source material at warm but still low temperatures in the parent body, then brecciated very early in the history of the Solar System (Mc Cord and Sotin, 2005). These alteration and brecciation occurred within a few million years of chondrule and CAI formation (McCord and Sotin, 2005).

Bland (2013) stated that Ceres is clearly composed of rocky material that could have been formed at the surface as water ice sublimates away and if non-ice material is present, it must be within the ice layers. Ceres surface could be covered by low-density dry clay-like material with a low thermal inertia and high porosity (Chamberlain et al., 2009) and iron-poor olivine at top of phyllosilicates (Castillo-Rogez and McCord, 2010 and references within). Possible minerals at the surface indicated by spectral observations could be OH-bearing and/or hydrated minerals (Lebofski et al., 1981), cronstedtite (Fe-phyllosilicate) (Rivkin et al., 2006; Milliken and Rivkin, 2009), magnetite or other darkening agents (Zolotov, 2014), Mg-bearing carbonates (Rivkin et al., 2006; Rivkin and Volquardsen, 2010), and Ca-carbonates (Rivkin et al., 2006; Castillo-Rogez and McCord, 2010; Zolotov, 2014).

According to Milliken and Rivkin (2009), Fe-bearing minerals and calcite are not expected to be abundant at Ceres' surface, but Mg-carbonates $MgCO_3$ and brucite $Mg(OH)_2$ are likely to exist. These minerals suggest that there were extensive alteration processes in the presence of liquid water and CO_2 (Milliken and Rivkin, 2009; Rivkin et al., 2006; Rivkin et al., 2010). The presence of Mg-carbonates is consistent with the alteration of brucite in the presence of CO_2 with graphite as its possible source (Rivkin et al., 2010). It is assumed that some materials on Ceres could be transported there by impacts of C- and H_2O-rich bodies during the Late Heavy Bombardment (LHB) (Zolotov, 2014).

Based on the bulk density of Ceres (see table 1-1) it is assumed that the water content could range between 0% (Zolotov, 2009) and 20% by mass (McCord and Sotin, 2005) depending on the mineral composition (Rousselot et al., 2011). As liquid water is instable on Ceres' surface (Castillo-Rogez and McCord, 2010) it seems possible that the formation of aqueous altered materials could have happened in the interior of Ceres or near the surface by transient fluids and/or on parent planetesimals of the impacting bodies (Zolotov, 2014). The water ice could have survived 4.5 Gyr at a depth of only 10 to 100 meter near the equator and less than 1 to 10 meters at latitudes larger than 40° (Fanale and Salvail, 1989). The alteration could occur at the base of an ice ocean or at the base of an unmelted ice and silicate crust prior to foundering of that crust (Rivkin et al., 2010). Materials then could have been brought up to the surface by cryovolcanism or after crustal foundering (Rivkin et al., 2010).

Küppers et al. (2014) investigated possible source regions of water vapor at Ceres. All observations (ground-based and HST) that detected water vapor from Ceres correlate dark regions at Ceres' surface as the likely source because these regions are warmer than the average surface resulting in sublimation of water-ice reservoirs. The water activity on Ceres' surface is not concentrated on Polar Regions as water ice is most stable in these regions. Küppers et al. (2014) proposed two possible mechanisms for the water vapor production on Ceres. First, it is possible that there is a cometary-like sublimation at the surface removing ice and near-surface dust and exposing fresh ice layers. Secondly, cryovolcanism could be responsible for the water vapor production.

1.2.2.3. Albedo and color variations

Ceres surface appears to be featureless and uniform (figure 1-18; Carry et al., 2008) and images of Ceres do not show strong albedo variations (Saint-Pe et al., 1993), The average albedo of Ceres is 0.086 with an albedo contrast of only a few percent at VIS wavelengths, whereas the NIR albedo variations are ±6% (Rivkin and Volquardsen, 2010; Moullet et al., 2010). Li et al. (2006) detected that surface albedo variations are between 0.02 and 0.16 and determined the visible albedo to be 0.09. This value is similar to the value of Tedesco (1989) who estimated the visible albedo to be 0.1. The geometric albedo was estimated by Millis et al. (1987) to be 0.073 (λ=5600A), whereas Parker et al (2002) calculated a geometric albedo of 0.056 (near-UV, λ=3636A), 0.029 mid-UV (λ=2795A) and 0.090 far-UV (λ=1621A). All these values are above the value for CM chondrites of 0.03-0.05 (3-5%). Thus, there must be a large fraction of high albedo material on Ceres' surface (McCord and Sotin, 2005) mixed with CM material or salts from aqueous alteration processes (McCord and Sotin, 2005).

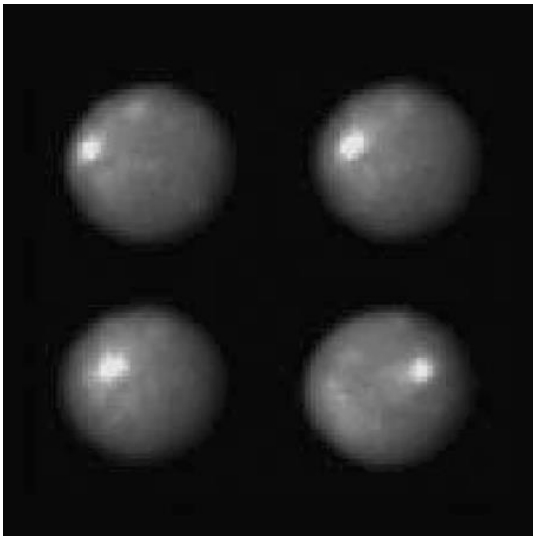

Figure 1-18. *Images of Ceres acquired with the HST. The high brightness of the bright spot in the images does not correspond to the real scaling, but only stresses its slightly higher albedo in comparison with the surrounding surface. From Lupishko and Mohamed (2009).*

Studies done by Carry et al. (2008) reveal a clear trend of bright features to display a higher H-band albedo than in the K-/J-band indicating a similar origin for the bright features (figures 1-18, 1-19, and 1-20). The bright features show spectral similarities to phyllosilicates and carbonates. Spectra of calcite and montmorillonite show that these minerals best fit the spectra of the bright features. Siderite, cronstedtite or augite spectra only match small percentage of Ceres' surface and could be minor compounds such as pyroxene and olivine. The dark features do not display a similar trend. This implies that the dark regions may be a result of various surface processes or represent different levels of surface aging. Their spectra are similar to enstatite but this mineral has a high density and thus is unlikely to be present at Ceres' surface. As water ice is not expected to be stable at the surface, it is possible that dirty ice could be present. The dark features are mainly found at high latitude above 30-40° and none of them is in the equatorial region. This matches the assumption that water ice is more stable at higher latitudes (Carry et al., 2008).

In figure 1-19 are shown several large albedo features that possibly could be impact craters (Li et al., 2006). Carry et al. (2008) categorized some of these features in the mid-latitudes at ~30°N as impact structures with diameters of 180 km and more (figure 1-19, 1-20). The two largest features shown below in figure 1-19 (red dots) were named A and B. Both A and B are large with a diameter of A~180 km, and with a diameter of B of ~350km. Both features appear to be homogenous indicating similar composition and/or a similar resurfacing history (Carry et al., 2008). Feature A could be interpreted as a geological feature like a basin or impact structure as there is a bright central peak possibly resembling the central peak often seen in craters from high energetic impacts (Carry et al., 2008). It is obvious that one hemisphere of Ceres is brighter than the other. There is a dark region running from North to South located at the boundary between the two hemispheres (figure 1-20; Carry et al., 2008).

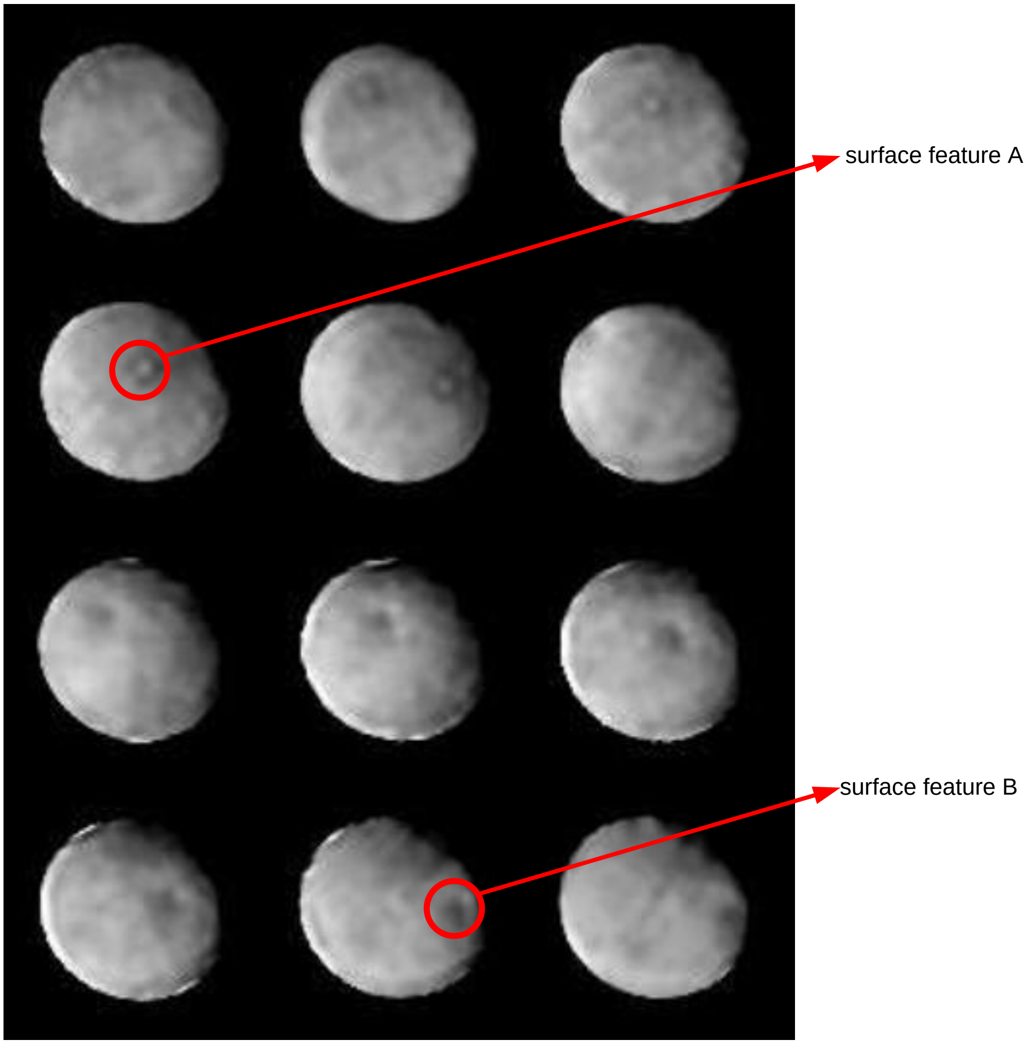

Figure 1- 19: *Selected views of Ceres in the K-band during ~200° of its rotation. The image is oriented with North up and East left. The two main surface features present on Ceres are indicated with the arrows A and B and can be followed during part of their rotation. The brighter spots visible near the limb of Ceres in some of the images are artifacts from the deconvolution. From Carry et al. (2008).*

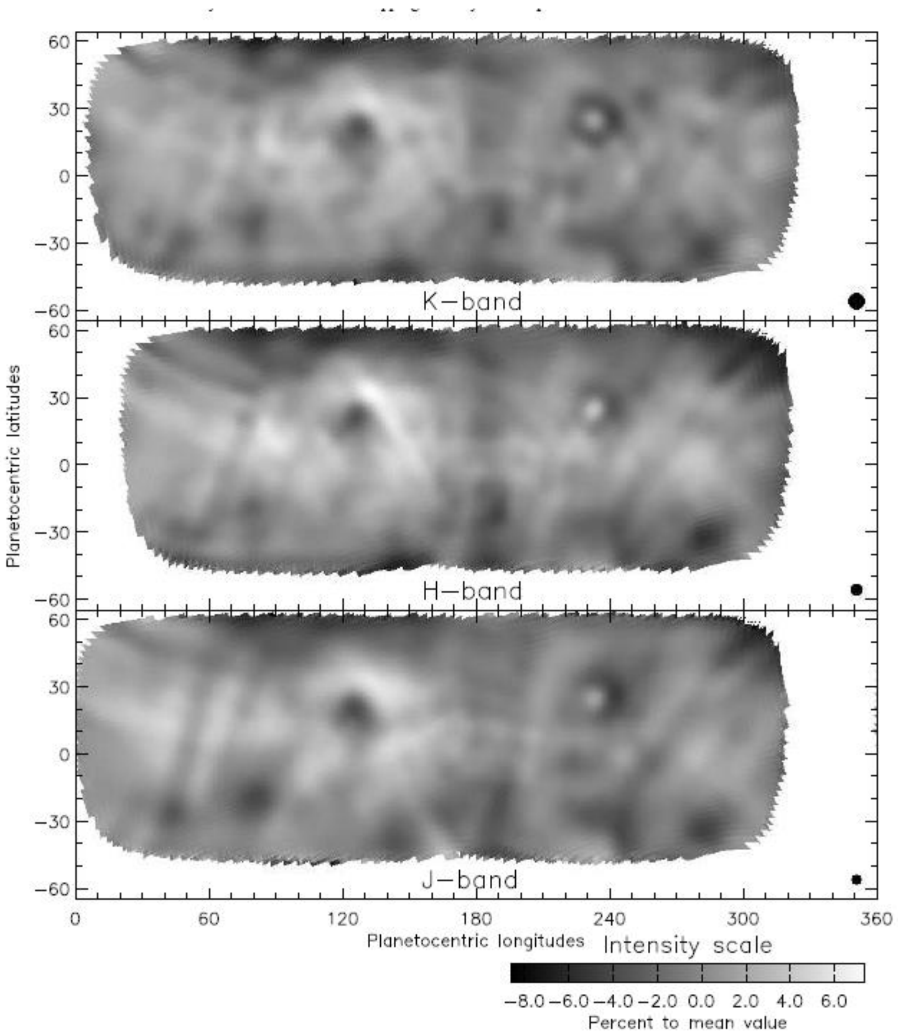

Figure 1-20. *J-, H- and K- band maps of Ceres covering ~80% of Ceres' surface. The areas in white are terra incognita due to rotational phases not imaged from Keck. The theoretical resolution elements at J/H/K bands are shown at the bottom-right corners. Albedo variations are within ±6% around the mean surface value for each map. The errors are estimated to be 2.5% maximum. Several round shaped features are visible including a dark feature with a bright center spot at ~(234°, +23°) (named "A") and a dark region at ~(125°, +20°) named "Piazzi" by Parker et al. (2002) (here "B"). Two other dark features are visible in the Southern hemisphere at ~(80°, -20°) and ~(285°, -35°) as well as other smaller features elsewhere. One hemisphere (0° to 180°) appears to be sensibly brighter (1%) than the other at these wavelengths. A dark region running North/South is located at the boundary between the two hemispheres and is present in all maps. From Carry et al,(2008).*

A team of astronomers at the Keck observatory headed by B. Carry produced albedo maps covering 80 percent of Ceres' surface, which appears to display a wealth of 40 to 160 km large geological features with intensity in reflected light varying by ~12 percent across the surface. They suggest that the variations could be due to terrain features, as well as differences in their surface composition and/or degree of alteration by space weathering effects such as aging of surface due to interaction of solar wind, and/or micrometeorites impacts, etc. (W.M. Keck Observatory).

The albedo of Ceres surface is much more uniform in the UV-VIS region than those of any other asteroid or satellite and this uniformity suggests that the color variations are relatively small (Rivkin et al., 2010). Color variations in the 2 to 4 µm region also vary with different longitude. Higher-albedo regions show evidence of a shallower band depth at 3.05 µm (Rivkin and Volquardsen, 2010) than low-albedo regions. Possible reasons for that are 1) brucite-rich areas having lower albedo and vice versa, 2) space weathering (as areas with smaller band depth are more weathered than those with deeper band depth) or 3) different particle sizes across Ceres' surface with finer particles resulting in a smaller band depth (Rivkin and Volquardsen, 2010). Albedos in the mid- and near-UV show no evidence for rotational phase-dependent variations (Parker et al., 2002).

1.2.2.4. Surface morphology (grain size, roughness, packing density)

The surface roughness and the grain size influence the amount of the reflected, scattered and absorbed part of the incident EM radiation (Arnold, 2014).

Ceres surface seems to be covered by fine-grained, dusty, and porous surface materials (Zolotov, 2014; Lupishko and Mohamed, 2009). It is possible that these materials are gravitationally sorted (Zolotov, 2014). Cohen et al. (1998) assumed in their work a particle size of 40-130 µm as the average particle size on Ceres' surface. This assumption is based on the fact that small asteroids with a low surface gravity are depleted in finer particles and are enriched in coarser material (Dollfus, et al., 1989). However, Ceres might have retained its finer particles at the surface due to a higher gravity.

Based on radar observations done by Mitchell et al. (1996) and by Ostro et al. (1979), Ceres’ surface seems to be fairly rough at a scale of 10 meters though its surface appears to be smoother than those of Vesta or the Moon. This could be explained due to the different surface composition and material strengths of the objects (Lupishko and Mohamed, 2009). Li et al. (2006) determined the roughness parameter of be 44°±5°. It is likely, that the roughness does not vary over the surface of Ceres indicated by a low topography based on the relaxed shape of Ceres (Thomas et al., 2005), and the uniform surface of Ceres (based on albedo and color variations; Li et al., 2006).

Radar observation of Ceres showed that the object has a low reflectivity indicating that the regolith layer is very loosely packed (Ostro et al., 1979).

1.2.2.5. Homogeneity

Ceres appears to be photometrically homogenous with little variations in the spectral signature across the surface (Lupishko and Mohamed, 2009; Carry et al., 2012). The dwarf planet does not appear to have regions with appreciably different surface mineralogies and appears to be spectrally uniform (Rivkin and Volquardsen, 2010) and be covered by a dusty regolith being a few centimeters thick. This layer was created by impacts of micrometeorites and larger bodies (Carry et al., 2008) and could be an explanation for the shallow spectra in the VIS and NIR and Ceres’ small albedo contrast (Carry et al., 2008). The low spectral contrast of Ceres could reflect impact homogenization by impact surges and gravitationally fallout of ejected material (Zolotov, 2014). A possible reason for the homogeneity of Ceres' surface is that an unstable ice-silicate crust would result in break-up and resurfacing of Ceres' surface, with mixing and deposition of minerals. These processes would erase major albedo and morphological features (Carry et al., 2012). Another reason could be resurfacing processes due to ancient cryo-volcanism (Carry et al., 2012).

1.2.2.6. Thermal properties

The temperature on airless bodies is dependent on the albedo of the surface (Moullet et al. 2010). All work done on Ceres' surface temperature concluded that the temperature is a function of the latitude (see figure 1-21), local topography and surface/sub-surface material. Fanale and Savail (1989) and McCord and Sotin (2005) determined the temperature range from 180K at the equator to 130 K at the poles. These values are for an albedo of 0.09 (McCord and Sotin, 2005). Li et al. (2006) estimated the temperature at the surface near the equator to be 235 K but stated that localized low albedo regions might have higher temperature than this. Lebofsky et al. (1981) based their temperature estimates on ammonium-bearing mineral species assuming their presence and suggested a secondary temperature of maximal 400 K (King et al., 1992). Bland (2013) and Bland et al. (2013) estimated the maximum surface temperature to be 178 K at the equator, 160 K at mid-latitude and 140 K at the poles or even below 100K.

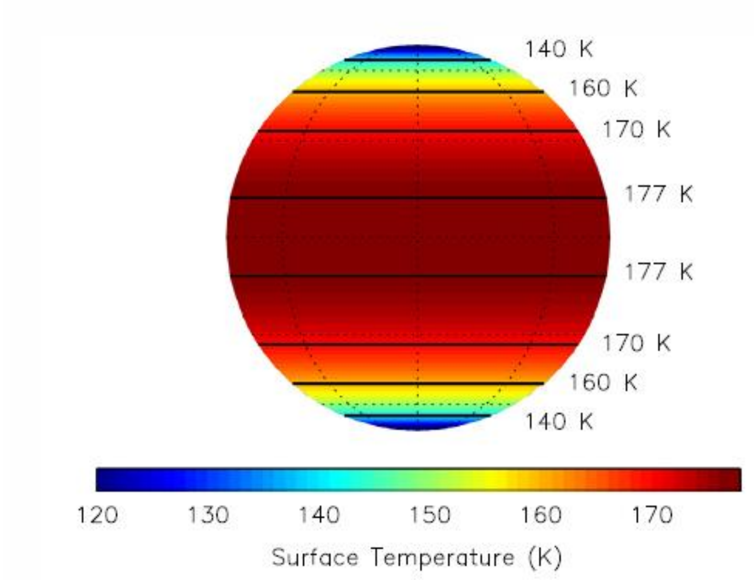

Figure 1-21. *Color map of theoretically-derived surface temperatures on Ceres. The maximum temperature is 177 K at the equator. Temperatures of 160 K and 140 K occur at latitudes of 49° and 67°, respectively. The maximum (subsurface average) temperature is 178 K at Ceres' equator. Temperatures decrease slowly across the mid-latitudes, decreasing to 160 K at ±49°, and 140 K at ±67°. Temperatures can theoretically drop below 100 K at very high latitudes (84°). From Bland (2013).*

1.3. Information on the Dawn mission

The Dawn mission is the ninth Discovery Program mission of the NASA/JPL to investigate the dwarf-planet 1 Ceres and the asteroid 4 Vesta, both are situated in the MAB. It is a mapping mission and the first one using an ion propulsion system. The main objectives of this mission are to increase the knowledge of the present state of the two bodies and to understand how they evolved over time, to characterize the surface of both objects and to probe their internal structures (Russell and Raymond, 2011). The instruments used on the DAWN spacecraft are a framing camera (FC), a visible and near infrared (VNIR) spectrometer and a gamma ray and neutron detector (GRaND).

The FC (see figure 1-22) is designed by the German Aerospace Institute (DLR) and will map Vesta and Ceres through a clear filter and 7 band-pass filters covering the wavelengths from the VIS to the NIR (Sierks et al., 2011). The camera will also be used to determine the physical parameters of both targets, the global shape as well as the local topography and surface geomorphology (Sierks et al., 2011). Furthermore, the FC will provide information on the composition of Ceres and Vesta via reflectance characteristics and it will serve for orbit navigation (Sierks et al., 2011). The resolution of the camera will be up to 12 meter per pixel in the low altitude mapping orbit at Vesta and 62 meter per pixel at Ceres (Sierks et al., 2011). For further information on a detailed view of the FC see Sierks et al. (2011).

Figure 1-22. *DAWNS's Framing Camera. From: S. Storms, LANL*

The DAWN spectrometer (VIR, see figure 1-23) is a hyperspectral spectrometer with imaging capability (De Sanctis et al., 2012). It covers the wavelength between 0.25-1.0 µm and 0.95-5.0 µm (Russell et al., 2006). The spatial resolution of the VIR is 0.250 mrad with spectral resolution varying from 30 to 170 (Russell et al., 2006). The main objectives of the VIR are the identification of the different materials and mixtures present in the bodies, the relevant minerals at their surfaces (e.g. silicates, hydrogen), the determination of the overall continuum slopes of the spectra and the mapping of the presence and extent of space weathering and of the entire bodies (De Sanctis et al., 2012).

Figure 1-23. *VIR built by Italian Space Agency ASI and National Institute for Astrophysics INAF; hyperspectral spectrometer; wavelength range: 0.25 to 5 µm; from: Selex Galiileo, INAF, and ASI.*

The Gamma Ray and Neutron Detector (GRaND; see figure 1-24) is a deck-mounted instrument, consisting of 21 sensors. These sensors are arranged to separately measure planetary gamma rays and neutrons from backgrounds originating from the spacecraft and the space environment (Prettyman et al., 2003; Russell et al., 2006). The gamma ray detector is a large bismuth germanate scintillator and cadmium zinc tellurite (Prettyman et al., 2003; Russell et al., 2006). The neutron spectroscopy uses Li-loaded glass and boron-loaded plastic scintillators to measure the different neutrons (Prettyman et al., 2003; Russell et al., 2006).

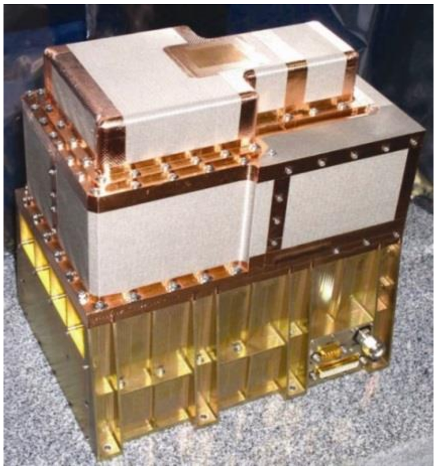

Figure 1-24. *The Gamma Ray and Neutron Detector (GRaND) instrument on board of the DAWN spacecraft. From Max-Planck Institute for Solar System Research MPS.*

Three orbits are planned (for further information see Russell and Raymond, 2011; figure 1-25 and 1-26) at each object with different altitudes (Russell et al, 2004) and with a nadir pointing direction during operations (Russell and Raymond, 2011). The spacecraft was launched on September 27, 2007 and reached 4 Vesta in 2011. Dawn is heading to Ceres now and will arrive there in spring 2015 (see figure 1-26 for trajectory of the DAWN spacecraft).

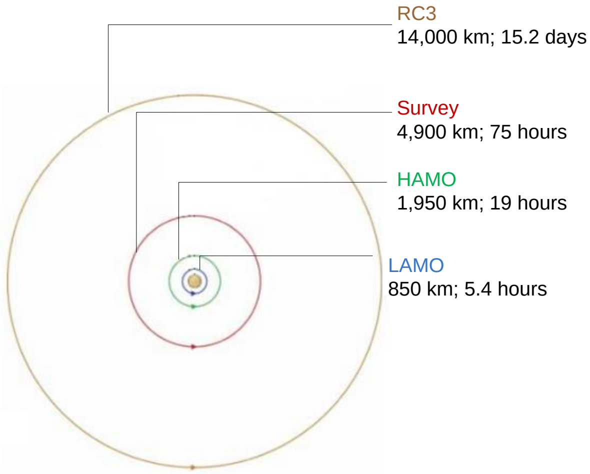

Figure 1- 25*: NASA's Dawn spacecraft will be getting an up-close look at the dwarf planet Ceres starting in late March or the beginning of April 2015. This graphic shows the science-gathering orbits planned for the spacecraft, with the altitudes above the surface noted for each of the orbits. Modified after NASA (a).*

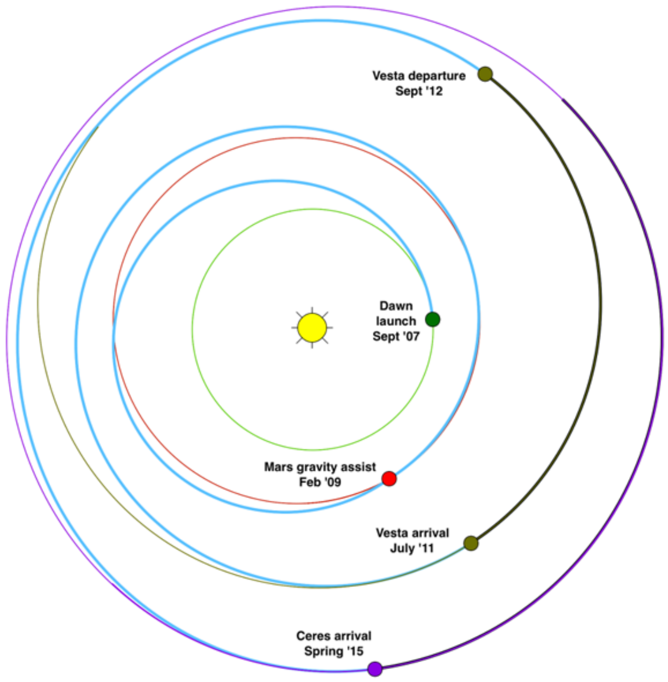

Figure 1- 26*: This graphic shows the planned trajectory of NASA's Dawn spacecraft from its launch in 2007 through its arrival at the dwarf planet Ceres in early 2015. When it gets into orbit around Ceres, Dawn will be the first spacecraft to go into orbit around two destinations in our solar system beyond Earth. Its journey involved a gravity assist at Mars and a nearly 14-month-long visit to Vesta. From: NASA (a).*

1.4. Goals and outline

The aim of this work is to review the previous visible and infrared earth-based observations and the supporting laboratory work that have been done so far to get an overview on the possible surface composition of Ceres prior to DAWN's arrival. These data will be compared to complementary spectral measurements of chosen meteorites (CM, CO, and CV chondrites), and minerals in the wavelength range of the VIR instrument onboard the DAWN spacecraft between 0.5 to 5 µm. Linear mineral mixings will be modeled to complete the database used in this work. To collect a wider range of data, spectral databases like Relab will be searched for available spectra of meteorites (including CM, CO, CV, and CI chondrites) and minerals (e.g. montmorillonite, carbonates, water ice and frost, pyrite, magnesite).

Minerals will be selected for measurements based on the composition of the meteorites investigated in this work and the data acquired until now by other scientists. Diagnostic features, like the wavelength of slope change, the spectral slope in the VIS and NIR, and the occurrence of spectral absorption bands in the spectra, will be determined and compared to the spectral characteristics of Ceres. Finally, the data collected in this work will be used to discuss implications for DAWN’s composition analysis and the studies of the nature and origin of Ceres’ surface. The comparison between the data collected in this work and the corresponding results from DAWN will give an insight into the reliability of ground-based observations to space-based observations.

Chapter 2 will elaborate on the methodology of this work, explaining the experimental set-up, the measured meteorites and minerals, the instruments, the limitations of this work, the software that have been used in this work and a short section on the origin of the spectral features. Chapter 3 will focus on the spectral data and the analysis of these data. In chapter 4 the spectral data from chapter 3 will be interpreted and in chapter 5 will be drawn the conclusions of the spectral analysis and interpretation. The last chapter will summarize all data gathered and draw conclusions.

CHAPTER 2

METHODOLOGY

2.1. Experimental set-up

2.1.1. Samples for Measurements

The review of research that has been done on Ceres' surface composition is the basis for the laboratory measurement and spectral investigation of possible analog materials. The measured samples will include meteorites and minerals. The measurements were done at the DLR, Berlin Adlershof (Planetary Emissivity Laboratory PEL; see Helbert et al. 2010), the Institute of Planetology at the University of Münster (Infrared and Raman for Interplanetary Spectroscopy, IR/IS) and at the DLR, Bremen (Complex Irradiation Facility CIF; Renger et al., 2014).

2.1.1.1.Meteorites

Cut slabs of meteoritic samples were provided by A. Bishop (Institute of Planetology at the Westfälische Wilhelms University in Münster; see appendix A for detailed sample description) and include the following:

- CM2: Cold Bokkeveld, Murchison, Banten, Nogoya
- CV3: Allende, Vigarano
- CO3: Kainsaz

2.1.1.2.Mono-minerals

Minerals for complementary measurements (pulverized and whole rock) were chosen on the basis of the meteorite compositions in section 1.2.2.1 and of the review of the work done so far on Ceres in section 1.2.2.1 and 1.2.2.2. Table 2-1 summarizes the measured minerals and the information on these minerals is found in appendix D and E (chemical analysis).

Table 2- 1: *Minerals measured at the DLR, Berlin Adlershof. The samples were prepared and pulverized by Ines Büttner (DLR, Berlin Adlershof). All samples were pulverized except the buddingtonite which was a whole rock.*

silicates	others
cronstedtite (serpentine group) **smectites:** saponite **oxides:** brucite Mg(OH) buddingtonite $NH_4AlSi_3O_8$	**sulfides:** tochilinite

2.1.2. Set up for spectral measurement

Reflectance spectra were obtained at the DLR in Berlin Adlershof, at the DLR in Bremen and at the IR/IS at the University of Münster. The measured wavelength range was 0.5 to 25 µm. The used spectrometers were an evacuated Bruker IFS66v/S, an evacuated Bruker Vertex 80, the Bruker Vertex 70v and the Bruker IFS 88.

The **IFS 66v/S** (DLR, Berlin) was used to measure the wavelength range between 1 and 25 µm using a Bruker A513 reflectance unit (see figure 2-1). The calibration standard for all measurements was diffuse reflecting gold-plated sandpaper or a gold mirror and the used IR source was a Globar-lamp. The beamsplitter was KBr (potassium bromide) in combination with a liquid-nitrogen cooled MCT-detector (mercury cadmium telluride detector). The pressure while measuring the samples was 0.2 mbar. The number of scans was chosen to be 500. The higher scan number was chosen due to increasing noise in the spectra related to the small aperture. The standard aperture was chosen to be 4 mm, dependent on the size of the sample. All measurements were done under room temperature conditions. The angle of incidence *i* and the exit angle *e* are individually chosen for each measurement. All samples were measured at i=e=15°.

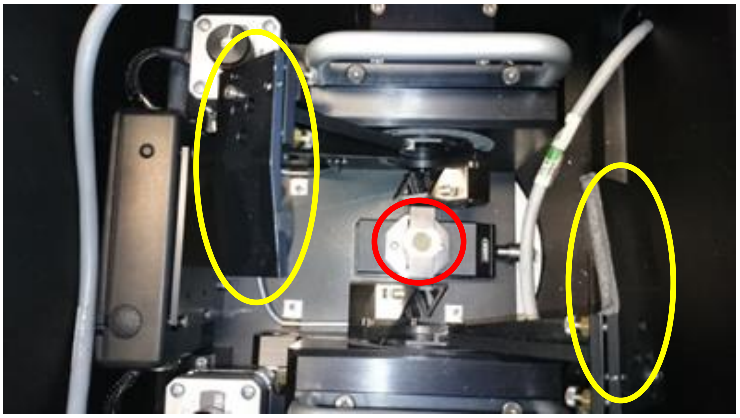

Figure 2-1. *A 513 measurement unit of the Bruker IFS 66v/s at the DLR, Berlin. The image show both mirrors that are individual adjustable (yellow circles) and a sample place in the sample holder (red circle).*

VIS spectra in the wavelength range between 0.45 and 1 µm were collected with a Bruker IFS88 at the DLR in Berlin Adlershof. A Harrick Seagull reflectance unit with pressed halon as a calibration standard was used. The beamsplitter was made of quartz with a Si-Diode-detector and the VIS source was a tungsten-lamp. Cups of powdered samples were rotated during the measurements, whereas the whole rocks were not rotated during measurement. The scan number was 500 and the aperture was 4 mm (standard, variations are due to sample size). The angle of incidence i and the exit angle e were equally chosen for this instrument (i=e=15°) as there is no possibility of varying these angles individually and all adjustments have to be made manually. The time between every measurement of the samples was 5 minutes as the chamber requires some time to be purged by dry air in order to have more or less similar measurement conditions.

To get a better overlapping for the spectra in the range between 1 and 2 µm, the buddingtonite, brucite and cronstedtite were measured with the Bruker Vertex 80v (DLR Berlin Adlershof), an FTIR spectrometer with a high spectral resolution greater than 0.2 cm^{-1}, and a resolving power of greater than 300,000:1 (Helbert et al., 2010). It can be operated under vacuum conditions to remove atmospheric features from the spectra. It covers the spectral range from 1 to 50 µm. The Bruker Vertex 80v has two detectors, one is a liquid nitrogen cooled MCT covering the wavelength range between 1-16 µm and a room temperature DTGS (deuterated tri-glycine sulfate) covering the wavelength range between 15 to 50 µm. It uses a KBr beamsplitter.

As the IFS88 is limited to wavelength >0.5 µm, the Vertex 80v of the DLR Institute of Space Systems in Bremen was used. It is possible to measure the samples in the wavelength range between 0.2 and 1.1 µm. This instrument has an A513 reflection unit. The source was a deuterium-lamp and the used standard was spectralon. The measurements were done under a pressure in the 10^{-10} mbar range. The sample and the standard were alternately measured (256 scans, 6 times each) to reduce variations in the resulting spectra as the source is not stable over time.

To get a better overlapping of the IFS66 and Vertex 80 data the Bruker Vertex 70v at IR/IS at the Institute of Planetology at the University of Münster was also used. This instrument uses a Globar lamp as a NIR source and has a CaF_2 beamsplitter (calcium fluoride). It is not required to cool the InGaAs detector (indium-gallium-arsenide detector). This instrument has an A513 reflection unit and the standard was spectralon. The spectra were corrected with a calibration curve received by the manufacturer of the spectralon. The measured spectra were multiplied by the reflectivity of the spectralon.

2.1.3. Limitations of the measurements

Some materials that are relevant to the surface composition of Ceres could not be measured at the DLR, Berlin Adlershof due to laboratory limitations. This includes water ices and frost as these materials require special set-ups in the laboratory that are not feasible with the current settings in this laboratory. Furthermore, as there is a wide range of organic material that could be potentially important to interpret Ceres' surface, only three members of organica were chosen. Other spectra of organic material if required will be taken from spectral libraries like Relab (http://www.planetary.brown.edu/relab/) or ASTER (http://speclib.jpl.nasa.gov/) or USGS http://speclab.cr.usgs.gov/spectral.lib06/ds231/datatable.html).

2.2. Spectra from other institutions and data bases

As mentioned above some spectra were taken from spectral libraries. To complete the data on the meteorites measured at the DLR laboratory, spectral reflectance data of CM, CI, CV and CO meteorites were taken from the Rrelab spectral database. Most of the mineral spectra were taken from Relab, as this library offers a variety of different mineral spectra with different measurement set-ups and grain sizes.

The data of water ice and frost were collected from ASTER spectral library. Spectral data of anthraxolite and kerite were delivered by L. Moroz. To get a wider range of data in the region between 1 and 2 µm data from other relevant materials like brucite, cronstedtite or buddingtonite were also collected from spectral libraries.

2.3. Software

The software that was used to collect the data during measurement and to process the raw data was OPUS. This software is provided by Bruker (www. Bruker.com) and is used for the measurement, the processing and the evaluation of IR, NIR and Raman spectra. Magic Plot (www.magicplot.com) was used to visualize and to analyze the measured data and the Relab data. This software is an application for scientific and engineering data analysis, graphing, nonlinear curve fitting and multi-peak fitting. IDL was used to normalize data to one spectrum and to model different mineral mixings. Finally, Plot Digitalizer, a freeware, was used to digitalize the different spectra of Ceres.

2.4. Origin of spectral features - fundamentals

Spectral signatures or features were used to identify specific materials (minerals, ices and organics) on Ceres' surface. These features are caused by the interaction of the incoming electromagnetic radiation with solid body materials. As a result of this interaction different mechanisms produce photon absorptions of the excitation radiation at appropriated wavelengths. The type of excitation depends on the wavelength of the incoming radiation; the shorter the wavelength, the higher the energy of the electromagnetic wave (Gaffey et al., 1993; Arnold, 2014, p.123f). The short wavelength VIS range is dominated by electronic processes, whereas for longer mid-infrared wavelengths lattice vibrations of atoms, molecules, and groups of molecules cause absorption features (fundamental vibration bands) for most of the relevant materials (Salisbury, 1993). In the transition range of the short wavelength, infrared from SWIR overtone and combination tone bands of the fundamental vibrations occur (Arnold, 2014, p. 124). These processes will be briefly elaborated in the following sections.

2.4.1. Absorption processes (transition processes)

2.4.1.1. Electronic transitions

Molecular electronic transitions are based on the excitement of electrons of the transition metals and Lanthanides in the crystal structure of a mineral (Burns et al., 1993). Absorption bands of electronically processes are produced at different energies because crystal structures incorporating cations into the solid body have variable symmetries. This led to the formation of absorption bands that have varying wavelength based on the amount of energy needed to produce them (Burns et al., 1993; Arnold, 2014, p. 126).

2.4.1.2. *Crystal field transitions CFT*

Crystal field transitions are the most common electronic process (Burns et al., 1993; Clark, 1999) and are formed by absorption of photons in the wavelength range from the UV to the NIR. CFTs are based on the crystal field theory developed by Van Vleck (1932). This theory is a model that describes the influence of the electronic field of the anions/ligands on the electrons of the d- and f-orbitals. This theory helps to characterize the interaction of electromagnetic radiation with minerals which have incorporated transition metals (e.g., Ni, Cr, Co, Fe, etc.; Burns et al., 1993; Clark, 1999). It was later extended and now includes the ligand field theory LFT (Hartman and Ilse, 1951). CFTs depend on the symmetry properties of the transition metal's 3d orbitals and their energy differences with the anions and ligands (Burns, 1993; Arnold, 2014, p, 130).

Most important for rock-building minerals are low degree symmetries producing the diagnostic Fe^{2+}/Fe^{3+} absorption bands in the VIS/NIR. Bands of the Fe^{2+} ions occur at 1.04 to 1.08 µm, 0.45 µm, 0.49 µm and 0.615 µm (Burns, 1993; Arnold, 2014, p.130). Fe^{3+} absorption features are generally weaker than Fe^{2+} transitions and occur in the wavelength range between 0.4 and 0.9 µm (Arnold, 2014, p. 134).

2.4.2. Charge Transfer

Charge transfer is the overlapping of orbitals of neighboring transitional metals during electron transitions between two adjacent cations (e.g. Burns, 1981; Amthauer and Rossmann, 1984).

2.4.2.1. *Intervalence-charge transfer (IVC*T) *transitions*

There are two different kinds of metal-metal charge transfers. There is the charge transfer between two equal metal ions with different valence (e.g., $Fe^{2+} \rightarrow Fe^{3+}$) or the charge transfer between two different metal ions with different valence (e.g., $Fe^{2+} \rightarrow Ti^{4+}$). Features are produced by photon absorption during the electron transition from one ion to the other when the energy level is increased. The band width is wider than those produced by CFTs (Sherman and Waite, 1985; Burns et al., 1993; Arnold, 2014, p. 135).

2.4.2.2. *Oxygen-metal charge transfer (OMCT) transitions*

This kind of transitions is between the central metal ion and an oxygen ligand. Features produced by photon excitation in the UV wavelength range have higher intensities than CFTs.

To summarize these fundamentals for the iron features based on the work done by Burns (1985a,b) and Arnold (2014, p136):

- Spin-allowed CFTs in Fe^{2+} → feature near 1 µm
- Spin-forbidden CFT in Fe^{2+} → weak but sharp feature in the VIS
- Spin-forbidden CFT in Fe^{3+}→ wide feature in the VIS wavelength range
- Fe^{2+} → Fe^{3+} IVCT → feature between 0.55 and 0.8 µm
- O → Fe OMCT → feature in the UV (0.262-0.263 µm)
- O^{2-} → Fe^{2+} OMCT → feature at 0.27 µm
- O^{2-} → Fe^{3+} OMCT → feature at 0.40 µm

2.4.3. Lattice vibrations

Lattice vibration bands arising from spectral selective absorption of radiance are caused by excitation of oscillations of atoms, ions or molecules in a solid state material. These vibrations depend on the mass, bond strength of these atoms/molecules, and on the crystal structure of the lattice. Therefore, they contain diagnostic spectral information for minerals and many solid organics. Comprehensive theoretical work exists in classifying the different lattice vibrations and applying this knowledge for planetary surface composition analysis (e.g. Hunt, 1982, Salisbury and Walter, 1989). There are fundamental vibrations (transitions between $\nu_j=0$ to $\nu_j=1$) causing so called Reststrahlen bands. For silicates such features are associated with Si-O stretching modes and occur between 8 and 12 µm. For water ice stretching and bending of the H_2O produce three bands - two between 2.9 and 3.2 µm and one near 6 µm. Overtone vibrations are the energies of the first overtone that have roughly the wave number of the fundamental multiplied by 2. Combination vibrations are based on the addition of two or more fundamental vibrations (e.g. $\nu_1 + \nu_2 + \nu_3$). The resulting features occur mostly in the SWIR and they are weaker than those resulting from the fundamental vibrations (Clark, 1999; Arnold, 2014, p. 139ff).

CHAPTER 3

SPECTRAL DATA AND ANALYSIS

3.1. Meteorite spectra in the 0.2 to 5 µm wavelength range

The base of this work is the measurement of available meteoritic samples and minerals and the analysis of their spectral behavior. To complete this data and to compare the data better to each other, Relab spectral data from the Brown University was also used. For details and sample descriptions see appendix A and Appendix B (chemical analysis).

Based on section 2.4 diagnostic absorption features have been identified and described. These include the wavelength of the slope change λ_{SC}, slope 1 (ΔR_1) and slope 2 (ΔR_2).

3.1.1. CI chondrites

3.1.1.1. Ivuna

The spectra of Ivuna are shown in figure 3-1a. The samples are dark (low mean reflectance). The spectra are mostly flat and weakly featured. A broader band between 2.7 and 3.7 µm can be attributed to structural water, OH-groups or adsorbed water (from the Earth's atmosphere). Measuring samples under terrestrial conditions often results in higher amounts of water adsorbed by the samples compared to expected conditions for the surfaces of an airless planetary object. This effect influences the spectral behavior in the 2.7 to 3.2 µm region, described in section 3.2.1 (p. 82-84) in more detail and has to be considered using this band for comparative spectral studies.

The Ivuna spectra show variable slopes from the visible to the infrared range. To determine characteristics of these differences, the spectral slopes of the spectra and the wavelength of slope change were introduced. To gain comparable results and to remove albedo differences, all data were scaled to one spectrum (Murchison, cgp096) at 0.7 µm (R=0.0504). To scale the spectra the value of each spectrum at 0.7 µm was determined and the R=0.0504 then divided by this value to get a factor. Each spectrum was multiplied by the respective factor. In figure 3-1a are shown the scaled spectra of Ivuna. These scaled spectra were used to determine the wavelength of the slope change λ_{SC}, slope 1 (ΔR_1) and slope 2 (ΔR_2) (see figure 3-1b). The λ_{SC}, slope 1 (visible spectral range) and slope 2 (near-infrared range) are characterized as follows:

- wavelength of the slope change $\boldsymbol{\lambda_{SC}}$ (µm) is defined as the wavelength where the slope changes (< 1 µm). It was determined by applying a linear function to the spectral slopes in the VIS and NIR wavelengths region. The intersection of both lines was defined as λ_{SC}. Appendix E summarizes the λ_{SC} values for the different meteorites and minerals.

- slope 1 **($\boldsymbol{\Delta R_1}$ in µm^{-1})** is defined as the slope of the function of the linear regression line adjusted to the spectrum shortward of the λ_{SC}. Appendix E summarizes the wavelength range of slope 1 for the different meteorites and minerals.

- slope 2 (**ΔR$_2$ in µm^{-1}**) is defined as the slope of the spectrum in the wavelength range longward of the λ_{SC} to 2 µm. In appendix E the wavelength range and the values of slope 2 are summarized for the different meteorites and minerals.

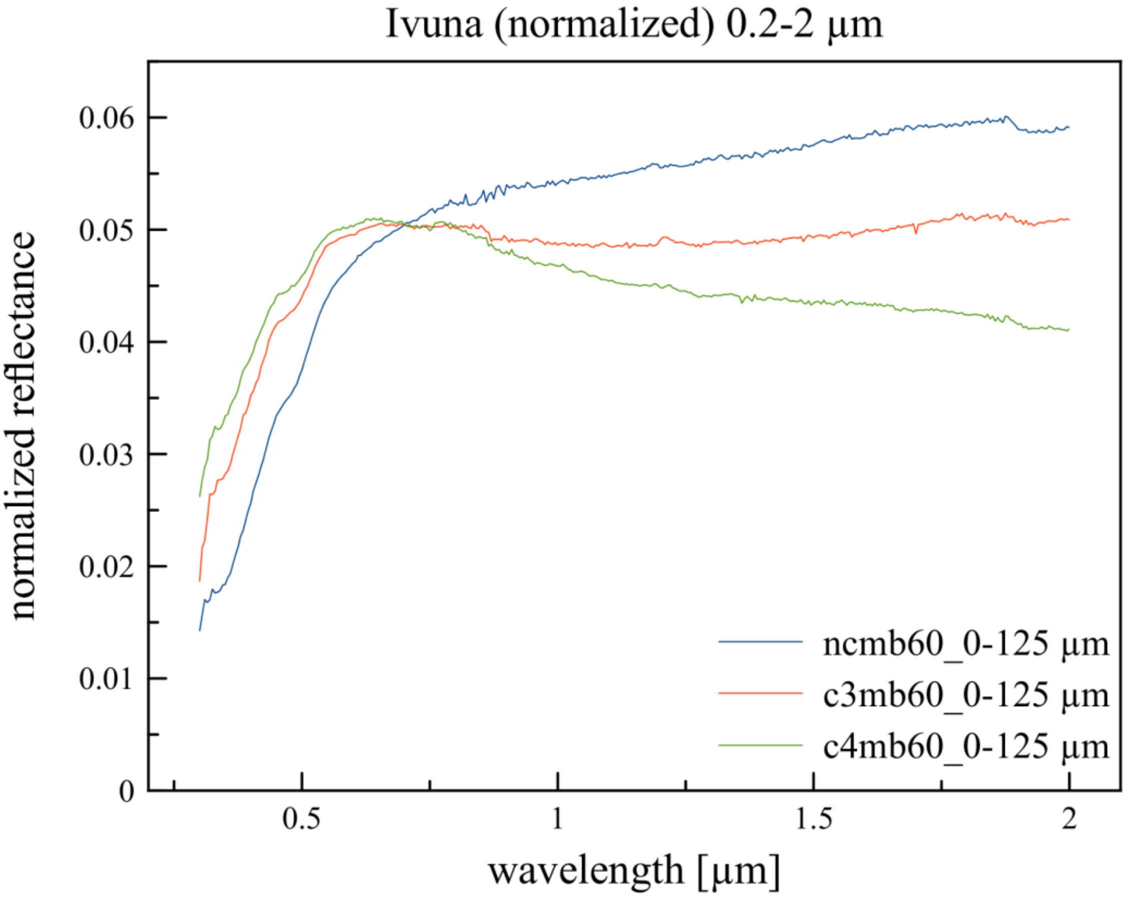

Figure 3-1a. *Scaled spectra of the meteorite Ivuna. The spectra show variations in slope 2 although they have the same grain size of 0-125 µm.*

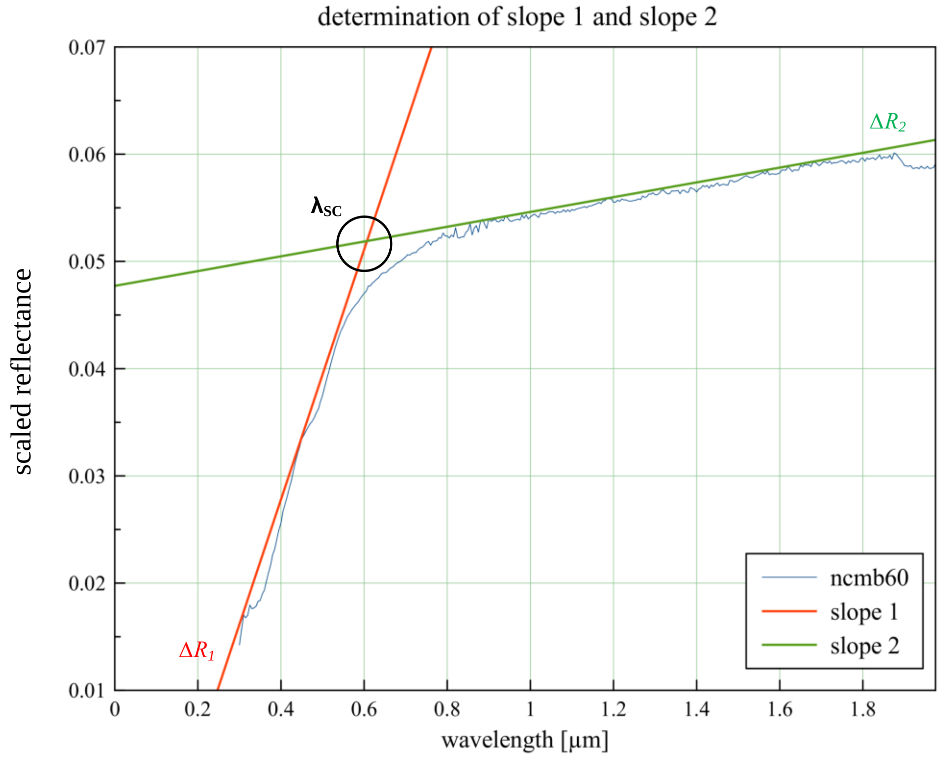

Figure 3-1b. *This plot shows the determination of* λ_{SC}, ΔR_1 *and* ΔR_2 *explained at a sample of the Ivuna meteorite.*

The spectra of Ivuna show a steep positive slope in the VIS changing to a shallower positive slope in the NIR. Although the samples have the same grain size of 0-125 µm they show variations in the NIR slope (figure 3-2), e.g. the c4mb60 spectrum has a negative slope in this region. The λ_{SCmean} is at 0.553 µm and the slope shortward is steeper (ΔR1:0.1002-0.1254 μm^{-1}) than the slope longward of the λ_{SC} (ΔR_2: -0.0076-0.0069 μm^{-1}). The black arrows in figure 3-1a mark possible absorption features seen in the single spectra of the Ivuna meteorite. The weak absorption feature at ~0.5 µm could be attributed to Fe-O in magnetite, maghemite or ferrihydrite (Cloutis et al., 2011a). There is another shallow feature seen in all three spectra at roughly 1.95 µm attributed to OH or water in the structure of phyllosilicates, carbonates or sulfates (Cloutis et al., 2011a).

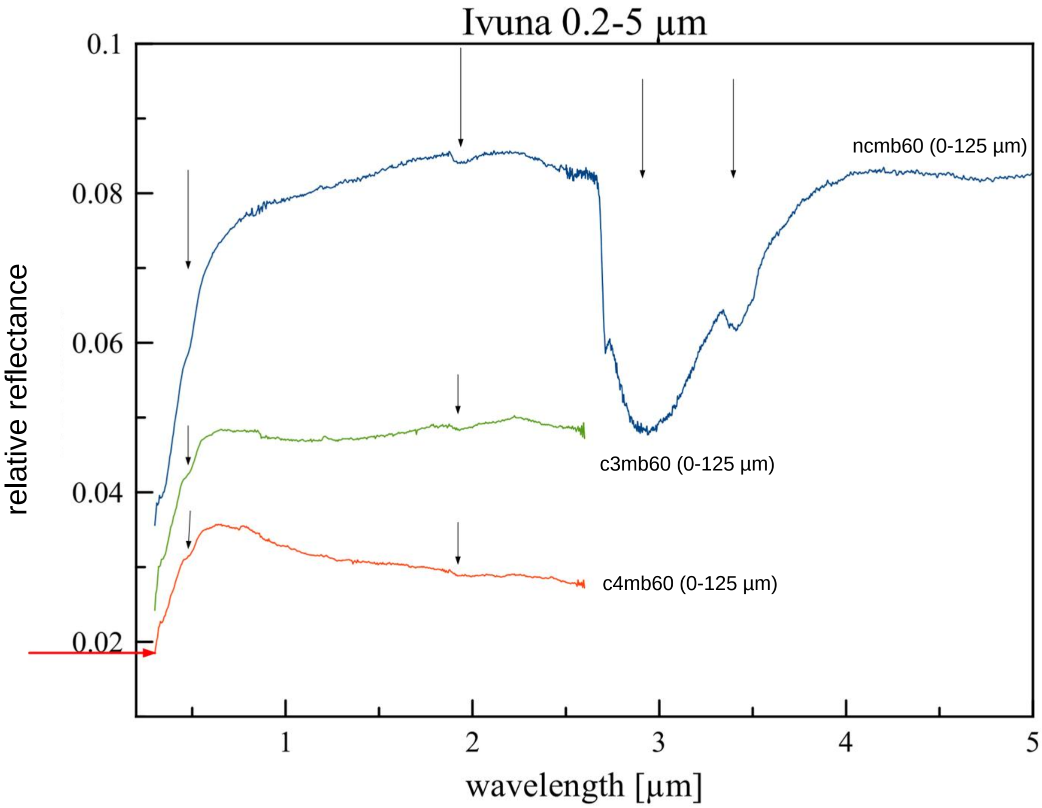

Figure 3-2. *Plot of spectral reflectance data of the meteorite Ivuna in the wavelength range from 0.2 to 5 µm. The offset between the single data is +0.01 (compared to the spectra marked by the red arrow). The data was taken from Relab. For detailed descriptions of the samples (including source of measurements) see appendix A.*

3.1.1.2. Orgueil

The different spectra of Orgueil are presented in figure 3-3, for information on the single spectra see appendix A. There is only information on the grain size of one sample available (ncmb57, 0-100 µm). The spectra are weakly featured in the wavelength range shortward of 2.7 µm and generally have a positive slope from 0.3 to 2.6 µm. The spectra have a weak negative slope in the wavelength range longward of 3.7 µm. The λ_{SCmean} is at 0.533 µm and the slopes in the shortward wavelength range are steeper (ΔR_1: 0.1078-0.1465 μm^{-1}) than those in the wavelength region > λ_{SC} (ΔR_2: 0.0013-0.0139 μm^{-1})

There are two weak features visible in nearly all spectra (black arrows in figure 3-3). The feature at ~0.45 µm could be attributed to phyllosilicates, magnetite and/or to organic material (Cloutis et al., 2011a). The other feature is at ~1.4 µm and appears to be due to hydroxyl or water in the structure of the minerals (Cloutis et al., 2011a). As there is also a feature at ~1.9 µm this meteorite seems to have bond water in its structure (Cloutis et al., 2011a). Orgueil also has a broad feature between 2.7 µm and 3.4 µm (for detailed description see section 3.2.1, p. 82-84). According to Osawa et al. (2005), the 2.71 µm feature could be attributed to serpentine (lizardite), whereas Zaikowski (1979) attributed this feature to chlorite and chamosite.

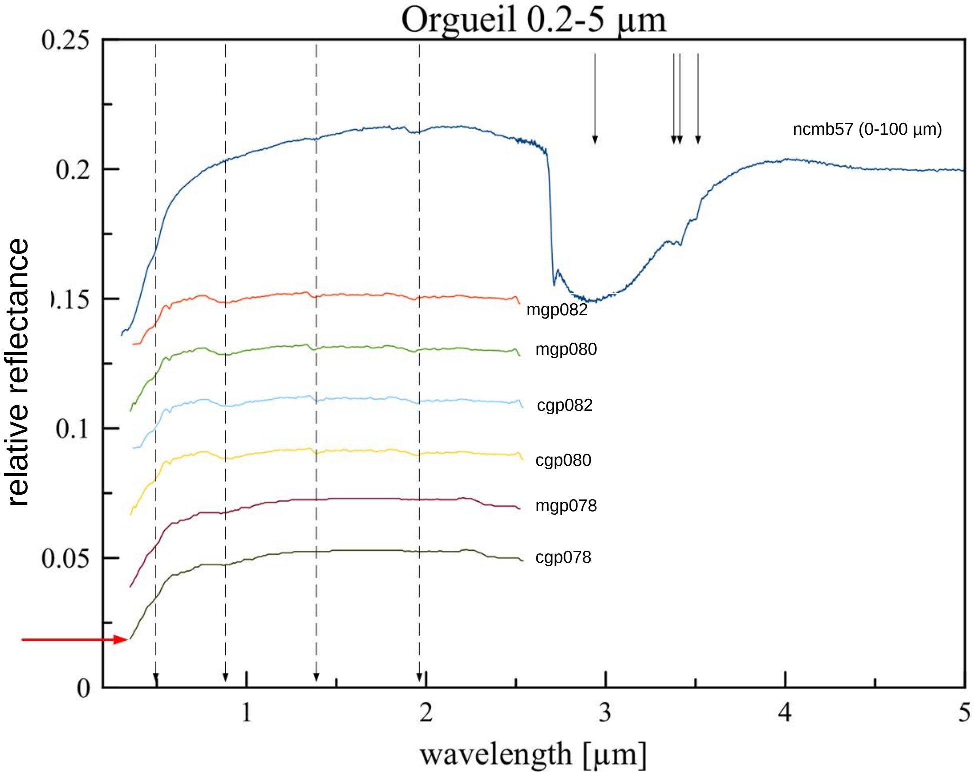

Figure 3-3. *Plot of spectral reflectance data of the meteorite Orgueil in the wavelength range from 0.2 to 5 µm. The offset between the single data is +0.02 (compared to the spectra marked by the red arrow). The data was taken from Relab. For detailed descriptions of the samples (including source of measurements) see appendix A.*

3.1.1.3. Alais

The spectrum of the CI chondrite Alais ranges from 0.2 to 2.6 µm and is illustrated in figure 3-4. There is no information on the grain size available. The data was taken from Relab (see appendix A). The spectrum Alais is characterized by a generally positive slope between 0.3 and 1.8 µm and by a negative slope after 2.0 µm. As in the other CI chondrite spectra, it is weakly featured in the wavelength range between 0.2-2.6 µm. The determined λ_{SCmean} is at 0.525 µm and the spectra have a steep ΔR_1 of 0.1344-0.1355 μm^{-1}, whereas ΔR_2 is shallower (0.0258-0.0261 μm^{-1}). One absorption feature appears around 0.45 µm (black arrows in figure 3-4) and could be attributed to Fe-O in magnetite, maghemite or ferrihydrite (Cloutis et al., 2011a). Both spectra show a clear feature at ~1.9 µm due to hydrated phases like saponite, ferrihydrite or hydrated sulfates (Cloutis et al., 2011a).

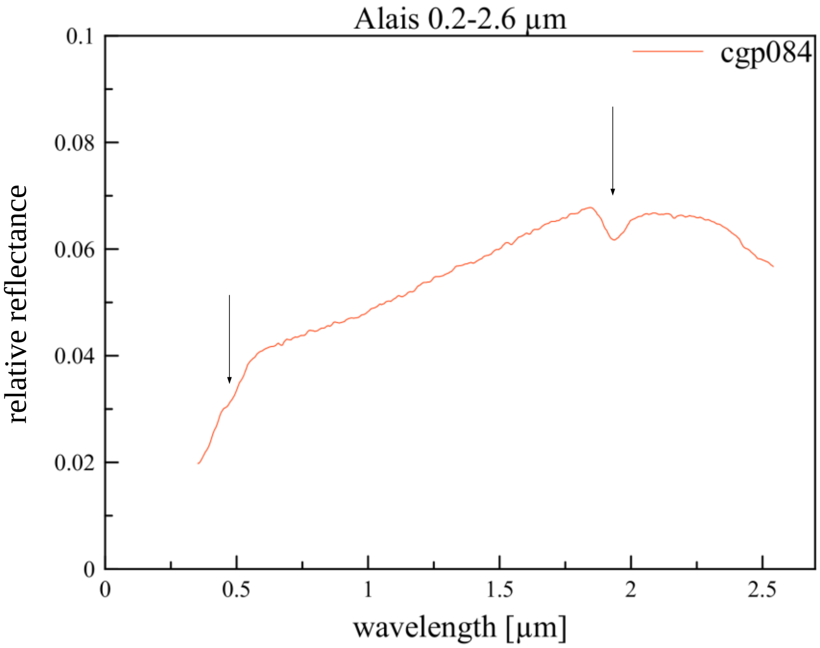

Figure 3-4. *Plot of spectral reflectance Data of the meteorite Alais in the wavelength range from 0.2 to 2.6 µm. The data was taken from Relab. For detailed descriptions of the samples (including source of measurement) see appendix B.*

3.1.2. CM chondrites

3.1.2.1. Murchison

Figure 3-5 and 3-6 illustrate the different spectra of Murchison. The Relab spectra are available in a variety of grain sizes indicated in figure 3-5 (e.g. s3mb64: 0-63 µm; c4mb64: 63-125 µm). The spectra of the meteorites measured at the DLR are shown in figure 3-6. All Murchison spectra have a positive slope in the VIS/NIR region, changing to negative longward of 3.5 µm. The λ_{SCmean} is at 0.495 µm. The ΔR_1 values are between 0.000964 and 0.178 μm^{-1} indicating a steeper slope than ΔR_2 (-0.0089-0.0237 μm^{-1}).

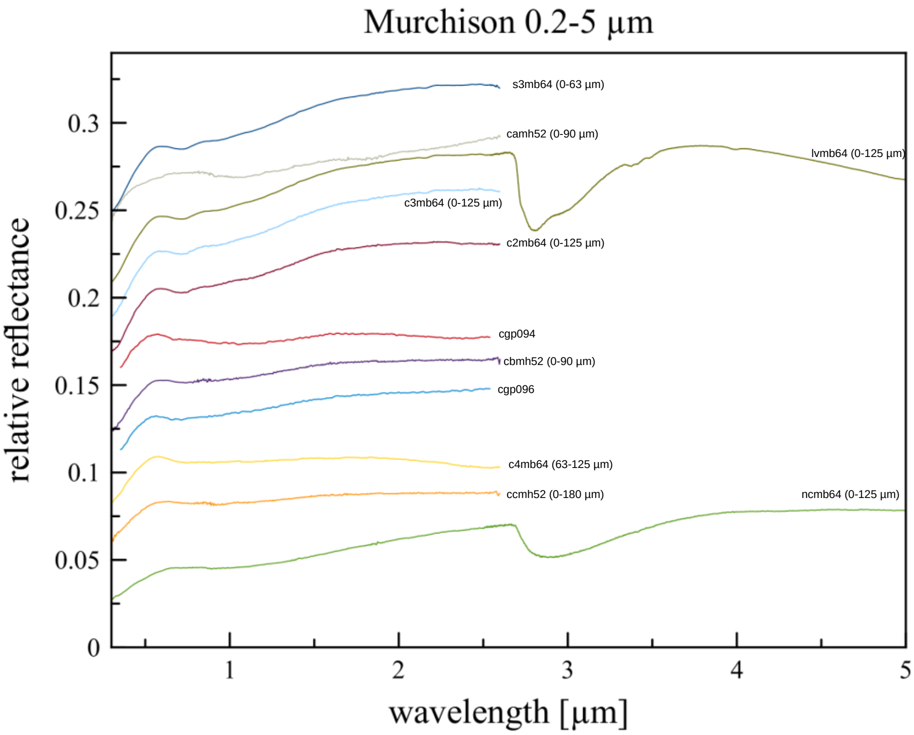

Figure 3-5. *Plot of spectral reflectance data of the meteorite Murchison in the wavelength range from 0.2 to 5 µm. The offset between the single data is +0.01. The data were taken from Relab. For detailed descriptions of the samples (including source of measurements) see appendix A.*

The spectra are weakly featured. The weak absorption feature at ~0.65 to 0.7 µm (black arrow in figure 3-5) could be attributed to saponite group minerals or Fe-bearing serpentines (Cloutis et al., 2011b). The spectra of Murchison show a feature at ~2.8 µm.

This feature is getting weaker in the lcmb64 spectrum and nearly disappears in the ncmb64a spectrum. This feature is described in section 3.2.1 (p. 82-84).

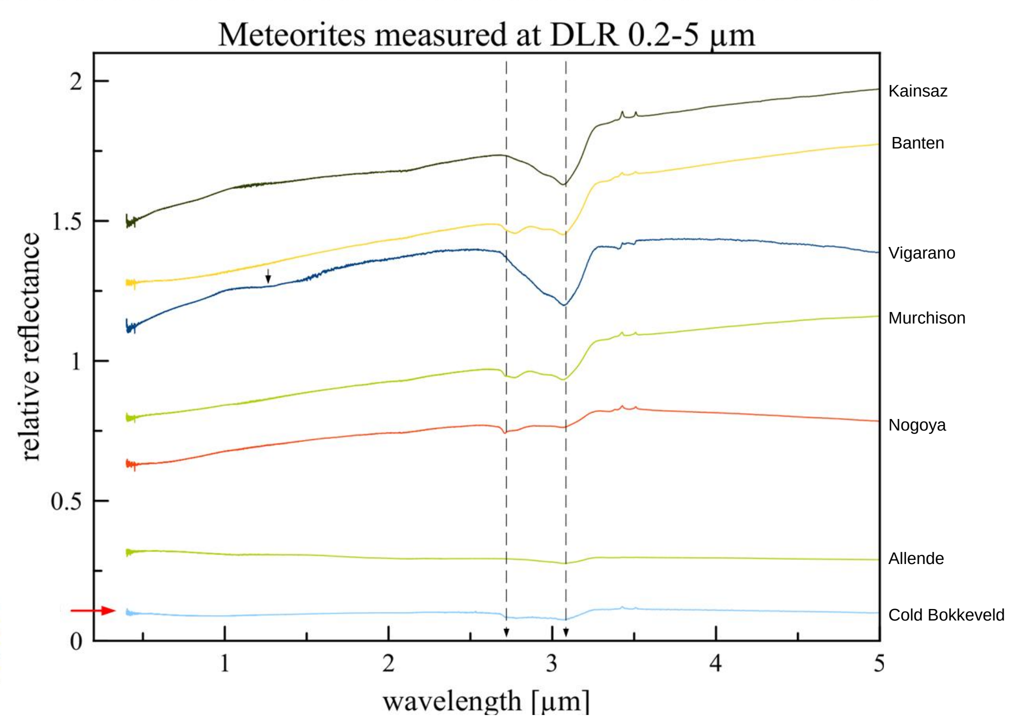

Figure 3-6. *Spectra of the meteorites that were measured at the DLR in Berlin Adlershof and Bremen and at the University of Münster. For detailed sample description see appendix A. The offset between the spectra is +0.02.*

3.1.2.2. Banten

Figure 3-7 shows the spectrum of the meteorite Banten, measured at the DLR in Berlin Adlershof as a whole rock. It has a positive slope in the wavelength range between 0.2 and 5 µm. The spectrum shows a general increase in the relative reflectance over this wavelength range. The change in slope was determined to be at a wavelength of <0.48 µm. The slope longward of the λ_{SC} is $\Delta R_{2=}0.0172$.

There is a shallow, narrow absorption feature marked by the black arrow at ~0.6 µm attributable to Fe^{2+}/Fe^{3+} possibly from cronstedtite or saponite (Cloutis et al., 2011b).

There is a double feature with minima at ~2.76 and 3.06 µm. The first band could be attributed to OH (Hunt, 1977) and the other feature could be due to water, brucite or saponite.

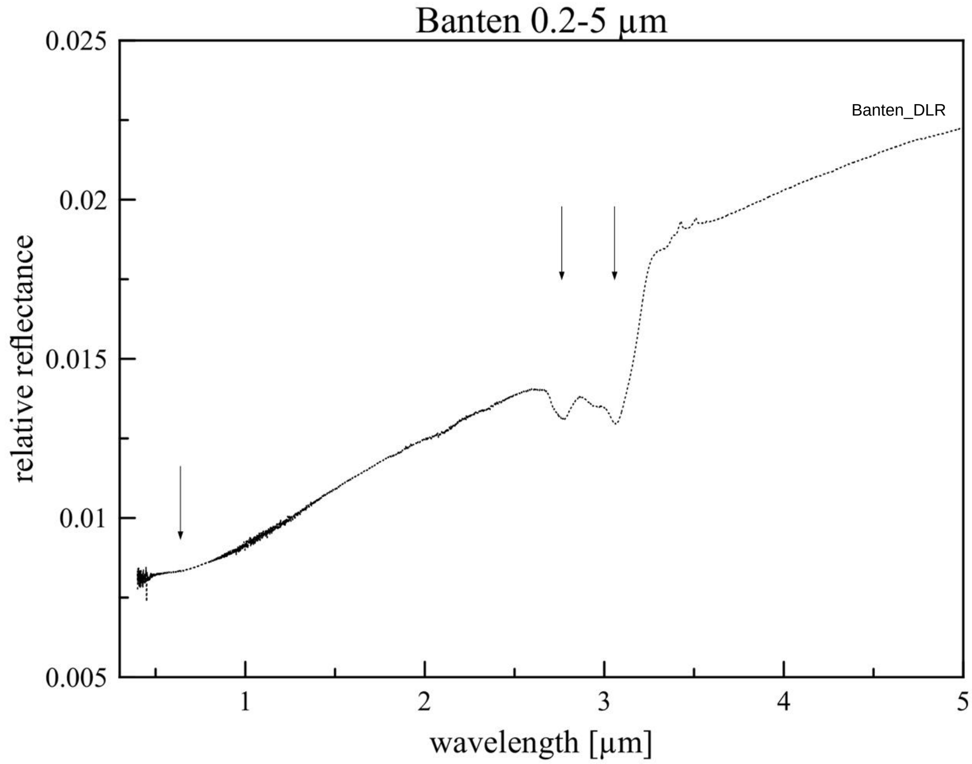

Figure 3-7. *Plot of spectral reflectance data of the meteorite Banten (whole rock) in the wavelength range from 0.2 to 5 µm. The data is from measurements at the DLR and there are no other spectra available in the spectral libraries. For detailed descriptions of the samples (including source of measurements) see appendix A.*

3.1.2.3. Cold Bokkeveld

The different Relab spectra of the CM chondrite Cold Bokkeveld are shown in figure 3-8 and the spectrum of the whole rock measured at the DLR is shown in figure 3-6. The Relab data are only available in the 0.3-2.6 µm range in different grain sizes (0-125 µm, 0-75 µm, 75-150 µm and 150-500 µm). The spectra collected from Relab have a general steep positive slope in the wavelength range shortward of 0.6 µm. Some spectra (e.g. c4mb61) show a negative slope in the wavelength range longward of 0.6 µm, whereas others like ColdBokkeveld_DLR (figure 3-6) or c1mb61 (figure 3-8) show a positive slope in this wavelength region. The λ_{SCmean} is at 0.481 µm. The ΔR_1 values range from 0.102-0.178 μm^{-1} and the ΔR_2 values are between -0.0089-0.0164 μm^{-1} which is much shallower than the slope 1 value. The spectra of Cold Bokkeveld are weakly featured as the other CM chondrite spectra. There appears to be a feature at ~0.6 to 0.7 µm in the ColdBokkeveld_DLR spectrum and it also appears in two Relab spectra (see figure 3-8) which could be attributed to saponites (Cloutis et al., 2011b). There is another possible absorption feature at ~1.4 µm occurring in three spectra (figure 3-8) attributed to OH (Sherman and Virgo, 1988). In the spectrum of ColdBokkeveld_DLR (figure 3-6) is seen a broad absorption feature at 2.6-3.3 µm that appears to be a double feature.

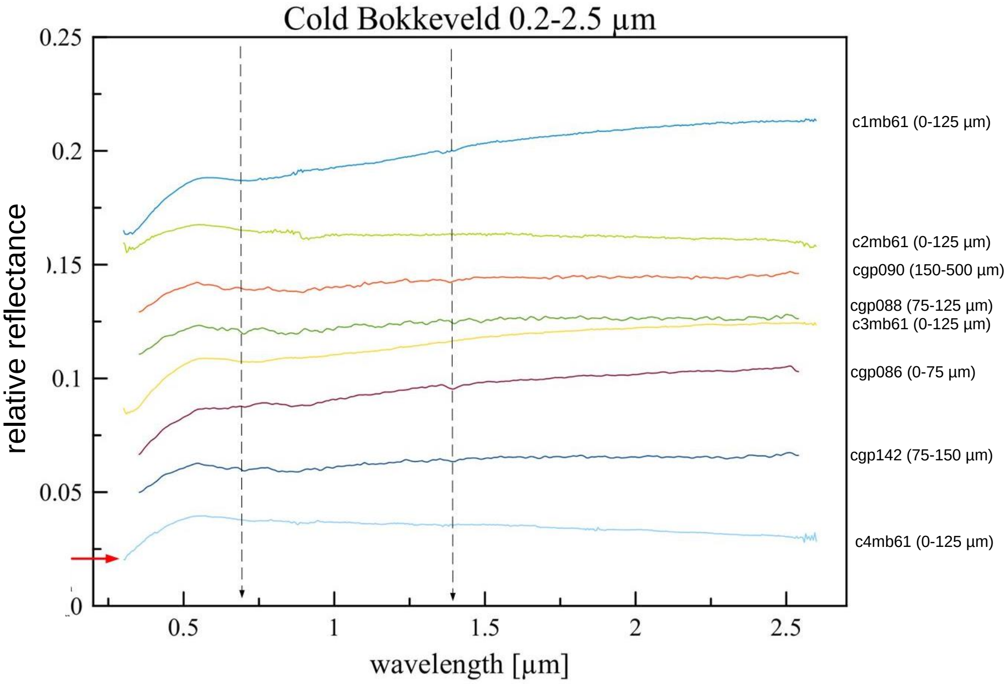

Figure 3-8. *Plot of spectral reflectance data of the meteorite Cold Bokkeveld in the wavelength range from 0.2 to 5 µm. The offset between the single data is +0.02 (compared to the spectra marked by the red arrow). The data were taken from Relab. For detailed descriptions of the samples (including source of measurements) see appendix A.*

3.1.2.4. Mighei

In figure 3-9 is shown the spectrum of the CM chondrite Mighei. There is only one spectrum available of this meteorite covering the spectral range from 0.3-2.5 µm (grain size: 0-75 µm). The sample has an overall low reflectance. The spectrum has a generally steep positive slope (ΔR_1=0.1423) in the wavelength range shortward of λ_{SC}=0.48 µm. The spectral slope then rises slightly positively indicated by ΔR_1=0.0124. The spectrum of the Mighei meteorite is weakly featured. There is one absorption feature at ~0.6 µm attributable to saponite (Cloutis et al., 2011b).

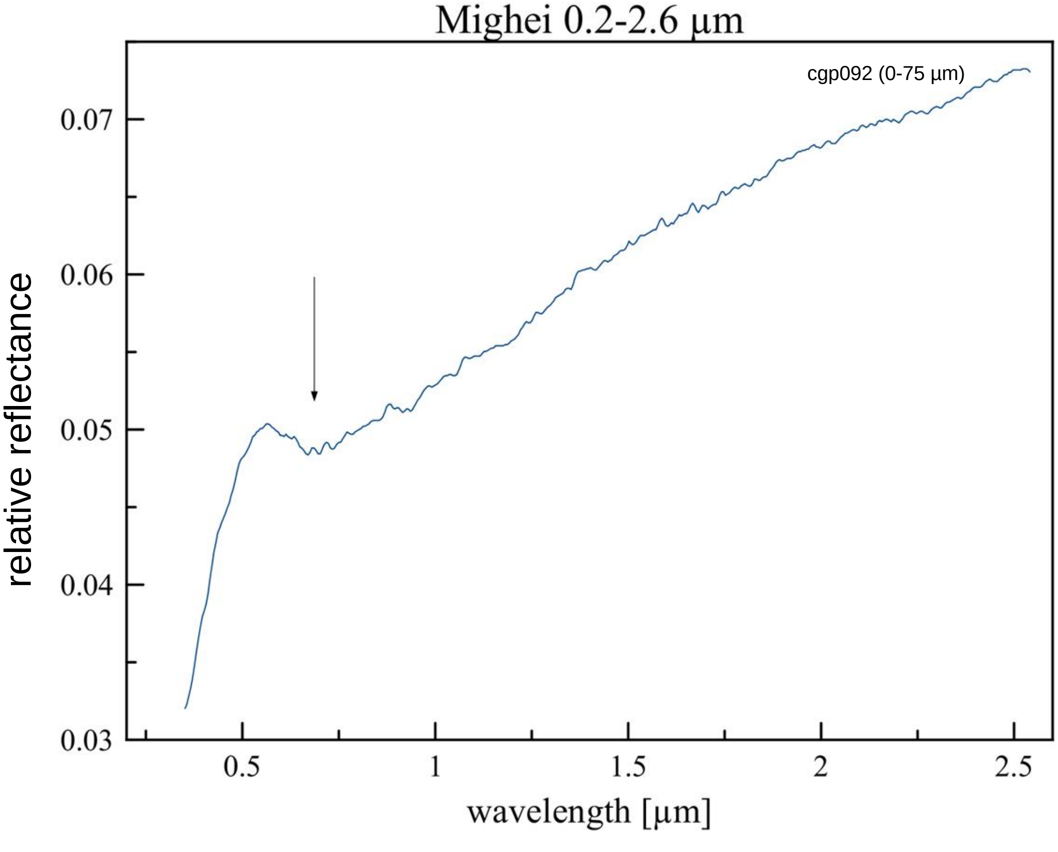

Figure 3-9. *Plot of spectral reflectance data of the meteorite Mighei in the wavelength range from 0.2 to 2.6 µm. The data was taken from Relab. For detailed descriptions of the samples (including source of measurement)s see appendix A.*

3.1.2.5. Murray

In figure 3-10 are shown the spectra of the CM chondrite Murray. The data was taken from Relab. Three spectra have a grain size of 0-100 µm and there is no data available on the grain size of the cgp098 spectrum. The samples are dark (low reflectance). The spectra have a general steep positive slope in the wavelength range shortward of λ_{SCmean} =0.513 µm. The ΔR_1 values are between 0.1296-0.1657 $µm^{-1}$, whereas the ΔR_2 values are between 0.0073-0.144 $µm^{-1}$ indicating a much shallower slope in the wavelength range longward of the λ_{SC}. The slope of the spectra is shallower in the range from ~1.5 to 1.6 µm to 2.6 µm and has a negative rise in the wavelength region longward of 3.9 µm.

The spectra of Murray show some weak absorption features. One is at ~0.75 µm (see figure 3-10, black arrows) attributed to serpentine phyllosilicates (Cloutis et al., 2011b) and another feature is at ~0.9 µm, possibly due to saponite or serpentines (Cloutis et al., 2011b). There is a weak absorption feature at ~1.4 µm, but this is only seen in the spectra of cgp098 (see figure 3-10). Ncmb56 shows a broad asymmetric absorption feature between 2.6 and 3.2 µm which is possibly a double feature (see figure 3-10). This spectral region is discussed in section 3.2.1 on pages 82-84.

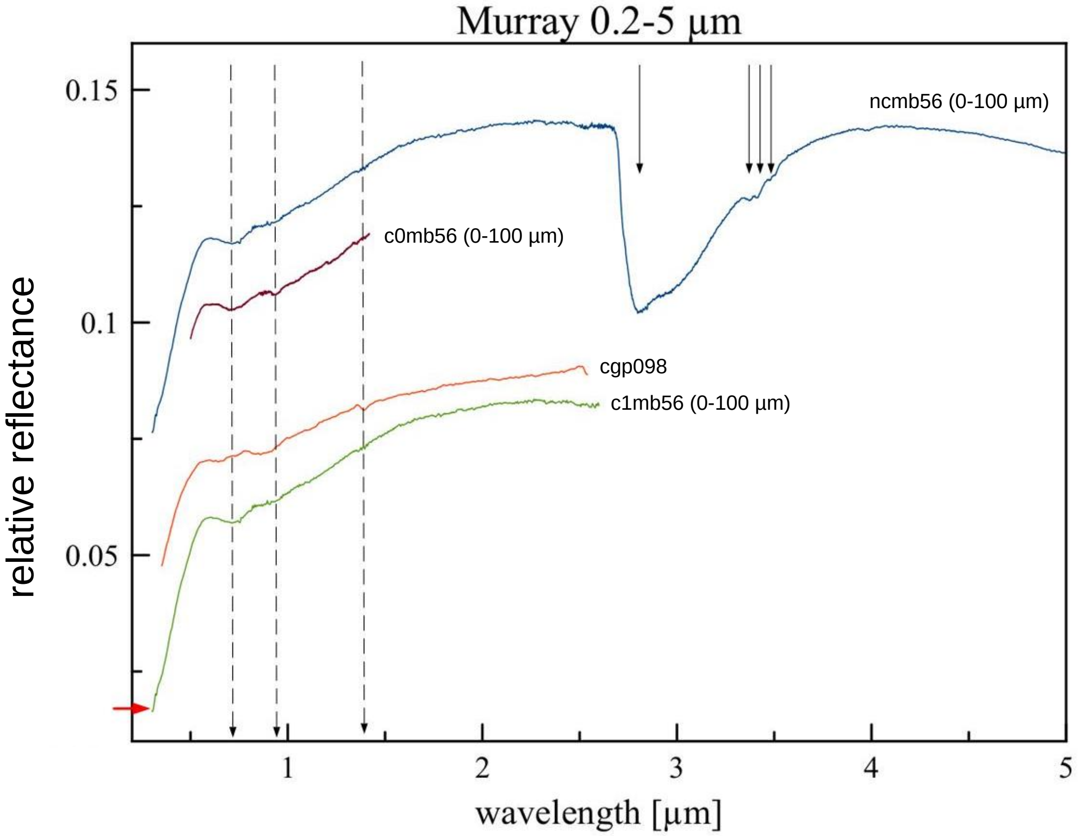

Figure 3-10. ***P****lot of spectral reflectance data of the meteorite Murray in the wavelength range from 0.2 to 5 µm. The offset between the single data is +0.02 (compared to the spectra marked by the red arrow). The data was taken from Relab. For detailed descriptions of the samples (including source of measurements) see appendix A.*

3.1.2.6. Nogoya

Figures 3-6 and 3-11 show the plot of the spectra of the meteorite Nogoya The samples measured at Relab are available in different grain sizes, e.g. c2mb62: 0-125 µm, c3mb62 :0-63 or c4mb62: 63-125µm. The spectra have a generally steeper positive slope in the wavelength region shortward of the λ_{SCmean}=0.49 µm. This is shown by the values of ΔR_1 ranging from 0.1373-0.1581 µm^{-1}. The ΔR_2 values of -0.0051 to 0.0168 µm^{-1} indicate a shallower slope in the NIR region of the spectra than in the VIS. The Relab spectra have a shallow positive slope from the λ_{SC} to ~2.6 µm whereas the sample measured at the DLR shows a steeper slope in this wavelength region (see figure 3-6 and

3-11). The DLR spectrum has a negative slope longward of 3.5 µm, but the ncmb62 spectrum has a slightly positive slope after 3.5 µm.

The spectra of Nogoya (figure 3-6 and figure 3-11) are only weakly featured. There is a small, shallow feature at ~0.6 to 0.7 µm seen in all spectra of Nogoya (see figure 3-11, black arrows) attributed to saponite group phyllosilicates and/or serpentines (Cloutis et al., 2011b). Three spectra show a weak absorption feature at ~2.2 to 2.3 µm which could be due to saponite group phyllosilicates and/or serpentine group minerals (Cloutis et al., 2011b). There is a double absorption feature in the spectrum of Nogoya_DLR between 2.6-3.3 µm (figure 3-6). This feature also appears in the Relab (ncmb62) spectrum as a single feature but is shallower and without the steep increase in reflectance at ~3.15 µm (for detailed discussion of this wavelength range see section 3.2.1 on pages 82-84.

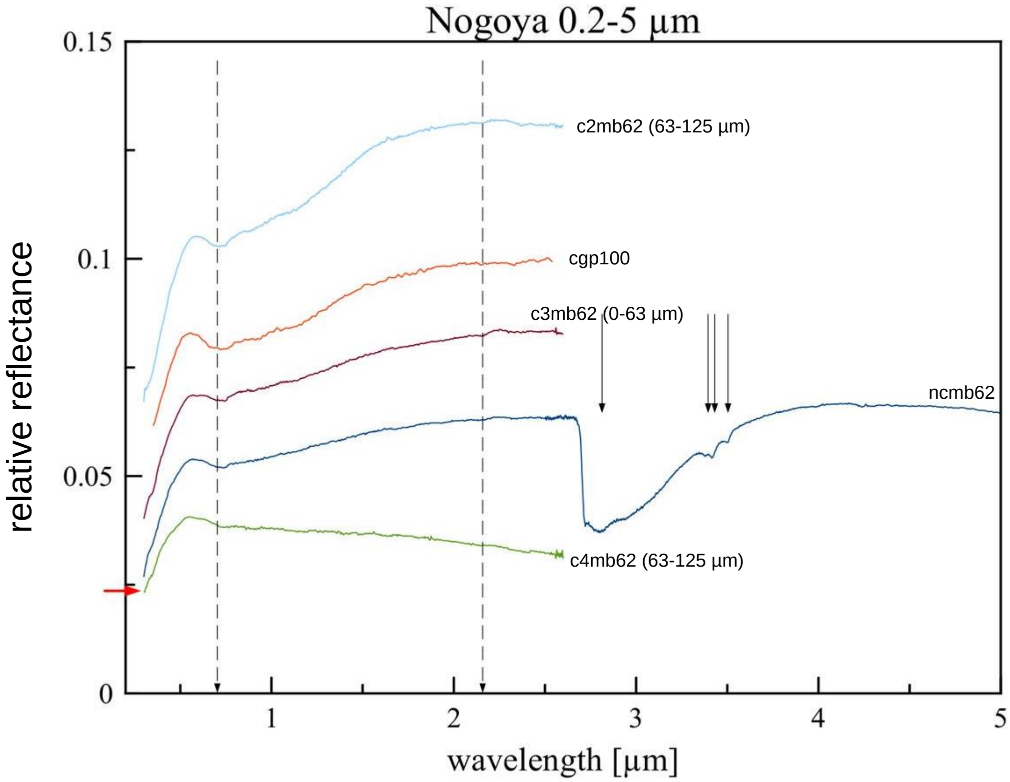

Figure 3-11. *Plot of spectral reflectance data of the meteorite Nogoya in the wavelength range from 0.2 to 5 µm. The offset between the single data is +0.05 (compared to the spectra marked by the red arrow). For detailed descriptions of the samples (including source of measurements) see appendix A.*

3.1.3. CV chondrites

3.1.3.1. Allende

The spectra of Allende are shown in figure 3-6 (own measurements) and 3-11 (Relab). The spectra of Allende have a steep slope of ΔR_1: 0.1885-0.3789 µm^{-1} shortward of the λ_{SCmean}=0.423 µm. The spectra flatten after the λ_{SCmean} and one spectrum has a negative slope (ΔR_2=-0.003 µm^{-1}) whereas the other spectra have a positive slope of ΔR_2 between 0.004 and 0.0075 µm^{-1}. The measurements included different grain sizes of the Allende meteorite (see figure 3-12 and appendix A) including the following fractions: 0-63 µm, 63-125 µm and 0-125 µm.

The spectra of Allende appear to be weakly featured in the wavelength range between 0.3 and 5 µm (see figure 3-12). Taking a closer look on the single spectra reveals that there are some absorption features in this wavelength range indicated by the black arrows (figure 3-6 and 3-12). One feature is at ~0.5 µm. This feature could be attributed to FeO-bearing minerals like maghemite or ferrihydrite (Cloutis et al., 2011a). There is one absorption feature at ~1.02 to 1.06 µm and another at ~2.09 to 2.1 µm. This feature could be attributed to Fe-rich olivine and spinel (Cloutis et al., 2012b). The spectrum cgp124 shows additional features at 0.51 µm, 0.89 and 1.39 µm which could be artefacts as they do not appear in any of the other spectra (Cloutis et al., 2012b).

Two spectra of Allende have an absorption feature between 2.7 and 3.3 µm. This wavelength range will be discussed in more detail in section 3.2.1 on pages 82-84.

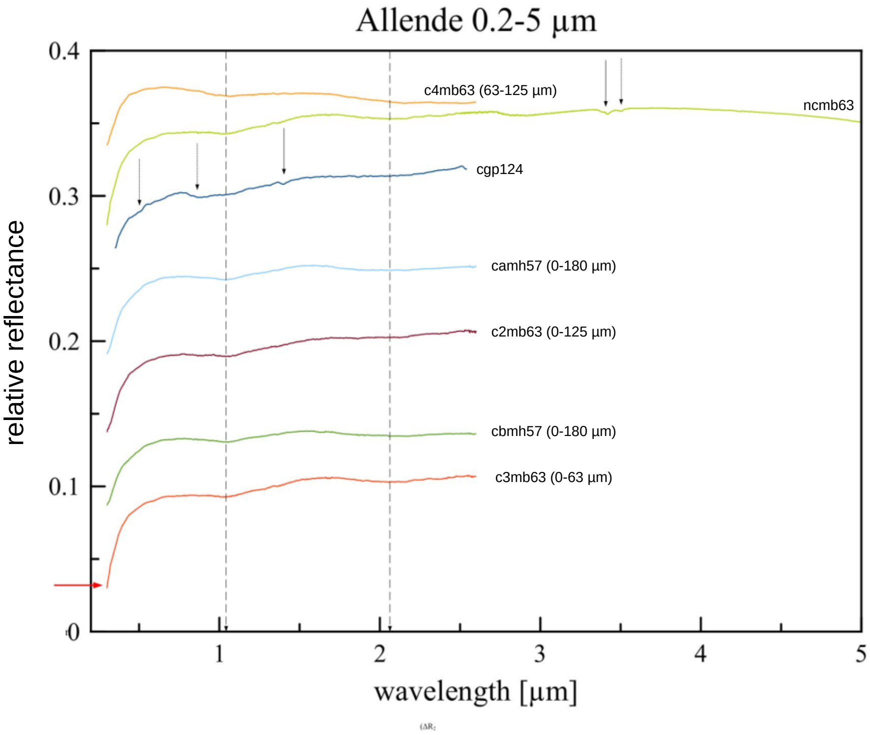

Figure 3-12. *Plot of spectral reflectance data of the meteorite Allende in the wavelength range from 0.2 to 5 µm. The offset between the single data is +0.05 (compared to the spectra marked by the red arrow). For detailed descriptions of the samples (including source of measurements) see appendix A.*

3.1.3.2. Vigarano

In figure 3-6 and 3-13 are shown the spectra of 3 different measurements of the Allende meteorite (Relab and DLR). The sample measured at DLR was a whole rock and the Relab samples have a grain size 0-100 µm. The spectrum of Allende is characterized by a steeper slope in the wavelength range shortward of the λ_{SC}=0.53 µm with a ΔR_1 between 0.049 to 0.151 μm^{-1}. The slope ΔR_{2mean} is shallower in the wavelength range longward of the λ_{SC} with ΔR_2: 0.0004 to 0.0132 μm^{-1}. The slope of the Vigarano_DLR spectrum shows a stronger positive rise in the wavelength range from the λ_{SC} to ~2.6 µm than the spectra taken from Relab. The spectrum of Allende has a lightly negative slope in the wavelength longward of ~3.25 µm.

The spectrum of Vigarano is weakly featured in the wavelength range between 0.2-5 µm. One possible absorption feature is at ~1.1 µm. This feature could be due to olivine (figure 3-13 black arrows; Cloutis et al., 2012b). There is a weak absorption feature at ~2.1 µm due to spinel (Cloutis et al., 2012b).The weak absorption band at ~2.3 µm in the spectrum of c2mb59 may be attributable to fassaite (Rajan and Gaffey, 1984). The feature seen between ~2.7 and 3.3 µm will be discussed in detail in section 3.2.1 on pages 82-84.

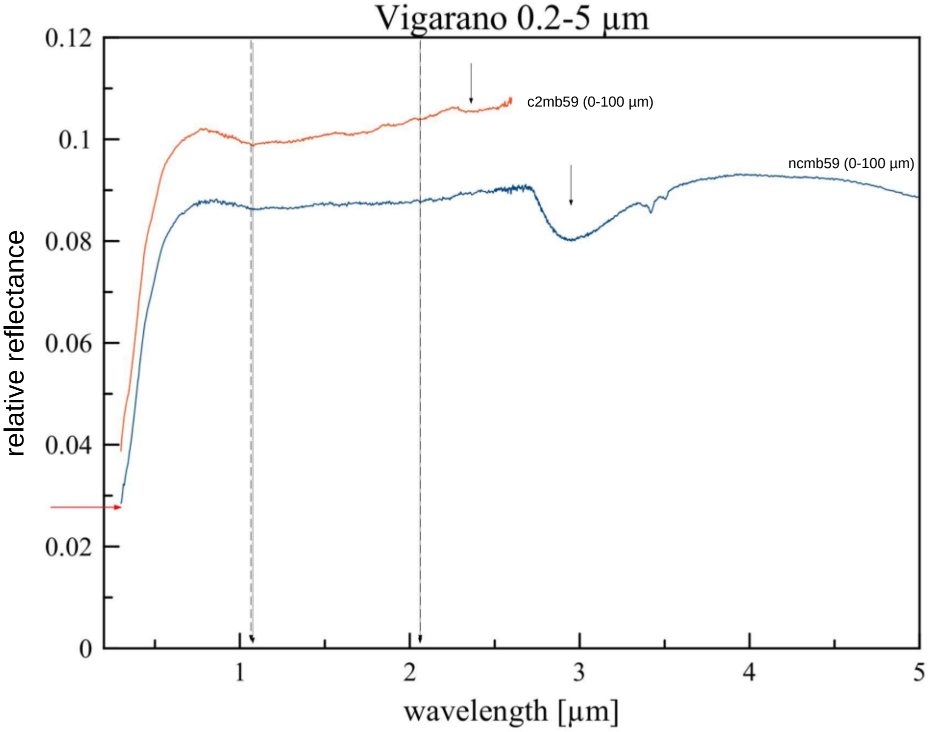

Figure 3-13. *Plot of spectral reflectance data of the meteorite Vigarano in the wavelength range from 0.2 to 5 µm. The offset between the single data is +0.1 (compared to the spectra marked by the red arrow). The data was taken from Relab. For detailed descriptions of the samples (including source of measurements) see appendix A.*

3.1.4. CO chondrites

3.1.4.1. Kainsaz

In figure 3-6 (whole rock, own measurement) and 3-14 (Relab, no information in grain size) are shown two spectra of the CO chondrite Kainsaz. The spectrum of Kainsaz has a steep positive slope of ΔR_1=0.058 to 0.127 µm^{-1} in the wavelength region shortward of the λ_{SCmean}=0.6 µm, whereas the slope longward of the λ_{SC} is shallower (ΔR_2=-0.00012 to 0.0017). The Kainsaz spectrum has a positive slope after ~3.1 µm (figure 3-6).

The spectra of Kainsaz are weakly featured in the wavelength range from 0.2-5 µm. The weak absorption feature at ~0.5 µm may be attributable to iron-bearing phases like magnetite or troilite (Cloutis et al., 2012b). At ~1.0 µm there is an absorption feature (see figure 3-5b), possibly attributable to olivine (Cloutis et al., 2012b). The weak absorption band at ~1.4 µm (figure 3-13) could be possibly an artefact as it is not seen in the spectra measured at the DLR. There is a broad asymmetric absorption feature between 2.6 and 3.1 µm. These features will be discussed in detail in section 3.2.1 on pages 82-84.

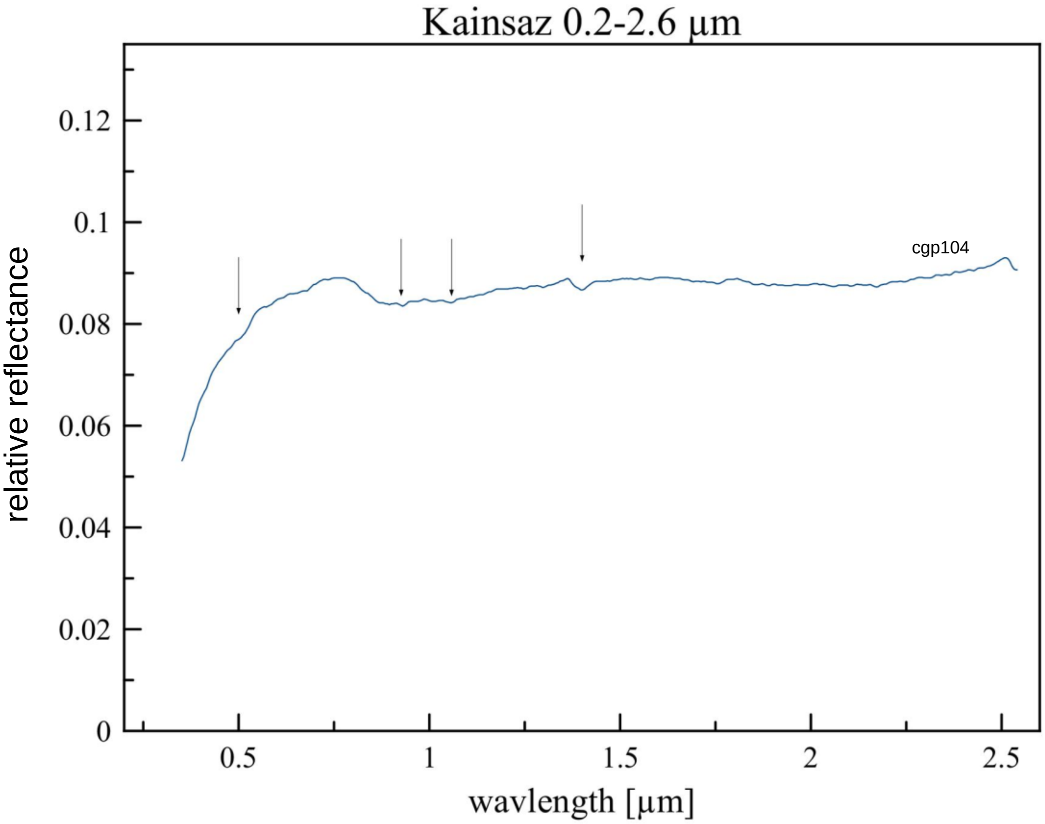

Figure 3-14. *Plot of spectral reflectance data of the CO chondrite Kainsaz in the wavelength range from 0.2 to 2.6 µm. The data was taken from Relab. For detailed descriptions of the samples (including source of measurement) see appendix A.*

3.1.5. Comparison of the DLR measurements to the database spectra

It is generally seen that the samples measured at the DLR show higher reflectance than the reflectance of the database spectra. Possible reasons for these higher reflectances are as follows:

- halon standard in UV and VIS wavelength which increases the reflectance
- measured samples were whole rocks and not pulverized as the database samples
- geometry effects.

The spectra of the DLR measurements show shallower spectral slopes in the UV and VIS wavelength range, whereas the IR wavelength range is characterized by a steeper spectral slope. The spectral absorption bands of the database spectra also appear in the spectra of the DLR measurements, which show stronger absorption features. An explanation for that is that differences are possibly due to merging process of the single spectra, as they had to be scaled to the Bremen measurements.

Generally, it has to be taken into consideration that the DLR samples were whole rocks, whereas the spectra taken from the databases were mainly pulverized samples. Each meteorite, investigated in terrestrial conditions, is heavily altered by Earth’s atmosphere influencing the composition of the meteorite and thus, the spectral measurements. In conclusion, the measurements of the meteorite spectra in the DLR fit well into the measurements collected in the spectral databases, when taking into account the above stated facts.

3.2. Mineral spectra in the 0.2-5 µm wavelength range

Based on the previous section and on table 1-5 minerals were chosen to characterize their spectral properties.

3.2.1. Montmorillonite

In figure 3-15 are shown different spectra of montmorillonite. The data was taken from Relab spectral database (see appendices C and D for further information). The spectrum of montmorillonite has a steep slope in the VIS shortward of the λ_{SCmean}=0.576 µm of ΔR_{1mean}=0.145. The slope longward of the λ_{SC} is shallower and has a value of ΔR_{2mean}=0.0145. The montmorillonite spectra have an overall positive slope between the λ_{SC} and ~2.6 µm where the reflectance drops off. The spectra have a slightly negative slope in the wavelength range longward of 3.5 µm.

The spectra of the different montmorillonite samples have a variety of absorption features in the considered wavelength range shown in figure 3-15 (black dotted arrows). There are absorption feature at ~0.6 µm and ~0.9 µm that could be attributed to Fe^{3+} (Prost, 1975; Cariati et al., 1993). The features at ~1.4 and ~1.9 µm indicate structural H_2O in the samples (Prost, 1975; Cariati et al., 1993). The feature at ~2.2µm could be attributed to Al-OH (Stubičan and Roy, 1961; Farmer, 1974; Cariati et al., 1983; Bishop et al., 1994). In figure 3-15 is shown that montmorillonite has a broad absorption feature starting at ~2.75 µm. This absorption bands could be attributed to structural OH (Stubičan and Roy, 1961; Farmer, 1974; Cariati et al., 1983; Bishop et al., 1994) or to bound water or to adsorbed water as the pulverized samples have been measured under terrestrial conditions and are contaminated by atmospheric water (adsorbed water) (Miyamoto and Zolensky, 1994; Sato et al., 1997; Rivkin et al., 2003). The use of vacuum chambers and dry conditions during measurement will reduce the adsorbed water amount and mimic the space environment (Takir et al., 2013). The spectral features that are seen in the wavelength between 2.7 and 3.2 µm have to be investigated carefully as it is hard to determine whether the visible bands are due to structural OH/H_2O or due to adsorbed water. This broad band has a steeper slope shortward the band center and a shallow slope longward the band center ranging from 2.75 – 3.5 µm.

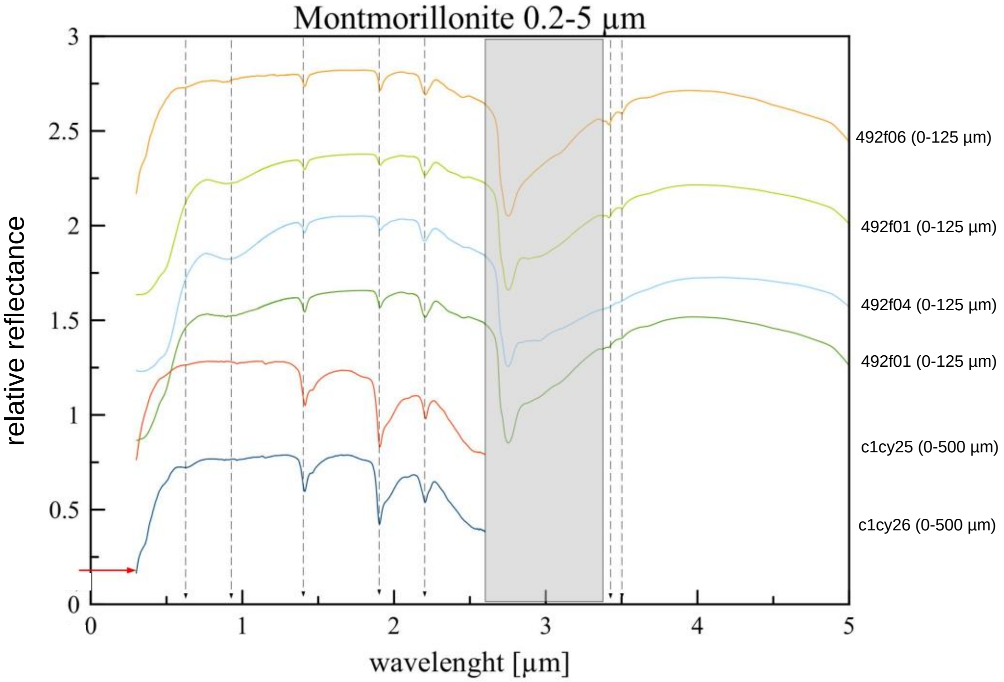

Figure 3-15. *Plot of the reflectance spectra of the mineral montmorillonite. The data were taken from Relab database. The individual offset between the spectra is +0.4. For detailed descriptions of the samples (including source of measurements) see appendices C and D. The grey bars mark the region around 3 µm which need to be characterized carefully due to adsorbed water from the Earth's atmosphere. The grain sizes that are available are 0-125 µm and 0-500 µm.*

The features at 1.41 µm, 1.91 µm and ~3.0 µm could be used to determine the grade of dehydration of the different montmorillonites as the depth of these bands decreases with increasing dehydration (Russell and Farmer, 1964; Russell and Fraser, 1971). This effect can be seen in figure 3-21: the first spectra have deep absorption features at these wavelengths whereas the other spectra show decreasing band depth indicating dehydration of the samples.

3.2.2. Saponite

In figure 3-16 are shown the spectra of different saponite samples. The dotted lines show the samples measured at the DLR Berlin Adlershof, the other data was taken from Relab spectral database. The spectra of saponite show a steep slope shortward of the λ_{SCmean}=0.67 µm of ΔR_{1mean}=0.171 whereas the slope longward of the λ_{SC} is shallower (ΔR_{2mean}=0.0271).

The spectra of saponite have a variety of absorption features in the wavelength region between 0.2 and 5 µm (see figure 3-16, black arrows). There is an absorption feature at ~0.6 to 0.7 µm caused by Fe^{2+}- Fe^{3+}-charge transfer (Sherman and Vergo, 1988). The spectra of saponite show a shallow absorption feature at ~1 µm which could be attributed to octahedral Fe^{2+} (Cloutis et al., 2011a). The spectrum of lasa58_Relab has this feature at shorter wavelength at ~0.9 µm and it also has an additional absorption feature at 1.2 µm. This feature does not occur in the other spectra and is due to octahedral Fe^{2+} (see figure 3-16; Cloutis et al., 2011a). Two spectra of saponite show a variety of absorption features between 2.3 and 2.5 µm. These features could be attributed to metal-OH absorption bands (Cloutis et al., 2011a). All spectra of the measured saponite samples show a broad asymmetric absorption feature in the 3.0 µm wavelength range (see figure 3-16) discussed in detail in section 3.2.1 (pages 82-84). The spectra of saponite measured at the DLR shows two double absorption features at ~3.3 to 3.4 µm and at ~3.9 to 4.0 µm (see figure 3-16). It is likely that these spectral bands are due to CO_3 in the saponite sample but there is no chemical analysis available for the saponite sample to clarify these features. The feature at ~3.4 to 3.5 μm is also seen in one of the Relab spectra.

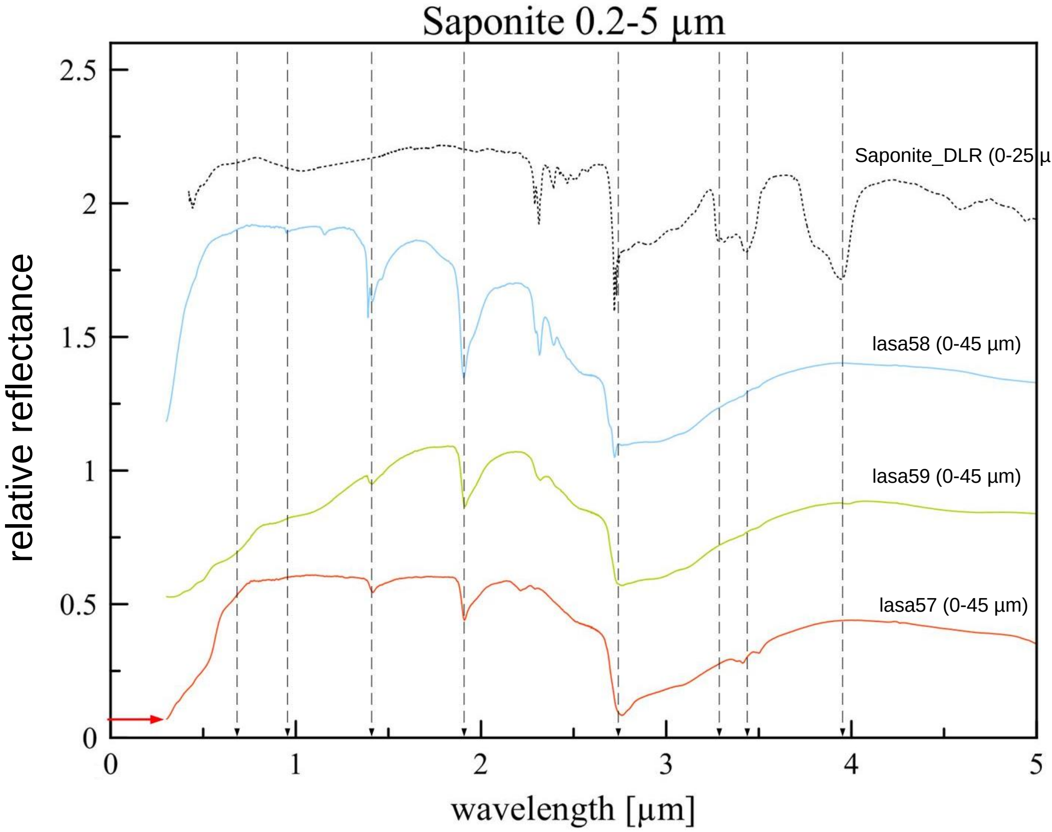

Figure 3-16. *Plot of the reflectance spectra of the mineral saponite. The dashed lines are the data measured at the DLR Berlin Adlershof. The other spectrum was taken from Relab database. The offset between the spectra is +0.5. For detailed descriptions of the samples (including source of measurements) see appendices C and D. The grain sizes that were available were 0-25 μm (DLR) and 0-45 μm (Relab).*

3.2.3. Brucite

Brucite, $Mg(OH)_2$, is a hydroxide typically found associated with serpentine, dolomite, magnesite and chromite as a decomposition product of magnesium silicates, especially serpentine. In figure 3-17 are illustrated the spectra of the mineral brucite. The dashed lines are measurements done at the DLR, Berlin Adlershof. The other spectrum was taken from the USGS database. The spectrum of brucite has a steep positive slope in the VIS and the slope drops off in the NIR. The ΔR_{1mean}=0.150 µm^{-1} shortward of the λ_{SCmean}=0.53 µm and ΔR_{2mean}=0.003 µm^{-1} longward of the λ_{SC}. The spectrum of brucite in the NIR has a negative slope. After 3 µm the slope changes to slightly positive and becomes negative in the wavelength range longward of 4 µm.

Brucite has some absorption features in the wavelength range between 0.3 and 5 µm. One small feature is at ~0.7 to 0.75 µm. This feature may be due to Fe^{3+} or could be due to OH. There are two narrow absorption features at ~0.9 µm and ~1.4 µm. They are due to combination vibrations of hydroxyl complex. The spectral feature at 1.4 µm, seen in figure 3-17, has a characteristic shape (narrow and sharp) and is indicative for brucite. There is another feature at ~2.2 µm due to a combination of the of the OH valence vibration of the OH deformation mode. There is another asymmetric feature at ~2.3 and ~2.5 µm. The first feature is due to the combination of the OH deformation mode with the Mg deformation mode and the second is due to the OH group (Mara and Sutherland, 1953). The brucite spectrum has some more absorption features at ~2.6 and at ~2.7 µm. These bands could be associated with CO_3 or the hydroxyl group. The wavelength range between 2.7 and 3.3 µm is discussed in detail in section 3.2.1 (pages 82-84).

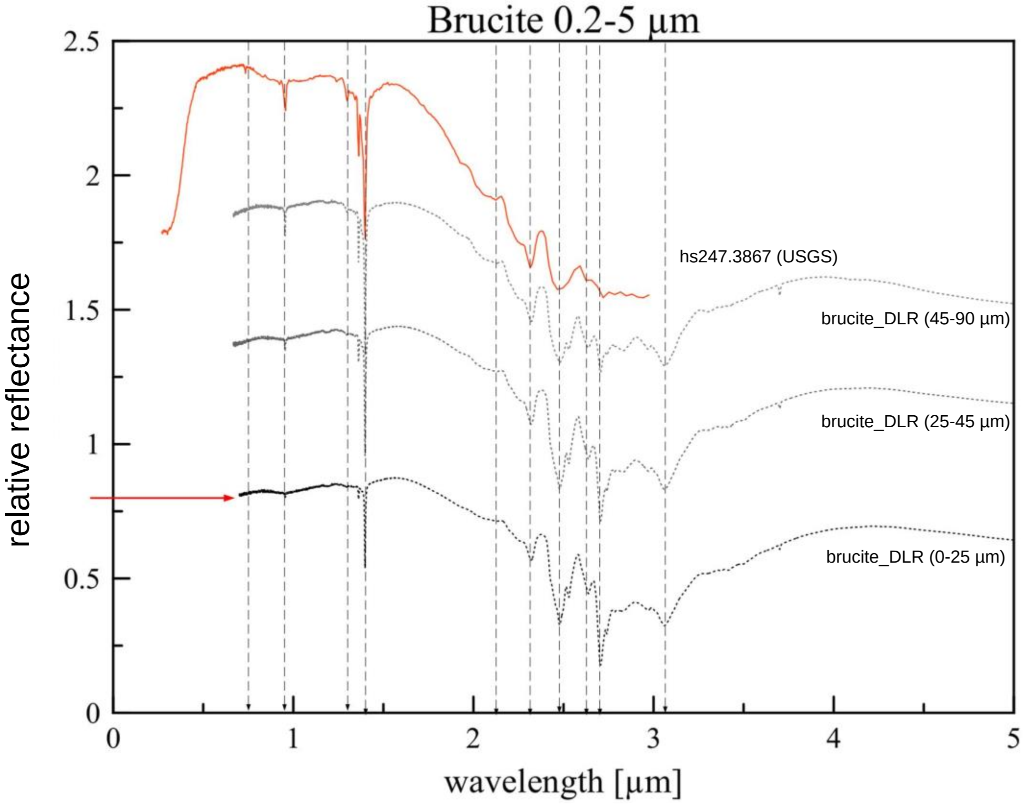

Figure 3-17. *Plot of the reflectance spectra of the mineral brucite. The dashed lines are the data measured at the DLR Berlin Adlershof. The other spectrum was taken from USGS database. The offset between the spectra is +0.5. For detailed descriptions of the samples (including source of measurements) see appendices C and D.*

3.2.4. Cronstedtite

In figure 3-18 is shown the spectrum of 3 different cronstedtite measurements. One sample was measured at the DLR Berlin Adlershof (dotted line in figure 3-18), the other samples are from Relab and USGS spectral library. The samples were all pulverized. The spectrum of cronstedtite shows a strong positive slope in the VIS (ΔR_1: 0.104 μm^{-1} to 0.1163 μm^{-1}) with a sharp slope change at λ_{SCmean}=0.563 µm. The spectrum of cronstedtite has a slightly positive slope of ΔR_2=0.003 μm^{-1} to 0.1071 μm^{-1} and a negative slope in the IR longward of 4.0 µm.

The spectrum of cronstedtite has some absorption features as seen in figure 3-18. One feature is at ~0.3 to 0.4 µm due to Fe^{3+} spin forbidden transitions. There is another small shallow feature at ~0.7 µm due to Fe^{2+}-Fe^{3+} CFT. There is a broad absorption feature between 1.0 and 1.4 µm (octahedral Fe^{2+} CFTs) and two small features at ~2.3 and ~2.4 µm. These features are Mg-OH (Clark et al., 1990; Takir et al., 2013). The absorption feature at ~2.8 and ~3.06 µm are discussed in detail in section 3.2.1 on pages 82-84.

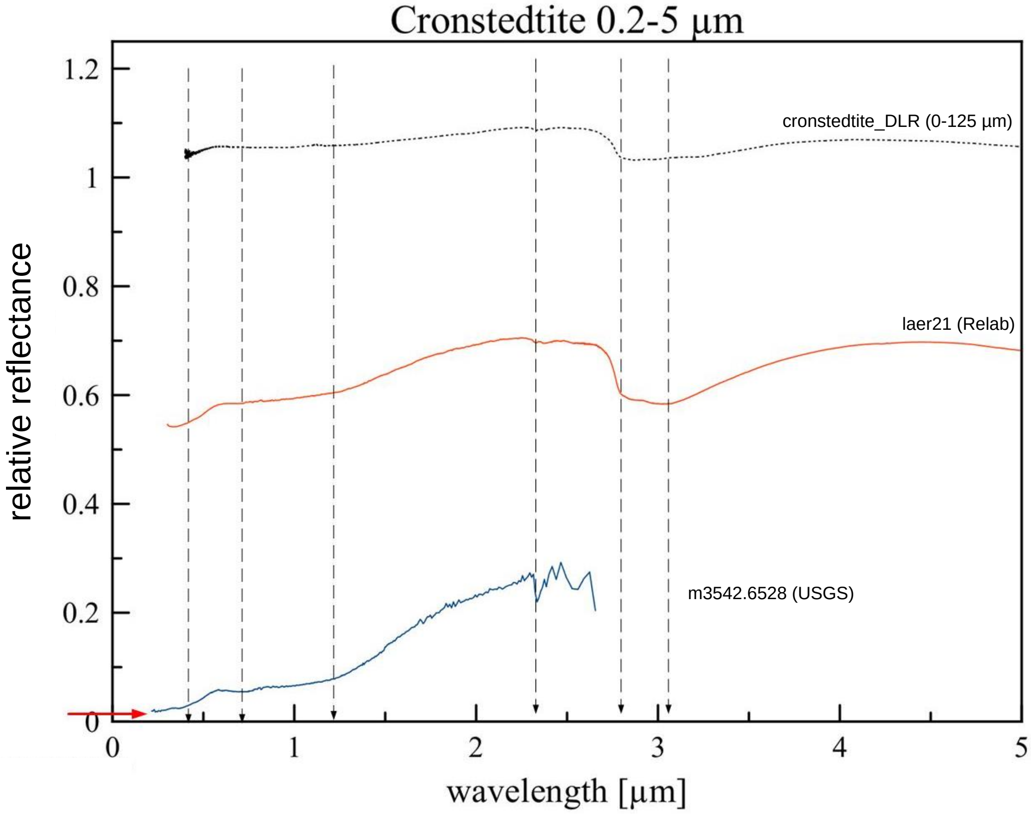

Figure 3-18. *Plot of the reflectance spectra of the mineral cronstedtite. The dashed lines are the data measured at the DLR Berlin Adlershof. The other spectrum was taken from the Relab database and from the USGS spectral library. For detailed descriptions of the samples (including source of measurements) see appendices C and D. The offset between the spectra is +0.5.*

3.2.5. Buddingtonite

The spectra of buddingtonite are plotted in figure 3-19. The dashed line shows the sample measured at the DLR Berlin Adlershof, the other samples are from the USGS spectral library. The spectrum of buddingtonite has a strong positive slope shortward of the λ_{SCmean} at 0.66 µm (ΔR_{1mean}=0.1051 μm^{-1}). The slope is shallower longward of the λ_{SC} (ΔR_{2mean}=0.0043 μm^{-1}). The spectrum of buddingtonite has an overall negative in the NIR to MIR wavelengths range.

The first absorption feature appears at ~1.4 µm, a small, symmetric, shallow feature due to the hydroxyl complex or bond water. There is another shallow feature at ~1.55 µm attributed to alunite (Clark, comments from USGS spectral library). The buddingtonite_DLR spectrum shows a small absorption feature at ~1.9 µm. This feature together with the feature at 1.4 µm indicates bond water incorporated into the mineral structure. There is a double absorption feature at ~2.0 and 2.1 µm are due to Mg. The region between~2.85 µm and 3.6 µm is indicative for NH_4^+ (Harlov et al., 2001). This region is seen in figure 3-19 as a broad absorption feature showing three small and shallow absorptions at ~2.85 µm, ~3.03 µm and 3.55 µm. This wavelength range is discussed in detail in section 3.2.1 on pages 82-84.

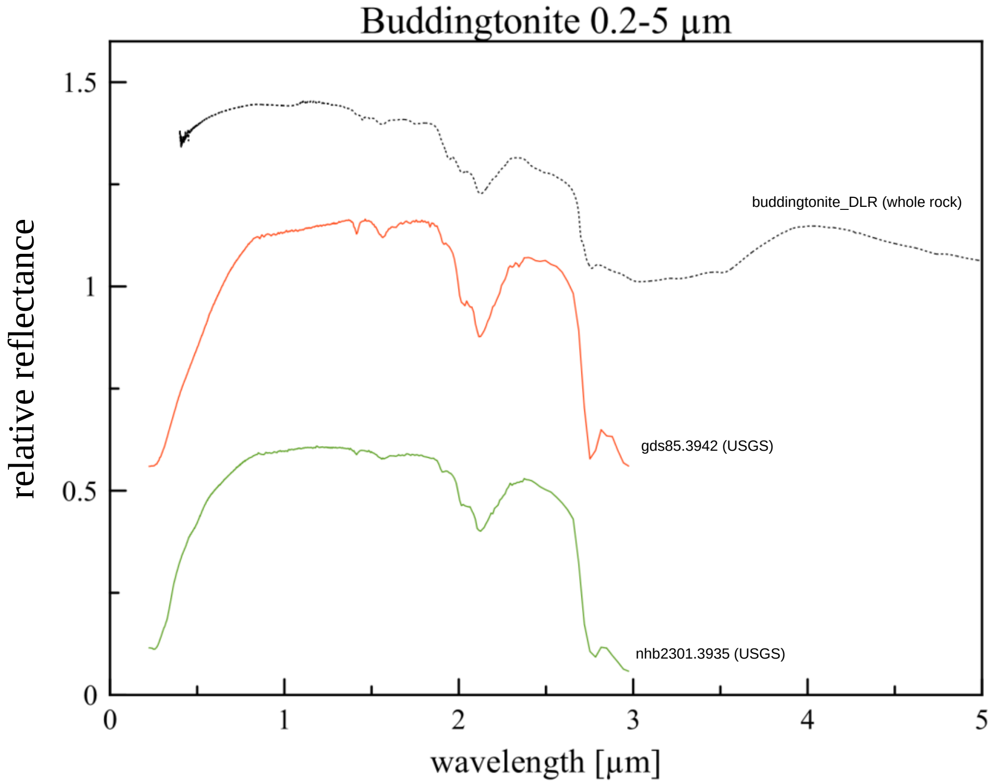

Figure 3-19. *Plot of the reflectance spectra of the mineral buddingtonite. The blue line is the data measured at the DLR Berlin Adlershof. The other spectra were taken from USGS database. The offset between the spectra is +0.5. For detailed descriptions of the samples (including source of measurements) see appendices C and D.*

3.2.6. Carbonates

In figure 3-20 to 3-23 are shown different spectra of different carbonates from Relab database and from the USGS spectral library. In table 3-1 are summarized the λ_{SCmean}, the ΔR_1 and the ΔR_2 values of the different carbonates. There is a gradually decrease in the λ_{SCmean} from siderite (0.7 µm) to calcite (0.43 µm). The slopes in the VIS are generally steeper than the slopes in the NIR region. Dolomite has the steepest slope 1 (mean, 0.170 μm^{-1}) and there is a gradually decrease in ΔR_{1mean} from dolomite to siderite (0.114 μm^{-1}) to calcite (0.084 μm^{-1}) to magnesite (0.068 μm^{-1}). There is also a decrease in the ΔR_{2mean} values from siderite (0.0491 μm^{-1}) to calcite (0.0027 μm^{-1}) to dolomite (0.002) to and to magnesite (-0.0008 μm^{-1}).

Table 3- 1: *Summary on the λ_{SCmean}, ΔR_1 and ΔR_2 values of the spectra of the different carbonates. See appendices C and D for further information on the individual samples and appendix F for further information on the λ_{SCmean} and ΔR values.*

Carbonate	ΔR_{1mean} [µm^{-1}]	ΔR_{2mean} [µm^{-1}]	λ_{SCmean} [µm]
calcite	0.084	0.0027	0.43
dolomite	0.170	0.002	0.49
magnesite	0.068	-0.0008	0.49
siderite	0.114	0.0491	0.7

The spectra of the different carbonates show a variety of absorption features in the wavelength range between 0.2 and 5 µm. In figure 3-20 to 3-23 are shown the spectra of calcite, dolomite, magnesite and siderite. There is a feature at ~1.0 µm seen in some spectra of dolomite (~1.0 µm) and magnesite (1.1 µm) and in all spectra of siderite (1.0 to 1.3 µm). This absorption feature is indicative for Fe^{2+} in the carbonates and appears in two of the dolomite spectra, in one magnesite and all siderite spectra as a broad double absorption feature (Gaffey, 1985, 1986). The green bar in the figures 3-20- 3-23 mark the features caused by CO_3 cation between 1.6 and 2.55 µm (Hexter, 1958; Hunt and Salisbury, 1971). The calcite spectrum shows an absorption feature at 2.8 µm. This is also seen in the spectra of dolomite at ~2.7 to 2.75 µm and in the spectra of siderite at ~2.85 µm. This is caused by water in the structure of the minerals (OH and H_2O fundamental; Gaffey, 1985, 1986). At ~3.5 µm and ~3.9 µm are seen in the spectra the combination vibrations and overtones of the CO_3 cation (Arnold, 2014). They appear in the calcite spectra at ~3.4 to 3.5 µm and at 3.95 µm as two double features. These features are at shorter wavelengths in the dolomite spectra, at ~3.3 to 3.4 µm and 3.8 to 3.9 µm, but are also double features. In the magnesite spectra only two spectra show well distinguishable double features at ~3.4 to 3.5 µm whereas the 3.9 to 4.0 µm feature is well determinable in the single spectra. Nearly all magnesite spectra show a broad absorption feature between 2.6 and 3.6 µm which could be due to adsorbed water or due to bond water (see section 3.2.1 on pages 82-84). All carbonate spectra show two weak absorption feature at ~ 4.6 µm caused by the sulfate ion (Hass and Sutherland, 1956; Salisbury et al., 1991).

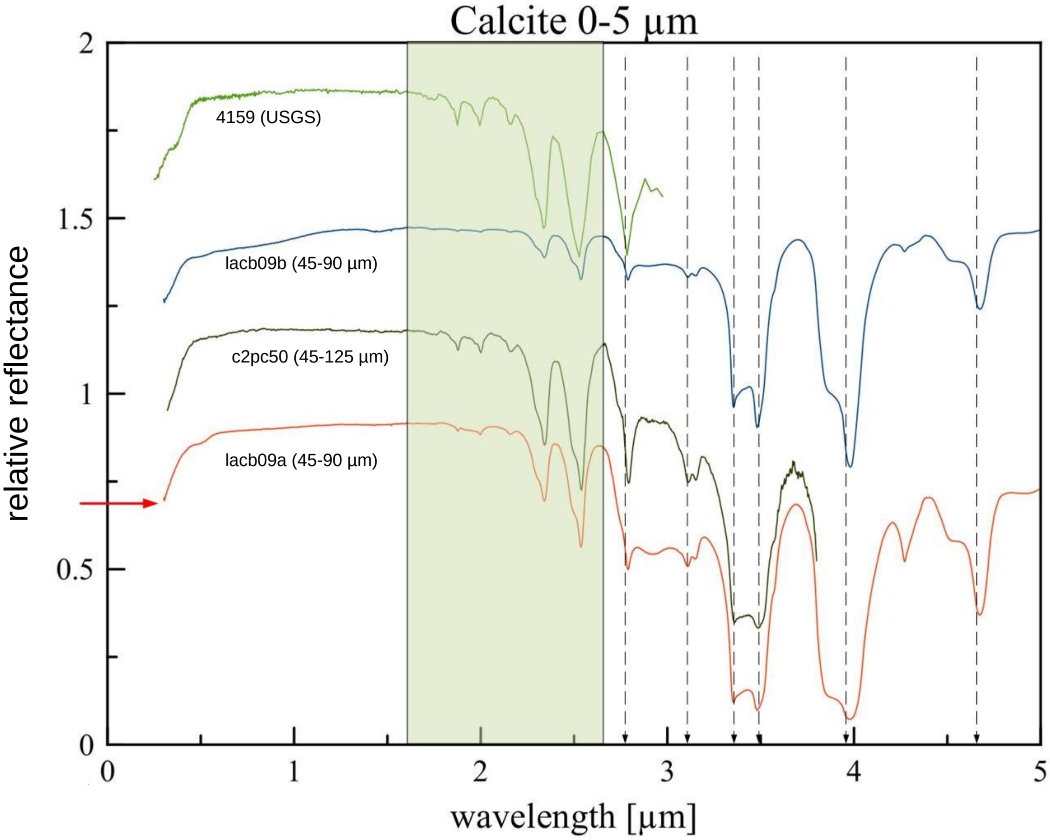

Figure 3-20. *Plot of the reflectance spectra of the mineral calcite. The data of the spectra was taken from Relab database and from the USGS database. The offset between the spectra is +0.3. For detailed descriptions of the samples (including source of measurements) see appendices C and D. The light green bar mark the wavelength range between 1.6 and 2.55 µm indicative for the* CO_3 *cation in carbonates.*

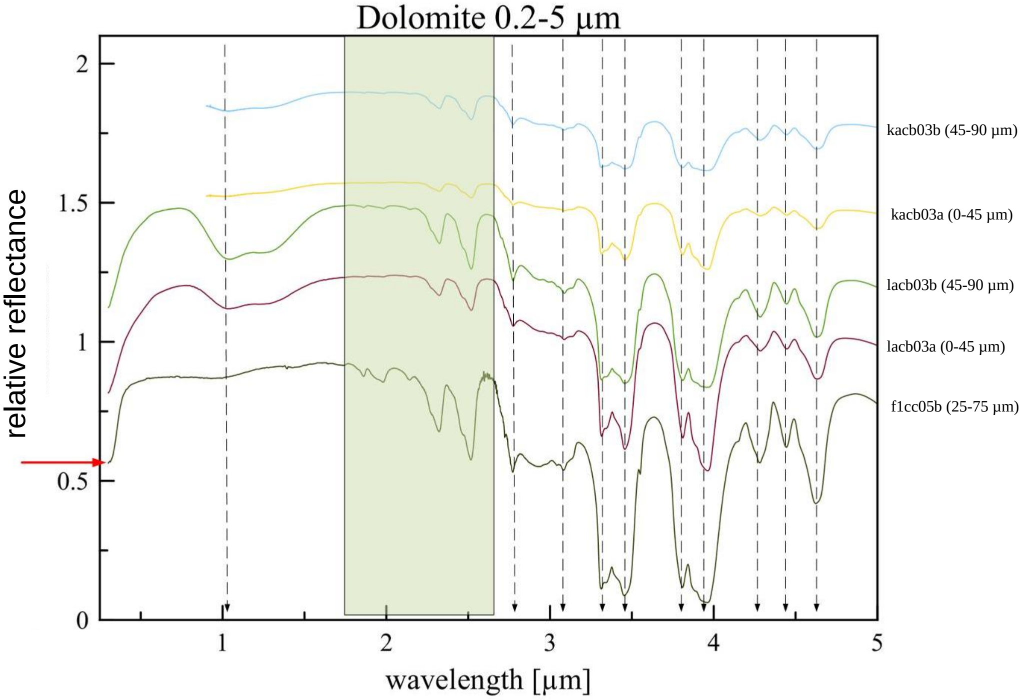

Figure 3-21. *Plot of the reflectance spectra of the mineral dolomite. The data of the spectra was taken from Relab database. The offset between the spectra is +0.4. For detailed descriptions of the samples (including source of measurements) see appendices C and D. The light green bar mark the wavelength range between 1.6 and 2.55 µm indicative for the* CO_3 *cation in carbonates.*

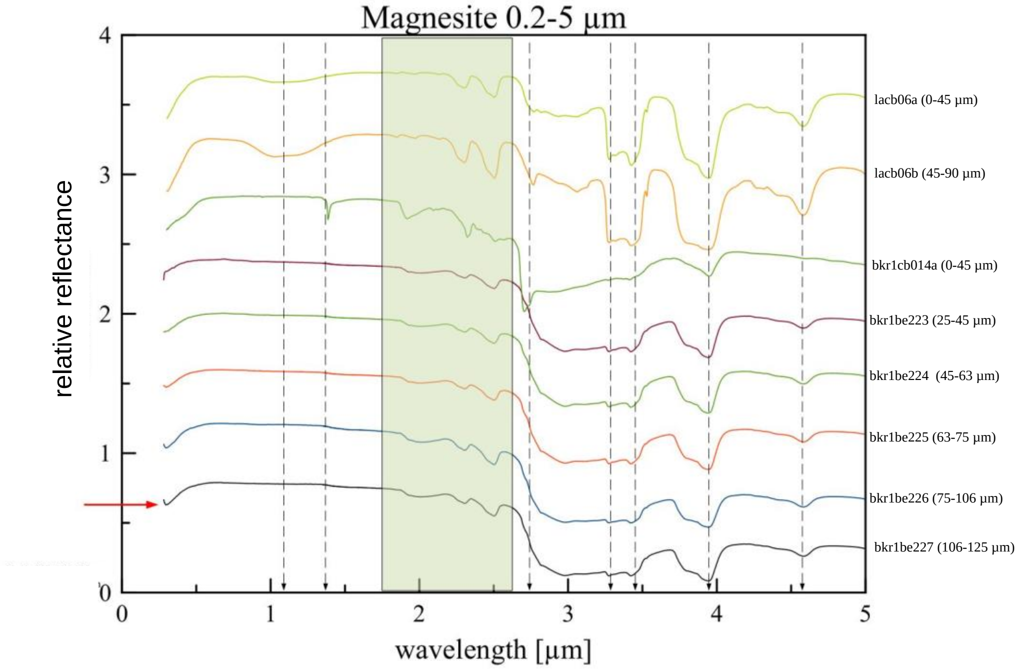

Figure 3-22. *Plot of the reflectance spectra of the mineral magnesite. The data of the spectra was taken from Relab database. The offset between the spectra is +0.4. For detailed descriptions of the samples (including source of measurements) see appendices C and D. The light green bar mark the wavelength range between 1.6 and 2.55 µm indicative for the* CO_3 *cation in carbonates.*

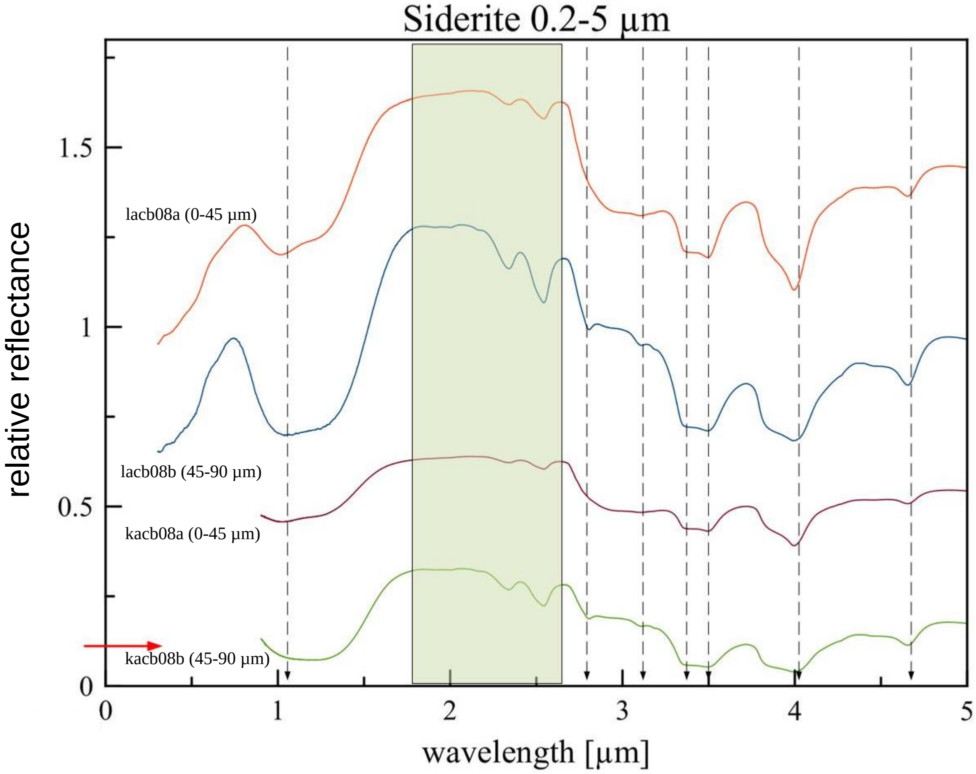

Figure 3-23. *Plot of the reflectance spectra of the mineral siderite. The data of the spectra was taken from Relab database. The offset between the spectra is +0.3. For detailed descriptions of the samples (including source of measurements) see appendices C and D. The light green bar mark the wavelength range between 1.6 and 2.55 µm indicative for the CO_3 cation in carbonates.*

3.2.7. Magnetite

In figure 3-24 are shown the different spectra of magnetite. The data was taken from Relab spectral database and from the USGS spectral library. The spectra of magnetite have an overall low reflectance. They show a steeper slope of ΔR_{1mean}=0.166 μm^{-1} in the VIS range shortward of the λ_{SCmean}=0.37 µm than in the NIR range (ΔR_{2mean}=0.0153 μm^{-1}).

The spectra of magnetite are only weakly featured. There is a weak feature at ~0.5 µm attributed to Fe^{3+} and a broad shallow absorption feature at ~1.0 to 1.3 µm due to octahedral Fe^{2+} (Cloutis et al., 2011a). One spectral (cjb253) shows a variety of absorption features in the wavelength range between 2.2 and 2.5 µm, but there is no chemical analysis for this sample available to determine why there are these features in this spectrum. Another spectrum shows a double absorption feature centered at ~3.0 µm possible to absorbed or bond water (see section 3.2.1. on pages 82-84). The other magnetite spectra are featureless in the NIR and MIR region.

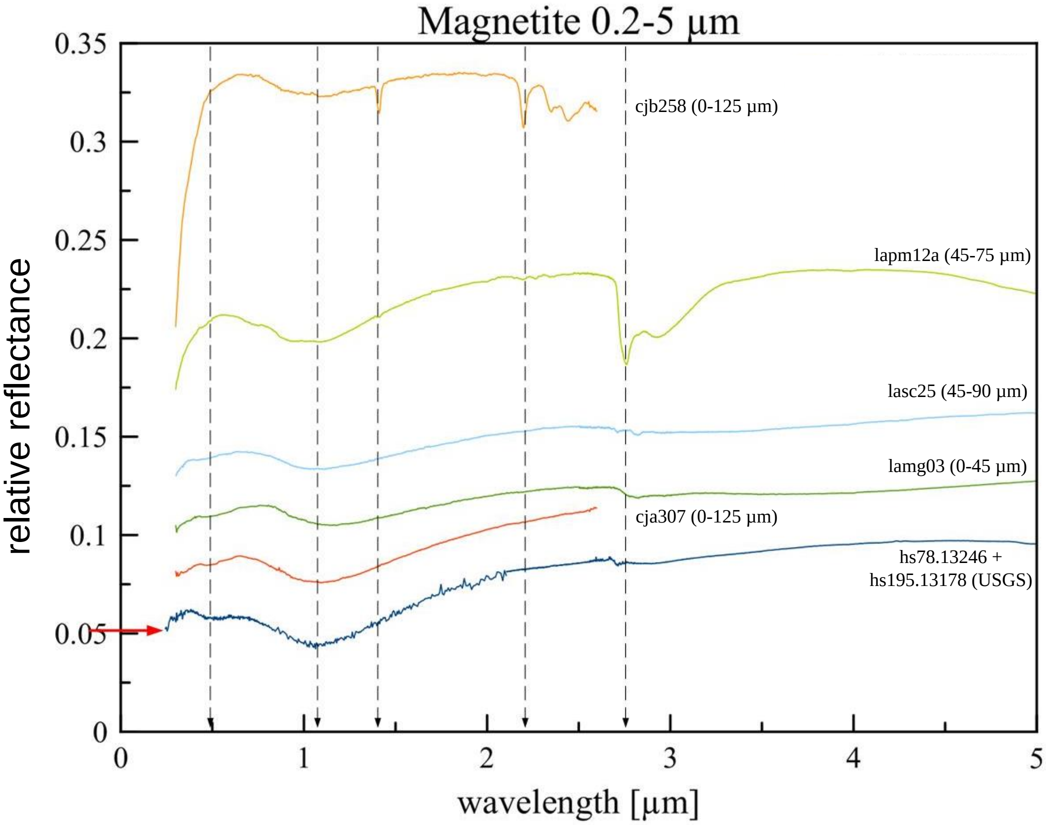

Figure 3- 24: *Plot of the reflectance spectra of the mineral magnetite. The data were taken from Relab database and from the USGS database. For detailed descriptions of the samples (including source of measurements) see appendices C and D.*

3.2.8. Tochilinite

In figure 3-25 are shown different spectra of the mineral tochilinite. The dotted lines indicate that the samples were measured at the DLR Berlin, Adlershof. The other data was taken from Relab spectral database. The spectra of the DLR samples have a different shape than the spectrum taken from Relab. The DLR spectra are weakly featured with an overall low reflectance which could be only distinguished by the difference in reflection level (Moroz et al., 1998), but the Relab spectrum shows a variety of absorption features. This difference could be due to the fact that the samples measured at the DLR are synthetic in origin (for further information see Moroz et al., 1998). Tochilinite has a steep slope in the VIS shortward of the λ_{SCmean}=0.69 µm of ΔR_1=0.292 μm^{-1} whereas the slope longward of the λ_{SC} is shallower and has a ΔR_{2mean} of 0.028 μm^{-1}.

The spectra of the tochilinite samples measured at the DLR laboratory are weakly featured. There is one weak absorption feature at ~1 µm. This band is also seen in the Relab spectrum (see figure 3-24) and could be attributed to Fe^{2+} (Moroz et al., 1998). The spectra of tochilinite show an absorption feature at ~1.4 µm due to OH in the structure of the mineral. The spectrum of the Relab sample shows a variety of absorption features between 2.0 and 2.5 µm which could be attributed to Magnesium. There is a sharp absorption feature at 2.7 to 2.8 µm possibly due to the hydroxyl ion (Moroz et al., 1998; see section 3.2.1. on pages 82-84).

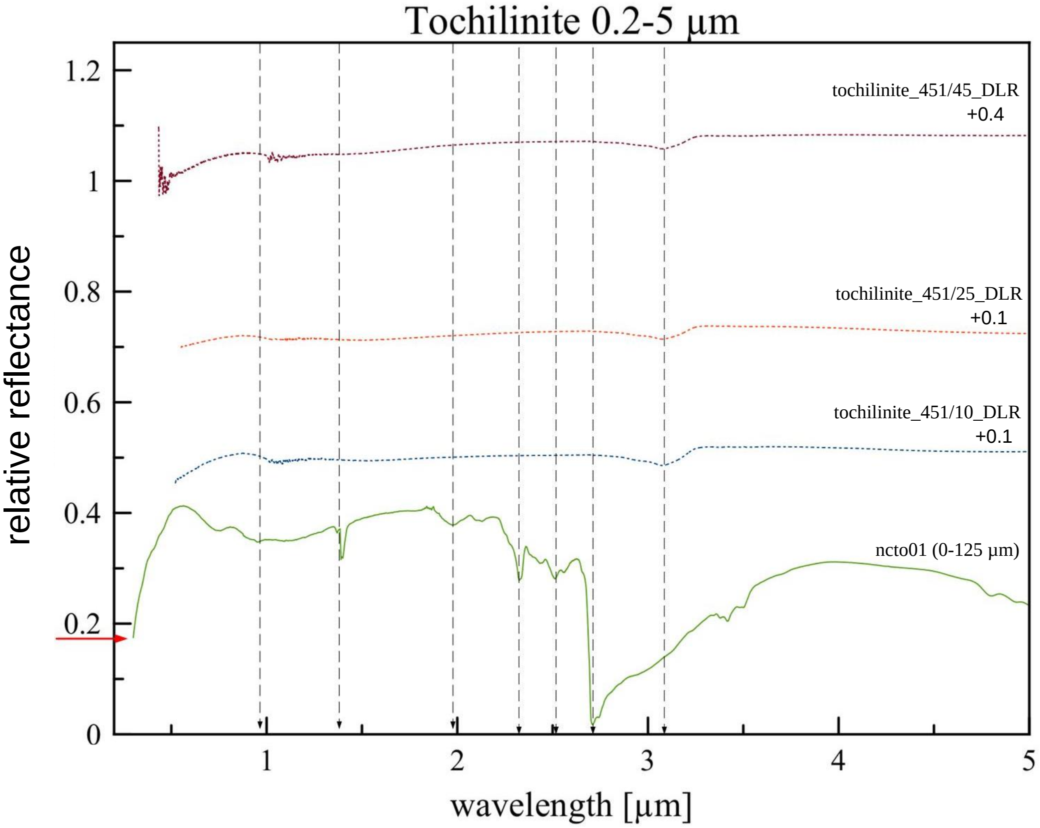

Figure 3-25. *Plot of the reflectance spectra of the mineral tochilinite. The dashed lines are the data measured at the DLR Berlin Adlershof. The other spectrum was taken from Relab database. The offset between the spectra is indicated in the figure. For detailed descriptions of the samples (including source of measurements) see appendices C and D.*

3.2.9. Troilite

In figure 3-26 are shown spectra of troilite. The data was taken from Relab spectral database. The spectrum of troilite is flat and weakly featured with an overall low reflectance. The slope shortward of the λ_{SCmean}=0.685 µm is steeper than longward of the λ_{SC} (ΔR_{1mean}=0.067 µm^{-1}, ΔR_{2mean}=0.0197 µm^{-1}). The spectra show a general positive slope over the wavelength range between 0.2 and 5.0 µm.

There are weak absorption features at ~0.45 µm and at ~0.5 µm with a steep longward shoulder attributable to sulfur compounds or to Fe^{2+}/Fe^{3+}. Another feature is at ~1 µm due to Fe^{2+}. All spectra of troilite have a broad shallow absorption feature with band center at 3.0 µm. This could be attributed to bond or adsorbed water (see section 3.2.1. on pages 82-84).

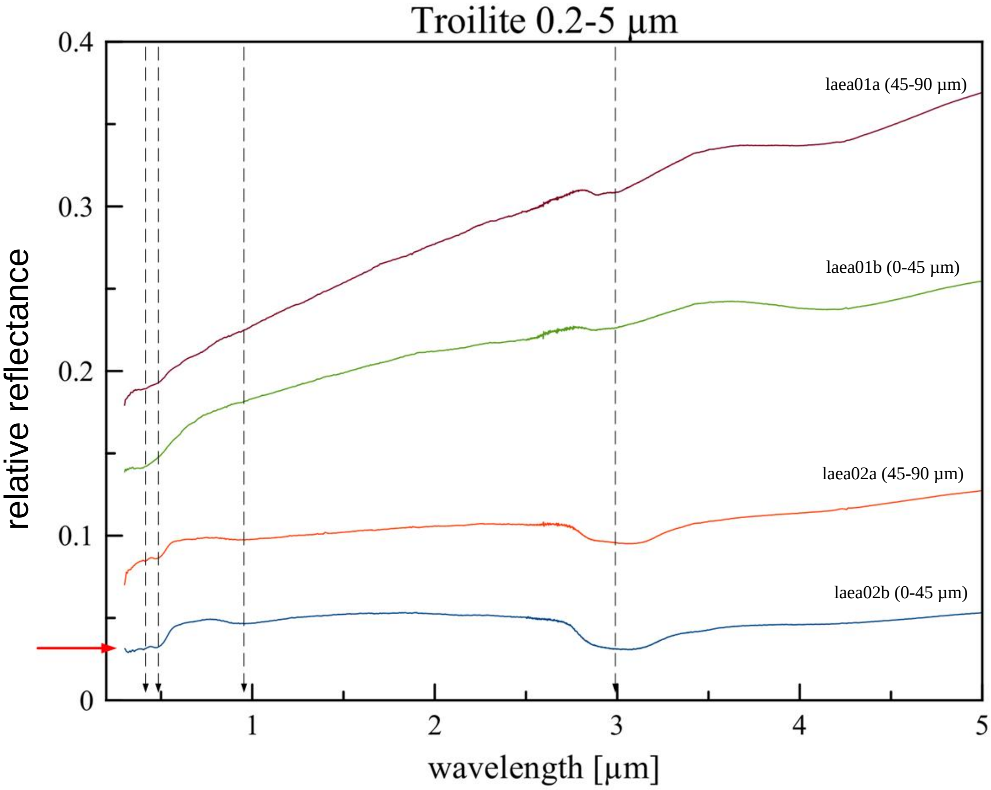

Figure 3-26. *Plot of the reflectance spectra of the mineral troilite. The data were taken from Relab spectral library. The offset between the spectra is+0.05. For detailed descriptions of the samples (including source of measurements) see appendices C and D.*

3.2.10. Pyrite

In figure 3-27 are shown different spectra of pyrite samples. The data was taken from Relab spectral database and from the USGS spectral library. The spectrum of pyrite has a steeper slope in the VIS (ΔR_{1mean}=0.087 μm^{-1}) than in the NIR (ΔR_{2mean}=0.017 μm^{-1}). The λ_{SCmean} occurs at 0.56 µm. The spectra shown in figure 3-27 have different forms and shapes. Two spectra have an overall positive slope between 0.2 and 5.0 µm whereas the other two spectra have a negative slope longward of 0.75 µm.

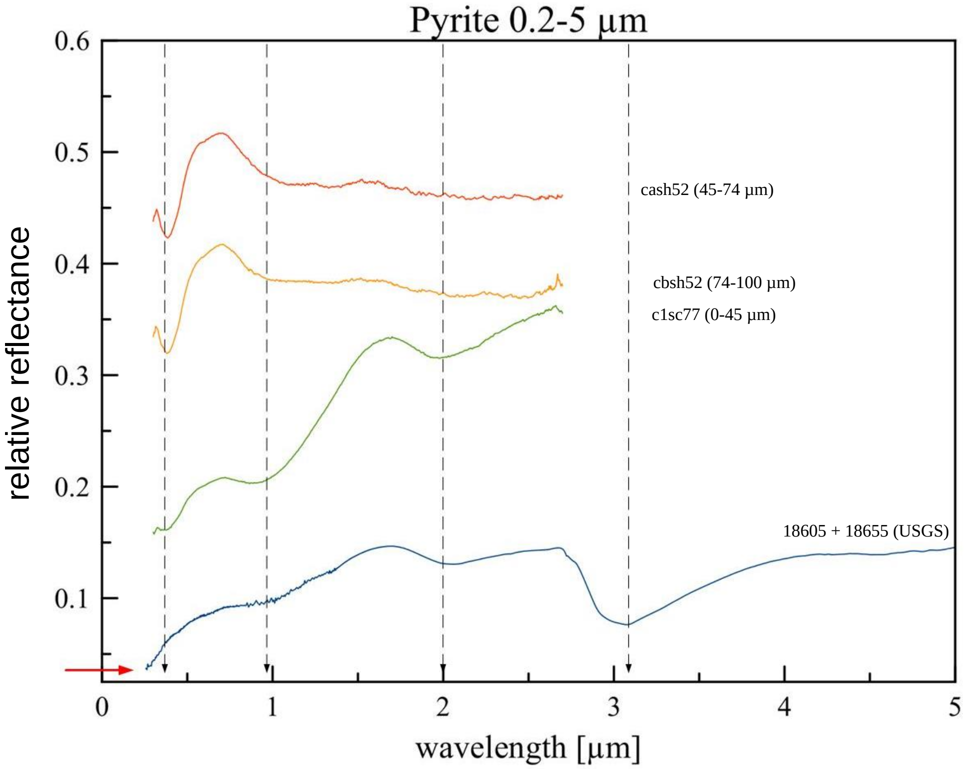

Figure 3-27. *Plot of the reflectance spectra of the mineral pyrite. The data were taken from Relab database and from the USGS database. The individual offset of each spectrum is relative to the red arrow is +0.1. For detailed descriptions of the samples (including source of measurements) see appendices C and D.*

The measured pyrite samples have a variety of absorption features between 0.2 and 5.0 µm. There is a narrow symmetric feature at ~0.85 µm that has a steep shoulder longward of the band center and which could be attributed to Fe^{2+}. Another feature is at ~0.9 to 1.0 µm (see figure 3-27). This feature is wide and shallow in three of the spectra and in one spectrum it is a narrow symmetric feature with a strong increase in reflectance longward of the band center. The 0.9 to 1.0 µm feature is due to Fe^{2+}. There is a broad absorption feature at ~2.0 µm seen in two of the spectra. It could be attributed to H_2O or Fe^{3+} in the sample (Dr. Arnold, personal communication). The spectrum of pyrite has a broad asymmetric feature with band center at ~3.0 µm. This feature could be due adsorbed water from the atmosphere or due to bond water (see section 3.2.1. on pages 82-84).

3.2.11. Organica

In figure 3-28 are illustrated the different organic materials measured by L. Moroz at the DLR laboratory in Berlin Adlershof. Additional spectra from the different organica are in appendix F. The data of these spectra is incorporated in the analysis of the slopes and the λ_{SC}. The spectra of medium anthraxolite (blue and black dotted lines in figure 3-28) appear to be weakly featured and have a general low reflectance. The spectra have a positive slope slowly rising toward the longer wavelength. The λ_{SCmean} was determined to be at 0.67 µm. The slope shortward of the λ_{SC} is shallower (ΔR_{1mean}=0.042 µm^{-1}) as ΔR_{2mean}=0.28 µm^{-1}.

The red and dark green dotted lines in figure 3-28 are the spectra of kerite. The high kerite sample has spectra similar to those of the anthraxolites whereas the other kerite sample has a spectrum with a higher positive slope and few absorption features in the wavelength range between 0.2 and 5 µm. The λ_{SC} values are divided into two groups, $\lambda_{SCmean1}$=0.51 µm and $\lambda_{SCmean2}$=0.76 µm (see appendix E). The ΔR_{1mean} is at 0.018 µm^{-1}, whereas the slope 2 values also have to be divided into two groups, ΔR_{2mean1}=0.03 µm^{-1} and ΔR_{2mean2}=0.306 µm^{-1}. A possible explanation for these differences in the slopes is a different chemical composition of the samples, but could not be further investigated as there are no chemical analyses available for these samples. Grain size effects as the reason for the differences could be excluded as the samples cover only grain sizes between 0-100 µm and 100-200 µm.

In figure 3-28 is also shown a spectrum of asphaltite (light green dotted line). Asphaltite has a λ_{SCmean} at ~0.57 µm and its spectrum is similar to that of kerite. The slope shortward of the λ_{SCmean} at 0.65 µm is between -0.0112 and 0.0524 µm^{-1}. The NIR slope is much steeper than the VIS slope with ΔR_{2min} =0.28 µm^{-1} to ΔR_{2max}=0.51 µm^{-1}. The absorption features are summarized in table 3-2.

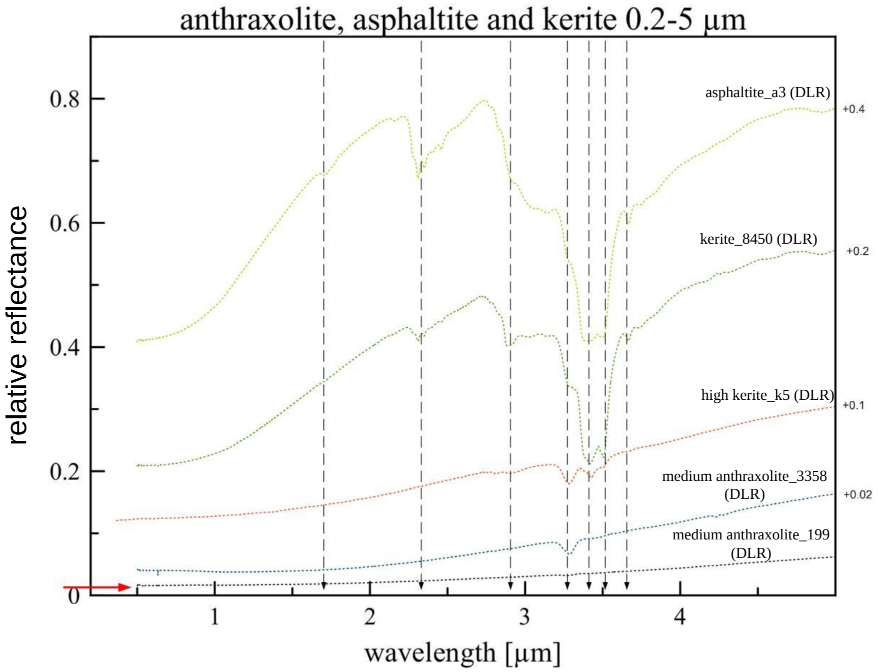

Figure 3-28. *Plot of the reflectance spectra of the organica anthraxolite, kerite and asphaltite. The data was measured by L. Moroz in the DLR laboratory (Moroz et al., 1998). The offset of the single spectra is indicated in the figure. For detailed descriptions of the samples see appendices C and D.*

There are a variety of spectral absorption feature in the wavelength range between 0.2 and 5 µm. The samples are generally dark in the VIS and have a broad absorption feature in the VIS-NIR range with the center in the UV region due to polycyclic aromatic hydrocarbons (Brown, 1955; McMichael et al., 1954; Painter et al., 1985; Ito et al., 1988). The edge of this feature is moving to longer wavelength and the reflectance drops of in the IR region with the loss of aliphatic H and O (see figure 3-28; Kmetko, 1951; McMichael et al., 1954). The absorption features at 2.2-2.6 µm, 3.4-3.5 µm are vibrations of aliphatic CH_2 and CH_3 (figure 3-28; Colthup, 1950; Bellamy, 1975; Brown, 1955; Tosi and Pinto, 1972; Painter et al., 1985; Fysh et al., 1985, Cloutis, 1990). In table 3-28 are summarized all important absorption features and their respective wavelengths seen in figure 3-28.

Table 3- 2: *Band assignments for the IR spectra of solid bitumens. Data were taken from Colthup, 1950; Bellamy, 1975; Brown, 1955; Tosi and Pinto, 1972; Painter et al., 1985; Fysh et al., 1985, Cloutis, 1990; Arnold, 2014.*

Wavelength [µm]	Band assignment
1.69-1.76	first overtones and combinations of CH_2 and CH_3 stretching modes
2.15-2.17	combination of aromatic C-H and C=C stretch
2.27	combination of CH_2 symmetric stretch and symmetric bend
2.31	combination of CH_3 symmetric stretch and symmetric bend
2.35	combination of CH_3 symmetric stretch and symmetric bend
2.46	CH_2
2.77	non-H bonded O-H
2.82-2.84	H_2O or OH stretch
2.89-2.92	H-bonded O-H stretch
3.04-3.05	H-bonded stretch
3.13-3.15	O-H stretch
3.27-3.29	aromatic CH stretch
3.38-3.39	aliphatic CH_3 groups
3.41-3.42	aliphatic CH_3 groups + aromatic CH_3 groups
3.48-3.50	aliphatic CH_3 groups
3.5	aliphatic CH2 groups
3.66-3.67	Ar_3CH or aldehyde groups

3.2.12. Water ice/frost

In figure 3-29 are shown the spectra of water ice (red) and water frost (blue). The spectrum of water frost has a high reflectance close to 1 in the VIS range. In the NIR the reflectance drops off to 0.1 in the NIR-MIR range. The first overtone of the OH stretch occurs at 1.4 µm and the combination of the H-O-H bend with the OH stretch is found at~1.9 µm (figure 3-29; Clark, 1981, 1999). Fundamental vibrations of water occur at 2.96 µm and 3.17 µm (Arnold, 2014). The other absorption features seen in figure 3-29 are due to combinations and overtones of the fundamental vibrations (Arnold, 2014).

They occur at 0.81 µm, 1.04 µm, 1.25 µm, 1.52 µm, 1.94 µm and 2.02 µm (see figure 3-29).

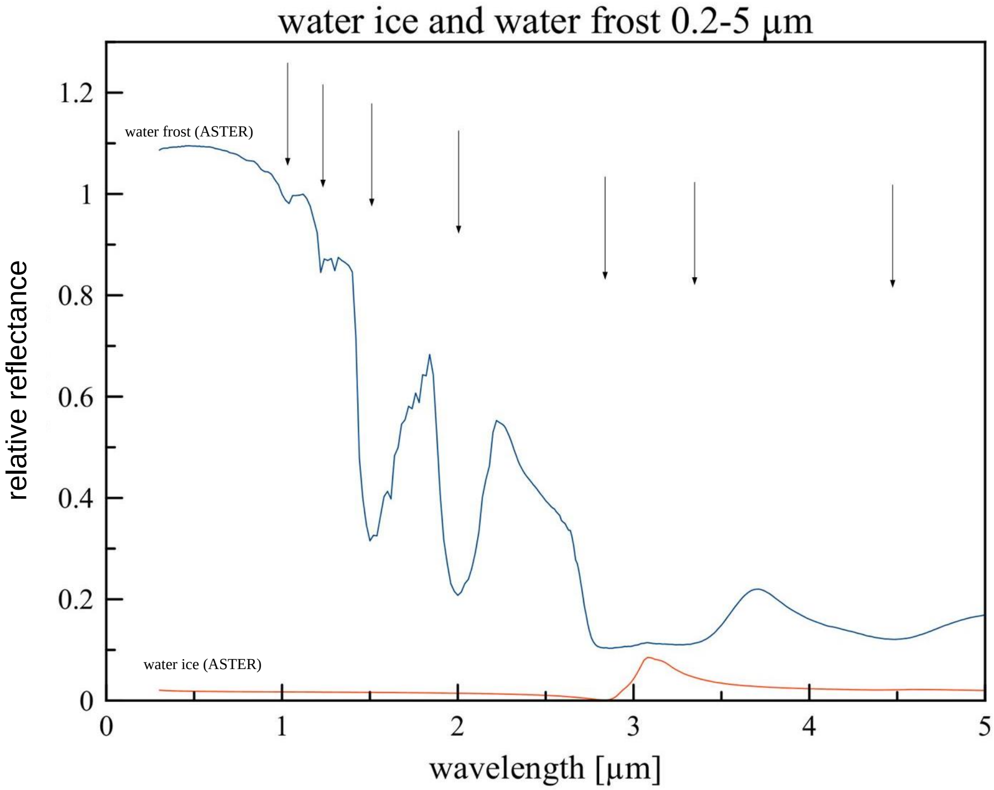

Figure 3-29. *Plot of the reflectance spectra of water ice and water frost. The data were taken from ASTER spectral library. The offset between the spectra is+0.1. For detailed descriptions of the samples see appendices C and D.*

3.3. Ceres' spectrum

Figure 3-30 and 3-31 show spectra of Ceres. The data was collected from publications and was digitalized with Plot Digitalizer. The Ceres spectrum is marked by a steep slope 1 of ΔR_1=0.0791 shortward of the λ_{SCmean} at 0.51 µm. Slope 2 is much shallower and has a value of ΔR_{2mean}=-0.0015.

The overall spectrum of Ceres shows well-defined, but not strong spectral features. There are weak features at ~0.6 µm (figure 3-31) and another feature centered at

~1.2 µm (figure 3-30 and 3-31). The spectrum in figure 3-31 shows a possible weak absorption feature at ~1.9 µm. There are a variety of absorption features between 2.5 and 3.7 µm indicated by the black arrows in figure 3-30 and 3-31. One feature is centered at ~3.0 to 3.1 µm marked by a sharp drop-off in reflectance and another smaller symmetric feature is at ~3.3 µm. There are two small double features between 3.8 and 3.9 µm which appear in figure 3-31 as one broad absorption feature.

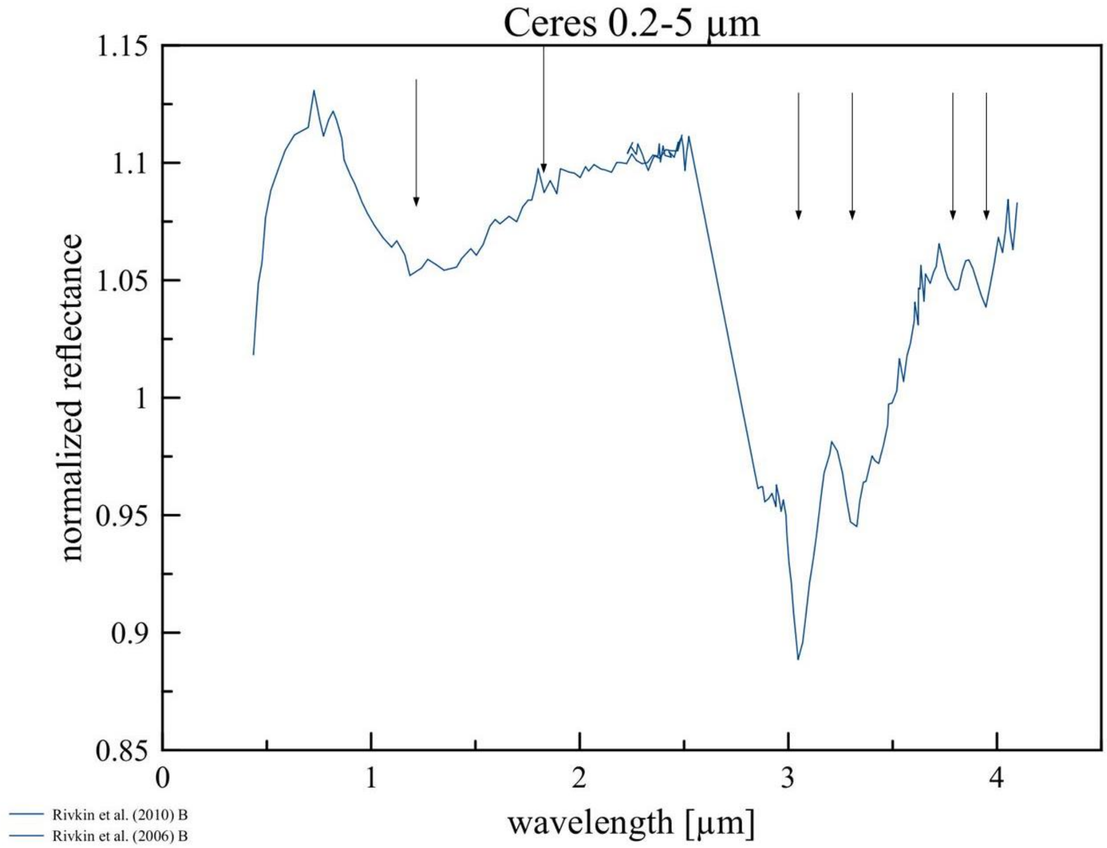

Figure 3-30. *Plot of Ceres' spectrum in the wavelength range between 0.2 and 5.0 µm. The data was taken from Rivkin et al. (2006, 2010) and was digitalized with Plot Digitalizer. Both datasets were merged together with MagicPlot. The Rivkin et al. (2010) data was shifted +0.1 to get an overlapping. The data from Rivkin et al. (2010) is composed of the data from Bus and Binzel (2002a, 2002b) as well as the data of the 52-color survey (Bell et al., 1988).*

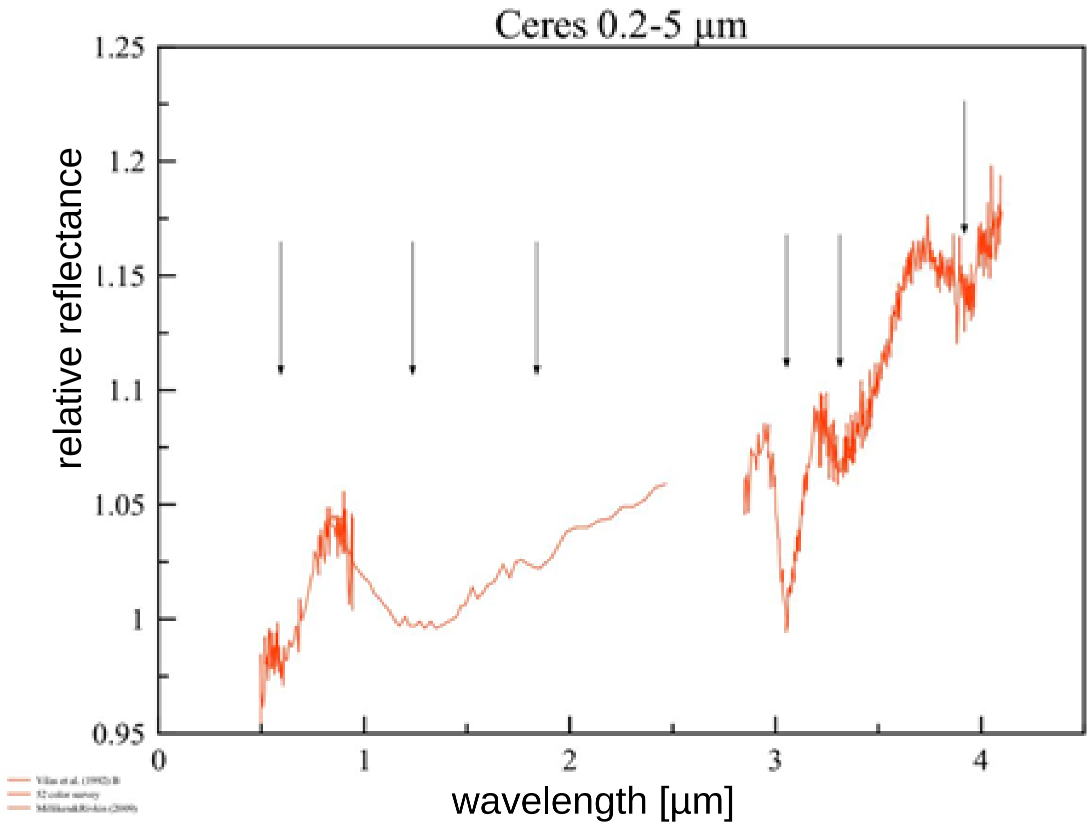

Figure 3-31. *Plot of Ceres‘ spectrum. The data was taken from Blewett and Levy (2013), the 52 color survey, Milliken and Rivkin (2009). The data was digitalized with Plot Digitalizer. The three datasets were merged together with MagicPlot. The data of the 52-color survey was shifted by a factor of 0.04 and the Milliken and Rivkin (2009) data was shifted by a factor of 0.2 to get an overlap of all data.*

CHAPTER 4

INTERPRETATION OF DATA

4.1. Comparison of λ_{SC}, ΔR_1 and ΔR_2

The spectra of the investigated C-chondrites are only weakly featured. Thus, it is important to define other characteristic features to better investigate the different chondrites. This work focuses on the investigation of Ceres' spectral absorption features and λ_{SC} (µm) and ΔR_1 vs. ΔR_2 (µm^{-1}) compared to the meteorites of section 3.1 (p 96ff) and minerals (section 3.2., p 91ff). In figure 4-1 are summarized the ΔR_1 vs. ΔR_2 values of the different meteorite classes. The grey point marks the ΔR_1 vs. ΔR_2 value of Ceres.

The data on the meteorites plot in four different clusters indicated by the colored ellipses in figure 4-1. The ellipse of the CI chondrites and the ellipse of the CM chondrites are overlapping. The CV chondrites (orange ellipse) are clustering at higher values of slope 1 and overlap with the other ellipses of the CM, CI, and CO chondrites. The CM and CI chondrites have generally lower ΔR_1 values (0.05-0.18 versus 0.125-0.38) as the CV chondrites but they cover a wider range of ΔR_2 values (-0.009-0.025 versus -0.003-0.0075). Some data points plot outside the ellipses of the respective meteorite class:

1) ΔR_1=0.1344 and ΔR_1=0.1355: these data are from the meteorite Alais.

2) -ΔR_2=0.178: this data is from the CM chondrites Cold Bokkeveld
3) ΔR_2=0.2316: this data point is from the CV meteorite Allende.

The values of the ΔR_1 vs. ΔR_2 of the CM chondrites are much more spread than those of the other CCs. There are some data points that lie close to the boundary of the ellipse. One sample plots close to the boundary of the CM chondrite ellipse at ΔR_2=-0.0089 μm^{-1}. This sample is from the CM chondrite Cold Bokkeveld and has the lowest ΔR_2 value of the CM chondrites. The CI chondrites plot in the field of the CM chondrites, but they have a more limited range of ΔR_1 vs. ΔR_2 values compared to the CM chondrites. There are two outliers that do not plot in the CI chondrite field. These meteoritic samples are from Alais. The ΔR_1 vs. ΔR_2 values of the CV chondrites plot above the clusters of the CI and CM chondrites which could be an albedo effect. The CV chondrites have generally a wider range of ΔR_1 values compared to the other meteorite classes, whereas the ΔR_2 values are a more limited. There is one outlier at the CV chondrite cluster at ΔR_1=0.2316 μm^{-1} and ΔR_2=-0.003 μm^{-1}. This data is from the measurement of an Allende sample with grain size of 63-125 µm. This sample has a larger grain size compared to the other measured samples. This larger particle size could possibly explain why this sample is outside the defined ellipse of the CV chondrites. The CO chondrites are the only meteorite class that has a circular cluster and they have the most limited range of ΔR_1 vs. ΔR_2 values.

The determined ΔR_1 vs. ΔR_2 value of Ceres plots in the ellipse of the CI, CO and CM chondrites, but only one spectrum of Ceres was analyzed, which is not sufficient as it does not display the whole surface of Ceres. The analysis of the whole surface will be possible after the data of the DAWN mission will be available for further investigation.

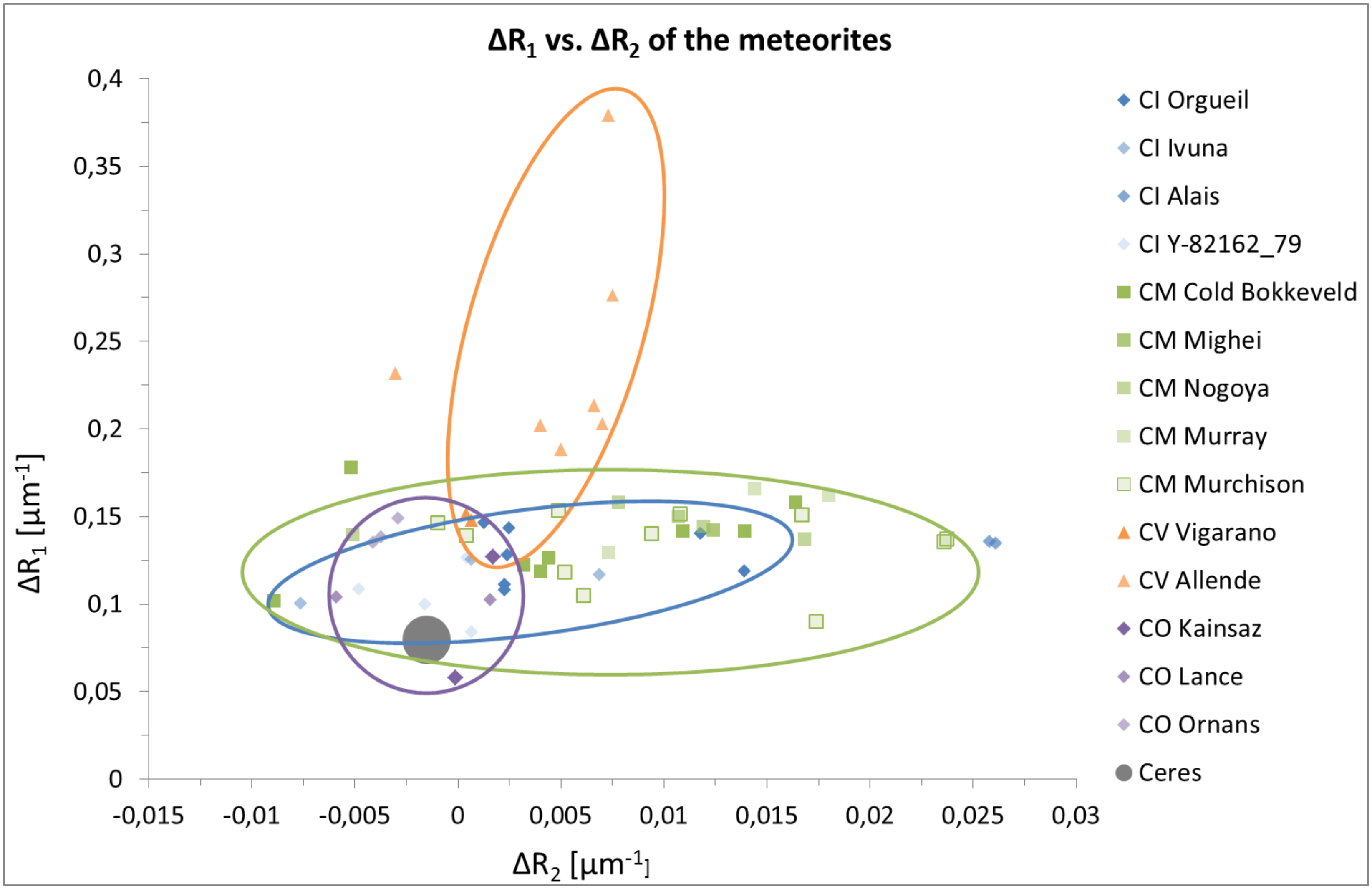

Figure 4-1. *Summary on the ΔR_1 vs. ΔR_2 values of the different meteorite classes. The ellipses mark the clustering of the single classes. The blue ellipse marks the CI chondrite data, the light green ellipse marks the cluster of the CM chondrites, the orange ellipse marks the cluster of the CV chondrites and the purple ellipse marks the data range for the CO chondrites. The grey point marks the ΔR_1 vs. ΔR_2 values of Ceres. The data for the CO chondrites include spectra of the CO chondrites Ornans and Lance that were not discussed in section 3.1 but are shown in appendix F*

In figure 4-2 the mean values of the slope change λ_{SC} for the different meteorite classes are illustrated. The black line marks the wavelength of the λ_{SC} of Ceres (λ_{SC}=0.51 µm), whereas the blue bars are the λ_{SC} values of the different CI chondrites. The unclassified CI chondrites have the lowest mean λ_{SC} of 0.41 µm compared to Ivuna (0.553 µm), Orgueil (0.533 µm), and Alais (0.525 µm). The wavelengths of the slope change of Orgueil and Alais are close to the λ_{SC} value of Ceres (figure 4-2). The unclassified CI chondrites have a much smaller slope change than Ceres whereas Ivuna has a higher value (figure 4-2).

The mean λ_{SC} values of the different CM chondrites are shown by the green bars in figure 4-2. Cold Bokkeveld and Mighei have the slope change at the shorter wavelength that the other CM chondrites (both at λ_{SC}=0.48 µm). Murray slope change occurs at λ_{SC} at 0.0.51 µm which is at longer wavelengths compared to Nogoya (0.49 µm), and Murchison (0.495 µm). From the meteorite Mighei is only spectrum available, thus, further measurements are needed to get a more representative λ_{SC} value. Mighei's wavelength of slope change is similar to the λ_{SC} of Ceres.

The mean λ_{SC} values of the CV chondrites are shown by the orange bars in figure 4-2. Allende has its wavelength of slope change at 0.423 µm, and Vigarano at 0.53 µm. The λ_{SC} of Allende occurs at a shorter wavelength than Ceres' λ_{SC}. Vigaranos's λ_{SC} is close to that of Ceres. The CO chondrites are shown by the purple bars in figure 4-2. Kainsaz (0.6 µm) and Lance (0.6 µm) have the λ_{SC} at longer wavelength than Ceres. Ornans wavelength of slope change (0.52 µm) is close to the λ_{SC} of Ceres.

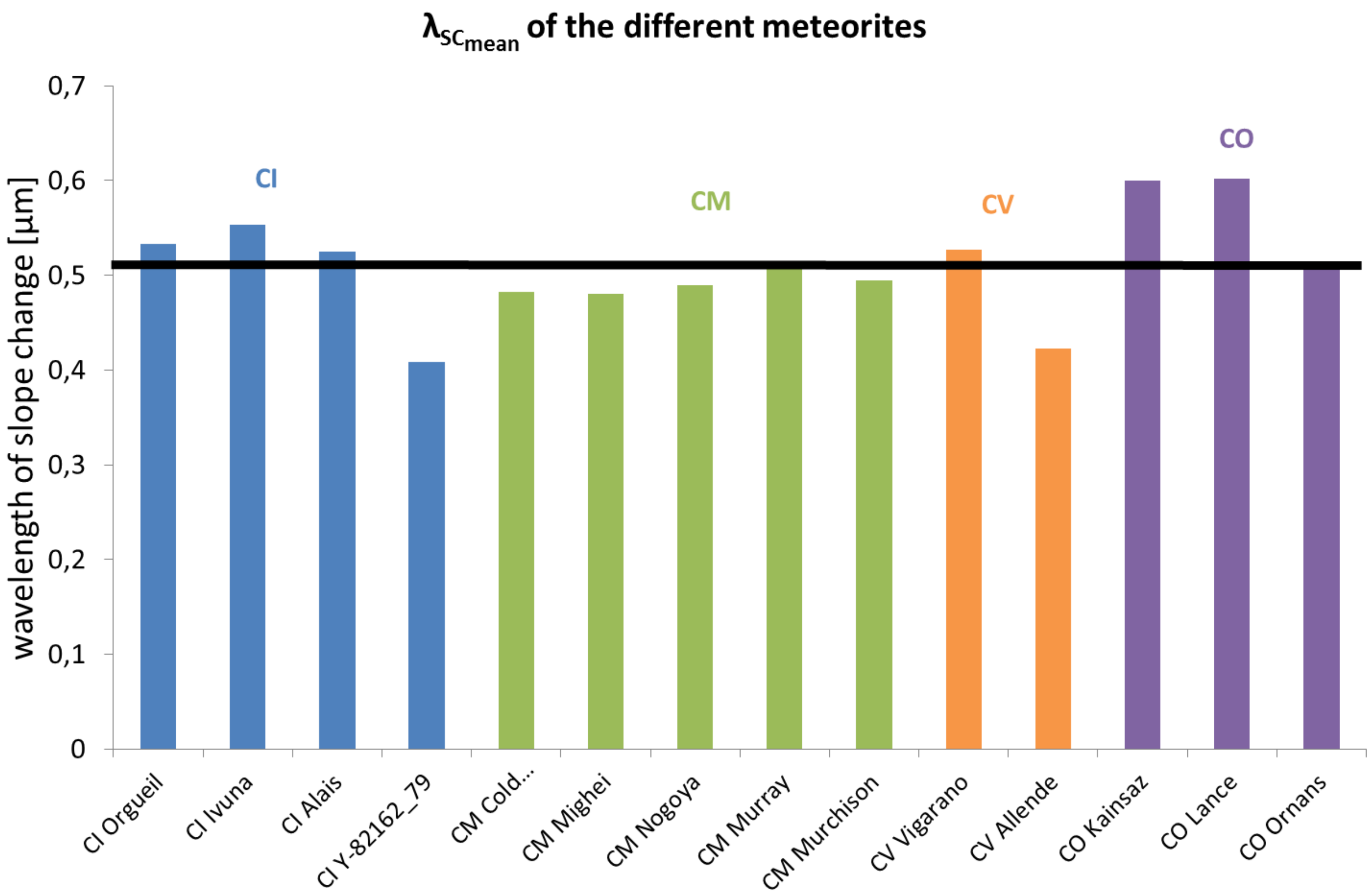

Figure 4-2. *Plot of the slope changes* λ_{SC} *for the different meteorites. Blue color indictaes CI chondrites, green color is for CM chondrites, orange color is for the different CV chondrites and the purple bars are the* λ_{SC} *values of the CO chondrites. The black line marks the* λ_{SC} *value for Ceres determined from the digitalized spectra (see figure 3-30).*

4.2. Grain size effects

Spectral characteristics of materials are dependent on multiple factors, e.g. temperature, grain size. One of these parameters, the grain size and its effects on spectral absorption features, will be discussed in this section. Particle size effects on albedo have been studied intensively by Adams and Filice (1967) and Hunt and Salisbury (1970). Spectra of meteorites measured at different grains sizes are shown in figure 4-3. The fine grain sizes (0-63 µm) are shown dashed and the coarser samples are shown by the solid line. Spectra of coarse grained and fine grained materials show different slope characteristics and different physical processes result in variable spectral behavior. These differences are based on two processes, 1) scattering at the surface and 2) volume scattering (Vincent and Hunt, 1968). The finer grain sizes have a shallower spectral slope in the VIS than the coarser grain sizes and show a lower reflectance in the VIS than the coarser grain sizes due to increasing multi-reflections with decreasing particle size (Arnold, 2014). The coarser grain sizes have a negative spectral slope in the NIR (figure 4-3) and the finer grain sizes show a positive slope in this wavelength range. The overall reflectance is decreasing with increasing particle size (figure 4-3). Figure 4-3 illustrates that different grain sizes do not affect every meteorite equally. Murchison has the biggest difference in slope (e.g., the difference at 2.43 µm is ~46.21%), whereas the difference at this wavelength of Nogoya at two different grain sizes is 36.7%. Allende and Cold Bokkeveld have the lowest difference in reflectance between the finer and coarser grain sizes (Allende: 24.39% at 2.43 µm and Cold Bokkeveld: 13.74% at 2.43 µm). In figure 4-4 the slope1 to slope 2 ratios in µm^{-1} is shown, the bold lines mark the decrease in the ratio of ΔR_1 vs. ΔR_2 depending on the particle size. The data of Murchison are not included in this figure as the spectral range of one Relab spectrum is not sufficient to get data on slope 1.

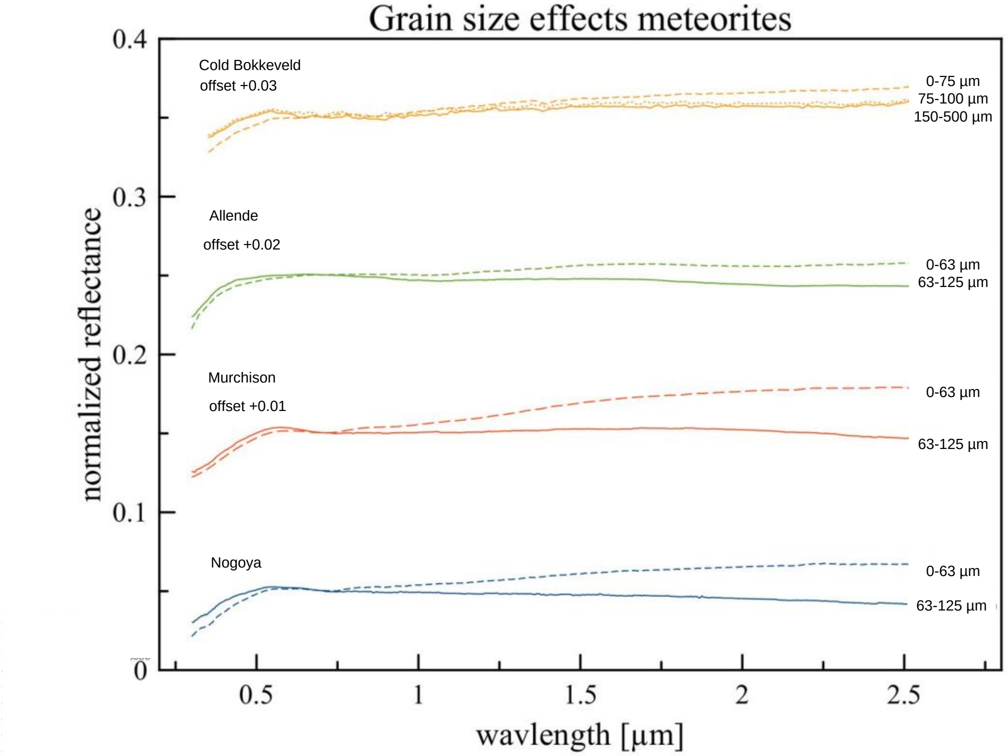

Figure 4-3. *Grain size effects of 3 different meteorites. The solid lines show grain sizes between 63-125 µm and the dotted lines show grain sizes between 0-63 µm. The offset between the meteorite types is +0.1.*

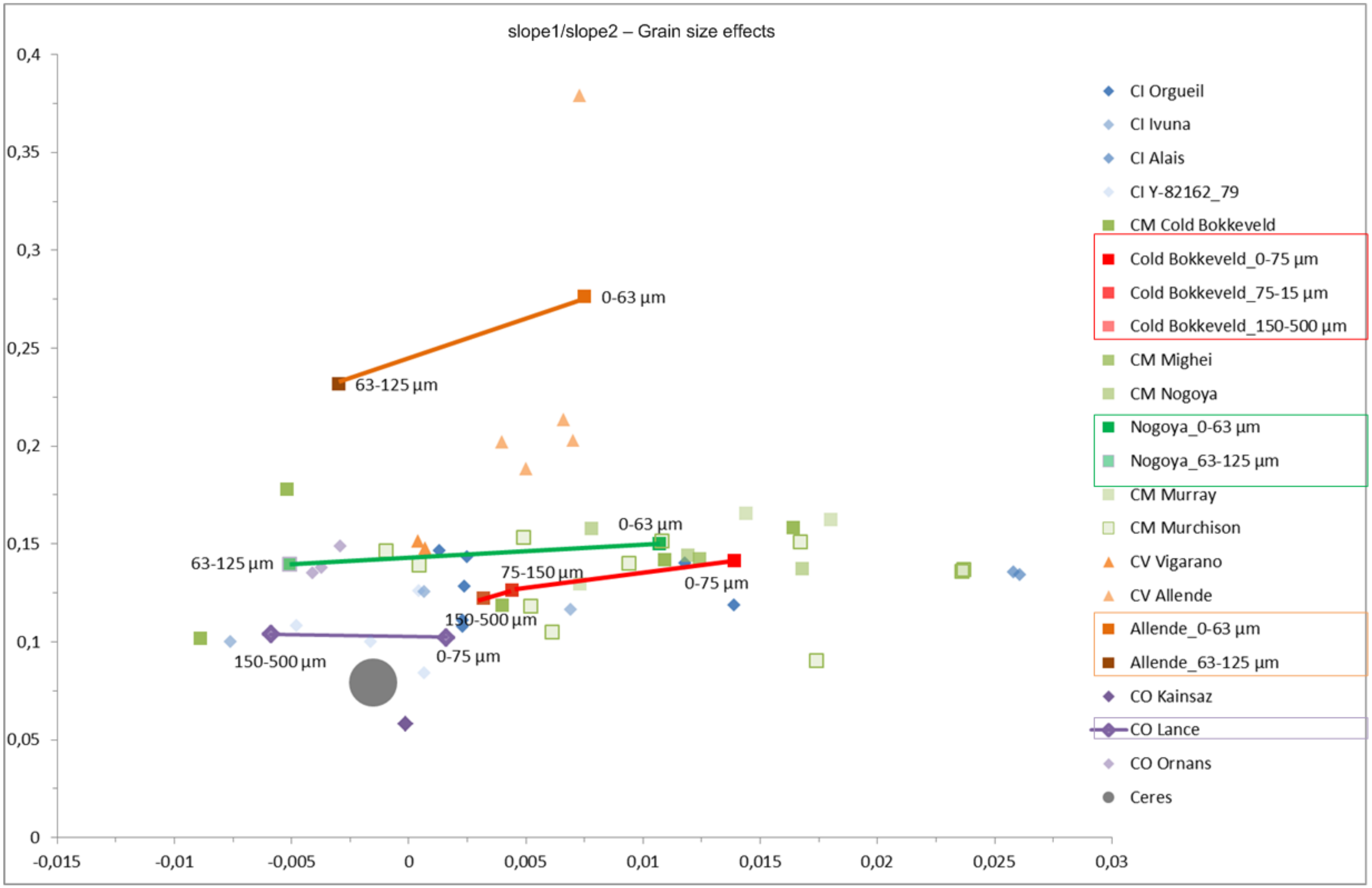

Figure 4-4. *The difference in the grain sizes of the meteorites are visible in the* ΔR_1 *vs.* ΔR_2 *ratios marked by the solid lines in the figure. The grain sizes are stated at the data points. There is a gradually decrease in the reflectance the coarser the samples are. The single meteorite types are differently affected by the grains sizes effects.*

4.3. Comparison of the spectral characteristics with Ceres' spectrum

In figure 4-5 all λ_{SCmean} values for the different minerals are shown. The black line marks the λ_{SC} for Ceres to better compare the minerals to Ceres. The ΔR_1 vs. ΔR_2 values for the minerals and Ceres (grey dot) are shown in figure 4-4.

According to the λ_{SC} (figure 4-5) the minerals magnesite (λ_{SCmean}=0.44), buddingtonite (λ_{SCmean}=0.47), brucite (λ_{SCmean}=0.47) and montmorillonite (λ_{SCmean}=0.475) are the best fit to the wavelength of the $\lambda_{SCCeres}$=0.51 µm. The organica (grey bars in figure 4-5) have λ_{SCmean} values that are higher than the value for Ceres (black line in figure 4-5) except kerite 2 samples which have their wavelength of slope change at 0.51 µm. The carbonates (blue bars in figure 4-5) have λ_{SC} at shorter wavelengths than Ceres, whereas the siderite samples have their λ_{SC} at longer wavelengths. Saponite, cronstedtite, troilite, buddingtonite, and pyrite have the λ_{SC} at longer wavelength than Ceres (figure 4-5). Tochilinite and magnetite have the λ_{SC} at shorter wavelength than Ceres.

The minerals brucite, magnesite, kerite 2, and dolomite have their slope changes at wavelengths similar to that of Ceres (figure 4-5).

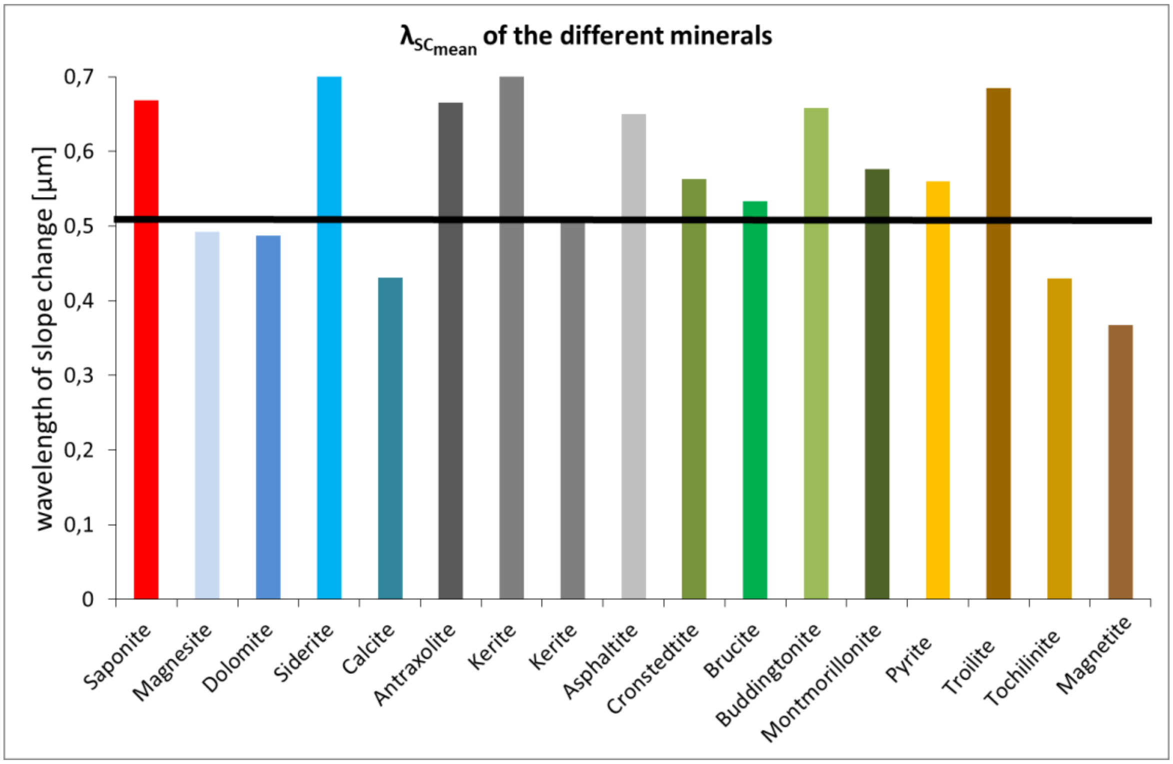

Figure 4-5. *Plot of the different* λ_{SCmean} *values for minerals discussed in section 3.2 and Ceres. The black line shows the value of Ceres. No single mineral perfectly matches the* λ_{SCmean} *of Ceres.*

The ΔR_1 vs. ΔR_2 values for the different minerals are shown in figure 4-6. Ceres plots close to the spectral slopes of the carbonates (magnesite, calcite), buddingtonite, troilite, cronstedtite and pyrite. Based on the mean ΔR_1 vs. ΔR_2 values (see appendix E) the minerals magnesite (0.068 vs. -0.0008 μm^{-1}) and calcite (0.084 vs. 0.0027 μm^{-1}) are close to Ceres (0.0791 vs. -0.015 μm^{-1}). The ΔR_{1mean} value of the following minerals fit well the ΔR_{1Ceres}=0.0791 μm^{-1}:

- troilite (0.067 μm^{-1}) is close to the value of whereas the λ_{SCmean}=0.69 µm is much higher than those of Ceres (0.51 µm) and the ΔR_{2mean}=0.0197 μm^{-1} is also much higher than the value determined for Ceres (-0.0015 μm^{-1}),
- pyrite (0.087 μm^{-1}) which has its slope change at longer wavelength than Ceres and has a higher ΔR_{2mean}.

The ΔR_{2mean} values of the following minerals are close to that of Ceres (ΔR_2=-0.0015 μm^{-1}):

- tochilinite (-0.0009 μm^{-1}),
- dolomite (0.002 μm^{-1})
- buddingtonite (0.1051 μm^{-1}) and
- brucite (0.003 μm^{-1})

However, the slope 1 values of these minerals are much higher (tochilinite: 0.292 μm^{-1}; dolomite: 0.161 μm^{-1}, buddingtonite: 0.1051 μm^{-1} and brucite: 0.150 μm^{-1}).

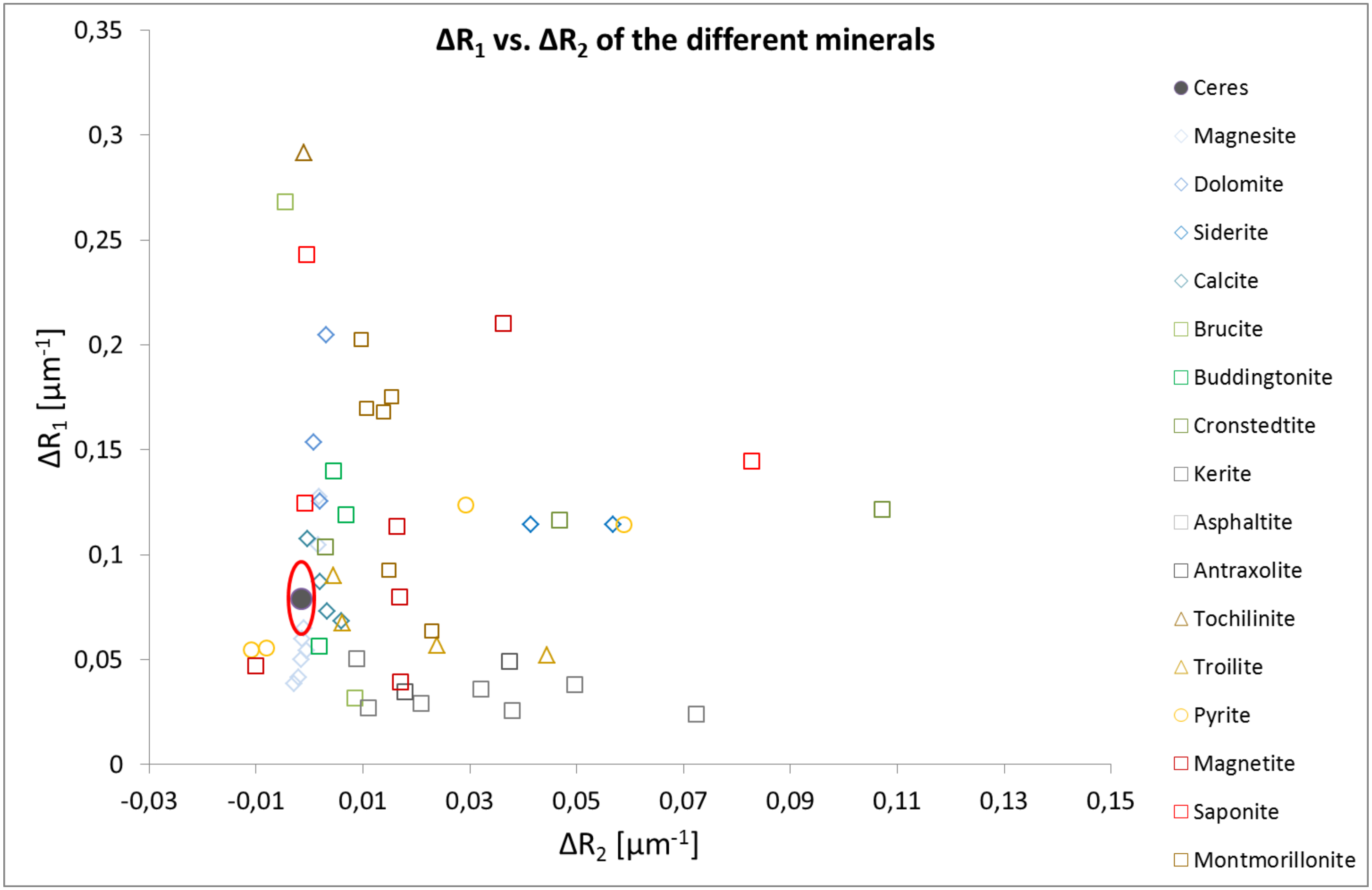

Figure 4-6. *Plot of the different slope 1 and slope 2 values for the minerals discussed in section 3.2 and the grey point marks Ceres. The unit of the slopes is R/wavelength in µm*$^{-1}$*. The red ellipse shows ±20% of the slope 1 and slope 2 values of Ceres.*

The Ceres spectrum (see section 3.3) is weakly featured and has just a few absorption features that can be considered for analysis. Thus, the spectra of the minerals were compared to the spectrum of Ceres to identify similarities. The data are summarized in table 4-1. Values similar to Ceres are marked red. Table 4-1 also contains the meteorites in which the different minerals occur.

The feature seen at ~0.6µm in the Ceres spectrum is just occurring in the saponite spectra between 0.65 to 0.68 µm and in the montmorillonite spectrum at 0.63 µm. This feature is shifted towards shorter wavelength in the spectra of troilite, pyrite and magnetite (0.39-0.48 µm) and towards longer wavelength in the tochilinite spectra (0.735 µm). The absorption feature in the Ceres spectrum at ~1.2 µm occurs in the spectra of saponite (1.2 µm) and in the spectrum of siderite (between 1.0 and 1.3 µm; table 4-1). This band is shifted toward shorter wavelength in all other spectra. An additional feature at ~1.9 µm is seen in all spectra excluding the spectrum of magnetite, troilite, cronstedtite and the organica. The spectrum of Ceres has a sharp drop-off in reflectance at ~2.5 µm, only occurring in the spectrum of montmorillonite at ~2.54 µm and in the spectrum of buddingtonite at 2.5 µm. All other spectra show a shift of this drop-off towards longer wavelength (2.6-2.7 µm). The absorption band at ~3.06 µm is seen in the spectra of

- the organic materials at slightly shorter wavelength (3.04- 3.05 µm),
- brucite at 3.067 µm,
- saponite at 3.06 µm,
- buddingtonite at 3.06 µm and
- magnesite at 3.06 µm.

The other minerals demonstrating this spectral feature show slightly shifted values, e.g. dolomite at 3.08 µm or calcite at 3.1 µm. The absorption feature at 3.3 µm is seen in the spectrum of the carbonates (table 4-1) at ~3.3 to 3.4 µm, in the spectrum of saponite sample, that was measured at the DLR, shows a spectral feature at this wavelength range, and in the spectra of the organic materials (3.27-3.29 µm).

Based on the spectral characteristics in section 4.1 and 4.2, it is most likely that combinations of the following minerals will be found at Ceres' surface. These combinations include carbonates (especially magnesite), buddingtonite, saponite and brucite. Darkening agents have also to be present, as otherwise the weaker spectral features and spectral flattening are not explainable. Most likely are organic compounds like kerite or anthraxolite and magnesite, as these minerals and organica are components of CM and CI chondrites. Tochilinite might also be present at Ceres' surface as this mineral is composed of layers of sulfides and brucite.

Table 4- 1: *Overview on the diagnostic features for comparison with Ceres. The values in red show that these values are close or similar to Ceres' values, black values show that the value are not similar to Ceres' values.*

mineral	λ_{SCmean} [μm]	ΔR_1 [μm-1]	ΔR_2 [μm^{-1}]	~0.6 μm [μm]	drop-off [μm]	~1.2 μm [μm]	~1.9 μm [μm]	3.05 to 3.07 μm [μm]	3.3 μm [μm]	found in meteorite type
Ceres	0.51	0.0791	-0.0015		2.5					-
magnetite	0.37	0.166	0.0153	0.48	2.65	1.06	-	2.76	-	Ornans Mighei Murchison Nogoya Alais Orgueil
pyrite	0.56	0.087	0.017	0.39	2.67	0.93	1.99	3.07	-	Orgueil
troilite	0.69	0.067	0.0197	0.49	2.81	-	-	3.08	-	Ornans Murchison Mighei Alais Orgueil Vigarano
tochilinite	0.43	0.2916	0.0028	0.735	2.63	0.9	1.98	-	3.41	Murchison Mighei Nogoya Alais Orgueil
siderite	0.7	0.114	0.0492	-	2.67	1.0-1.3	1.99	3.11	3.35	
calcite	0.43	0.084	0.0027	-	2.66		1.88	3.1	3.35	Murchison Mighei Nogoya Alais Orgueil

Table 4- 1: *Cont.*

mineral	λ_{SCmean} [µm]	ΔR_1 [µm^{-1}]	ΔR_2 [µm^{-1}]	~0.6 µm [µm]	drop-off [µm]	~1.2 µm [µm]	~1.9 µm [µm]	3.05 to 3.07 µm [µm]	3.3 µm [µm]	found in meteorite type
dolomite	0.49	0.161	0.003	-	2.6	1.02	1.85	3.08	3.3	Murchison Nogoya Alais Orgueil
magnesite	0.49	0.068	-0.0008	-	2.6	1.1	1.915	3.06	3.26	Orgueil
buddingtonite	0.66	0.1051	0.0043	-	2.5	-	1.905			
saponite	0.67	0.171	0.0271	0.65-0.68	2.62	1.2	1.9	3.06	3.28	Orgueil Vigarano
montmorillonite	0.58	0.145	0.0145	0.63	2.54	0.9	1.91	2.75	3.41	Orgueil Vigarano
brucite	0.53	0.150	0.003	-	2.38	0.95	1.925	3.067		Mighei
cronstedtite	0.56	0.114	0.052		2.65					Murchison Mighei Nogoya Vigarano
anthraxolite	0.67	0.042	0.028	-	~3.3	-	-	3.04-3.05	3.27-3.29	
asphaltite	0.65	0.025	0.3778	-	~3.3	-	-	3.04-3.05	3.27-3.29	
kerite	0.51	0.0018	0.18	-	~3.3	-	-	3.04-3.05	3.27-3.29	

4.4. Linear mineral mixing

The investigation of the spectral characteristics of the minerals and meteorites has shown that Ceres' composition could not be explained by a single mineral or meteorite. Thus, it is necessary to investigate mineral mixtures. A possible assemblage is determined based on the previous section and on section 1.2.2.1 and 1.2.2.2 to demonstrate how the spectrum changes with varying mineral amounts.

The usage if linear mixings is limited and only lead to useful results in the longer wavelength (IR) and is not this accurate for short wavelength regions (UV and VIS). Non-linear mixings would be better to describe the wavelength regions in the UV and VIS.

From figure 4-1 and 4-2 (page 108 and 110) it seems reasonable to choose minerals that are related to CM and CI chondrites as the base for the mineral mixing models. The composition of those two meteorite classes is intensely investigated by Cloutis et al. (2011a) and Cloutis et al. (2011b) and is shortly described in section 1.2.2.1.

It is seen in figures 4-1, 4-2, 4-5 and 4-6 (pages 108, 110, 115 and 117) that some minerals and meteorites fit well to the ΔR_1, ΔR_2 or λ_{SC} values but none of the materials fits Ceres in all three values. Thus, it is necessary to take into consideration the spectral absorption features of the terrestrial analogue minerals. The minerals chosen for the linear mineral mixing are brucite, cronstedtite, a darkening agents (magnetite) as well as magnesite (Mg-carbonate). The mineral mixings components and amounts are listed in table 4-2. The minerals were mixed with a routine written in IDL (linear mixing model).

The mineral spectra were interpolated on the magnesite spectrum. The used equation used in IDL was:

%brucite + %cronstedtite + %magnetite + %magnesite=100%.

Table 4-2. *Components and amounts of minerals used in the linear mineral mixing. The amount is given in percent. The formula is stated in the text above.*

Mixing	brucite	cronstedtite	magnetite	magnesite
Mixing 1	40	20	20e	20
Mixing 2	30	20	30	20
Mixing 3	10	20	40	30
Mixing 4	20	10	20	50
Mixing 5	15	30	15	50
Mixing 6	10	50	10	30

The spectra of the mineral mixings are shown in figure 4-7 and for reasons of comparison a spectrum of Ceres from section 3.3 was incorporated. Figure 4-7 illustrates that with a decreasing amount of brucite and an increasing amount of magnetite (mixing 1-3) the characteristic spectral absorption features get weaker. The ΔR_2 values decrease (see appendix E), whereas the ΔR_1 values increase in this mixing. In mixings 4 to 6 the amount of cronstedtite increases and the amount of the other three minerals decreases. The spectral characteristics of magnesite and brucite get weaker with an increasing cronstedtite amount and the ΔR_1 values increase. The ΔR_2 values decrease and get slightly negative in this mixings.

The spectra of the mineral mixing do not fit the existing Ceres spectrum well. The spectral absorption features are weaker in the Ceres spectrum and the slope 1 and 2 do not correlate well with Ceres' ΔR_1 vs. ΔR_2 values. Possible reasons for that are grain size effects or effects of the geometry. However, the mixings clearly show that different amounts of minerals affect the spectral slopes in the VIS and NIR.

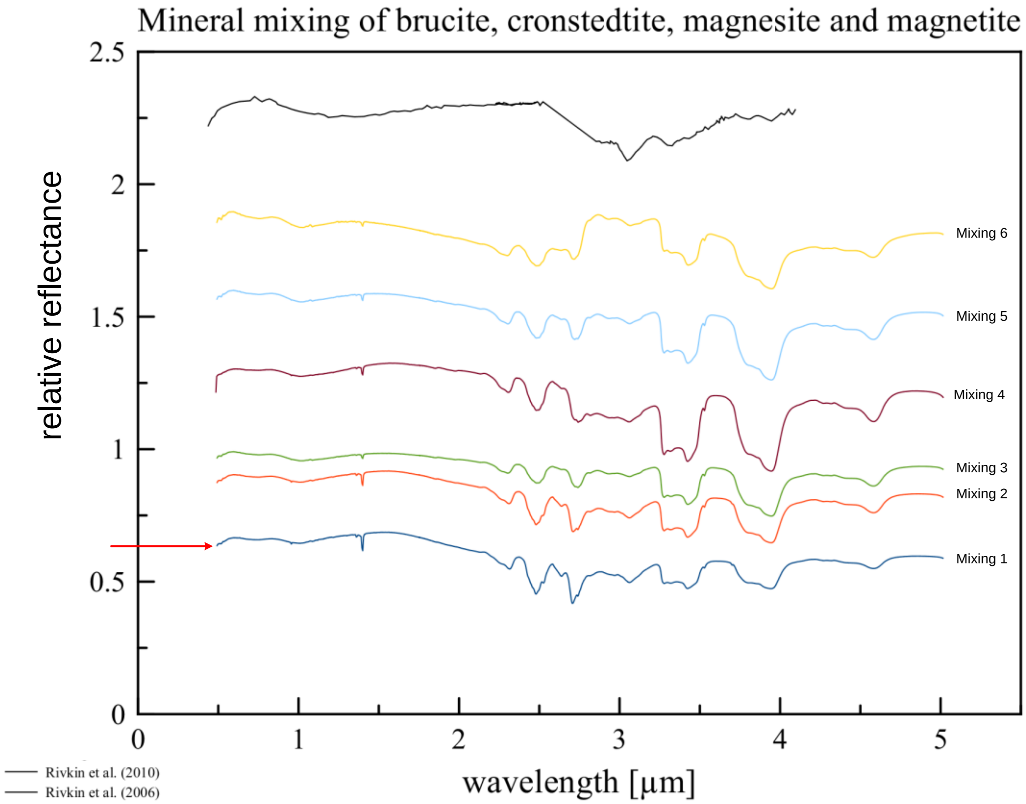

Figure 4-7. *Plot of mineral mixtures from table 4-2. The minerals were mixed with a routine written in IDL. The spectral data of the single minerals was interpolated on the spectrum of magnesite. The spectrum of Ceres is included in the plot to better see relationships between the models and Ceres. The offset of the spectra is +0.2.*

CHAPTER 5

CONCLUSION

This work focusses on reviewing the spectral analysis of the surface of the asteroid Ceres, an object thought to have undergone aqueous alteration processes. The spectral characterization of Ceres is difficult due to its few and weak features in its spectrum. There is currently no material or mixing of different minerals that fit perfectly the whole spectrum of Ceres. There are also no meteorites that could be correlated directly with Ceres. The spectra of Ceres show different diagnostic spectral features that can be related to its surface composition. These features include absorption feature at 0.25 µm, at 0.6 to 0.67 µm, at 1.0 µm, at 1.1 µm, at 3.06 µm, at 3.3 to 3.4 µm, at 3.9 µm, at 10.0 µm, and at 11.2 µm. Previous laboratory measurements have shown that these features could be attributed to a variety of minerals. Mineral mixings were modelled and spectrally investigated to show how the spectral characteristics are affected by different mineral mixings. The mineral mixing used in this work is a mixture of the minerals brucite, cronstedtite, magnetite as a darkening agent and carbonates, most preferably magnesite (Mg-carbonate).

Complementary measurements of the spectral reflectance in the 0.5 to 5 µm region of CCs (Murchison, Nogoya, Cold Bokkeveld, Banten, Vigarano, Allende, Kainsaz), minerals (brucite, cronstedtite, saponite, tochilinite, and buddingtonite), and organic components (anthraxolite, asphaltite and kerite) that have been studied in this work contribute to previous studies and enlarge the existing data base of Ceres' surface analog materials.

This work analyzes diagnostic spectral characteristics of C-meteorites, terrestrial samples, which are proposed to be reasonable analogues for the Ceres' surface composition. Additionally, existing spectra of spectral data catalogues like Relab were also reviewed for spectral characteristics. The method of spectral measurements of minerals and meteorites fulfils the requirements to detect several diagnostic features that can be related to Ceres. The wavelength of slope change λ_{SC} and the spectral slopes in the VIS-NIR and NIR-IR are diagnostic tools to characterize and to differentiate between the single meteorite classes and meteorite types. Different C-type meteorites show different slopes and slope changes at various wavelengths, which are correlated to the type of meteorite. The CM and CI meteorites are the best match to the spectral characteristics of Ceres. The investigation of both meteorite classes in this work has shown that the unclassified CI chondrites show similar λ_{SC} and spectral slopes. Nearly all CM and CI chondrites have the wavelength of slope change at a similar wavelength like Ceres. Most meteorites have a steeper slope in the VIS wavelength range than Ceres except the unclassified CI chondrites having slopes similar to Ceres. All meteorites have generally shallow slopes in the NIR, especially the CI and CM chondrites show NIR slopes like Ceres.

The VIS-NIR (ΔR_1) und NIR-IR slope (ΔR_2) are dependent on the grain size of the material. Coarser materials tend to have lower ΔR_2 values, whereas the ΔR_1 values seem to be not strongly affected by the grain size indicated by the relative steady ΔR_1

values (figure 4-3 and 4-4). The investigated meteorites are affected by grain size effects to varying degrees. The data of the meteorites can be grouped in 4 clusters. The clusters of the CV, CO, and CI chondrites intersect with the field of the CM chondrites. The ΔR_1 and ΔR_2 for Ceres determined from spectra of other scientists are situated in the cluster of the CI, CM and CO chondrites. In addition to the λ_{SC} and the spectral slopes in the VIS and NIR, spectral features of meteorites and minerals were investigated. Compared to Ceres, the CM and CI chondrites show the best fit according to the λ_{SC} and the spectral slope in the VIS and NIR. The meteorites Ornans (CO) and Vigarano (CV) can be related to the λ_{SC} of Ceres. The spectral slope of Ceres also can be related to the CO chondrites. The spectra of the meteorites are weakly featured and only some of them, e.g. Banten, Cold Bokkeveld, Murray, Mighei or Nogoya, show characteristic absorption features that can be used for further characterization. The mineral spectra described in section 3.2 display a variety of diagnostic features that could be investigated. This work presents spectra of brucite, buddingtonite and cronstedtite measured in the range from 0.5 to 22 µm, and not being available in other catalogues so far.

The measurements and the analyses of the spectral data in this work will contribute to future analyses of Ceres' surface composition for spatial and temporary variations. This work focusses on the investigation of the occurrence of spectral absorption features in combination with the wavelength of slope change λ_{SC} and the spectral slope in the VIS and NIR. These spectral characteristics in combination with the spectral absorption bands defined in this work are a useful tool to determine the minerals at Ceres' surface. Table 1-4 shows that no single mineral matches all characteristic features defined in this work. But some of the investigated minerals are, based on the spectral features in table 4-1, most likely to be present on Ceres' surface. These minerals include carbonates, especially magnesite, dolomite and calcite, saponite, brucite and buddingtonite. This result is consistent with the work done by other scientists, e.g. Vilas and Gaffey, 1989; Feierberg et al., 1981; King et al., 1992 or Milliken and Rivkin, 2009. These minerals are components of the CM and CI chondrites, described in section 1.2.2.1. Minerals expected to be components of Ceres' surface are consistent with the composition of the CI chondrite Orgueil (compositional analysis based on Cloutis et al., 2011a). Water ice, frost and ice-mineral-mixtures were not measured and in detail analyzed in this work but have to be considered for research on Ceres' surface composition.

The detection of carbonates at the surface of Ceres would indicate that tertiary weathering processes, forming salts like carbonates or sulfates, were or are still active. Furthermore, there have to be upward moving processes, like rising groundwater, bringing the carbonates to the surface. The dark areas on Ceres could be possible source regions of carbonates. As there is no clear CO_3 absorption feature seen in Ceres's spectrum, the wavelength region between 3.3 and 3.5 µm could be used to determine whether carbonates are present. This feature is often not considered as the CO_3 absorption bands described in section 3.2.6 (green bar in table 4-19 to 4-22) are most indicative for carbonates. However, the wavelength range between 3 and 4 µm is also indicative for CO_3 as in this wavelength range occur 2 overtone and combination tone bands of the fundamental vibrations (Arnold, 2014, p. 157).

Organic materials show a variety of absorption features that can be used to detect them at Ceres' surface (section 3.2.11). The spectra of Ceres show none of the absorption bands shortward of 3.0 µm of organic materials summarized in table 3-2 and thus, it is necessary to use the wavelength range between 3.0 to 4.0 µm to detect organic materials. After the detection of organic materials on the comet P67 (Rosetta mission; Capaccioni et al., 2015) it is likely that such materials are present on Ceres' surface, possibly only localized due to exogenic sources. If organic materials are present all over the surface of Ceres, endogenic processes have led to the formation of these materials. The detection of these materials on Ceres' surface would give fundamental insights into the Solar System's history. If water is present on Ceres' surface it will be seen in the spectra (e.g. at 1.4 µm, 1.9 µm, 2.7 µm) of the respective area on the surface (e.g. the bright spots). It is possible to distinguish between bond water and OH-groups, as both have characteristic spectral absorption features at different wavelengths and as there is no adsorbed water producing additional water bands. OH has the absorption bands at 1.4 µm, 2.66 µm, and 6.27 µm, whereas bond water shows the absorption bands at 1.4 µm, 1.9 µm, 2.903 µm, 3.106 µm, and 6.079 µm. The region at ~3 µm is indicative for hydrated minerals and features seen in the spectra are indicating phyllosilicates or other OH-bearing minerals like brucite. These minerals, if present will be found everywhere at Ceres' surface.

Previous spectral investigations of Ceres done by e.g. Lebofsky, 1978; McCord and Sotin, 2005; Rivkin et al., 2010; Rivkin et al., 2011; De Sanctis et al., 2012 and the detection of water vapor exhausted by Ceres by the Herschel telescope have shown that the surface material of Ceres is most likely composed of aqueous alteration products indicating that liquid water was or even is still present in Ceres' interior. The residues of these alteration processes are spectrally visible. The detection of water on Ceres' surface, most likely in the form of water ice, and primary weathering products of water will imply that the object is still active as water is not stable on Ceres' surface and is lost to space quickly. It is also possible that water is present in liquid form in aquifers in deeper layers of the object. This would be in correlation with the current interior models described in section 1.2.1.7. Impact craters are best to search for signs of activity. Images taken by one of DAWN's instruments show light spots at the surface which could be icy material that was brought to the surface by an impact or internal process (up-welling if Ceres is not in hydrostatic equilibrium). The weathering products themselves are characteristic to describe the processes that have shaped Ceres' surface. It is possible to detect the amount of water incorporated into the crystal structure of a mineral, e.g. described in section 3.2.1 on montmorillonite.

The work done in this thesis has shown that the spectral characteristics determined are reliable tools to characterize surface materials of Solar System objects, but it is necessary to intensify the research on the λ_{SC}, spectral slopes in the VIS and NIR, and diagnostic absorption features. Most important would be to gain a wider range of data including mineral mixtures, different meteorites and terrestrial analogue minerals. It would also be better to measure the samples under similar conditions, e.g. measure in comparable geometry conditions (bidirectional reflectance at various incidence and emergence angles for photometric analyses). The linear mineral mixings offer a reliable method to simulate Ceres' spectrum. The mixings done in this work have shown how the spectral absorption features are influenced by varying compositions.

This work shows the feasibility to draw conclusions on the surface composition and therefore, on the history and evolution of Ceres with the described method and spectral analyses. The comparison between the data collected in this work and the corresponding results from DAWN will give an insight into the reliability of ground-based observations to space-based observations.

ABBREVIATIONS

λ_{SCmean}	wavelength of slope change in µm
ΔR_1	spectral slope in the VIS to NIR
ΔR_2	spectral slope in the IR
ACS	Advanced Camera for Surveys
Al	aluminum
Ar	argon
ASTER	Advanced Spaceborne Thermal Emission and Reflection Radiometer
AU	Astronomical units
CaF_2	calcium fluoride
CAI	Calcium Aluminum Intrusions
CC	carbonaceous chondrite
CF	Christiansen frequency
CFT	crystal field transition
CI	Ivuna-like carbonaceous chondrite
CIF	Complex Irradiation Facility
CM	Murchison-like CC
CO	Ornans-like CC
CO_2	carbon dioxide
Co	cobalt

Cr	chromium
CV	Vigerano-like CC
Dec	declination
DLR	German Aerospace Institute
DTGS	deuterated tri glycine sulfate
e	exit angle
EM	electromagnetic
erg	ergon, unit of energy and mechanical work, 1erg=10^{-7} Joule
Fe	iron
FC	Framing camera
FIR	far infrared
FTIR	Fourier transform infrared spectroscopy
g	gram
GRaND	Gamma Ray and Neutron Detector
Gya	billion years
HED	howardite-eucrite-diogenite
HRC	High Resolution Channel
hrs	hours
HST	Hubble Space Telescope
i	angle of incidence
IDL	Interactive Data Language (software program)
InGaAs detector	indium-gallium-arsenide detector
IR/IS	Infrared and Raman for Interplanetary Spectroscopy
IUE	International Ultraviolet Explorer

IVCT	intervalence charge transfer
K	Kelvin
KBr	potassium-bromide
km	kilometer
Kr	krypton
LFT	ligand field theory
LHB	late heavy bombardment
JPL	Jet Propulsion Laboratory
MAB	Main Asteroid Belt
MCT	Mercury Cadmium Tellur detector
MIR	middle infrared
MPS	Max-Planck-Institute for Solar System Research
Myr	million years
mm	millimeter
mrad	milli-rad
NASA	National Aeronautics and Space Administration
NH_3	ammonia
N_2	nitrogen gas
Ni	nickel
NIR	near infrared
OH	hydroxyl
OMCT	oxygen-metal charge transfer
PEL	Planetary Emissivity Laboratory
RA	right ascension
s	second

SBC	Solar Blind Channel
λ_{SC}	wavelength of slope change
Si	silicium
Ti	titanium
USGS	U.S. Geological Survey
UV	ultraviolet
VIS	visible
VNIR	Visible and Near Infrared
vol%	volume percent
wt%	weight percent
Xe	xenon
yrs	years
µm	micrometer

APPENDICES

Appendix A

Sample Description: Meteorites

Table A- 1. *Description of the meteorites that were measured at the DLR Berlin.*

type	**meteorite**	**Spectra**	**Size**	**Origin**	**Source**	**image #**
CM chondrite	Murchison	Murchison_DLR	whole rock	fell in 1969; Murchison Victoria (Met.Bulletin Database)	A. Bischof, Institute of Planetology, Westfälische Wilhelms University, Münster	
	Banten	Banten_DLR	whole rock	fell in 1933; Java, Indonesia (Met. Bulletin Database)		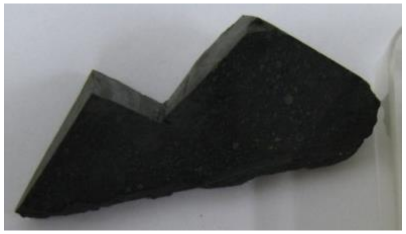
	Cold Bokkeveld	ColdBokkeveld_ DLR	whole rock	fell in 1838; Koue Bokkeveld Mtn., South Africa (Met. Bulletin Database)		
	Nogoya	Nogoya_DLR	whole rock	fell in 1879; Entre Rios, Argentina (Met. Bulletin Database)		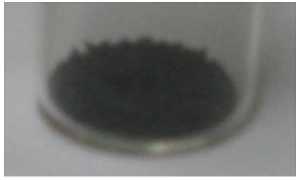

Table A-1. cont.

type	meteorite	Spectra	Size	Origin	Source	image #
CV chondrite	Vigarano	Vigarano_DLR	whole rock	fell in 1910; Emilia-Romagna, Italy (Met. Bulletin Database)	A. Bischof, Institute of Planetology, Westfälische Wilhelms University, Münster	
	Allende	Allende_DLR	whole rock	fell in 1969; Chihuahua, Mexico (Met. Bulletin Database)		
CO chondrite	Kainsaz	Kainsaz_DLR	whole rock	fell in 1937; Respublika Tatarstan, Russia (Met. Bulletin Database)		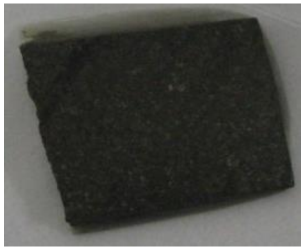

Meteoritical Bulletin Datsbase:
http://www.lpi.usra.edu/meteor/metbull.php

Table A- 2. *Sample description of the meteorite spectra taken from the Relab database.*

Sample Name	Sample ID	Spectrum ID	Type	Size	Spec Code	Res.	Atmosphere	Origin	Chem#	Text	measured by
Ivuna	MB-TXH-060	**C3MB60**	CI	0-125	BD-VNIR	5,0	Ambient	Tanzania		M. Zolensky Sample	Hiroi, T.X. (Brown University)
		C4MB60			BD-VNIR	5,0	Ambient				
		NCMB60			BD-VNIR+BC-FTIR1	9,0	Ambient+Dry				
Orgueil	MB-TXH-057	**NCMB57**	CI	0-100	BD-VNIR+BC-FTIR1	9.0	Ambient+Dry	Montauban, France		M. Zolensky Sample	
Orgueil	MR-MJG-105	**CGP078**	CI		DHC-VNIR	5,0	Ambient	Montauban, Tarn-et-Garonne, France	177	Fell May 14, 1864	Gaffey, M.J. (University of North Dakota)
		CGP080			DHC-VNIR	5,0	Ambient				
		CGP082			DHC-VNIR	5,0	Ambient				
		MGP078			DH-VNIR	5,0	Ambient				
		MGP080			DH-VNIR	5,0	Ambient				
		MGP082			DH-VNIR	5,0	Ambient				
Alais	MR-MJG-106	**CGP084**	CI		DHC-VNIR	5,0	Ambient	Gard, France		Fell March 15, 1806	
Y-82162,79 <125 um	MB-CMP-019-A	**C3MB19**	CI Unusual	0-125	BD-VNIR	5,0	Ambient	Yamato Mtns, Antarctica		NIPR - Brown	Pieter, C.M. (Brown University)
		NCMB19			BD-VNIR+BC-FTIR1	9,0	Ambient+Dry				
Y-82162,79 <63 um	MB-CMP-019-B	**C4MB19**		0-63	BD-VNIR	5,0	Ambient				
Y-82162,79 63-125 um	MB-CMP-019-C	**CCMB19**		63-125	BD-VNIR	5,0	Ambient				

Table A-2. *cont.*

Sample Name	Sample ID	Spectrum ID	Type	Size	Spec Code	Res.	Atmosphere	Origin	Chem#	Text	measured by
Murchison <125 um	MB-TXH-064-A	**C2MB64**	CM2	0-125	BD-VNIR	5,0	Ambient	Victoria, Australia		(C3)<63um, (C4)63-125um, (C2)<125um (C3 & C4 mix), dry-sieved.	Hiroi, T.X. (Brown University)
	MB-TXH-064-B	**C0MB64**			BD-VNIR	1,0	Ambient				
	MB-TXH-064-B	**C3MB64**			BD-VNIR	5,0	Ambient				
	MB-TXH-064-B	**LCMB64**			BD-VNIR+BC-FTIR1	9,0	Ambient+Dry				
	MB-TXH-064-B	**NCMB64**			BD-VNIR+BC-FTIR1	9,0	Ambient+Dry				
Murchison <63 um	MB-TXH-064-B	**S3MB64**	CM2	0-63	BD-VNIR	5.0	Ambient	Victoria, Australia		(C3)<63um, (C4)63-125um, (C2)<125um (C3 & C4 mix), dry-sieved.	
Murchison 63-125 um	MB-TXH-064-C	**C4MB64**	CM2	63-125	BD-VNIR	5,0	Ambient				
Murchison	MH-FPF-052-A	**CAMH52**	CM, Primitive, 2	0-90	BD-VNIR	5,0	Ambient			Fusion	Fanale, F.P. (University of Hawaii)
Murchison	MH-FPF-052-B	**CBMH52**	CM, Primitive, 2	0-90	BD-VNIR	5,0	Ambient				
Murchison	MH-FPF-052-C	**CCMH52**	CM, Primitive, 2	0-180	BD-VNIR	5,0	Ambient				
Murchison	MR-MJG-109	**CGP094**	CM2		DHC-VNIR	5,0	Ambient	Victoria, Australia	197	Fell Sept. 28, 1969	Gaffey, M.J. (University of North Dakota)
		CGP096			DHC-VNIR	5,0	Ambient				
Murray	MR-MJG-110	**CGP098**	CM2		DHC-VNIR	5,0	Ambient	Calloway County, Kentucky	188	Fell Sept. 20, 1950	

Table A-2. *cont.*

Sample Name	Sample ID	Spectrum ID	Type	Size	Spec Code	Res.	Atmosphere	Origin	Chem#	Text	measured by
Murray	MB-TXH-056	**C0MB56** **C1MB56** **NCMB56**	CM2	0-100	BD-VNIR BD-VNIR BD-VNIR+BC-FTIR1	1.0 5.0 9.0	Ambient Ambient Ambient+Dry	Murray Co. , Kentucky		M. Zolensky sample	Hiroi, T.X. (Brown University)
Meghei (Mighei)	MR-MJG-108	**CGP092**	CM2	0-75	DHC-VNIR	5,0	Ambient	Olviopol, Kherson, Ukraine	178	tvj, ps=<0.075mm Fell June 18, 1889	Gaffey, M.J. (University of North Dakota)
Nogoya	MR-MJG-111	**CGP100**	CM2		DHC-VNIR	5,0	Ambient	Entre Rios, Argentina	237	Fell June 30, 1879	
Nogoya	MB-TXH-062		CM2					Entre Rios, Argentina			Hiroi, T.X. (Brown University)
		NCMB62			BD-VNIR+BC-FTIR1	9.0	Ambient+Dry				
Nogoya <125 um	MB-TXH-062-A	**C2MB62**	CM2	0-125	BD-VNIR	5,0	Ambient			(C2) <125 um (mixture of C3 & C4), dry-sieved	
Nogoya <63 um	MB-TXH-062-B	**C3MB62**	CM2	0-63	BD-VNIR	5,0	Ambient				
Nogoya 63-125 um	MB-TXH-062-C	**C4MB62**	CM2	63-125	BD-VNIR	5,0	Ambient				
Cold Bokkeveld	MB-TXH-061	**C1MB61**	CM2	0-125	BD-VNIR	5,0	Ambient	Cape Province, RSA		M. Zolensky Sample	
		C2MB61			BD-VNIR	5,0	Ambient				
		C3MB61			BD-VNIR	5,0	Ambient				
		C4MB61			BD-VNIR	5,0	Ambient				

Table A-2. *cont.*

Sample Name	Sample ID	Spectrum ID	Type	Size	Spec Code	Res.	Atmosphere	Origin	Chem#	Text	measured by
Cold Bokkeveld	MR-MJG-107-P1	**CGP086**	CM2	0-75	DHC-VNIR	5,0	Ambient	Cape Province, South Africa		tvj, ps<0.075mm Fell Oct. 13, 1838	Gaffey, M.J. (University of North Dakota)
	MR-MJG-107-P2	**CGP088**	CM2	75-150	DHC-VNIR	5,0	Ambient			tvj, ps=0.15-0.50mm Fell Oct. 13, 1838	
		CGP142			DHC-VNIR	5,0	Ambient				
	MR-MJG-107-P3	**CGP090**		150-500	DHC-VNIR	5,0	Ambient		227	tvj, ps=150-500mm Fell Oct. 13, 1838	
Allende	MB-TXH-063	**NCMB63**	CV3		BD-VNIR+BC-FTIR1	9.0	Ambient+Dry	Chihuahua, Mexico			Hiroi, T.X. (Brown University)
Allende <125 um	MB-TXH-063-A	**C2MB63**	CV3	0-125	BD-VNIR	5,0	Ambient			(C2) <125 um (mixture of C3 & C4), dry-sieved	
Allende <63 um	MB-TXH-063-B	**C3MB63**	CV3	0-63	BD-VNIR	5,0	Ambient				
Allende 63-125 um	MB-TXH-063-C	**C4MB63**	CV3	63-125	BD-VNIR	5,0	Ambient				
Allende	MH-FPF-057-A	**CAMH57**	CV3	0-180	BD-VNIR	5,0	Ambient	Mexico		a- non-fusion crust fragment Allende crust	Fanale, F.P. (University of Hawaii)
Allende	MH-FPF-057-B	**CBMH57**	CV3	0-180	BD-VNIR	5,0	Ambient	Mexico		b- fusion crust fragment Allende crust	
Allende	MR-MJG-117	**CGP124**	CV3		DHC-VNIR	5,0	Ambient	Chihuahua, Mexico		Fell Feb. 8, 1969	Gaffey, M.J. (University of North Dakota)

Table A-2. *cont.*

Sample Name	Sample ID	Spectrum ID	Type	Size	Spec Code	Res.	Atmosphere	Origin	Chem#	Text	measured by
Vigarano	MB-TXH-059	**C2MB59**	CV3	0-100	BD-VNIR	5,0	Ambient	Ferrara, Italy		M. Zolensky Sample	Hiroi, T.X. (Brown University)
		NCMB59			BD-VNIR+BC-FTIR1	9,0	Ambient+Dry				
Kainsaz	MR-MJG-113	**CGP104**	CO3		DHC-VNIR	5,0	Ambient	Muslyumov, Tatar Republic, USSR	247	Fell Sep. 13, 1937	Gaffey, M.J. (University of North Dakota)
Lance	MR-MJG-114-P1	**CGP106**	CO3	150-500	DHC-VNIR	5,0	Ambient	Vendome, Loir-et-Cher, France	191	tvj, ps=0.15-0.50mm Fell July 23, 1872	
	MR-MJG-114-P2	**CGP108**		0-75	DHC-VNIR	5,0	Ambient			tvj, ps<0.075mm Fell July 23, 1872	
Ornans	MR-MJG-115	**CGP110**			DHC-VNIR	5,0	Ambient	Doubs, France	179	Fell July 11, 1868	
		CGP112			DHC-VNIR	5,0	Ambient				
		CGP114			DHC-VNIR	5,0	Ambient				

Table A- 3. *Spectrometers used in the Relab measurements.*

SpecCode	**Spectrometer**	**Measurement Mode**	**Affiliation**
BCF-FTIR1	Biconical Off-Axis FT-IR (Nicolet 740)	Reflectance	RELAB, Brown University
BCF-FTIR2	Biconical Off-Axis FT-IR (Thermo Nicolet Nexus	Reflectance	RELAB, Brown University
BC-FTIR1	Biconical FT-IR (Nicolet 740)	Reflectance	RELAB, Brown University
BC-FTIR2	Biconical FT-IR (Thermo Nicolet Nexus 870)	Reflectance	RELAB, Brown University
BD-VNIR	Bidirectional Visible-NIR	Reflectance	RELAB, Brown University
BD-VNIR+BCF-FTIR1	BD-VNIR & BCF-FTIR1 combined	Reflectance	RELAB, Brown University
BD-VNIR+BCF-FTIR2	BD-VNIR & BCF-FTIR2 combined	Reflectance	RELAB, Brown University
BD-VNIR+BC-FTIR1	BD-VNIR & BC-FTIR1 combined	Reflectance	RELAB, Brown University
BD-VNIR+BC-FTIR2	BD-VNIR & BC-FTIR2 combined	Reflectance	RELAB, Brown University
DHC-VNIR	Directional-Hemispherical Visible-NIR (Wavelength	Reflectance	J. B. Adams & M. J. Gaffey
DH-VNIR	Directional-Hemispherical Visible-NIR	Reflectance	J. B. Adams & M. J. Gaffey

Appendix B

Sample Description: chemical analysis meteorites

Table B-1. *Chemical analysis of the meteorites. The source of the analysis is stated in the table.*

Sample ID elements	Cold Bokkeveld	Murchison	Banten	Allende
SiO2	21.05	29.07	28.86	34.23
TiO2	0.28	0.13	0.12	0.15
Al2O3	17.26	2.15	2.19	3.27
Cr2O3	0.04	0.48	0.37	0.52
Fe2O3				
FeO	31.05	22.39	21.88	27.15
MnO	0.21	0.20	0.29	0.18
MgO	11.3	19.94	19.82	24.62
CaO	0.61	1.89	1.892	2.61
Na2O	0.28	0.24	0.61	0.45
K2O	0.03	0.04	0.07	0.03
P2O5	0.02	0.23	0.24	0.23
H2O+		8.95	8.51	<0.1
H20-		1.14	2.19	0
Fe(m)	0.13	0.13	0.14	0.17
Ni				0.36
Co				0.01
FeS		7.24	6.28	4.03
C		1.85	1.78	0.29
others		3.73	4.56	1.68
Fe(t)		22.13	21.14	23.85
NiO	0.06	1.78	1.66	
CoO		0.08	0.08	
SO3	0.59	0.09	2.27	
CO2		1.00	0.55	
Source	Schirmeyer et al. (1996)	Jarosewich (1971)	Jarosewich, (1990)	Clarke et al. (1971)

Table B- 2. *Chemical analysis of the meteorites taken from the Relab spectral library.*

Rec #	177	178	186	188	197	225
Sample ID	MR-MJG-105	MR-MJG-108	MR-MJG-063	MR-MJG-110	MR-MJG-032	MR-MJG-109
Mineral	BULK	BULK	BULK	BULK	BULK	BULK
%SiO2	10,55	13	39,78	13,4	16,4	23,4
%TiO2	0,04	0,05	0,12	0	0	0
%Al2O3	0,87	1,14	2,24	0,98	1,06	3,1
%Cr2O3	0,25	0,25	0,55	0,29	0,31	0,3
%Fe2O3	0	0	0	0	0	0
%FeO	18,28	21,2	14,78	23,8	29,2	34,1
%MnO	0,15	0,16	0,34	0,17	0,24	0,2
%MgO	9,54	11,73	24,65	11,9	13,9	15,1
%CaO	0,87	1,18	1,87	1,36	1,18	0,9
%Na2O	0,05	0,04	0,94	0,14	0,52	0
%K2O	0,06	0,04	0,12	0,03	0,08	0
%P2O5	0,12	0,13	0,26	0	0	0
Cu(ppm)	0	0	0	118	87	0
Ni(ppm)	0	0	1,16	0	0	0,08
Co(ppm)	500	600	700	460	930	0
Zn(ppm)	0	0	0	150	52	0
V(ppm)	0	0	0	0	0	0
Sr (ppm)						
Zr (ppm)						
Cr (ppm)						
LOI						
total						
Source				DM Shaw & RS Harmon, Meteor. 1975,10,p253	DM Shaw & RS Harmon, Meteor. 1975,10,p253 (factor analysis)	LH Fuchs,et al, Smith.Contrib.Earth Sci.,1973 (10)
Text	Orgueil Meteorite (C1) (Pure elments, not oxides)	Mighei Meteorite (C2M) (Pure elements, not oxides)	Tourinnes-la-Grosse Meteorite (L6) (Ni=%, not ppm)	Murray Meteorite (C2) (Pure elements, not oxides)	Pantar Meteorite (H5) (Pure elem's, not oxides)	Murchison Meteorite (C2M) (Matrix; NiO = 1.5%; Ni = 0.08%)

LOI: Loss of ignition

n.d.: not determined

ppm: parts per million

Table B-2. *Cont*

Rec #	179	191	227	237	247
Sample ID	MR-MJG-115	MR-MJG-114	MR-MJG-107	MR-MJG-111	MR-MJG-113
Mineral	BULK	BULK	BULK	BULK	BULK
%SiO2	15,6	33,95	12,24	27,18	34,86
%TiO2	0,11	0,1	0,06	0	0,13
%Al2O3	1,35	2,91	1,09	2,35	2,7
%Cr2O3	0,38	0,44	0	0,35	0,56
%Fe2O3	0	0	0	0	0
%FeO	25,83	22,84	19,49	20,28	32,88
%MnO	0,18	0,24	0,16	0,07	0,22
%MgO	14,66	23,74	10,95	19,05	24,17
%CaO	1,4	2,2	1,19	2,52	2,18
%Na2O	0,41	0,59	0	0,18	0,58
%K2O	0,14	0,05	0,05	0	0,05
%P2O5	0,15	0,34	0,09	0,15	0,27
Cu(ppm)	0	0	0	0	0
Ni(ppm)	0	0	0	0	1,88
Co(ppm)	1,36	1,36	0	0	0
Zn(ppm)	820	700	0	0	0
V(ppm)	0	0	0	0	0
Sr (ppm)	0	0			
Zr (ppm)					
Cr (ppm)					
LOI					
total					
Source			H Von Michaelis,et al, Earth Planet.Sci.Lett., 1969,5,p387	Geochimica et Cosmochimica Acta, 1956, p279	LH Ahrens, et al, Meteor. 1973,8,p133
Text			Cold Bokkeveld Meteorite (C2M) (Pure elements, not oxides)	Nogoya Meteorite (C2M)	Kainsaz Meteorite (C3O) (Ni = %NiO)

LOI: Loss of ignition	
n.d.: not determined	
ppm: parts per million	

Sample description: minerals

Table C- 1. *Sample description of the minerals measured at the DLR Berlin.*

Mineral	chem. Formular	Sample ID	Size [µm]	Origin	Source	additional information	chem. Analysis	image #
Brucite	$Mg(OH)_2$	MFN_MIN_ 1999_3785	0-25 25-45 45-90	Lancaster Co., Pennsylvannia, USA	Naturkundemuseum Berlin, Germany	Petrographical and Geological Collection, curator Mr. Schmitt; pulverized by Ines Büttner, DLR Berlin Adlershof	see chemical analysis section	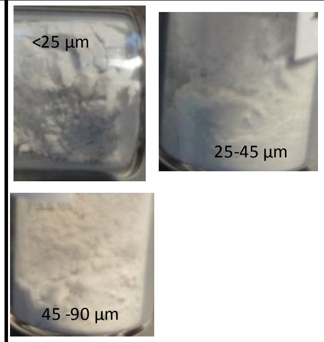
Cronstedtite	$Fe^{2+}{}_2Fe^{3+}(Si,Fe^{3+}O_5)(OH)_4$	MFN_MIN_ 2000_5070	<125 µm	Wheal Mandlin Mine, Cornwall, UK	Naturkundemuseum Berlin, Germany			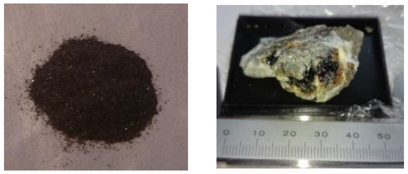
Montmorillonite	$(Na,Ca)_{0.33}(Al,Mg)_2(Si_4O_{10})(OH)_2 \cdot nH_2O$	Ikomont NNB90A	0-25 25-63 63-125	Crook County, Wyoming, USA	University of Missouri - Columbia, Source Clay Minerals Repository 101 Geological Sciences Bldg. Columbia, MO 65211 USA	pulverized by Ines Büttner, DLR Berlin Adlershof dry sieved	see chemical analysis section	

Table C-1. *cont.*

Mineral	chem. Formular	Sample ID	Size [µm]	Origin	Source	additional information	chem. Analysis	image #
Saponite	$Mg_3[(OH)_2\vert(Si,Al)_4O_{10}]x(Ca,Na)_x(H_2O)_y$		0-25	Cornwall, England	DLR, Berlin, Germany	pulverized by Ines Büttner, DLR Berlin Adlershof dry sieved		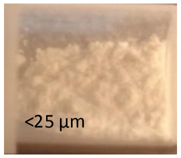 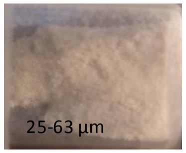
			25-63					
			63-125					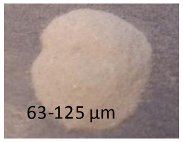
Buddingtonite	$(NH_4)AlSi_3O_8 \cdot 0.5\ H_2O$	MFN_MIN_ 1978_0379	whole rock	Menlo Park, California, USA	Naturkundemuseum Berlin, Germany	Petrographical and Geological Collection, curator Mr. Schmitt size: 4x3x3 cm		
Tochilinite	$6Fe0.9S \bullet 5(Mg,Fe{+}{+})(OH)_2$			synthetic, produced by L. Moroz	Moroz et al. (1997)	major matrix components of CM carbonaceous chondrites (Zolensky et al., 1993); similar to brucite, intergrown with phyllosilicates (Buseck und Hua, 1993; Brearley and Jones, 1998)		  
Anthraxolite		199/201			Moroz et al., 1998	medium anthraxolite	see chemical analysis section	no image
		3358						no image
Kerite		k5				high kerite		no image
		8450						no image

Table C- 2. *Sample description of the minerals taken from the Relab spectral library.*

Sample Name	Sample ID	Spectrum ID	Type	Size [µm]	Spec Code	Res.	Atmosphere	Origin	Chem#	Text	measured by
Cronstedtite CRO101	CR-EAC-021	**LACR21**	Silicate (Phyllo)	0-45	BD-VNIR+BC-FTIR1	9.0	Ambient+Dry	411 level, Llallagua, Bolivia	✖	Obtained from Smithsonian Institution (#193910) Dry-sieved.	Cloutis, E.A. (University of Winnipeg)
Montmorillonite	JB-CMP-001	**492F01**	Silicate (Phyllo)	0-125	BD-VNIR+BC-FTIR1	8.0	Ambient+Dry	Relab D2	427	100% of cation exchange capacity exchanged with Fe.	Pieters, C.M. (Brown University)
	JB-CMP-002	**492F02**			BD-VNIR+BC-FTIR1	8.0	Ambient+Dry			200% CEC Fe-exchanged	
	JB-CMP-004	**492F04**			BD-VNIR+BC-FTIR1	8.0	Ambient+Dry			600% CEC Fe-exchanged	
	JB-CMP-006	**492F06**			BD-VNIR+BC-FTIR1	8.0	Ambient+Dry			100% Ca Exchanged	
	CY-PLH-025	**C1CY25**	Smectite, Ca-Montmorillonite	0-500	BD-VNIR	5.0	Ambient	Gonzales, TX		Clay Minerals Society ST x-1 IGCP4, SMC403	Hauff, P.L. (spectral research)
	CY-PLH-026	**C1CY26**	Smectite Na-Montmorillonite		BD-VNIR	5.0	Ambient	Crook Co., WY		Clay Minerals Society SWY-1 IGCP5, SMC402	
Calcite 45-125	PC-CMP-050	**C2PC50**	Carbonate	45-125	BD-VNIR	4.0	Ambient	Cherokee Co. Kansas		From Buck Sharpton's Wards collection of minerals	Pieters, C.M. (Brown University)

Table C-2. *cont.*

Sample Name	Sample ID	Spectrum ID	Type	Size [µm]	Spec Code	Res.	Atmosphere	Origin	Chem#	Text	measured by
Calcite CRB109 <45 um	CB-EAC-009-A	**LACB09A**	Carbonate	0-45	BD-VNIR+BC-FTIR1	9,0	Ambient+Dry	Univ. of Winnipeg	767	University of Alberta GEOL330 laboratory collection	Cloutis, E.A. (University of Winnipeg)
Calcite CRB109 45-90 um	CB-EAC-009-B	**LACB09B**	Carbonate	45-90	BD-VNIR+BC-FTIR1	9,0	Ambient+Dry	Univ. of Winnipeg		University of Alberta GEOL330 laboratory collection	
Magnesite MGC 25-45 um	BE-JFM-223	**BKR1BE223**	Carbonate	25-45	BD-VNIR+BCF-FTIR2	4.0	Ambient+Dry			For modeling of mixtures (PGG, Active missions)	Mustard, J.F. (Brown University)
Magnesite MGC 45-63 um	BE-JFM-224	**BKR1BE224**	Carbonate	45-63	BD-VNIR+BCF-FTIR2	4.0	Ambient+Dry			For modeling of mixtures (PGG, Active missions)	
Magnesite MGC 63-75 um	BE-JFM-225	**BKR1BE225**	Carbonate	63-75	BD-VNIR+BCF-FTIR2	4.0	Ambient+Dry			For modeling of mixtures (PGG, Active missions)	
Magnesite MGC 75-106 um	BE-JFM-226	**BIR1BE226**	Carbonate	75-106	BCF-FTIR2	4,0	Dry air			For modeling of mixtures (PGG, Active missions)	
		BKR1BE226	Carbonate		BD-VNIR+BCF-FTIR2	4,0	Ambient+Dry				
		C1BE226	Carbonate		BD-VNIR	5,0	Ambient				
Magnesite MGC 106-125 um	BE-JFM-227	**BKR1BE227**	Carbonate	106-125	BD-VNIR+BCF-FTIR2	4,0	Ambient+Dry			For modeling of mixtures (PGG, Active missions)	

Table C-2. *cont.*

Sample Name	Sample ID	Spectrum ID	Type	Size [μm]	Spec Code	Res.	Atmosphere	Origin	Chem#	Text	measured by
Magnesite CRB114	CB-EAC-014-A	**BKR1CB014A**	Carbonate	0-45	BD-VNIR+BCF-FTIR2	4.0	Ambient+Dry	Currant Creek, Nevada	769	Particulate Ground Dry-Sieved	Cloutis, E.A. (University of Winnipeg)
Magnesite CRB106 <45 um	CB-EAC-006-A	**LACB06A**	Carbonate	0-45	BD-VNIR+BC-FTIR1	9.0	Ambient+Dry	Snarum, Norway			
Magnesite CRB106 45-90 um	CB-EAC-006-B	**LACB06B**	Carbonate	45-90	BD-VNIR+BC-FTIR1	9,0	Ambient+Dry	Snarum, Norway			
Dolomite	CC-JFM-005-B	**F1CC05B**	Carbonate	25-75	BD-VNIR+BC-FTIR1	9,0	Ambient+Dry	Franklin, Sussex Co., New Jersey			Mustard, J.F. (Brown University)
Dolomite CRB103 <45 um	CB-EAC-003-A	**KACB03A**	Carbonate	0-45	BC-FTIR1	9.0	Dry Air	Bamle, Telemark, Norway	✖		Cloutis, E.A. (University of Winnipeg)
		LACB03A			BD-VNIR+BC-FTIR1	9.0	Ambient+Dry				
Dolomite CRB103 45-90 um	CB-EAC-003-B	**KACB03B**		45-90	BC-FTIR1	9,0	Dry air	Bamle, Telemark, Norway			
		LACB03B			BD-VNIR+BC-FTIR1	9,0	Ambient+Dry				
Siderite CRB108 <45 um	CB-EAC-008-A	**KACB08A**		0-45	BC-FTIR1	9,0	Dry air	Frederikshaab District, W. Greenland	✖	Ivigtut, in the Arksuk Fiord, Frederikshaab District, West Greenland.	
		LACB08A			BD-VNIR+BC-FTIR1	9,0	Ambient+Dry				
Siderite CRB108 45-90 um	CB-EAC-008-B	**KACB08B**		45-90	BC-FTIR1	9.0	Dry air	Frederikshaab District, W. Greenland		Ivigtut, in the Arksuk Fiord, Frederikshaab District, West Greenland.	
		LACB08B			BD-VNIR+BC-FTIR1	9.0	Ambient+Dry				

Table C-2. *cont.*

Sample Name	Sample ID	Spectrum ID	Type	Size [µm]	Spec Code	Res.	Atmosphere	Origin	Chem#	Text	measured by
Saponite SAP101	SA-EAC-057	**LASA57**	Silicate (Phyllo)	0-45	BD-VNIR+BC-FTIR1	9.0	Ambient+Dry	Menzenberg, Rheinish Prussia, Germany	✖	Obtained from Smithsonian Institution (#C3810) Dry-sieved.	Cloutis, E.A. (University of Winnipeg)
Saponite SAP102	SA-EAC-058	**LASA58**			BD-VNIR+BC-FTIR1	9.0	Ambient+Dry	Ballaray, CA	✖	Obtained from Smithsonian Institution (#170279) Dry-seived.	
Saponite SAP103	SA-EAC-059	**LASA59**		0-45	BD-VNIR+BC-FTIR1	9.0	Ambient+Dry	Griffith Park, Los Angeles Co., CA	✖	Obtained from Mineral Unlimited. Dry-sieved.	
Tochilinite	TO-TXH-001	**NCTO01**		0-125	BD-VNIR+BC-FTIR1	9.0	Ambient+Dry	Jeffrey Mine, Asbestos, Quebec		From Roger Burns through Tom Burbine	Hiroi, T.X. (Brown University)
Magnetite	JA-JLB-307	**CJA307**	Oxide	0-125	BD-VNIR	5.0	Ambient			Fairly pure from spectra	Bishop, J.L. (SETI Institute)
		CJB258	Oxide	0-125	BD-VNIR	5.0	Ambient	Michigan		Magnetite Fe2+Fe3+O4; R. Mancinelli Lab	
MAG101	SC-EAC-025	**LASC25**	Oxide	45-90	BD-VNIR+BC-FTIR1	9.0	Ambient+Dry	Sao Paulo State, Brazil	31		Cloutis, E.A. (University of Winnipeg)
Magnetite 75		**LAPM12A**	Oxide	45-75	BD-VNIR+BC-FTIR1	9.0	Ambient+Dry	Ishpeming, Mich		Magnetite for mixing experiment	
Magnetite MAG103	MG-EAC-003	**LAMG03**	Oxide	0-45	BD-VNIR+BC-FTIR1	9.0	Ambient+Dry	Langesundfjord, Norway	✖	Acquired from Minerals Unlimited.	

Table C-2. *cont.*

Sample Name	Sample ID	Spectrum ID	Type	Size [µm]	Spec Code	Res.	Atmosphere	Origin	Chem#	Text	measured by
Pyrite 101	SC-EAC-077	**C1SC77**	Sulfide	0-45	BD-VNIR	5.0	Ambient	Alberta, Canada		Sample PRT101, Pyrite	Cloutis, E.A. (University of Winnipeg)
Pyrite	SH-SJG-052-A	**CASH52**	Sulfide	45-74	BD-VNIR	5.0	Ambient	RPI			Gaffey, S.J.
	SH-SJG-052-B	**CBSH52**		74-100	BD-VNIR	5.0	Ambient	RPI			
Troilite TRO201 45-90 um	EA-EAC-001-A	**LAEA01A**		45-90	BD-VNIR+BC-FTIR1	9.0	Ambient+Dry	Canyon Diablo, Coconico Co., AZ	✖	Troilite separated from Canyon Diablo iron meteorite.	Cloutis, E.A. (University of Winnipeg)
Troilite TRO201 <45 um	EA-EAC-001-B	**LAEA01B**		0-45	BD-VNIR+BC-FTIR1	9.0	Ambient+Dry	Canyon Diablo, Coconico Co., AZ		Troilite separated from Canyon Diablo iron meteorite.	
Troilite TRO202 45-90 um	EA-EAC-002-A	**LAEA02A**		45-90	BD-VNIR+BC-FTIR1	9.0	Ambient+Dry	ESPI Corp.			
Troilite TRO202 <45 um	EA-EAC-002-B	**LAEA02B**		0-45	BD-VNIR+BC-FTIR1	9.0	Ambient+Dry	ESPI Corp.			
Kerite, 5	MS-CMP-018	**CAMS18**	Organic	0-100	BD-VNIR	5	Ambient	USSR			Pieters, C.M. (Brown University)
		N1MS18	Organic		BD-VNIR+BC-FTIR1	10	Ambient+Dry				
Kerite, 6	MS-CMP-019-A	**CAMS19**	Organic	0-100	BD-VNIR	5	Ambient	USSR			
Kerite, 11	MS-CMP-020-A	**CAMS20**	Organic	0-100	BD-VNIR	5	Ambient	USSR			
Kerite, 11	MS-CMP-020-B	**CBMS20**	Organic	100-200	BD-VNIR	5	Ambient	USSR			
Kerite, 12	MS-CMP-021-A	**CAMS21**	Organic	0-100	BD-VNIR	5	Ambient	USSR			
Kerite, 12	MS-CMP-021-B	**CBMS21**	Organic	100-200	BD-VNIR	5	Ambient	USSR			
Kerite, 13	MS-CMP-022	**CAMS22**	Organic	0-100	BD-VNIR	5	Ambient	USSR			
Kerite, 14	MS-CMP-023	**CAMS23**	Organic	0-100	BD-VNIR	5	Ambient	USSR			
		N1MS23	Organic		BD-VNIR+BC-FTIR1	10	Ambient+Dry				

Table C-2. *cont.*

Sample Name	Sample ID	Spectrum ID	Type	Size [µm]	Spec Code	Res.	Atmosphere	Origin	Chem#	Text	measured by
Kerite, 15	MS-CMP-024	**CAMS24**	Organic	0-100	BD-VNIR	5	Ambient	USSR			Pieters, C.M. (Brown University)
Kerite, 16	MS-CMP-025	**CAMS25**	Organic	0-100	BD-VNIR	5	Ambient	USSR			
Kerite, 19	MS-CMP-028	**CAMS28**	Organic	0-100	BD-VNIR	5	Ambient	USSR			
Kerite, 20	MS-CMP-029	**CAMS29**	Organic	0-100	BD-VNIR	5	Ambient	USSR			
Kerite	MS-CMP-010-F	**CFMS10**	Organic	0-200	BD-VNIR	5	Ambient	USSR			
Asphaltite, 17	MS-CMP-026	**CAMS26**	Organic	0-100	BD-VNIR	5	Ambient	USSR			
Asphaltite, 18	MS-CMP-027	**CAMS27**	Organic	0-100	BD-VNIR	5	Ambient	USSR			
Asphaltite, 21	MS-CMP-030	**CAMS30**	Organic	0-100	BD-VNIR	5	Ambient	USSR			
Anthraxolite	MS-CMP-006	**CCMS06**	Organic	0-200	BD-VNIR	5	Ambient	USSR		Highly Graphitic Coal	
	MS-CMP-011-F	**CFMS11**	Organic	0-200	BD-VNIR	5	Ambient	USSR		Graphitic Coal	

Table C- 3. *Sample description of the minerals taken from ASTER spectral library.*

Sample Name	formula	sample ID	grain size	spectra	Measurement	mineral type	collection locality	chem. Analysis	source	text
water frost	H_2O	FROST.SNW	10 µm		Directional (10°) Hemispherical Reflectance	frost			Collected at John Hopkins University IR Spectroscopy Lab	The spectrum from 0.3 to 2.08 micrometers was modeled, while that from 2.08-14 µm was measured
water ice	H_2O	ICE.DAT	solid		Directional (10°) Hemispherical Reflectance	ice				

Table C- 4. *Sample description of the minerals taken from USGS spectral library.*

Sample Name	formula	sample ID	grain size	spectra	mineral type	collection locality	chem. Analysis	source	text	image
Magnetite	$Fe^{+2}Fe^{+3}{}_2O_4$	HS78	74-250 µm, dry sieved	splib06a r 13246	Oxide (Spinel group)	Farmington County, Colorado		Hunt, G.R., J.W. Salisbury, and C.J. Lenhoff, 1971, Visible and near-infrared spectra of minerals and rocks: III. Oxides and hydroxides. Modern Geology, v. 2, p. 195-205.	Forms series with Gaspeite and with Siderite.	
		HS195		splib06a r 13178		Ishpeming, Michigan		Hunt, G.R., J.W. Salisbury, and C.J. Lenhoff, 1971, Visible and near-infrared spectra of minerals and rocks: III. Oxides and hydroxides. Modern Geology, v. 2, p. 195-205.	Forms a series with Magnesioferrite and with Jacobsite	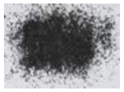
Buddingtonite	$(NH_4)AlSi_3O_8{\bullet}\frac{1}{2}H_2$ 0	GDS5 (D-206)	50 µm	splib06a r 3924	tectosilicate (feldspar group)	Sulphur Bank, California	Quartz Buddingtonite no alunite	Konnert, Judith and Marta Flohr, 1992, unpublished data, USGS Reston, VA	weak bands at 1.4 and 1.55 µm. The 1.55 might be due to alunite. If so, the buddingtonite feature is more than 10 times stronger, so the buddingtonite 2.1-µm feature is probably spectrally pure. Similar arguments for the 1.4 band. If these features are due to buddingtonite itself, then it is even more spectrally pure. Roger N. Clark	

Table C-4. *cont.*

Sample Name	formula	sample ID	grain size	spectra	mineral type	collection locality	chem. Analysis	source		image
Buddingtonite	$(NH_4)AlSi_3O_8 \bullet \frac{1}{2}H_2 0$	NHB2301	8 µm	splib06a r 3935	tectosilicate (feldspar group)	Sharon Heights #2, San Mateo, CA		Kruse, F.A. and P.L. Hauff, eds., 1992, The IGCP-264 Spectral Properties Database. IUGS/UNESCO, Special Publication, 211p., (in press)		no image
Brucite	Mg(OH)2	HS247	74-250 µm	splib06a r 3867	Hydroxide	Lodi, Nevada	Brucite plus medium amount dolomite plus small amount of other. (Norma Vergo)	Hunt, G.R., J.W. Salisbury, and C.J. Lenhoff, 1971, Visible and near-infrared spectra of minerals and rocks: III. Oxides and hydroxides. Modern Geology, vol. 2, pp 195-205.		
Cronstedtite	$Fe_2^{+2}Fe^{+3}(Si,Fe^{+3}) O_5(OH)_4$	M3542		splib06a r 6528		Cornwall, England			occurs with quartz and may contain as much as 5% quartz	no image
Pyrite	FeS	S142-1		splib06a r 18605		Basal Shawangunk Formation, US Highway 84, Port Jervis S. Quad, NY	26-34	Friedman, Jules D., Mutschler, Felix E., Zartman, Robert E., Briggs, Paul H., Swayze, Gregg A., Theisen, Arnold F., 1989, Shawangunk Ore District, New York: Geochemical and Spectral Data, U.S. Geological Survey Open File Report 89-193.	Forms series with Cattierite (CoS_2). Dimorphous with Marcasite. Field sample from a study done on the Shawangunk Region of New York.	no image
		GDS483	30-60 µm	splib06a r 18655		Armejun, Spain	Major pyrite with minor szomolnokite and minor rhomboclase		Forms series with Cattierite (CoS_2). Dimorphous with Marcasite	no image
Calcite	$CaCO_3$	WS272	410 µm	splib06a r 4159 splib06a r 4172	Carbonate	Tunguska, Siberia, USSR		Clark, R.N., T.V.V. King, M. Klejwa, G. Swayze, and N. Vergo, 1990, High spectral resolution reflectance spectroscopy of minerals: J. Geophys Res. 12653-12680	Forms series with Rhodochrosite. Trimorphous with Aragonite and Vaterite	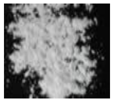

Appendix D

Sample description: chemical analysis minerals

Table D- 1. *Chemical analysis of the minerals taken from Relab spectral database.*

Rec #					
Sample ID	CB-EAC-003	CB-EAC-008	SA-EAC-057	SA-EAC-058	SA-EAC-059
Mineral		Saponite	Saponite	Saponite	
%SiO2	0.02	0.00	62.89	56.31	
%TiO2	0.02	0.03	0.90	0.72	1.07
%Al2O3	0.00	0.08	18.72	5.14	16.17
%Cr2O3					
%Fe2O3	n.d.	55.08	7.29	0.42	
%FeO	n.d.	35.67	0.39	0.54	
%MnO	0.14	3.83	0.04	0.03	0.29
%MgO	32.42	0.76	1.85	30.86	7.82
%CaO	60.19	0.07	2.30	2.18	8.68
%Na2O	0.16	0.66	2.12	2.87	2.84
%K2O	0.00	0.01	2.69	0.41	0.39
%P2O5	0.02	0.03	0.16	0.13	0.13
Cu(ppm)		n.d.			
Ni(ppm)					
Co(ppm)					
Zn(ppm)					
V(ppm)	20	45	117	50	204
Sr (ppm)	144	25	386	70	299
Zr (ppm)	5	5	580	316	104
Cr (ppm)	<2	<2	52	32	204
LOI	46.66	32.63	12.27	14.36	6.16
total	99.79	100.19	99.43	99.61	99.83
Source	Cloutis et al. 2011a	Cloutis et al. (2011a)	Cloutis et al. (2011a)	Cloutis et al. (2011a)	Cloutis et al. (2011a)
Text					

LOI: Loss of ignition
n.d.: not determined
ppm: parts per million

Table D-1. *Cont.*

Rec#		**Rec #**		769	427	767
Sample ID	EA-EAC-001	**Sample ID**	MG-EAC-003	CB-EAC-014-A	JB-CMP-001	CB-EAC-009-A
		Mineral	Magnetite	Magnesite	Mon	CAL
Fe wt%	61.50	**%SiO2**	0.00	31.21	57.73	0.11
Ni	0.03	**%TiO2**	7.28	0.00	0.10	0
Ni	0.01	**%Al2O3**	0.43	0.00	18.10	0.01
Na2O	37.71	**%Cr2O3**			0.0	0
S	0.00	**%Fe2O3**	60.38	0.00	5.20	0
V	0.02	**%FeO**	28.80	0.00	0.00	0
Co	0.00	**%MnO**	2.00	0.01	0.01	0.01
P	0.32	**%MgO**	<0.01	53.79	2.12	1.41
Cr	0.00	**%CaO**	0.00	14.63	0.32	98.04
Mg	0.00	**%Na2O**	0.00	0.02	1.71	0.41
Mn	0.02	**%K2O**	n.d.	0.00	0.28	0
Al2O3	0.02	**%P2O5**	n.d.	0.04	0.01	0.02
Zn	0.08	**Cu(ppm)**	n.d.	n.d.	0.0	0
V(ppm)		**Ni(ppm)**			0.0	0
Sr (ppm)		**Co(ppm)**			0.0	0
Zr (ppm)		**Zn(ppm)**				0
Cr (ppm)		**V(ppm)**	n.d.	10	0.0	0
LOI		**Sr (ppm)**	n.d.	327		
total	99.69	**Zr (ppm)**	n.d.	20		
		Cr (ppm)	n.d.	12		
		LOI	n.d.	34.57	13.21	
		total	99.37	99.70		
	Cloutis et al. 2011a	**Source**	Cloutis et al. 2011a	Cloutis et al. 2011a		Stan Mertzman- Franklin and Marshall College
		Text				

LOI: Loss of ignition

n.d.: not determined

ppm: parts per million

Table D- 2. *Chemical analysis of the minerals taken from USGS spectral library.*

Rec #	26-34
Sample ID	142-1 (USGS)
Mineral	Pyrite
Al%	0.89
Ca%	0.02
Fe%	35
K%	0.37
Mg%	0.06
Na%	0.03
P%	<0.005
Ti%	0.37
Mn%	9
Ag%	6
As ppm	480
Au ppm	<8
Ba ppm	17
Co(ppm)	<1
Bi ppm	<10
Cd ppm	<2
Ce ppm	29
Co ppm	150
Cr ppm	13
Cu ppm	800
Eu ppm	<2
Ga ppm	<4
Ho ppm	<4
La ppm	12
Li ppm	5
Mo ppm	22
Nb ppm	29
Nd ppm	14
Ni ppm	260
Pb ppm	630
Sc ppm	2
Sn ppm	340
Sr ppm	10
Ta ppm	<40
Th ppm	8
U pm	<100
V ppm	10
Y ppm	5
Yb ppm	1
Zn ppm	68

Table D- 3. *Chemical analysis of the minerals measured at the DLR.*

Sample ID / elements	199/201	3358	8450
f a.n.m.r.	0.69	0.66	0.50
C	85.9	92.8	86.5
H	2.4	2.25	8.3
N	2.2	0.76	2.0
S	1.2	0.15	1.4
O	5.8	1.9	1.8
sum	97.5	97.9	100
H/C (at.)	0.34	0.29	1.15
O/C (at.)	0.051	0.015	0.016
C/C+H+N+S+O) (at.)	0.71	0.76	0.46
d002 (Å)	3.43	3.41	3.45
Lc (Å)	15.52	17.88	17.12
SiO2			
TiO2			
Al2O3			
Fe2O3			
FeO			
Mn			
MgO			
CaO			
Na2O			
K2O			
F			
P2O5			
CO2			

Appendix E

Analytical Data Meteorites and Minerals

Table E- 1. *Determined values of the meteorites for the wavelength of slope change, the spectral slopes in the VIS and NIR (slope 1 and 2), the wavelength of slope 1 and 2 and the mean values of the slope change.*

meteorite	spectrum ID	slope1 (ΔR_1)	slope 2 (ΔR_2)	λ_{SC}	wavelength range ΔR_1	wavelength range ΔR_2	λ_{SCmean}
CV Vigarano	c2mb59	0,1513	0,000395	0,525	0,3-0,525	0,525-1,84	0,5275
	ncmb59	0,1479	0,00069	0,53	0,3-0,53	0,53-0,795	
	DLR	0,0357	0,0154	0,82	0,45-0,82	0,82-1,8	
CV Allende	c3mb63	0,2764	0,0075	0,41	0,305-0,365	0,65-1,615	0,423
	cbmh57	0,2021	0,004	0,435	0,3-0,375	0,74-1,545	
	c2mb63	0,203	0,007	0,439	0,3-0,39	0,69-1,59	
	camh57	0,1885	0,005	0,442	0,3-0,395	0,645-1,54	
	cgp0124	0,2135	0,0066	0,43	0,351-0,381	0,755-1,547	
	ncmb63	0,3789	0,0073	0,385	0,3-0,345	0,65-1,645	
	c4mb63	0,2316	-0,003	0,42	0,3-0,39	0,65-1,695	
	DLR	0,0189	-0,0066	0,52	0,45-0,52	0,52-1,6	
CI Orgueil	ncmb57	0,1186	0,0139	0,535	0,3-0,45	0,86-1,255	0,532857143
	mgp082	0,1281	0,0024	0,45	0,405-0,44	0,735-1,335	
	mgp080	0,1108	0,0023	0,56	0,365-0,445	0,73-1,33	
	cgp082	0,1434	0,0025	0,535	0,406-0,446	0,744-1,347	
	cgp080	0,1078	0,0023	0,6	0,366-0,446	0,739-1,347	
	mgp078	0,1465	0,0013	0,5	0,35-0,45	0,74-1,19	
	cgp078	0,1403	0,0118	0,55	0,351-0,446	0,75-1,121	
CI Ivuna	ncmb60	0,1165	0,0069	0,61	0,315-0,61	0,61-1,705	0,553333333
	c3mb60	0,1254	0,000662	0,52	0,315-0,52	0,52-1,79	
	c4mb60	0,1002	-0,0076	0,53	0,32-0,53	0,53-1,875	
CI Alais	cgp084	0,1355	0,0258	0,525	0,361-0,446	0,587-1,692	0,525
	mgp084	0,1344	0,0261	0,525	0,355-0,445	0,585-1,615	
CM Cold Bokkeveld	c1mb61	0,1583	0,0164	0,485	0,33-0,425	0,56-1,345	0,482777778
	c2mb61	0,1019	-0,0089	0,46	0,335-0,405	0,55-0,845	
	cgp090	0,1223	0,0032	0,49	0,356-0,446	0,547-1,467	
	cgp088	0,1266	0,0044	0,48	0,356-0,436	0,557-1,552	
	c3mb61	0,1419	0,0109	0,495	0,33-0,445	0,555-1,52	
	cgp086	0,1417	0,0139	0,495	0,351-0,456	0,567-1,352	
	cgp142	0,1188	0,004	0,49	0,356-0,441	0,542-1,552	
	c4mb61	0,178	-0,0052	0,45	0,305-0,395	0,57-1,625	
	DLR	0,0092	-0,0011	0,5	0,45-0,5	0,5-2,00	
CM Mighei	cgp092	0,1423	0,0124	0,48	0,351-0,446	0,562-1,402	0,48
CM Nogoya	ncmb62	0,1581	0,0078	0,485	0,32-0,485	0,485-1,55	0,49
	c2mb64	0,1373	0,0168	0,51	0,315-0,51	0,51-1,55	
	cgp100	0,1443	0,0119	0,495	0,351-0,495	0,495-1,697	
	c3mb62	0,15	0,0107	0,49	0,31-0,49	0,49-1,655	
	c4mb62	0,1395	-0,0051	0,47	0,305-0,47	0,47-1,465	
	DLR	0,0083	0,0217	0,63	0,45-0,63	0,63-1,1	
CM Murray	c1mb56	0,1623	0,018	0,52	0,32-0,52	0,52-1,575	0,513333333
	cgp098	0,1657	0,0144	0,48	0,351-0,48	0,48-1,457	
	c0mb56	0,1296	0,0073	0,54	0,5-0,54	0,54-0,88	

Table E-1. *Cont.*

meteorite	spectrum ID	slope1 (ΔR_1)	slope 2 (ΔR_2)	λ_{SC}	wavelength range ΔR_1	wavelength range ΔR_2	λ_{SCmean}
CM Murchison	camh52	0,105	0,0061	0,45	0,3-0,45	0,45-1,7	0,494545455
	cgp096	0,1516	0,0108	0,48	0,351-0,48	0,48-1,632	
	ncmb64	0,0903	0,0174	0,56	0,315-0,56	0,56-1,875	
	c0mb64	0,1533	0,0049	0,505	0,327-0,448	0,505-1,938	
	lcmb64	0,1358	0,0236	0,47	0,305-0,47	0,47-1,635	
	c3mb64	0,1369	0,0237	0,475	0,3-0,475	0,475-1,65	
	c2mb64	0,1511	0,0167	0,5	0,325-0,5	0,5-1,625	
	cgp094	0,1393	0,000422	0,48	0,48-0,426	0,48-1,687	
	cbmh52	0,1402	0,0094	0,51	0,51-0,45	0,51-1,665	
	c4mb64	0,1463	-0,000964	0,5	0,3-0,5	0,5-1,635	
	ccmh52	0,1184	0,0052	0,51	0,3-0,51	0,51-1,695	
CO Kainsaz	cgp104	0,058	-0,00012	0,61	0,431-0,61	0,61-1,362	0,6
	DLR	0,1269	0,0017	0,59	0,525-0,59	0,59-2,00	
Ceres	Rivkin et al. (2010)	0,0791	-0,0015	0,512	0,4358-0,4592	0,726-1,8	
CO Lance	cgp106	0,1039	-0,0059	0,585	0,361-0,572	0,707-1,652	0,6015
	cgp108	0,1023	0,0016	0,618	0,431-0,567	0,712-1,592	
CO Ornans	cgp110	0,1489	-0,0029	0,5	0,361-0,436	0,76-1,567	0,515
	cgp112	0,135	-0,0041	0,53	0,371-0,456	0,792-1,582	
	cgp114	0,138	-0,0037	0,515	0,36-0,446	0,771-1,572	
CI Y-82162_79	ccmb19	0,1083	-0,0048	0,422	0,31-0,406	0,535-1,345	0,4085
	ncmb19	0,1	-0,0016	0,433	0,33-0,38	0,625-1,525	
	c3mb19	0,084	0,0006635	0,411	0,31-0,385	0,535-1,62	
	c4mb19	0,1262	0,0004485	0,368	0,3-0,35	0,54-2,025	

Table E- 2. *Determined values of the meteorites for the wavelength of slope change, the spectral slopes in the VIS and NIR (slope 1 and 2), the wavelength of slope 1 and 2 and the mean values of the slope change.*

mineral	spectrum ID	slope1 (ΔR_1)	slope 2	SC	slope 1 µm	slope 2 µm	Sc_{mean}	slope 1 mean	slope 2 mean
Saponite							0,668333333	0,170766667	0,027110672
	lasa58	0,2431	-0,00049608	0,485	0,3-0,485	0,485-1,265			
	lasa59	0,1448	0,0827	0,81	0,345-0,81	0,81-1,65			
	lasa57	0,1244	-0,0008719	0,71	0,31-0,71	0,71-1,85			
Magnesite							0,491875	0,0676625	-0,000758899
	lacb06b	0,1277	0,0018	0,49	0,305-0,49	0,49-1,6669			
	lacb06a	0,1044	0,0016	0,49	0,3-0,49	0,49-1,65			
	bkr1cb014a	0,0542	-0,00047119	0,57	0,31-0,57	0,57-1,255			
	bkr1be223	0,0387	-0,0029	0,435	0,28-0,435	0,435-1,3663			
	bkr1be224	0,0414	-0,002	0,51	0,28-0,51	0,51-1,3574			
	bkr1be225	0,05	-0,0016	0,48	0,3-0,48	0,48-1,205			
	bkr1be226	0,06	-0,0014	0,48	0,3-0,48	0,48-1,305			
	bkr1be227	0,0649	-0,0011	0,48	0,305-0,48	0,48-1,315			
Dolomite							0,486666667	0,1612	0,001940217
	f1cc05	0,2045	0,0031	0,4	0,315-0,4	0,4-1,36			
	lacb03a	0,1256	0,0019	0,54	0,305-0,54	0,54-1,8934			
	lacb03b	0,1535	0,00082065	0,52	0,3-0,52	0,52-1,8113			
Siderite							0,7	0,11445	0,04915
	lacb08b	0,1144	0,0568	0,685	0,31-0,685	0,685-1,675			
	lac08a	0,1145	0,0415	0,715	0,315-0,715	0,715-1,819			

Table E.2. *Cont.*

mineral	spectrum ID	slope1 (ΔR_1)	slope 2 (ΔR_2)	λ_{SC}	wavelength range ΔR_1	wavelength range ΔR_2	λ_{SCmean}	mean slope1 (ΔR_{1mean})	mean slope 2 (ΔR_{2mean})
Calcite	USGS4159	0,0731	0,0033	0,3331	0,2586-0,3331	0,4933-0,894	0,430775	0,084025	0,002736185
	lacb09b	0,0685	0,006	0,48	0,305-0,41	0,57-1,185			
	c2pc50	0,1076	-0,00035526	0,45	0,32-0,404	0,844-1,664			
	lacb09a	0,0869	0,002	0,46	0,305-0,385	0,645-1,26			
Antraxolite							0,665	0,0419	0,02765
	ccms06	0,049	0,0375	0,5	0,37-0,5	0,5-1,245			
	cfms11	0,0348	0,0178	0,83	0,465-0,83	0,83-1,79			
Kerite							0,58	0,017886667	0,1801
	cams18	0,0381	0,0497	0,955	0,37-0,955	0,955-2,0			
	cams19	0,0258	0,0379	0,435	0,355-0,435	0,435-1,215	0,757		0,306333333
	cams20	0,0269	0,011	0,46	0,335-0,46	0,46-0,92	0,506111111		0,033242857
	cams21	0,0205	0,2538	0,61	0,355-0,61	0,61-1,875			
	cams22	0,0252	0,372	0,81	0,3-0,78	0,81-1,875			
	cams23	0,0132	0,3045	0,54	0,3-0,54	0,54-1,62			
	cams24	-0,0086	0,3414	0,535	0,3-0,535	0,535-1,515			
	cams25	0,0053	0,2972	0,53	0,31-0,53	0,53-1,38			
	cams28	-0,0185	0,2882	0,52	0,305-0,52	0,52-1,575			
	cams29	-0,0138	0,3102	0,535	0,305-0,535	0,535-1,53			
	cbms20	0,0505	0,0088	0,48	0,365-0,48	0,48-1,675			
	cbms21	0,0293	0,0208	0,53	0,35-0,53	0,53-1,875			
	cfms10	0,0242	0,0724	0,88	0,355-0,88	0,88-2,00			
	n1ms18	0,0358	0,0321	0,36	0,365-0,36	0,36-1,34			
	n1ms23	0,0144	0,3015	0,52	0,3-0,52	0,52-1,575			
Asphaltite							0,65	0,0248	0,3778
	cams26	-0,0112	0,5056	0,73	0,305-0,73	0,73-1,595			
	cams27	0,0524	0,2787	0,57	0,31-0,57	0,57-1,55			
	cams30	0,0332	0,3491	0,65	0,31-0,65	0,65-1,34			
Cronstedtite							0,563333333	0,113866667	0,052266667
	lacr21	0,1163	0,0467	0,57	0,38-0,57	0,57-2,00			
	USGS6528	0,1216	0,1071	0,565	0,2891-0,565	0,565-1,732			
	DLR	0,1037	0,003	0,555	0,4-0,555	0,555-1,9204			
Brucite									
	USGS3867	0,2683	-0,0045	0,467	0.3281-0.4248	0,6822-1,5915	0,5335	0,15005	0,002825
	0-25 µm	0,0318	0,0084	0,6	0.4-0.5272	0,6364-1,548			
	25-45 µm		0,003			0,7928-1,1651			
	45-90 µm		0,0044			0,7894-1,2325			
Buddingtonite							0,658333333	0,105166667	0,004333333
	DLR	0,0565	0,0018	0,67		0,8001-1,2068			
	USGS3924	0,1191	0,0068	0,71	0,2636-0,5133	0,828-1,3735			
	USGS3935	0,1399	0,0044	0,595	0,2536-0,4613	0,851-1,2485			
Montmorillonite							0,575666667	0,145383333	0,0145
	c1cy26	0,1754	0,0153	0,483	0,31-0,483	0,483-0,775			
	c1cy25	0,2027	0,0096	0,43	0,31-0,43	0,43-0,735			
	492f01	0,1697	0,0106	0,63	0,37-0,63	0,63-1,3409			
	492f04	0,0638	0,0228	0,65	0,39-0,65	0,65-1,3423			
	492f02	0,0927	0,0149	0,68	0,375-0,68	0,68-1,3556			
	492f06	0,168	0,0138	0,581	0,32-0,581	0,581-0,79			
Pyrite							0,56	0,087075	0,01725
	c1sc77	0,1143	0,0589	0,53	0,395-0,53	0,53-1,6			
	cbsh52	0,0555	-0,0081	0,635	0,315-0,635	0,635-1,695			
	cash52	0,0546	-0,011	0,625	0,32-0,625	0,625-1,615			
	USGS18605	0,1239	0,0292	0,45	0,2636-0,45	0,45-1,3785			

Table E.2. *Cont.*

mineral	spectrum ID	slope1 (ΔR_1)	slope 2 (ΔR_2)	λ_{SC}	wavelength range ΔR_1	wavelength range ΔR_2	λ_{SCmean}	mean slope1 (ΔR_{1mean})	mean slope 2 (ΔR_{2mean})
Troilite							0,685	0,0666	0,0197
	laea01a	0,0521	0,0445	0,79	0,35-0,79	0,79-1,73			
	laea01b	0,0567	0,0238	0,745	0,305-0,745	0,745-1,445			
	laea02a	0,0674	0,0061	0,585	0,365-0,585	0,585-1,865			
	laea02b	0,0902	0,0044	0,62	0,405-0,62	0,62-1,665			
Tochilinite							0,43		0,027838733
	ncto01	0,2916	-0,0009838	0,43	0,3-0,43	0,43-1,785			
	451/10		0,0489						
	451/25		0,0356						
	451/45								
Magnetite							0,3675	0,165983333	0,015266667
	cjb258	0,5059	0,0152	0,36	0,3-0,36	0,36-0,64			
	lasc25	0,1136	0,0163	0,36	0,3-0,36	0,36-0,63			
	lamg03	0,08	0,0169	0,37	0,31-0,37	0,37-0,655			
	cja307	0,0392	0,017	0,405	0,33-0,405	0,405-0,655			
	lapm12	0,2103	0,0363	0,36	0,3-0,36	0,36-0,54			
	13178	0,0469	-0,0101	0,35	0,2731-0,35	0,35-0,704			
Mineral Mixing	Mixing 1	1,7227	0,0017	0,495	0,395-0,495	0,56-1,615	0,495		
	Mixing 2	1,7481	0,0012	0,49	0,4-0,49	0,55-1,68	0,49		
	Mixing 3	2,143	-0,000507	0,49	0,395-0,49	0,53-2,00	0,49		
	Mixing 4	0,935	0,0016	0,49	0,4-0,49	0,58-1,625	0,49		
	Mixing 5	2,285	-0,0000525	0,495	0,385-0,495	0,55-1,655	0,495		
	Mixing 6	3,53	-0,0033	0,49	0,385-0,49	0,56-2,00	0,49		

Appendix F

Additional spectra used for analysis

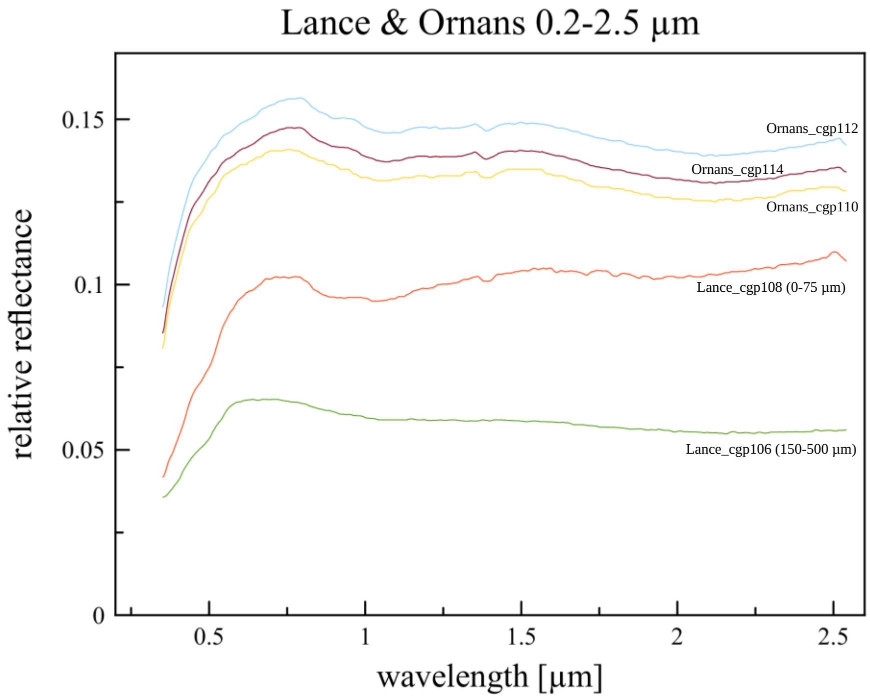

Figure F- 1. *Spectra of the CO chondrites Lance and Ornans (relative reflectance). Data was taken from Relab spectral library, for detailed sample description see appendix A.*

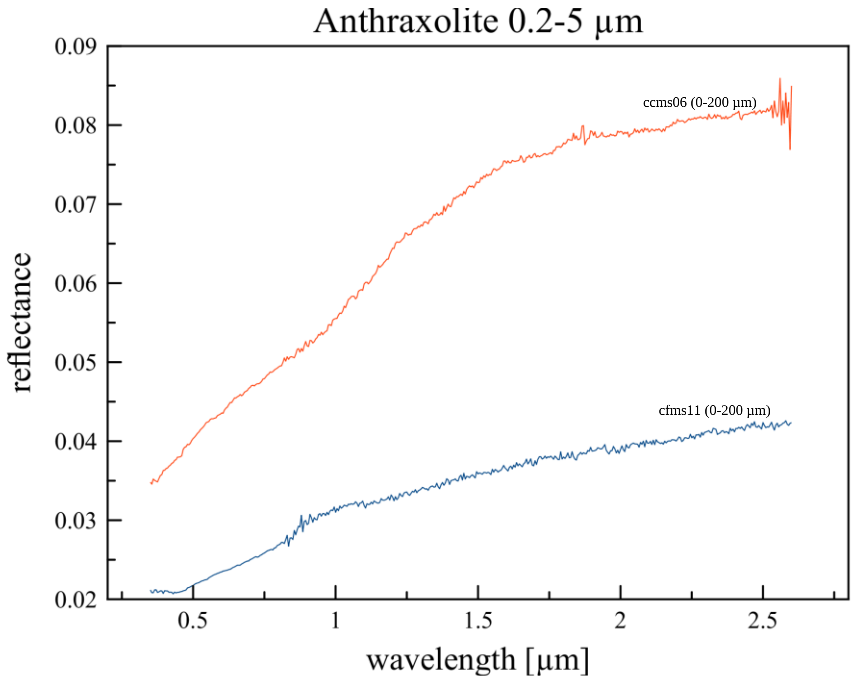

Figure F- 2. *Spectra of anthraxolite (relative reflectance). The data was taken from Relab spectral database. For sample description see appendix D.*

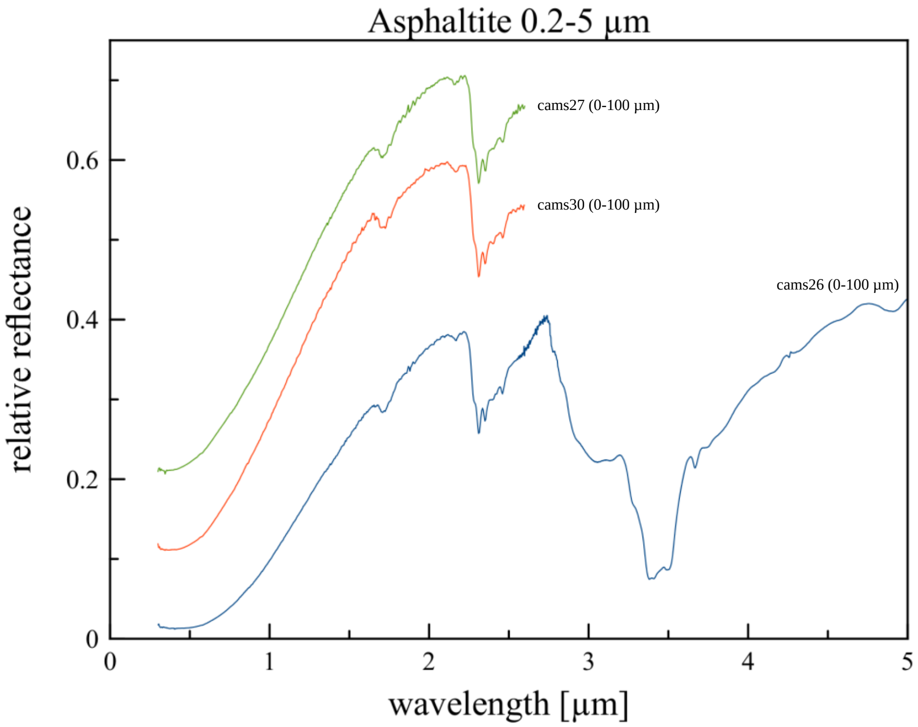

Figure F- 3. *Spectra of asphaltite (relative reflectance). The data was taken from Relab spectral database. The offset between the spectra is 0.1. For sample description see appendix D.*

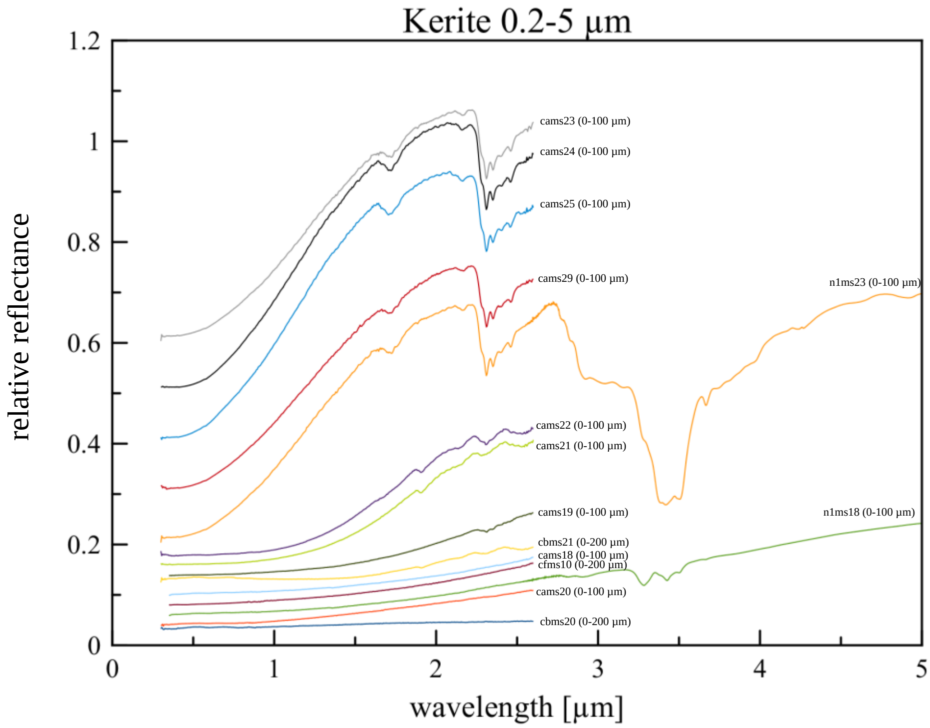

rela

Figure F- 4. *Spectra of kerite (relative reflectance). The data was taken from Relab spectral database. The offset between the spectra is 0.02. For sample description see appendix D.*

REFERENCES

Adams, J. B., & Filice, A. L. (1967). Spectral reflectance 0.4 to 2.0 microns of silicate rock powders. *Journal of Geophysical Research*, **72**(22), 5705-5715.

A'Hearn, M. F., & Feldman, P. D. (1992). Water vaporization on Ceres. *Icarus*, **98**(1), 54-60.

Ahrens, L. H., Willis, J. P., & Erlank, A. J. (1973). The chemical composition of Kainsaz and Efremovka. *Meteoritics*, **8**(2), 133-139.

Alexander, C. O. D., Fogel, M., Yabuta, H., & Cody, G. D. (2007). The origin and evolution of chondrites recorded in the elemental and isotopic compositions of their macromolecular organic matter. *Geochimica et Cosmochimica Acta*, **71**(17), 4380-4403.

Amthauer, G., & Rossmann, G.R. (1984). Mixed valence of iron minerals with cation clusters. *Physics and Chemistry of Minerals*, **11**(1), 37-51.

Anderson, J. D., Lau, E.L., Sjorgren, W.L., Schubert, G. & Moore, W.B. (1996). Gravitational constraints on the internal structure of Ganymede. *Nature*, **384**, 541–543.

Anderson, J. D.; Jacobson, R. A.; McElrath, T. P.; et al.; Schubert, G.; Thomas, P. C. (2001). "Shape, mean radius, gravity field and interior structure of Callisto". *Icarus,* **153**(1): 157–161. doi:10.1006/icar.2001.6664.

Arnold, G. (2014). Spektrale Fernerkundung der terrestrischen Planetenoberflächen von Merkur, Venus und Mars vom visuellen bis in den infraroten Wellenlängenbereich. Habilitation dissertation at the University of Potsdam, Germany, pp. 573.

Asteroids Dynamic Site, AstDys. “(1) Ceres-summary” http://hamilton.dm.unipi.it/astdys/index.php?pc=1.1.0&n=ceres Last updated: October 2011.

Barber, D.J. (1985). Phyllosilicates and other layer-structured materials in stony meteorites. *Clay Minerals* **20**, 414-454.

Barucci, M. A., Capria, M. T., Coradini, A., & Fulchignoni, M. (1987). *Icarus*, **72**, 304

Bell, J.F., Owensby, P.D., Hawke, B.R., & Gaffey, M.J. (1988). The 52-color asteroid survey: final results and interpretation. Lunar and Planetary Science Conference Vol. 19, p. 57.

Bell J.F., Davis, D.R., Hartman, W.K. & Gaffey, M.J. (1989). Asteroids: The big picture, in *Asteroids II*. Editors R.P. Binzel, T. Gehrels and M.S. Matthews, Univ. Arizona Press, Tucson, Arizona, US, pp. 921-945.

Bellamy, L. J. (1975). *The infra-red spectra of complex molecules*, Vol. 1, pp. 386-388, London: Chapman and Hall.

Bills, B. G., & Nimmo, F. (2011). Forced obliquities and moments of inertia of Ceres and Vesta. *Icarus*, **213**(2), 496-509. doi:http://dx.doi.org/10.1016/j.icarus.2010.09.002

Bishop, J.L., Pieters, C.M., Edwards, J.O., 1994. Infrared spectroscopic analyses on the nature of water in montmorillonite. *Clays and Clay Minerals*, **42**, 702–716.

Bland, P.A., Cressey, G., Menzies, O.N. (2004). Modal mineralogy of carbonaceous chondrites by X-ray diffraction and Mössbauer spectroscopy. *Meteoritics & Planetary Science*, **39**(1), 3-16.

Bland, M. T., Singer, K. N., & McKinnon, W. B. (2013) The surface topography of Ceres: Pre-dawn predictions for extensive viscous relaxation. LPI Contributions, 1719, Abstract #1655.

Bland, M. T. (2013). Predicted crater morphologies on Ceres: Probing internal structure and evolution. *Icarus*, **226**(1), 510-521. doi:http://dx.doi.org/10.1016/j.icarus.2013.05.037

Blewett, D. T., & Levy, C. L. (2013) Radiative-transfer model reflectance spectra of potential Ceres mineral assemblages. 44th Lunar and Planetary Science Conference, Abstract #1271.

Bobrovnikoff, N.T. (1929). The spectra of minor planets. *Lick Observatory Bulletin*, **407**, 18-27.

Bowell, E., Chapman, C.R., Gradie, J.C., Morrison, D. & Zellner, B. (1978). Taxonomy of asteroids. *Icarus*, **35**, 313-335.

Brearley, A.J. & Jones, R.H. (1998). Chondritic meteorites. *Reviews in Mineralogy and Geochemistry*, **36**, p. 3.1-3.398.

Brown, J. K. (1955). The infrared spectra of coals. *Journal of the Chemical Society*, 744-752. doi: 10.1039/JR9550000744.

Burbine, T. H., Binzel, R. P., Bus, S. J., & Clark, B. E. (2001). K asteroids and CO3/CV3 chondrites. *Meteoritics & Planetary Science*, **36**(2), 245-253.

Burns, R. G. (1981). Intervalence transitions in mixed-valence minerals of iron and titanium. *Annual Review of Earth and Planetary Sciences*, **9,** 345.

Burns, R. G. (1985). Electronic spectra of minerals, in *Chemical Bonding and Spectroscopy in Mineral Chemistry*. Springer Netherlands, pp. 63-101.

Burns, R. G. (1985a).Thermodynamic data from crystal field spectra. *Reviews in Mineralogy and Geochemistry*, **14,** 277-316.

Burns, R. G. (1993). Ultraviolet, visible, and near-infrared reflectance spectroscopy: Laboratory spectra of geologic materials, *in Remote Geochemical Analysis: Elemental and Mineralogical Composition*. Editors C. M. Pieters and P. A. J. Englert, Cambridge University Press, New York, NY, pp. 3-30.

Bus, S. J., & Binzel, R. P. (2002a). Phase II of the small main-belt asteroid spectroscopic survey: A feature-based taxonomy. *Icarus*, **158**(1), 146-177.

Bus, S. J., & Binzel, R. P. (2002b). Phase II of the small main-belt asteroid spectroscopic survey: The observations. *Icarus*, **158**(1), 106-145.

Bus, S. J., Vilas, F., & Barucci, M. A. (2002). Visible-wavelength spectroscopy of asteroids, in *Asteroids III*. The University of Arizona Space Science Series, Univ. of Arizona, Tucson, pp. 169-182.

Buseck, P. R., & Hua, X. (1993). Matrices of carbonaceous chondrite meteorites. *Annual Review of Earth and Planetary Sciences*, **21**, 255-305.

Capaccioni, F., Coradini, A., Filacchione, G., Erard, S., Arnold, G., Drossart, P., ... & Tiphene, D. (2015). The organic-rich surface of comet 67P/Churyumov-Gerasimenko as seen by VIRTIS/Rosetta. *Science*, **347(**6220), aaa0628.

Cariati, F., Erre, L., Micera, G., Piu, P., and Gessa, C. (1983). Water molecules and hydroxyl groups in montmorillonites as studied by near-infrared spectroscopy. *Clays and Minerals,* Vol. **29**(2), 157-159.

Carry, B., Dumas, C., Fulchignoni, M., Merline, W. J., Berthier, J., Hestroffer, D., . . . Tamblyn, P. (2008). Near-infrared mapping and physical properties of the dwarf-planet Ceres. *Astronomy and Astrophysics,* **478**(1), 235-244. doi:10.1051/0004-6361:20078166

Carry, B., Vernazza, P., Dumas, C., Merline, W. J., Mousis, O., Rousselot, P., . . . Zucconi, J. M. (2012). The remarkable surface homogeneity of the dawn mission target (1) Ceres. *Icarus,* **217**(1), 20-26. doi:http://dx.doi.org/10.1016/j.icarus.2011.10.015

Castillo-Rogez, J. C., & McCord, T. B. (2010). Ceres' evolution and present state constrained by shape data. *Icarus,* **205**(2), 443-459. doi:10.1016/j.icarus.2009.04.008

Castillo-Rogez, J. C. (2011). Ceres -neither a porous nor salty ball. *Icarus,* **215**(2), 599-602.

Castillo-Rogez, J. C., & McCord, T. B. (2010). Ceres' evolution and present state constrained by shape data. *Icarus,* **205**(2), 443-459. doi:http://dx.doi.org/10.1016/j.icarus.2009.04.008

Chamberlain, M. A., Sykes, M. V., & Esquerdo, G. A. (2007). Ceres lightcurve analysis-□”Period determination. *Icarus,* **188**(2), 451-456. doi:10.1016/j.icarus.2006.11.025

Chamberlain, M. A., Lovell, A. J., & Sykes, M. (2009). Submillimeter photometry and lightcurves of Ceres and other large asteroids. *Icarus,* **202**(2), 487-501. doi:10.1016/j.icarus.2009.03.002

Chapman, C.R., McCord, T.B. & Johnson, T.V. (1973). Asteroid spectral reflectivities. *Astronomical Journal*, **78**,126-146.

Chapman, C.R. & Salisbury, J.W. (1973). Comparison of meteorite and asteroid spectral reflectivities. *Icarus*, **19**, 507-522.

Chapman, C.R. & Gaffey, M.J. (1979). Reflectance spectra for 277 asteroids, in *Asteroids*. Editor T. Gehrels, University of Arizona Press, Tucson, Arizona, USA, pp. 655-687.

Chen, J. H., & Wasserburg, G. J. (1981). The isotopic composition of uranium and lead in Allende inclusions and meteoritic phosphates. *Earth and Planetary Science Letters*, **52**(1), 1-15.

Clarke Jr, R. S., Jarosewich, E., Mason, B., Nelen, J., Gomez, M., & Hyde, J. R. (1971). The Allende, Mexico, meteorite shower. *Smithsonian Contributions to the Earth Sciences*, **5**, 1-53.

Clark, R. N. (1981). Water frost and ice: The near-infrared spectral reflectance 0.65–2.5 μm. *Journal of Geophysical Research: Solid Earth (1978–2012)*, **86**(B4), 3087-3096.

Clark, R. N., King, T. V., Klejwa, M., Swayze, G. A., & Vergo, N. (1990). High spectral resolution reflectance spectroscopy of minerals. *Journal of Geophysical Research: Solid Earth (1978–2012)*, **95**(B8), 12653-12680.

Clark, R. N. (1999). Spectroscopy of rocks and minerals, and principles of spectroscopy. *Manual of remote sensing*, **3**, 3-58.

Cloutis, E.A. (1990). Identification, detection and characterization of individual tar sand phases using diffuse reflectance spectroscopy (0.35-2.6 µm). *AOSTRA Journal of Research,* **6**, 17-27.

Cloutis, E.A., McCormack, K.A., Bell III, J.F., Hendrix, A.R., Bailey, D.T., Craig, M.A., Mertzman, S.A., Robinson, M.S., & Riner, M.A. (2008). Ultraviolet spectral reflectance properties of common planetary minerals. *Icarus*, **197**, 321-347.

Cloutis, E. A., Hiroi, T., Gaffey, M. J., Alexander, C. M., & Mann, P. (2011a). Spectral reflectance properties of carbonaceous chondrites: 1. CI chondrites. *Icarus,* **212**(1), 180-209.

Cloutis, E. A., Hudon, P., Hiroi, T., Gaffey, M. J., & Mann, P. (2011b). Spectral reflectance properties of carbonaceous chondrites: 2. CM chondrites. *Icarus,* **216**(1), 309-346.

Cloutis, E. A., Hudon, P., Hiroi, T., Gaffey, M. J., & Mann, P. (2012a). Spectral reflectance properties of carbonaceous chondrites – 5.: CO chondrites. *Icarus*, **220**(1), 466-486.

Cloutis, E. A., Hudon, P., Hiroi, T., Gaffey, M. J., Mann, P. & Bell III, J.F. (2012b). Spectral reflectance properties of carbonaceous chondrites – 6.: CV chondrites. *Icarus*, **221**(1), 328-358.

Cohen, M., Witteborn, F. C., Roush, T., Bregman, J., & Wooden, D. (1998). Spectral irradiance calibration in the infrared. VIII. 5-14 micron spectroscopy of the asteroids Ceres, Vesta, and Pallas. *The Astronomical Journal,* **115**(4), 1671-1679.

Colthup, N. B. (1950). Spectra-structure correlations in the infra-red region. *JOSA*, **40**(6), 397-400.

Conel, J. E. (1969). Infrared emissivities of silicates: Experimental results and a cloudy atmosphere model of spectral emission from condensed particulate mediums. *Journal of Geophysical Research*, **74(**6), 1614-1634.

Coradini, A., Turrini, D., Federico, C., & Magni, G. (2011). Vesta and Ceres: Crossing the history of the solar system. *Space Science Reviews*, **163**(1-4), 25-40. doi:10.1007/s11214-011-9792-x

Cruikshank, D.P. & Morrison, D. (1973). Radii and albedos of nine asteroids. *Bulletin of the American Astronomical Society*, **5**, 308.

Cyr, K.E., Sears, W.D. & Lunine, J.I. (1998). Distribution and Evolution of Water Ice in the Solar Nebula: Implications for Solar System Body Formation. *Icarus* **135**(2), 537–548.

De Sanctis, M. C., Coradini, A., Ammannito, E., Filacchione, G., Capria, M. T., Fonte, S., . . . Dami, M. (2012). The VIR spectrometer. In *The dawn mission to minor planets 4 Vesta and 1 Ceres,* editors C. T. Russell, C. Raymond, Springer, New York, USA, pp. 329-369.

Dollfus, A., Wolff, M., Geake, J. E., Dougherty, L. M., & Lupishko, D. F. (1989). Photopolarimetry of asteroids. In *Asteroids II,* ed. R. P. Binzel, T. Gehrels, & M. S. Matthews, University of Arizona Press, Tucson, USA, pp. 594-616.

Drummond, J., & Christou, J. (2008). Triaxial ellipsoid dimensions and rotational poles of seven asteroids from Lick Observatory adaptive optics images, and of Ceres. *Icarus*, **197**(2), 480-496.

European Space Agency ESA. “Space Science: Herschel discovers water vapour around dwarf planet Ceres” http://www.esa.int/Our_Activities/Space_Science/Herschel/Herschel_discovers_water_vapour_around_dwarf_planet_Ceres Last updated: December 2014.

Fanale, F. P., & Salvail, J. R. (1989). The water regime of asteroid (1) Ceres. *Icarus,* **82**(1), 97-110. doi:http://dx.doi.org/10.1016/0019-1035(89)90026-2

Farmer, V. C. (1974). *Infrared spectra of minerals*. Mineralogical society.

Feierberg, M. A., Lebofsky, L. A., & Larson, H. P. (1981). Spectroscopic evidence for aqueous alteration products on the surfaces of low-albedo asteroids. *Geochimica et Cosmochimica Acta*, **45**(6), 971-981.

Fuchs, L.H., Olsen, E. & Jensen, K.J. (1973). Mineralogy, mineral-chemistry and composition of the Murchison (C2) meteorite. Smithson. Contrib. Earth Sci. No. 10, 39 pp.

Fysh, S. A., Swinkels, D. A., & Fredericks, P. M. (1985). Near-infrared diffuse reflectance spectroscopy of coal. *Applied Spectroscopy*, **39**(2), 354-357.

Gaffey, M.J. (1976). Spectral reflectance chracteristics of the meteorite classes. *Journal of Geophysical Research*, **81**, 905-920.

Gaffey, M.J., Burbine, T.H. & Binzel, R.P. (1993). Asteroid Spectroscopy: Progress and perspectives. *Meteoritics* **28**(2), 161-187.

Gaffey, S. J. (1985). Reflectance spectroscopy in the visible and near-infrared (0.35–2.55 μm): Applications in carbonate petrology. *Geology*, **13**(4), 270-273.

Gaffey, S. J. (1986). Spectral reflectance of carbonate minerals in the visible and near infrared (0.35-2.55 microns); calcite, aragonite, and dolomite. *American Mineralogist*, **71**(1-2), 151-162.

Gaffey, S. J., L. A. McFadden, D. Nash, and C. M. Pieters (1993. Ultraviolet, visible, and near-infrared reflectance spectroscopy: Laboratory spectra of geologic materials, in *Remote Geochemical Analysis: Elemental and Mineralogical Composition*. Editors C. M. Pieters and P. A. J. Englert, Cambridge University Press, New York, NY, pp. 43-77.

Greenwood, R. C., & Franchi, I. A. (2004). Alteration and metamorphism of CO3 chondrites: Evidence from oxygen and carbon isotopes. *Meteoritics & Planetary Science*, **39(**11), 1823-1838.

Grossman, L., & Olsen, E. (1974). Origin of the high-temperature fraction of C2 chondrites. *Geochimica et Cosmochimica Acta*, ***38*****(**1), 173-187.

Guimon, R.K., Symes, S.J.K., Sears, D.W.J., & Benoit, P.H. (1995). Chemical and physical studies of type 3 chondrites XII: The metamorphic history of CV chondrites and their components. *Meteoritics*, **30**(6), 704-714.

Gounelle, M., & Zolensky, M. E. (2001). A terrestrial origin for sulfate veins in CI1 chondrites. *Meteoritics & Planetary Science*, **36(**10), 1321-1329.

Gyollai, I., Nagy, S., Bérczi, S., & Gucsik, A. (2011). Comparison of aqueous alteration of two CV3 (Kaba and Yamato-86751) chondrites. Lunar and Planetary Science Conference, vol. 42, p. 1039.

Harlov, D. E., Andrut, M., & Pöter, B. (2001). Characterisation of buddingtonite (NH4)[AlSi3O8] and ND4-buddingtonite (ND4)[AlSi3O8] using IR spectroscopy and Rietveld refinement of XRD spectra. *Physics and Chemistry of Minerals*, **28**(3), 188-198.

Hartmann, H., & Ilse, F.E. (1951). Thermsysteme elektrostatischer Komplexionen der Übergangsmetalle mit einem d-Elektron. *Zeitschrift für physikalische Chemie*, **197**, 239; *Zeitschrift für Naturforschung*, **6**, 751.

Hass, M., & Sutherland, G. B. (1956). The infra-red spectrum and crystal structure of gypsum. *Proceedings of the Royal Society of London. Series A. Mathematical and Physical Sciences*, **236**(1207), 427-445.

Helbert, J., Maturilli, A. and D’Amore, M. (2010). High-temperature Emission Spectroscopy – The Planetary Emissivity Laboratory (PEL) at DLR. 41st Lunar and Planetary Science Conference (2010), LPI Contribution No. 1533.

Herschel W. (1802). Observations on the two lately discovered celestial bodies. *Philosophical Transactions of the Royal Society of London*, 213-232.

Hexter, R. M. (1958). High-resolution, temperature-dependent spectra of calcite. *Spectrochimica Acta*, **10(**3), 281-290.

Hilton, J.L. (1998). US naval observatory ephemerides of the largest asteroids. *The Astronomical Journal*, **117**, 1077-1086.

Hiroi, T., Zolensky, M. E., Pieters, C. M., & Lipschutz, M. E. (1996). Thermal metamorphism of the C, G, B, and F asteroids seen from the 0.7 μm, 3 μm, and UV absorption strengths in comparison with carbonaceous chondrites. *Meteoritics & Planetary Science*, **31**(3), 321-327.

Howard, K. T., Benedix, G. K., Bland, P. A., & Cressey, G. (2009). Modal mineralogy of CM2 chondrites by X-ray diffraction (PSD-XRD). Part 1: Total phyllosilicate abundance and the degree of aqueous alteration. *Geochimica et Cosmochimica Acta*, ***73***(15), 4576-4589.

Howard, K. T., Benedix, G. K., Bland, P. A., & Cressey, G. (2009a). Modal mineralogy of CV3 chondrites by PSD-XRD: mineralogic insights into a complex evolutionary history. Lunar and Planetary Science Conference, *v*ol. 40, p. 1235.

Howard, K. T., Benedix, G. K., Bland, P. A., & Cressey, G. (2011). Modal mineralogy of CM chondrites by X-ray diffraction (PSD-XRD): Part 2. Degree, nature and settings of aqueous alteration. *Geochimica et Cosmochimica Acta*, ***75***(10), 2735-2751.

Hunt, G.R.. (1982). Spectroscopic properties of rocks and minerals, in *Handbook of Physical properties of rocks Volume I.* Editor R. S. Carmichael, CRC Press, Boca Raton, 295-385.

Hunt, G. R., & Salisbury, J. W. (1970). Visible and near infrared spectra of minerals and rocks. I. Silicate minerals. *Modern Geology*, **2,** 23-30.

Hunt, G. R., & Salisbury, J. W. (1971). Visible and near infrared spectra of minerals and rocks. II. Carbonates. *Modern Geology*, **1,** 283-300.

Hunt, G. R. (1977). Spectral signatures of particulate minerals in the visible and near infrared. *Geophysics*, **42**(3), 501-513.

Ito, O., Seki, H., & Iino, M. (1988). Diffuse reflectance spectra in near-ir region of coals; a new index for degrees of coalification and carbonization. *Fuel*, **67**(4), 573-578.

Jaraosewich, E. (1971). Chemical analysis of the Murchison meteorite. *Meteoritics*, **6**(1), 49-52.

Jarosewich, E. (1990). Chemical analysis of meteorites: A compilation of stony and iron meteorite analysis. *Meteoritics*, **25**(4), 323-337.

Johnson, W.A. (1939). Spectrophotometric study of three asteroids. *Harvard College Observatory Bulletins*, **911**, 13-16.

Johnson, T.V. & Fanale, F.P. (1973). Optical properties of carbonaceous chondrites and their relationship to asteroids. *Journal of Geophyisical Research*, **78**(35), 8507-8518.

JPL Small-Body Database Browser. "1 Ceres" http://ssd.jpl.nasa.gov/sbdb.cgi#top Last updated: November 2014.

W.M. Keck Observatory. "Images of Dwarf Planet Ceres" http://www.keckobservatory.org/recent/entry/images_of_dwarf_planet_ceres Last updated: December 2014.

Keller, L. P., & Buseck, P. R. (1990a). Matrix mineralogy of the Lancé CO3 carbonaceous chondrite: A transmission electron microscope study. *Geochimica et Cosmochimica Acta*, **54**(4), 1155-1163.

Keller, L. P., & Buseck, P. R. (1990b) Aqueous alteration products in CV3 and CO3 carbonaceous chondrite meteorites: Phyllosilicates. Lunar and Planetary Science 21, pp. 619-620.

Keller, L. P., & McKay, D. S. (1993). Aqueous alteration of the Grosnaja CV3 carbonaceous chondrite. *Meteoritics*, **28**, 378.

King, T. V., Clark, R. N., Calvin, W. M., Sherman, D. M., & Brown, R. H. (1992). Evidence for ammonium-bearing minerals on Ceres. *Science*, **255**(5051), 1551-1553. doi:10.1126/science.255.5051.1551

Kmetko, E. A. (1951). Infrared absorption and intrinsic semiconductivity of condensed aromatic systems. *Physical Review*, **82**(3), 456.

Konopliv, A. S., Asmar, S. W., Bills, B. G., Mastrodemos, N., Park, R. S., Raymond, C. A., . . . Zuber, M. T. (2011). The dawn gravity investigation at Vesta and Ceres. *Space Science Reviews*, **163**(1-4), 461-486. doi:10.1007/s11214-011-9794-8

Kovacevic, A., & Kuzmanoski, M. (2007). A new determination of the mass of (1) Ceres. *Earth, Moon, and Planets*, **100**(1-2), 117-123. doi:10.1007/s11038-006-9124-4

Küppers, M., O'Rourke, L., Bockelée-Morvan, D., Zakharov, V., Lee, S., von Allmen, P., . . . Moreno, R. (2014). Localized sources of water vapour on the dwarf planet (1) Ceres. *Nature Letter*, **505**(7484), 525-527. doi:10.1038/nature12918

Lagerkvist, C. I., and P. Magnusson (1990). Analysis of asteroid light curves II—Phase curves in a generalized HG-system. *Astronomy and Astrophysics Supplementary Series*, **86**, 119–165.

Larson, H. P., Feierberg, M. A., Fink, U., & Smith, H. A. (1979). Remote spectroscopic identification of carbonaceous chondrite mineralogies: Applications to Ceres and Pallas. *Icarus*, **39**(2), 257-271. doi:http://dx.doi.org/10.1016/0019-1035(79)90168-4

Lebofski, L. A. (1978). Asteroid 1 Ceres: Evidence for water of hydration. *Monthly Notices of the Royal Astronomical Society*, **182**(1), 17-21.

Lebofsky, L. A., Feierberg, M. A., Tokunaga, A. T., Larson, H. P., & Johnson, J. R. (1981). The 1.7-to 4.2-μm spectrum of asteroid 1 Ceres: Evidence for structural water in clay minerals. *Icarus*, **48**(3), 453-459.

Li, J. Y., McFadden, L. A., Parker, J. W., Young, E. F., Stern, S. A., Thomas, P. C., . . . Sykes, M. V. (2006). Photometric analysis of 1 ceres and surface mapping from HST observations. *Icarus*, **182**(1), 143-160. doi:10.1016/j.icarus.2005.12.012.

Li, J.Y., McFadden, L.A., A'Hearn, M.F., Feaga, L.M., Russell, C.T., Coradini, A., De Sanctis,C., & Ammanito, E. (2009) UV absorption features of asteroid 1 Ceres. Lunar and Planetary Science Conference, Vol. 40, Abstract #2101.

Lim, L. F., McConnochie, T. H., Bell III, J. F., & Hayward, T. L. (2005). Thermal infrared (8–13 μm) spectra of 29 asteroids: The Cornell mid-infrared asteroid spectroscopy (MIDAS) survey. *Icarus,* **173**(2), 385-408. doi:10.1016/j.icarus.2004.08.005

Lupishko, D. F., & Mohamed, R. A. (2009). Asteroids 1 Ceres and 4 Vesta: Objects of the Dawn space mission. *Solar System Research,* **43**(6), 475-482.

Macke, R. J., Guy J. Consolmagno, G.J. & Britt, D.T. (2011). Density, porosity, and magnetic susceptibility of carbonaceous chondrites. *Meteoritics & Planetary Science,* **46**(12), 1842–1862. doi: 10.1111/j.1945-5100.2011.01298.x

Mara, R. T., & Sutherland, G. B. B. M. (1953). The Infrared Spectrum of Brucite [Mg $(OH)_2$]. *Journal of the Optical Society of America A*, **43**(11), 1100-1102.

MPS Max-Planck-Institute for Solar System Research. "Dawn mission" https://www.mps.mpg.de/3928939/Framing_Camera_1_MPS_JPG, Last updated: March 2015.

McCord,T. B. & Sotin, C. (2003). The Small Planet Ceres: Models of Evolution and Predictions of Current State. American Astronomical Society, DPS meeting #35, #34.17*; Bulletin of the American Astronomical Society*, **Vol. 35,** p.979.

McCord, T. B., & Sotin, C. (2005). Ceres: Evolution and current state. *Journal of Geophysical Research: Planets (1991–2012),* **110(**E5).

McKinnon, W. B. (2008). Could Ceres be a refugee from the kuiper belt? LPI Contributions, Abstract #8389.

McKinnon, W. B. (2012). Where did Ceres accrete? LPI Contributions, Abstract #6475.

McMichael, B. D., Kmetko, E. A., & Mrozowski, S. (1954). An aromatic detector for the infrared. *Journal of the Optical Society of America A*, **44**(1), 26-30.

McSween Jr, H. Y. (1977). Carbonaceous chondrites of the Omans type: A metamorphic sequence. *Geochimica et Cosmochimica Acta*, **41**(4), 477-491.

McSween Jr, H. Y. (1979). Alteration in CM carbonaceous chondrites inferred from modal and chemical variations in matrix. *Geochimica et Cosmochimica Acta*, ***43***(11), 1761-1770.

McSween Jr, H. Y. (1979a). Are carbonaceous chondrites primitive or processed? A review. *Reviews of Geophysics and Space Physics*, **17**(5), 1059-1078.

Michalak, G. (2000). Determination of asteroid masses---I.(1) Ceres,(2) Pallas and (4) Vesta. *Astronomy and Astrophysics*, **360,** 363-374.

Milliken, R. E., & Rivkin, A. S. (2009). Brucite and carbonate assemblages from altered olivine-rich materials on Ceres. *Nature Geoscience*, **2**(4), 258-261. doi:10.1038/ngeo478.

Millis, R. L., Wasserman, L. H., Franz, O. G., Nye, R. A., Oliver, R. C., Kreidl, T. J., . . . Goff, R. (1987). The size, shape, density, and albedo of Ceres from its occultation of BD 8 471. *Icarus*, **72**(3), 507-518.

Mitchell, D. L., Ostro, S. J., Hudson, R. S., Rosema, K. D., Campbell, D. B., Vélez, R., Chandler, J.F., Shapiro, I.I., Giorgini, J.D., and Yeomans, D. K. (1996). Radar observations of asteroids 1 Ceres, 2 Pallas, and 4 Vesta. *Icarus*, **124**(1), 113-133. doi:http://dx.doi.org/10.1006/icar.1996.0193.

Miyamoto, M., & Zolensky, M. E. (1994). Infrared diffuse reflectance spectra of carbonaceous chondrites: Amount of hydrous minerals. *Meteoritics*, **29**(6), 849-853.

Morbidelli, A., Chambers, J., Lunine, J. I., Petit, J. M., Robert, F., Valsecchi, G. B., & Cyr, K. E. (2000). Source regions and timescales for the delivery of water to the Earth. *Meteoritics & Planetary Science*, **35**(6), 1309-1320.

Moroz, L. V., Arnold, G., Korochantsev, A. V., & Wäsch, R. (1998). Natural Solid Bitumens as Possible Analogs for Cometary and Asteroid Organics: 1. Reflectance spectroscopy of pure bitumens. *Icarus*, **134**(2), 253-268.

Moullet, A., Gurwell, M., & Carry, B. (2010). Thermal rotational lightcurve of dwarf-planet (1) Ceres at 235 GHz with the submillimeter array. *Astronomy and Astrophysics*, **516**(id.L10), 1-4. doi:10.1051/0004-6361/201014792.

Mousis, O., & Alibert, Y. (2005). On the composition of ices incorporated in Ceres. *Monthly Notices of the Royal Astronomical Society*, **358**(1), 188-192. doi:10.1111/j.1365-2966.2005.08777.x

Nagy, B. (1975). *Carbonaceous meteorites*. Amsterdam: Elsevier, 747pp.

NASA Jet Propulsion Laboratory (a). “Solar System Exploration: Ceres” http://solarsystem.nasa.gov/planets/profile.cfm?Object=Dwa_Ceres Last updated: August 2014.

NASA Jet Propulsion Laboratory (b). “Solar System Exploration: Ceres: Facts and Figures” http://solarsystem.nasa.gov/planets/profile.cfm?Object=Dwa_Ceres&Display=Facts Last updated: August 2014.

Nelson, M. L., Britt, D. T., & Lebofsky, L. A. (1993). *Review of asteroid compositions. Resources of near-earth space*, pp. 493-522.

O’Brien, D. P., & Sykes, M. V. (2011). The origin and evolution of the asteroid belt—implications for Vesta and Ceres. *Space Science Reviews*, **163**(1-4), 41-61. doi:10.1007/s11214-011-9808-6

Osawa, T., Kagi, H., Nakamura, T., & Noguchi, T. (2005). Infrared spectroscopic taxonomy for carbonaceous chondrites from speciation of hydrous components. *Meteoritics & Planetary Science*, **40**(1), 71-86.

Ostro, S. J., Pettengill, G. H., Shapiro, I. I., Campbell, D. B., & Green, R. R. (1979). Radar observations of asteroid 1 Ceres. *Icarus*, **40**(3), 355-358. doi:http://dx.doi.org/10.1016/0019-1035(79)90027-7

Painter, P. C., Starsinic, M., & Coleman, M. M. (2012). Determination of functional groups in coal by Fourier transform interferometry. *Fourier Transform Infrared Spectroscopy*, **4**, 169-240.

Parker, J. W., Stern, S. A., Thomas, P. C., Festou, M. C., Merline, W. J., Young, E. F., . . . Lebofsky, L. A. (2002). Analysis of the first disk-resolved images of Ceres from ultraviolet observations with the Hubble Space Telescope. *The Astronomical Journal*, **123**(1), 549-557. doi:10.1086/338093

Parker, J. W., McFadden, L. A., Russell, C. T., Stern, S. A., Sykes, M. V., Thomas, P. C., & Young, E. F. (2006). Ceres: High-resolution imaging with HST and the determination of physical properties. *Advances in Space Research*, **38**(9), 2039-2042. doi:10.1016/j.asr.2004.12.040

Pearson, V. K., Sephton, M. A., Franchi, I. A., Gibson, J. M., & Gilmour, I. (2006). Carbon and nitrogen in carbonaceous chondrites: Elemental abundances and stable isotopic compositions. *Meteoritics & Planetary Science*, **41**(12), 1899-1918.

Prettyman, T. H., Feldman, W. C., Ameduri, F. P., Barraclough, B. L., Cascio, E. W., Fuller, K. R., . . . Tokar, R. L. (2003). Gamma-ray and neutron spectrometer for the DAWN mission to 1 Ceres and 4 Vesta. *IEEE Transactions on Nuclear Science,* **50**(4), 1190-1197. doi:10.1109/TNS.2003.815156

Prost, R. (1975) l) Etude de l'hydration des argiles: interactions eau-minrral et mrcanisme de la retention de l'eau. II. L'tude d'une smectite: Ann. Agron. 26, 463-535.

Rajan, S., & Gaffey, M. J. (1984, March). Spectral reflectance characteristics of Allende white inclusions. Lunar and Planetary Science Conference 15, pp. 659-660.

Renger, T., Sznajder, M., Witzke, A., & Geppert, U. R. (2014). The Complex Irradiation Facility at DLR-Bremen. In *Advances in Solar Sailing*, editor M. Macdonald, Springer Berlin Heidelberg, pp. 541-557.

Richardson, S. M. (1978). Vein formation in the C1 carbonaceous chondrites. *Meteoritics*, **13**(1), 141-159.

Rivkin, A. S., Davies, J. K., Johnson, J. R., Ellison, S. L., Trilling, D. E., Brown, R. H., & Lebofsky, L. A. (2003). Hydrogen concentrations on C-class asteroids derived from remote sensing. *Meteoritics & Planetary Science*, **38(**9), 1383-1398.

Rivkin, A. S., Volquardsen, E. L., & Clark, B. E. (2006). The surface composition of Ceres: Discovery of carbonates and iron-rich clays. *Icarus*, **185(**2), 563-567. doi:10.1016/j.icarus.2006.08.022

Rivkin, A. S., Castillo-Rogez, J. C., Cohen, B. A., Conrad, P. G., Li, J., Lim, L. F., ... McKinnon, W. B. (2010). The Case for Ceres: Report to the Planetary Science Decadal Survey Committee. American Astronomical Society, DPS meeting #41, #16.22.

Rivkin, A. S., & Volquardsen, E. (2010). Rotationally-resolved spectra of Ceres in the 3-μm region. *Icarus*, **206**(1), 327-333. doi:10.1016/j.icarus.2009.08.026

Rivkin, A. S., Li, J. Y., Milliken, R., Lim L., Lovell, A., Schmidt, B., & McFadden, L. B. (2011). The surface composition of Ceres. *Space Science Reviews,* **163**(1), 95-116. doi:10.1007/s11214-010-9677-4

Roettger, E.E. & Buratti, B.J. (1994). Ultraviolet spectra and geometric albedos of 45 asteroids. *Icarus*, **112**(2), 496-512.

Rogozin, Y. I. (2014). On the possible origin of the asteroid (1) Ceres. *arXiv preprint arXiv:1403.4579*.

Rousselot, P., Jehin, E., Manfroid, J., Mousis, O., Dumas, C., Carry, B., . . . Zucconi, J. -. (2011). A search for water vaporization on Ceres. *The Astronomical Journal,* **142**(4), 125 (6pp). doi:10.1088/0004-6256/142/4/125

Rubin, A. E., James, J. A., Keck, B. D., Weeks, K. S., Sears, D. W., & Jarosewich, E. (1985). The Colony meteorite and variations in CO3 chondrite properties. *Meteoritics*, **20**(2), 175-196.

Rubin, A. E., Trigo-Rodríguez, J. M., Huber, H., & Wasson, J. T. (2007). Progressive aqueous alteration of CM carbonaceous chondrites. *Geochimica et Cosmochimica Acta*, ***71***(9), 2361-2382.

Russell, J. D., & Farmer, V. C. (1964). Infra-red spectroscopic study of the dehydration of montmorillonite and saponite. *Clay Minerals Bulletin*, **5**(32), 443-464.

Russell, J. D., & Fraser, A. R. (1971). IR spectroscopic evidence for interaction between hydronium ions and lattice OH groups in montmorillonite. *Clays and Clay Minerals*, **19**, 55.

Russell, C. T., Coradini, A., Christensen, U., De Sanctis, M., Feldman, W., Jaumann, R., H.U. Keller, H.U., Konopliv, A.S., McCord, T.B., McFadden, L.A., McSween, H.Y., Mottola, S., Neukum, G., Pieters, C.M., Prettyman, T.H., Raymond, C.A., Smith, D.E., Sykes, M.V., Williams, B.G., Wise, J., and Zuber, M.T.. (2004). Dawn: A journey in space and time. *Planetary and Space Science,* **52**(5), 465-489.

Russell, C. T., Capaccioni, F., Coradini, A., Christensen, U., De Sanctis, M. C., Feldman, W. C., . . . Zuber, M. T. (2006). Dawn discovery mission to vesta and ceres: Present status. *Advances in Space Research,* **38**(9), 2043-2048. doi:10.1016/j.asr.2004.12.041

Russell, C. T., & Raymond, C. A. (2011). The dawn mission to Vesta and Ceres. *Space Science Reviews,* **163**(1-4), 3-23. doi:10.1007/s11214-011-9836-2

Sato, K., Miyamoto, M., & Zolensky, M. E. (1997). Absorption bands near three micrometers in diffuse reflectance spectra of carbonaceous chondrites: Comparison with asteroids. *Meteoritics & Planetary Science*, **32**(4), 503-507.

Saint-Pé, O., Combes, M., & Rigaut, F. (1993). Ceres surface properties by high-resolution imaging from earth. *Icarus*, **105**(2), 271-281. doi:http://dx.doi.org/10.1006/icar.1993.1125

Salisbury, J. W., & Walter, L. S. (1989). Thermal infrared (2.5–13.5 μm) spectroscopic remote sensing of igneous rock types on particulate planetary surfaces. *Journal of Geophysical Research: Solid Earth (1978–2012)*, **94**(B7), 9192-9202.

Salisbury, J. W., Walter, L. S., Vergo, N., & D'Aria, D. M. (1991). Infrared (2.1–25 micrometers) spectra of minerals. In *Infrared (2.1-25 micrometers) Spectra of Minerals*. John Hopkins University Press, Baltimore, MA, USA.

Salisbury J. W. (1993) Ultraviolet, visible, and near-infrared reflectance spectroscopy: Laboratory spectra of geologic materials, in *Remote Geochemical Analysis: Elemental and Mineralogical Composition*, edited by C. M. Pieters and P. A. J. Englert, Cambridge University Press, New York, NY, pp. 79-98.

Schirmeyer, S., Bischoff, A., Stephan, T., & Jessberger, E. K. (1996). Lithium-bearing Phases in Ca, Al-rich Inclusions from CM-Chondrites: Indication of Nebular Alteration Processes. Lunar and Planetary Institute Science Conference 27, p. 1141.

Shaw, D.M. & Harmon, R.S. (1975). Factor analysis of elemental abundances in chondritic and achondritic meteorites. *Meteoritics*, **10**, 253-282.

Sherman, D. M., Burns, R. G., & Burns, V. M. (1982). Spectral characteristics of the iron oxides with application to the Martian bright region mineralogy. *Journal of Geophysical Research: Solid Earth (1978–2012)*, **87**(B12), 10169-10180.

Sherman, D.M. & Waite, T.D. (1985). Electronic spectra of Fe^{3+} oxides and oxide hydroxides in near IR and near UV. *American Mineralogist*, **70**, 1262-1269.

Sherman, D. M., & Vergo, N. (1988). Optical (diffuse reflectance) and Mössbauer spectroscopic study of nontronite and related Fe-bearing smectites. *American Mineralogist*, **73(**11-12), 1346-1354.

Sierks, H., Keller, H. U., Jaumann, R., Michalik, H., Behnke, T., Bubenhagen, F., ... & Tschentscher, M. (2011). The Dawn framing camera. *Space science reviews*, **163**(1-4), 263-327.

Stubičan, V., & ROY, R. (1961). Infrared Spectra of Layer-Structure Silicates. *Journal of the American Ceramic Society*, **44**(12), 625-627.

Solar System Dynamics: JPL Small-Body Database Browser. "1 Ceres" http://ssd.jpl.nasa.gov/sbdb.cgi#top Last updated: August 2014.

Takir, D., Emery, J. P., Mcsween, H. Y., Hibbitts, C. A., Clark, R. N., Pearson, N., & Wang, A. (2013). Nature and degree of aqueous alteration in CM and CI carbonaceous chondrites. *Meteoritics & Planetary Science*, **48**(9), 1618-1637.

Tedesco, E. F. (1989). Asteroid magnitudes, UBV colors, and IRAS albedos and diameters, in *Asteroids II*. Editors R. P. Binzel, T. Gehrels & M. S. Matthews, United States: University of Arizona Press, pp. 1090-1138.

Tholen, D.J. (1984). Asteroid taxonomy from cluster analysis of photometry. Ph.D. thesis, University of Arizona, Tucson, pp. 150.

Tholen, D.J., and Barucci, M.A. (1989). Asteroid taxonomy, in *Asteroids II*. Editors R.P. Binzel, T. Gehrels and M.S. Matthews, University of Arizona Press, Tucson, pp. 298-315.

Thomas, P. C., Parker, J. W., McFadden, L. A., Russell, C. T., Stern, S. A., Sykes, M. V., & Young, E. F. (2005). Differentiation of the asteroid Ceres as revealed by its shape. *Nature*, **437**(7056), 224-226. doi:10.1038/nature03938

Tosi, C., & Pinto, A. (1972). Near-infrared spectroscopy of hydrocarbon functional groups. *Spectrochimica Acta Part A: Molecular Spectroscopy*, **28**(3), 585-597.

Turekian, K.K & J.Laurence Kulp, J. (1956). The geochemistry of strontium. *Geochimica et Cosmochimica Acta*, **10** (5-6), 245–296.

Van Vleck, J. (1932). Theory of the variations in paramagnetic anisotropy among different salts of the iron group. *Physical Review* **41**: 208.

Vernazza, P., Mothé-Diniz, T., Barucci, M. A., Birlan, M., Carvano, J. M., Strazzulla, G., . . . Migliorini, A. (2005). Analysis of near-IR spectra of 1 Ceres and 4 Vesta, targets of the dawn mission. *Astronomy and Astrophysics*, **436**(3), 1113-1121. doi:10.1051/0004-6361:20042506

Vilas, F. & Gaffey, M.J. (1989). Identification of phyllosilicates absorption features in main-belt and outer-belt asteroid reflectance spectra. *Science*, **246**, 790-792.

Vilas, F., Larson, S. M., Hatch, E. C., & Jarvis, K. S. (1993). CCD reflectance spectra of selected asteroids. II. Low-albedo asteroid spectra and data extraction techniques. *Icarus*, **105**(1), 67-78.

Vincent, R. K., & Hunt, G. R. (1968). Infrared reflectance from mat surfaces. *Applied Optics*, **7**(1), 53-59.

Von Michaelis, H. (1969). The composition of stony meteorites—III. Some inter-element relationships. *Earth and Planetary Science Letters*, **5**, pp. 395–400.

Warner, B.D., Harris, A.W., Pravec, P. (2009). *Icarus* **202**, 134-146. *http://www.MinorPlanet.info/lightcurvedatabase.html* Last updated: February 2015.

Webster, W. J., Johnston, K. J., Hobbs, R. W., Lamphear, E. S., Wade, C. M., Lowman, P. D., . . . Seidelmann, P. K. (1988). The microwave spectrum of asteroid Ceres. *The Astronomical Journal,* **95**, 1263-1268.

Zaikowski, A. (1979). Infrared spectra of the Orgueil (C-1) chondrite and serpentine minerals. *Geochimica et Cosmochimica Acta***, 43** (1979), pp. 943–945.

Zellner, B., Gehrels, T., & Graide, J. (1974). Minor planets and related objects. XVI – Polarimetric diameters. *Astrophysical Journal*, **79**, 1100-1110.

Zolensky, M., & McSween Jr, H. Y. (1988). Aqueous alteration. *Meteorites and the early solar system*, **1,** 114-143.

Zolensky, M. Barrett, R., & Browning, L. (1993). Mineralogy and composition of matrix and chondrule rims in carbonaceous chondrites. *Geochimica et Cosmochimica Acta*, **57**(13), 3123-3148.

Zolotov, M. Y. (2009). On the composition and differentiation of Ceres. *Icarus*, **204**(1), 183-193. doi:http://dx.doi.org/10.1016/j.icarus.2009.06.011

Zolotov, M. Y. (2014). Formation of brucite and cronstedtite-bearing mineral assemblages on Ceres. *Icarus*, **228**, 13-26. doi:http://dx.doi.org/10.1016/j.icarus.2013.09.020